UNIVERSITY OF CALIFORNIA
RIVERSIDE

Exploring the Geochemical Fingerprints of an Oceanic Anoxic Event During the Late Cretaceous: the Global and Biological Implications

A Dissertation submitted in partial satisfaction
of the requirements for the degree of

Doctor of Philosophy

in

Geological Sciences

by

Jeremiah David Owens

December 2013

Dissertation Committee:
Dr. Timothy W. Lyons, Chairperson
Dr. Gordon D. Love
Dr. Richard A. Minnich

The Dissertation of Jeremiah David Owens is approved:

_____

_____

_____
Committee Chairperson

University of California, Riverside

Acknowledgements

This truly has been a fantastic journey and has been filled with great experiences which was made possible through the support of friends, family and colleagues (many of these lines blurring) throughout my unconventional journey. First, I would like to start by thanking my committee Tim Lyons, Gordon Love and Rich Minnich for all of the scientific guidance and knowledge you have provided throughout my tenure at UCR. Tim, I thank you for your patients and guidance as an advisor and being a great friend but, in particular, I am indebted for your confidence and trust in me as an incoming student. I would be remised to not acknowledge those who have significantly impacted my career through their inspiration and mentorship in my most formative years – Silke Severmann, Rob Raiswell, Ben Gill and Gordon Love. I owe Hugh Jenkyns a debt of gratitude for all the support, guidance, sample and analytical expertise over the last four years.

Throughout my graduate tenure I have been surrounded by a tremendously talented, fun and unselfish group of people whom I am proud to have as friends. This group has provided many great times over the last 7 years – camping, concerts, shooting hoops, mountain biking, feuerzangenbowle parties, pig roasts, etc. Additionally, this group has been instrumental in all my scientific endeavors and I have been incredibly lucky to have on-going collaborations with nearly the entire group. Thank you to all of my friends: Steve Bates, Anthony Chappaz, Mike Formolo, Bill Gilhooly, Ben Gill, Leanne Hancock, Dalton Hardisty, Carina Lee, Noah Planavsky, Natascha Riedinger, Andy Robinson, Megan Rohrssen, Clint Scott, Silke Severmann, Laura Wehrmann, and the tremendous amount of visitors to pass through the Lyons Lab. To those friends that balanced my life outside of work: Susan Gill, Francie and Alex Ortiz, Johnny ‘fingers’

McKinney, Phillip and Mackensey Farmer, Mark and Laurie Pertile, Ryan McKenzie, Clara Lee and Katy Zimmermann, thank you.

Importantly, my family disserves a tremendous amount of credit for this accomplishment as they have always been a source of inspiration and support throughout my life. My interest and desire for understanding our surroundings was cultivated by my parents – they have always been the driving force for my successes which will continue through life. While my general love of science likely stem from my uncle Darol and my interest in Geology originates from Papa's love of rocks which was my first introduction to the stories encapsulated by rocks. My brother has always been a great friend and provided lofty goals to strive for through his example. Thank you to my wife and best friend, Carolyn, everyday you inspire me with your work ethic, compassion and dedication to better those around you encourages me to reach higher. Thank you for allowing me to join your incredible family as the last ten years have been an incredible ride and none of this have been possible without your love and support on this academic rollercoaster.

Finally, the text of this dissertation, in part, is a reprint of the material and was initially part of my master degree as is appears in Owens, J.D., Lyons, T.W., Li, X., Macleod, K.G., Gordon, G., Kuypers, M.M.M., Anbar, A., Kuhnt, W., Severmann, S., 2012. Iron isotope and trace metal records of iron cycling in the proto-North Atlantic during the Cenomanian-Turonian oceanic anoxic event (OAE-2). Paleoceanography 27, PA3223. The co-author, Timothy W. Lyons, listed in the publications directed and supervised the research which forms the basis for this dissertation. All other co-authors provided supporting data and samples, analytical and commentary during the writing the manuscripts.

ABSTRACT OF THE DISSERTATION

Exploring the Geochemical Fingerprints of an Oceanic Anoxic Event During the Late Cretaceous: the Global and Biological Implications

by

Jeremiah David Owens

Doctor of Philosophy, Graduate Program in Geological Sciences
University of California, Riverside, December 2013
Dr. Timothy W. Lyons, Chairperson

Understanding the causes and consequences of oceanic anoxic events (OAEs) has been at the forefront of paleoceanography studies for the last several decades. The Mesozoic Era is noted for numerous OAEs that are diagnostically expressed by widespread organic-carbon deposition and coeval positive carbon-isotope excursions. OAEs have been extensively studied from angles but there is still minimal understanding of the global nature of these events. Through the work presented here I aim to quantify the global extent of euxinia (water column that is anoxic and contains sulfide) and seek to understand global extent of anoxia using a multi-geochemical-proxy approach. This work includes high-resolution studies spanning multiple sections with a global distribution for each proxy (sulfur isotopes, Mo, V and Cr trace metal, Fe isotopes) from OAE2, the Cenomanian-Turonian boundary event (~93.9 Ma).

Coupled carbon and sulfur isotopes show positive isotope excursions at each locality during OAE2; although, the peak magnitudes of these shifts are offset by approximately a few hundred thousand years due to a waning burial of organic carbon and pyrite burial. Geochemical box modeling suggests 2 to 7% of the seafloor sediments were deposited under euxinic conditions. While, Mo trace metal geochemistry suggests

similar results with values of ~10% euxinia and V and Cr depletions prior to euxinia imply increased global anoxia prior to the OAE. An organic carbon compilation suggest the known burial of organic carbon during OAE2 may account for the entire isotope excursion observed unless there is an major change increase in volcanic or weathering fluxes. However, Fe isotopes suggest there was not a pervasive increased signal for hydrothermal delivery of Fe except to the know euxinic basins. Quantitative consideration of these cycles is of paramount importance for constraining the budgets of carbon and sulfur, but also oxygen and other key biological elements, as we seek to improve our understanding of the mechanisms behind the initiation and termination of OAEs.

TABLE OF CONTENTS

CHAPTER 7

LIST OF FIGURES

CHAPTER 1

CHAPTER 2

CHAPTER 3

CHAPTER 4

CHAPTER 5

CHAPTER 6

LIST OF TABLES

Chapter 1

Introduction to Oceanic Anoxic Events (OAEs)

Introduction

The minor chemical gas constituents, i.e. CH_4 and CO_2, of the atmosphere are important for self regulating the Earth's climate throughout the geologic history. However, the atmospheric gas constituents have dramatically changed through time (Canfield, 2005; Holland, 1984; Lyons and Reinhard, 2009). Understanding global climate feedbacks during periods of high and rapid increases of the 'greenhouse gas' CO_2 which has become a focus for Earth science research due to the anthropogenic increase of CO_2 primarily due to the burning of fossil fuels. Also, human activities such as excessive fertilizer use and improper sewage handling have exacerbated natural oxygen consumption so that anthropogenic low oxygen conditions (hypoxia) has become a major concern in many coastal regions throughout the world (Fig. 1.1) and predictions suggest increased deoxygenation in the future (Diaz and Rosenberg, 2008; Falkowski et al., 2011; Virginia, 2010). To help understand future climate change it is important to recognize and appreciate natural climate related variability and the rate of change. For example, extent of ocean deoxygenation, ocean acidification, extinction rates and rise of CO_2. Therefore, understanding natural climate variability in the geologic record has been a locus of interest with a focus on glacial-interglacial cyclicity, perturbations to the organic carbon burial events in the Mesozoic [termed as oceanic anoxic events (OAEs)] and hyperthermal events in the Cenozoic (i.e. Paleocene-Eocene Thermal Maximum).

In order to understand the oxygen, an important atmospheric gas for animals, cycle it is imperative to fully recognize the interplay between geochemical cycles which include, sulfur (S) and iron (Fe) but most importantly carbon (C) which is integral in regulating atmospheric oxygen throughout Earth's history (Berner, 1992; Berner, 2001; Berner, 2006; Berner and Canfield, 1989). The short term carbon cycle, days to thousands of years, is driven by biologically induced activity. Photosynthesis and

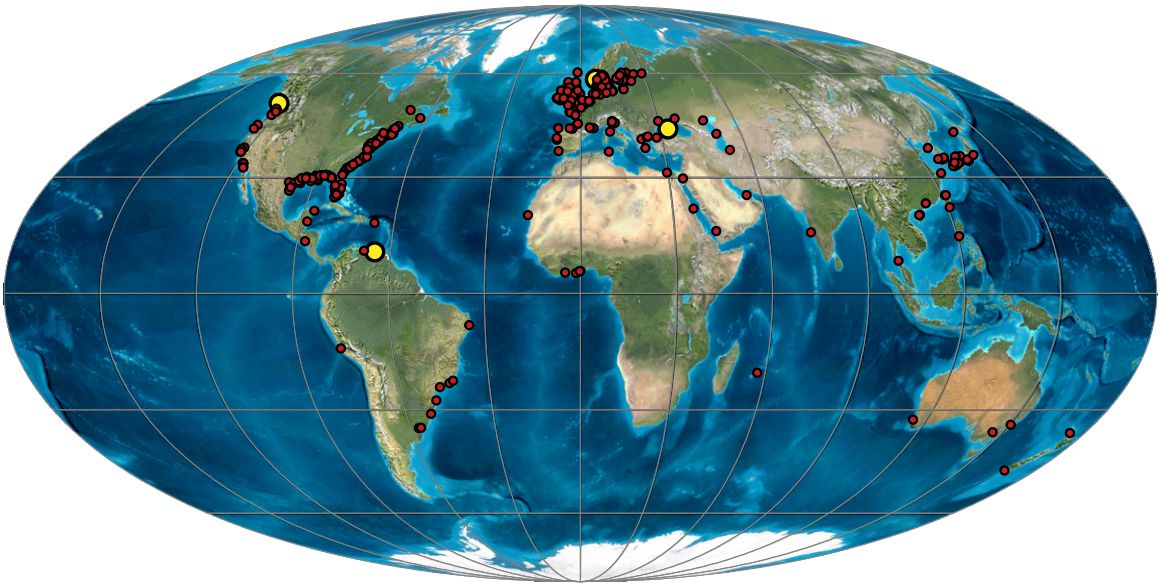

Figure 1.1: A global compilation of all the modern reducing [low oxygen (hypoxic) localities (●) which includes sulfidic (euxinic) basins (◉)] sites recorded in world since 1960. The data is from (Diaz and Rosenberg, 2008) and the map is from the PALEOMAP Project (Scotese, 2008).

respiration is represented as:

$$CO_2 + H_2O \xleftarrow[\leftarrow\text{respiration}\quad\text{photosynthesis}\rightarrow]{\text{energy}} \text{"}CH_2O\text{"} + O_2 \qquad \text{(Equation 1.1)}$$

where photosynthesis by terrestrial and marine primary producers consume CO_2 and produce organic matter, "CH_2O" (overly simplified in Eq. 1.1), and release O_2 as a byproduct but during steady state conditions all of the organic matter and O_2 is consumed during respiration which releases CO_2 and H_2O. However, the long-term carbon cycle is driven by the burial and uplift of organic carbon where a small portion of the produced organic matter "escapes" respiration and is buried in sedimentary rocks that allows for increased atmospheric oxygen. During tectonic processes this buried carbon will eventually be exhumed and weathered which consumes oxygen therefore this process, on a geologic timescale, is in steady state. Therefore, in order for O_2 to accumulate in the

atmosphere there must be some imbalance between the rate of burial and exhumation (Berner and Canfield, 1989). Importantly, much of Earth's history has been spent with little to no atmospheric oxygen with a significant increase at the onset of the Phanerozoic to near modern oxygen values which are roughly constant (Fig. 1.2; Berner, 2006; Canfield, 2005; Lyons et al., 2009; Lyons and Reinhard, 2009; Lyons et al., 2012). The oxygen concentrations in the ocean roughly mirrored the atmosphere in the Precambrian; however, in the Phanerozoic there are short-lived ocean deoxygenation events such as OAEs.

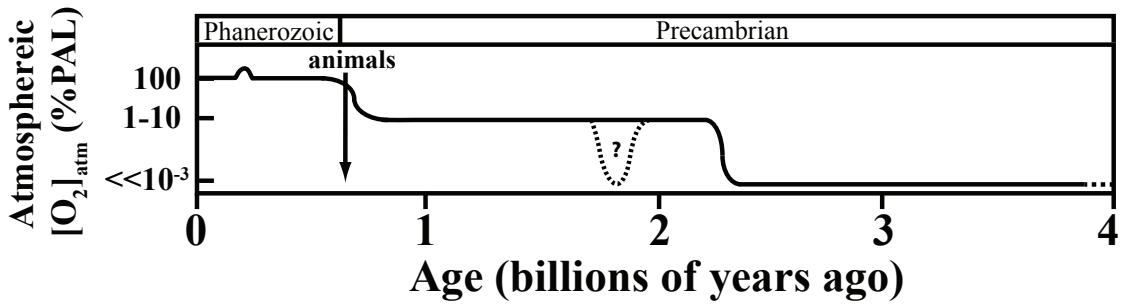

Figure 1.2: A general schematic of the atmosperhic O_2 level relative to the Present Atmospheric Level (PAL) of ~21% (adapted from Lyons et al., 2012).

The Cretaceous numerous OAEs which are generally defined as widespread organic carbon burial events (Arthur et al., 1987; Jenkyns, 2010; Schlanger et al., 1987; Schlanger and Jenkyns, 1976) with at least two globally, several ocean basins containing organic rich deposits and C isotope excursions registered in both organic and inorganic carbon [OAE1a (~120Ma) and OAE2 (~94Ma) (Leckie et al., 2002)]. OAE2, a short-lived event is estimated to be 400 to 850 ka (thousand years; Kuhnt et al., 2005; Sageman et al., 2006; Voigt et al., 2008), is the 7th largest extinction in the last 250 Ma (million years) and considered a 2nd order extinction event due to the demise of 26% of genera and extremely high extinction rates at the species level, especially in marine invertebrates

(Leckie et al., 2002; Raup and Sepkoski, 1986; Sepkoski, 1989). Understanding the initiation and termination mechanisms for OAE2 and other OAEs is important for understanding Earth natural feedbacks but it is difficult to unravel the timing and decouple all the parameters [increased hydrothermal fluxes, temperature, CO_2, increased spreading rates, enhanced weathering, nutrient increases, anoxia etc. (Fig. 3; Jenkyns, 2010)] as they are all interrelated and all likely played a role in the initiation, duration and termination of OAE2. The wide range of sample types and localities for OAE2 provides an ideal background to study this paleoceanographic phenomenon and to test several geochemical hypotheses to further understand the global nature of this event.

This dissertation seeks to resolve a small portion of the unconstrained issues using a variety of perspectives and geochemical tools. In Chapter 2, empirical data on sedimentary sulfur (S) isotope systematic and geochemical box modeling are used to quantify the global extent of euxinic (water column containing hydrogen sulfide) environments, less than 10% of the seafloor, which is much less than previous estimates and suggest organic carbon and pyrite burial slowly waned post-OAE. Chapter 3 explores the possibility of the timing of bioessential trace metal limitations, Mo and V, globally during OAE2 and its effect on the ecology and recorded extinction rates. In Chapter 4, a comparison of the known organic carbon burial and estimates of organic carbon burial from a geochemical box model suggests that nearly all of the organic carbon can be accounted for but it is expected that there are increased organic carbon burial on the eastern boundaries of ocean basins; however, if increased weathering rates liberated carbon then there is a significant amount of unknown organic carbon buried in the ocean during OAE2. Chapter 5, compares numerous geochemical proxies (trace metals, Fe speciation, sulfur isotopes and I/Ca) from both carbonates and organic-rich sediments at a unique locality which alternates between lithologies prior to the OAE where trace

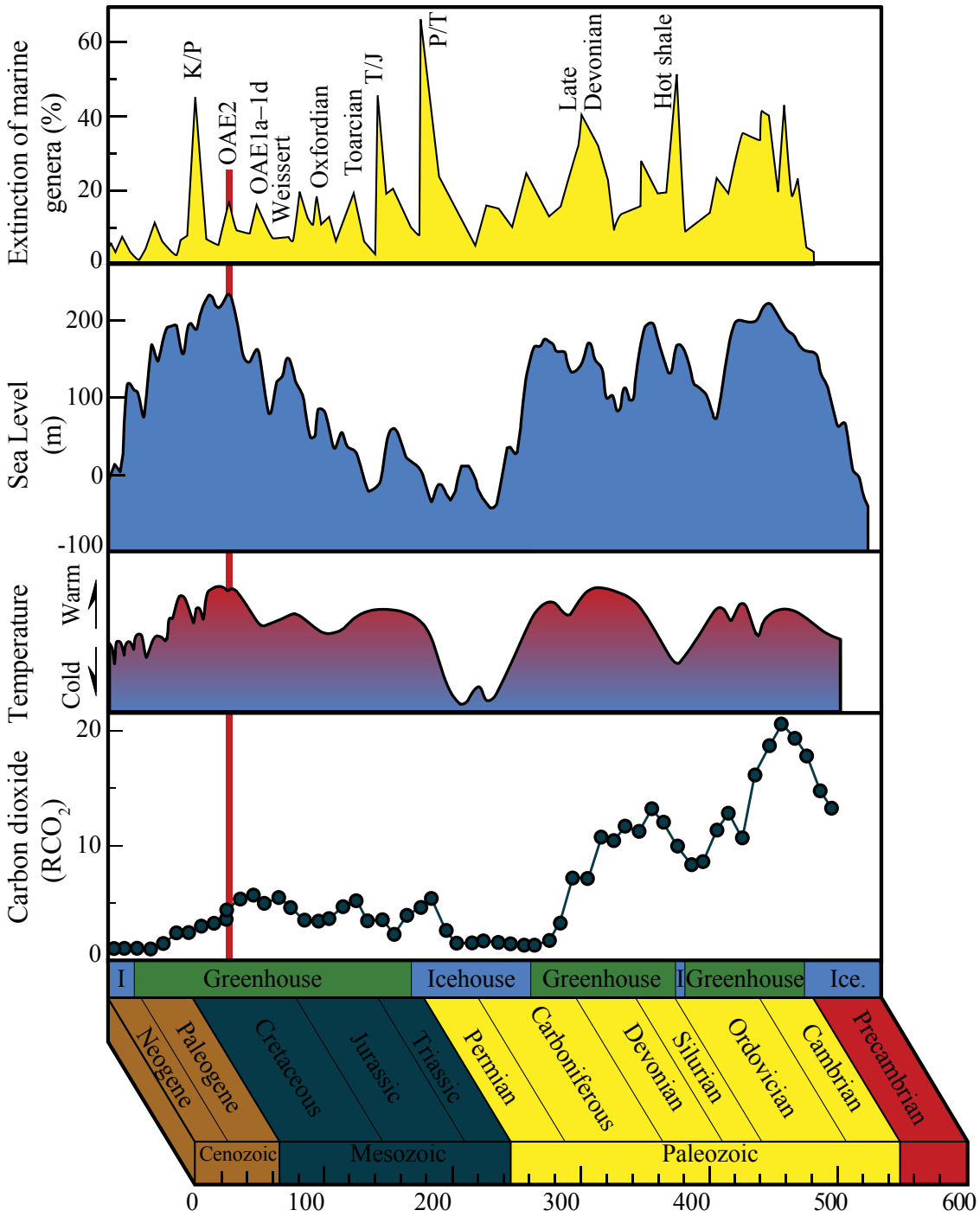

Figure 1.3: An overview schematic of the Phanerozoic Eon. OAE2 is marked by the red line. Figure adapted from Takashima et al (2006).

metals, Fe speciation and I/Ca suggest local anoxia prior to the OAE while Fe speciation and depleted trace metals suggest local and global increased euxinia. Finally, Chapter 6 explores the plausibility of global increase in hydrothermal activity delivering an important and often biolimiting nutrient, iron (Fe), by accessing total Fe enrichments by normalizing to aluminum (Fe_T/Al) and Fe isotopes which suggests the euxinic basins were influenced by hydrothermal activity but other non-euxinic sites show limited evidence for hydrothermal activity.

References

Arthur, M.A., Schlanger, S.O., Jenkyns, H.C., 1987. The Cenomanian-Turonian Oceanic Anoxic Event, II. Palaeoceanographic controls on organic-matter production and preservation. Geological Society, London, Special Publications 26, 401–420.

Berner, R.A., 1992. Palaeo-CO_2 and climate. Nature 358, 114.

Berner, R.A., 2001. Modeling atmospheric O_2 over Phanerozoic time. Geochimica et Cosmochimica Acta 65, 685–694.

Berner, R.A., 2006. GEOCARBSULF: A combined model for Phanerozoic atmospheric O_2 and CO_2. Geochimica et Cosmochimica Acta: A Special Issue Dedicated to Robert A. Berner 70, 5653–5664.

Berner, R.A., Canfield, D.E., 1989. A new model for atmospheric oxygen over Phanerozoic time. American Journal of Science 289, 333–361.

Canfield, D.E., 2005. The Eearly History of Atmopheric Oxygen: Homage to Robert M. Garrels. Annual Review of Earth and Planetary Sciences 33, 1–36.

Diaz, R.J., Rosenberg, R., 2008. Spreading Dead Zones and Consequences for Marine Ecosystems. Science 321, 926–929.

Falkowski, P.G., Algeo, T., Codispoti, L., Deutsch, C., Emerson, S., Hales, B., Huey, R.B., Jenkins, W.J., Kump, L.R., Levin, L.A., Lyons, T.W., Nelson, N.B., Schofield, O.S., Summons, R., Talley, L.D., Thomas, E., Whitney, F., Pilcher, C.B., 2011. Ocean deoxygenation: Past, present, and future. EOS, Transactions American Geophysical Union 92, 409–410.

Holland, H., 1984. The Chemical Evolution of the Atmosphere and Oceans. Princeton University Press, Princeton, NJ.

Jenkyns, H.C., 2010. Geochemistry of oceanic anoxic events. Geochemistry, Geophysics, Geosystems 11, Q03004.

Kuhnt, W., Luderer, F., Nederbragt, S., Thurow, J., Wagner, T., 2005. Orbital-scale record of the late Cenomanian-Turonian oceanic anoxic event (OAE-2) in the Tarfaya Basin (Morocco). International Journal of Earth Sciences 94, 147–159.

Leckie, R.M., Bralower, T.J., Cashman, R., 2002. Oceanic anoxic events and plankton evolution: Biotic response to tectonic forcing during the mid-Cretaceous. Paleoceanography 17, PA000623.

Lyons, T.W., Anbar, A.D., Severmann, S., Scott, C., Gill, B.C., 2009. Tracking Euxinia in the Ancient Ocean: A Multiproxy Perspective and Proterozoic Case Study. Annual Review of Earth and Planetary Sciences 37.

Lyons, T.W., Reinhard, C.T., 2009. Early Earth: Oxygen for heavy-metal fans. Nature 461, 179–181.

Lyons, T.W., Reinhard, C.T., Love, G.D., Xiao, S., 2012. Geobiology of the Proterozoic Eon, in: H. Knoll, D.E.C.a.K.O.K. (Ed.), Fundamentals of Geobiology. John Wiley & Sons, Ltd, pp. 371–402.

Raup, D.M., Sepkoski, J.J., 1986. Periodic extinction of families and genera. Science 231, 833–836.

Sageman, B.B., Meyers, S.R., Arthur, M.A., 2006. Orbital time scale and new C-isotope record for Cenomanian-Turonian boundary stratotype. Geology 34, 125–128.

Schlanger, S.O., Arthur, M.A., Jenkyns, H.C., Scholle, P.A., 1987. The Cenomanian-Turonian Oceanic Anoxic Event, I. Stratigraphy and distribution of organic carbon-rich beds and the marine δ13C excursion, in Marine Petroleum Source Rocks, edited by J. Brooks and A. J. Fleet. Geological Society, London, Special Publications 26, 371–399.

Schlanger, S.O., Jenkyns, H.C., 1976. Cretaceous anoxic events: causes and consequences. Geologie en Mijnbouw 55, 179–184.

Sepkoski, J.J., 1989. Periodicity in extinction and the problem of catastrophism in the history of life. Journal of the Geological Society 146, 7–19.

Virginia, G., 2010. Oceanography: Dead in the water. Nature 466, 812–814.

Voigt, S., Erbacher, J., Mutterlose, J., Weiss, W., Westerhold, T., Wiese, F., Wilmsen, M., Wonik, T., 2008. The Cenomanian Turonian of the Wunstorf section (North Germany): global stratigraphic reference section and new orbital time scale for Oceanic Anoxic Event 2. Newsletters on Stratigraphy 43, 65–89.

Chapter 2

Sulfur isotopes track the global extent and dynamics of euxinia during Cretaceous Oceanic Anoxic Event 2

Abstract

The Mesozoic Era is characterized by numerous oceanic anoxic events (OAEs) that are diagnostically expressed by widespread marine organic-carbon burial and coeval carbon-isotope excursions. Here we present coupled high-resolution carbon- and sulfur-isotope data from four European OAE2 sections spanning the Cenomanian–Turonian boundary that show roughly parallel positive excursions. Significantly, however, the interval of peak magnitude for carbon isotopes precedes that of sulfur isotopes with an estimated offset of a few hundred thousand years (ka). Based on geochemical box modeling of organic-carbon and pyrite burial, the sulfur-isotope excursion can be generated by transiently increasing the marine burial rate of pyrite precipitated under euxinic (i.e., anoxic and sulfidic) water-column conditions. In order to replicate the observed isotopic offset, the model requires that enhanced levels of organic-carbon and pyrite burial continued a few hundred ka after peak organic-carbon burial, but that their isotope records responded differently due to dramatically different residence times for dissolved inorganic carbon and sulfate in seawater. The significant inference is that euxinia persisted post-OAE, but with its global extent dwindling over this time period. The model further suggests that only ~5% of the global seafloor area was overlain by euxinic bottom waters during OAE2. Although this figure is ~30 times greater than the small euxinic fraction present today (~0.15%), the result challenges previous suggestions that one of the best-documented OAEs was defined by globally pervasive euxinic deep waters. Our results place important controls instead on local conditions and point to the difficulty in sustaining whole-ocean euxinia.

Introduction

The Mesozoic stratigraphic record, particularly the Cretaceous, is populated with numerous intervals of widespread marine organic-rich facies. Because of the approximately coeval stratigraphic occurrence of these organic-rich mudrocks (black shales) in multiple ocean basins, Schlanger and Jenkyns (Schlanger and Jenkyns, 1976) referred to the causative paleoceanographic phenomena as oceanic anoxic events (OAEs). During the OAEs the enhanced burial of organic carbon (OC) led to major perturbations of the carbon cycle (Arthur et al., 1988; Schlanger et al., 1987; Scholle and Arthur, 1980), which is recorded globally as positive isotope excursions in sedimentary organic and inorganic carbon (Arthur et al., 1988; Schlanger and Jenkyns, 1976). Throughout the Cretaceous, elevated atmospheric carbon dioxide concentrations (Berner, 2006; Takashima et al., 2006) contributed to high temperatures (Huber et al., 1995; Jenkyns et al., 2004; Jenkyns et al., 2012). However, during the relatively short time interval of OAE2 (Cenomanian-Turonian boundary event [~93.9Ma]), which lasted approximately 500 ka (Kuhnt et al., 2005; Sageman et al., 2006; Voigt et al., 2008), there are multiple lines of evidence for fluctuations in atmospheric pCO_2 (Jarvis et al., 2011; van Bentum et al., 2012), sea-surface temperatures and redox conditions (Forster et al., 2008; Gale and Christensen, 1996; Jarvis et al., 2011). Such fluctuations are mostly linked to widespread but non-uniform burial of vast amounts of OC (as reviewed in Jenkyns, 2010) and enhanced continental weathering (Blättler et al., 2011; Frijia and Parente, 2008).

Accelerated burial of OC and the accompanying positive carbon-isotope excursion are generally linked to two controls acting singly or in combination: increased primary production (Schlanger and Jenkyns, 1976) and enhanced organic-matter preservation under oxygen-deficient depositional conditions (Schlanger et al., 1987). Currently, increased primary production is favored (Jenkyns et al., 2007) as at least the initial driver, but both

mechanisms likely played a role in carbon sequestration that affected the isotopic composition of the ocean–atmosphere system. Furthermore, Cretaceous oceans were primed for major episodes of anoxia and associated carbon burial because of generally elevated temperatures and thus lower oxygen solubility in seawater. A previously unquantified portion of the ocean became sufficiently reducing to allow hydrogen sulfide to accumulate in the water column during OAE2, leading to at least regionally persistent euxinic conditions (Jenkyns, 2010) marked by organic-rich, laminated black shales across the basins, particularly in the southern portion of the proto-North Atlantic Ocean. Unlike many OAEs in the Mesozoic, OAE2 has been documented from multiple drill cores and outcrop sections and, in the Indian, Pacific and Atlantic Ocean basins, at various depths, latitudes and depositional settings (Schlanger et al., 1987). The most renowned lithological manifestation of OAE2 is the so-called Bonarelli Level that crops out in the Marche–Umbrian Apennines of central Italy (Schlanger and Jenkyns, 1976).

Sustained increases in primary production during OAE2 require at least transient enhanced delivery of nutrients and bio-essential metals (N, P, Fe, etc.) to the ocean. Identification of the mechanisms behind such increased nutrient delivery has been a major topic of investigation (Meyer and Kump, 2008), and three main mechanisms have been proposed: [1] hydrothermal activity (MacLeod et al., 2008; Snow et al., 2005), [2] enhanced continental weathering (Blättler et al., 2011; Frijia and Parente, 2008) and [3] increased phosphorus recycling due to reduction of iron-bearing phases with bound phosphate (Kraal et al., 2010; Van Cappellen and Ingall, 1994). The hydrothermal model for supplying Fe is challenged by the *assumption* of widespread euxinia in the water column and the insolubility of iron under those conditions; not surprisingly, the record of hydrothermal Fe signal does not correlate in a straightforward manner with the distribution of organic-rich facies throughout the entire North Atlantic (Jenkyns et al., 2007; Owens et al., 2012).

However, neodymium isotope ratios in fish teeth from the western equatorial Atlantic (Demerara Rise) and the north European Chalk Sea may reflect hydrothermal input from the Caribbean and/or Arctic Large Igneous provinces (MacLeod et al., 2008; Zheng et al., 2013). Alternatively, geochemical box modeling suggests that enhanced P from continental weathering was important for the initiation of OAE2, followed, as a positive feedback, by its sustained availability due to the widespread reduction of P-bearing iron oxides (Ozaki et al., 2011) and more generally enhanced P recycling under anoxic conditions (Van Cappellen and Ingall, 1994).

OAE2 is the most studied of the oceanic anoxic events, yet considerable gaps remain in our understanding of its causes and effects. Evidence from organic biomarkers from multiple sites in the proto-North Atlantic indicates photic-zone euxinia just before and during OAE2 (as reviewed in Jenkyns, 2010), and evidence for local oxygen depletion in seawater has been documented using Mn/Ca (Pearce et al., 2009), I/Ca ratios (Lu et al., 2010) and trace-metal enrichments (as reviewed in Jenkyns, 2010). Recent modeling by Monteiro et al. (Monteiro et al., 2012) suggests that 50% of the global ocean was anoxic. Nevertheless, the spatial extent of anoxic and more specifically, euxinic deposition, remains poorly constrained, particularly for the Pacific and Indian Oceans. Much of the work to date has focused on the proto-North Atlantic, the Western Interior Seaway (WIS), a handful of Pacific sites, and various continental margins (Takashima et al., 2006). The data are limited, but the equatorial Pacific appears to have been a locus for OC burial (Schlanger et al., 1987 and references therein). Certain, contemporaneous, marginal Pacific sites show evidence for oxic conditions (Hasegawa et al., 2013; Takashima et al., 2011), and the redox state of the vast majority of the ocean, specifically the Pacific Ocean, remains unknown. Here, we present new sulfate S-isotope data from multiple sites spanning several ocean basins recording OAE2. By combining our dataset with existing sulfate-S and carbonate-C

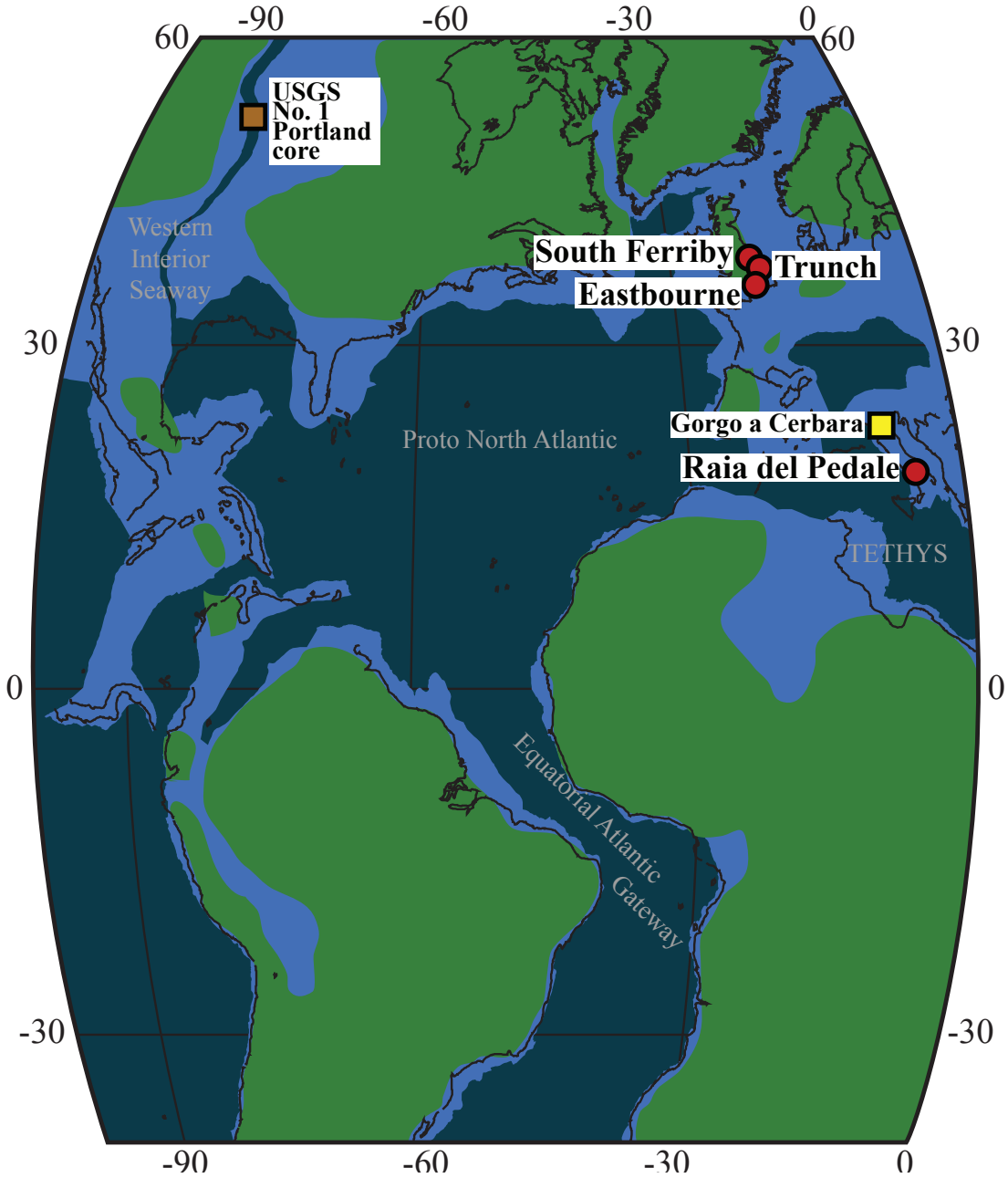

Figure 2.1: Paleogeographical reconstruction (generated using GEOMAR [http://www.odsn.de/odsn/ services/paleomap/paleomap.html]) for OAE 2 showing all sample locations used for analysis of carbonate-associated sulfate sulfur isotopes: (●) llocations analyzed in this study, (■) Gorgo a Cerbara (Marche–Umbria, Italy deep-marine Tethyan continental margin) of Ohkouchi et al. (Ohkouchi et al., 1999) and (◆) USGS Portland Core from the Western Interior Seaway of Adams et al. (Adams et al., 2010). The dark gray color indicates the landmasses, the light gray color represents shallow-marine settings, and white designates deep-marine settings for the late Cretaceous.

isotope data, we explore the dynamics of the global sulfur cycle during OAE2 and ultimately gain a novel global perspective on the extent of euxinic conditions during one of the best-studied OAEs.

Sulfur biogeochemistry background

Most studies of the Cretaceous sulfur cycle have focused on broad, 10^8-year secular trends seen in the marine sulfate-S isotope record (Paytan et al., 2004). However, two high-resolution investigations have specifically targeted the sulfur cycle during OAE2 (Adams et al., 2010; Ohkouchi et al., 1999). Much of this past work has focused on regional aspects of sulfur cycling (Adams et al., 2010; Ohkouchi et al., 1999), including the possibility of enhanced hydrothermal sulfur delivery to the WIS before OAE2 (Adams et al., 2010). For the first time, we present a comprehensive, geographically widespread sulfate-S isotope data set and apply a numerical box model to constrain the history of the global redox state of the ocean during OAE2.

The concentration and isotopic composition of the marine sulfate reservoir is a reflection of the inputs and outputs of sulfur to the ocean. The significant inputs are weathering of sulfide-and sulfate-bearing minerals from continental rocks and emissions from volcanic/hydrothermal systems (as reviewed in Bottrell and Newton, 2006). The magnitudes of these input fluxes vary temporally and spatially, but their isotopic signatures are similar and cluster in a relatively narrow $\delta^{34}S$ (definition below) range of 0 to 8‰, and it is unlikely that this isotopic range has changed significantly through time. The primary outputs of sulfur from the ocean are through the precipitation and burial of gypsum, organic-S compounds (which may be particularly important during OAEs) and pyrite in sediments. Over geologic time scales, gypsum burial can exert a control on marine sulfate

concentrations (Wortmann and Paytan, 2012), but this burial mechanism has little effect on the global isotopic composition of seawater sulfate due to the small fractionation (1 to 2‰) during gypsum precipitation (Raab and Spiro, 1991). In stark contrast, pyrite burial has a large effect on the isotopic composition of the marine sulfate reservoir (Kurtz et al., 2003 and references therein). The large isotopic offset between pyrite-S and the starting sulfate reflects the preference for lighter sulfur isotopes during microbial sulfate reduction and the concomitant production of isotopically light hydrogen sulfide. This sulfide combines with reactive Fe to form pyrite within the water column or below the sediment/water interface. The isotopic offset between sulfate-S and sulfide ($\Delta^{34}S$) is captured and preserved in the sedimentary pyrite and can be as great as 70‰ (e.g., Canfield et al., 2010). At times in the geologic past, pyrite burial was the dominant sink for dissolved sulfate (Gill et al., 2011b; Hurtgen et al., 2002), especially during episodes of widespread reducing conditions within the ocean, such as OAEs (Gill et al., 2011a; Gill et al., 2011b). Organic sulfur could be an additional reduced sulfur sink particularly when pyrite formation is limited by the availability of iron (i.e. under euxinic conditions). The isotopic y offset between organic S and sulfate is general less than pyrite's. Within this framework, shifts to more-positive $\delta^{34}S$ values recorded stratigraphically in tracers of ancient seawater, most commonly gypsum (anhydrite), barite and carbonate-associated sulfate (CAS), reflect enhanced pyrite burial, while negative $\delta^{34}S$ shifts indicate the greater relative importance of input fluxes. Ultimately, the size of the seawater sulfate reservoir (and, by association, its residence time) controls the magnitude and the potential rate of isotopic change.

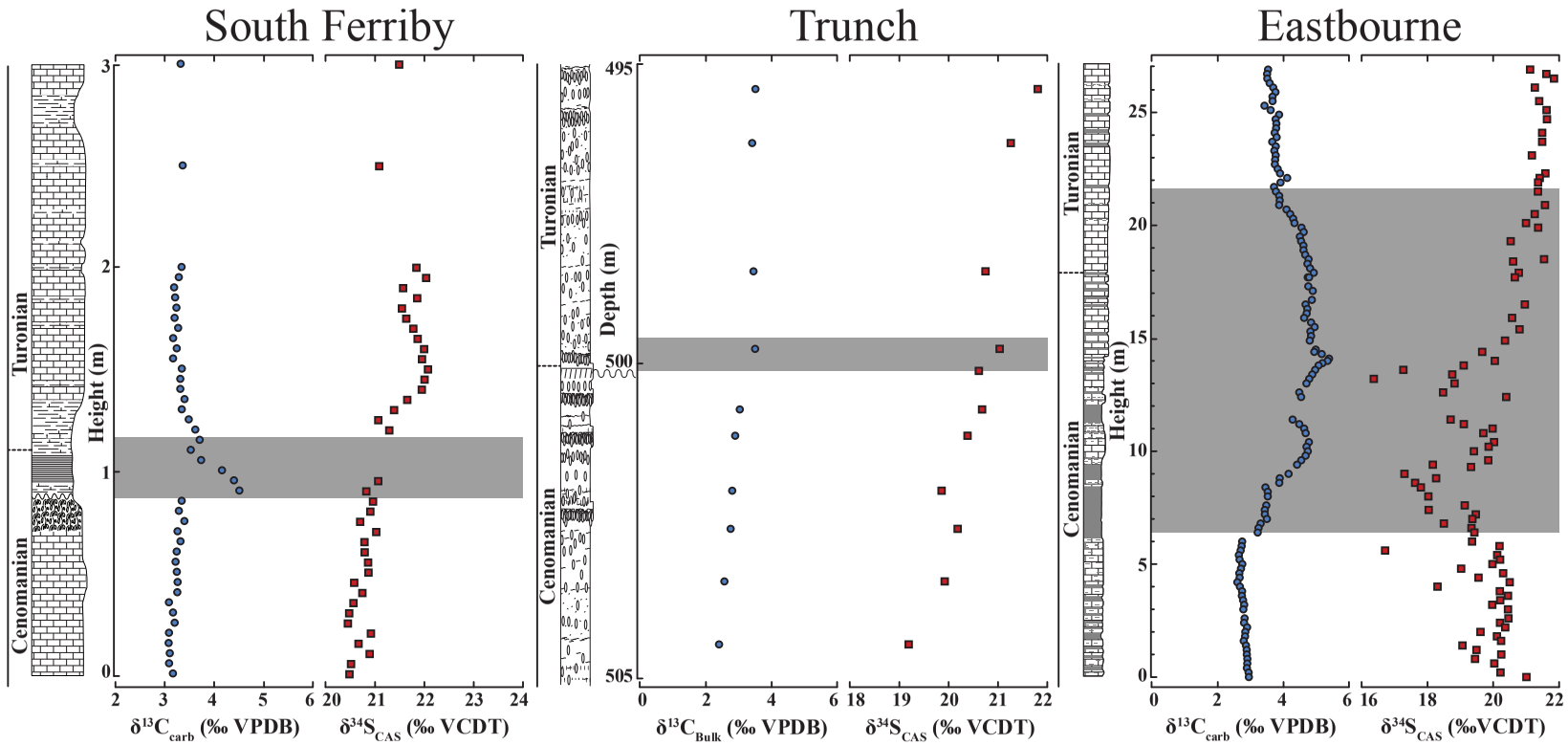

Figure 2.2: Chemostratigraphic plots of $\delta^{13}C$ (●) and $\delta^{34}SCAS$ (■) for the three UK Chalk sites. The gray bar indicates the previously labeled OAE as defined by the positive carbon-isotope excursion. Lithostratigraphic sections and carbon isotopes for South Ferriby from Jenkyns et al. (Jenkyns et al., 2007), stratigraphy for Trunch borehole from Jarvis et al. (Jarvis et al., 2006) (note $\delta^{13}C$ from bulk pelagic carbonate) and stratigraphic data and carbon isotopes for the Eastbourne section from Tsikos et al. (Tsikos et al., 2004).

Carbon- and sulfur-isotope trends

The $\delta^{34}S_{CAS}$ profiles from all four sections (Fig. 2.1) show positive excursions that coincide roughly with the positive carbon-isotope excursion (Figs. 2.2 and 2.3). The pre-event (baseline) values for all the sections are between 19‰ and 21‰ (see below). These values are relatively close to the published seawater value of 19.4‰ for the Cenomanian and Turonian based on the analysis of barite collected from open-ocean sediments (Paytan et al., 2004), although the pre-OAE sulfur-isotope values for CAS from the WIS (Adams et al., 2010) and Italy (Ohkouchi et al., 1999) are less positive (14‰ to 16‰). A return to pre-OAE $\delta^{34}S_{CAS}$ values after the event is observed only at Raia del Pedale and South Ferriby, where relatively extended stratigraphic sections are available.

The northernmost section, South Ferriby, shows a relatively stable $\delta^{34}S_{CAS}$ profile (average of 20.7‰) with no obvious positive isotope excursion during the OAE interval. A positive shift does, however, occur after the event, with a peak value of 22.1‰. This peak coincides stratigraphically with a return to the bulk carbon-isotope baseline value ($\delta^{13}C_{bulk}$) following the positive excursion. $\delta^{34}S_{CAS}$ values nearly return to the pre-OAE baseline at the top of the section, 1.8 meters above the termination level of the OAE.

The next section to the south, Trunch, is the most condensed and has an unconformity just below the OAE interval, although it still captures a significant portion of the upper Cenomanian leading into the OAE. The baseline values at this locality trend more positively before the event, but the average pre-OAE values are typical of those from the other sections (19.4‰). Once again, the most positive $\delta^{34}S_{CAS}$ values (21.8‰) post-date the OAE (as defined by the carbon-isotope data), with a $\delta^{34}S_{CAS}$ excursion of 2.4‰.

Eastbourne is the southernmost section in the UK and the most expanded stratigraphically due to comparably high sedimentation rates (Gale et al., 1993); the OAE

spans nearly 10 meters of section. This site shows relatively high variability in the $\delta^{34}S_{CAS}$ composition, while the $\delta^{13}C_{carb}$ record shows a more systematic increase and subsequent decrease during the OAE. Specifically, the pre-OAE baseline for $\delta^{34}S_{CAS}$ is comparatively stable with an average value of 19.9‰, but there is pronounced variability in the first half of the OAE interval with many of the data points departing from the overall positive trend (see Supplementary Information). The most positive $\delta^{34}S_{CAS}$ value after the event (21.8‰) yields a maximum magnitude for the excursion of 1.9‰, although there is very little available section post-dating the OAE. Given that the other sites show maxima well after the peak $\delta^{13}C_{carb}$ values, the most positive $\delta^{34}S_{CAS}$ values may not have been captured at this section.

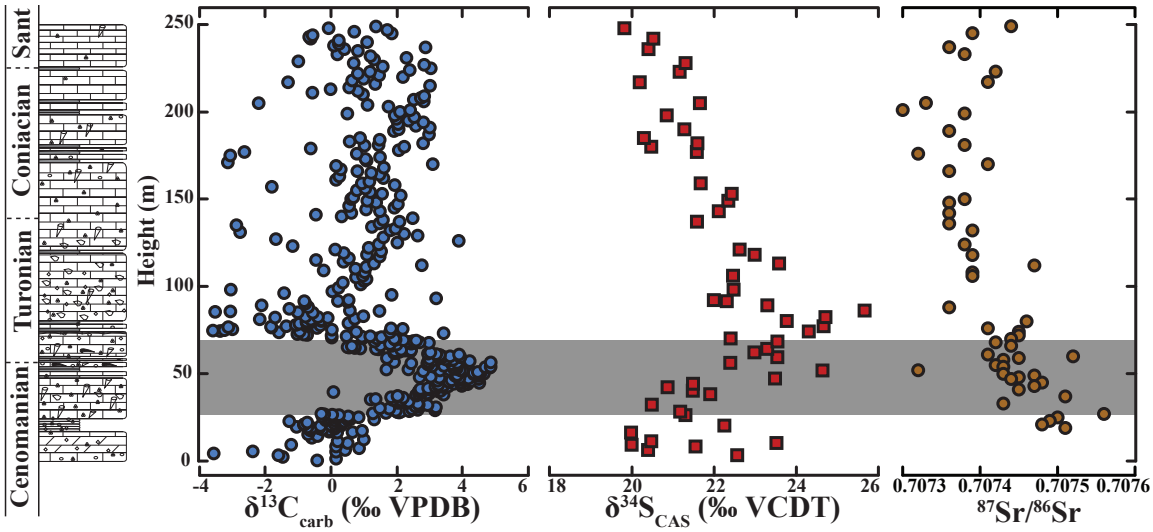

Figure 2.3: Chemostratigraphic plot for Raia del Pedale of $\delta^{13}C$ (●), $\delta^{34}SCAS$ (■) and $^{87}Sr/^{86}Sr$ (●). The gray bar indicates the previously labeled OAE defined by the $\delta^{13}C$ positive carbon-isotope excursion.

The Italian section, Raia del Pedale, is a shallow-water equivalent to the deep-sea pelagic section that contains the Bonarelli Level black shale characteristic of OAE2 (Jenkyns, 2010; Ohkouchi et al., 1999). Importantly, our sample set from Raia del Pedale

has the added benefit of high-resolution sampling throughout the entire carbonate section deposited during the OAE, allowing for continuous CAS analysis and stratigraphic coverage that extends well after the event, as determined by the carbonate C- and Sr-isotope records (Fig. 2.3). The Sr-isotope data from Raia del Pedale can be compared to the long-term composite record (Jones and Jenkyns, 2001 and references therein) to determine the best age correlation for this section following the OAE. Although there is some scatter before the event, the $\delta^{34}S_{CAS}$ baseline at this locality, with an average value of 21.1‰, is similar to pre-event data from the other UK sections. Once again, the peak $\delta^{34}S_{CAS}$ value (25.7‰) occurs stratigraphically well after the $\delta^{13}C_{carb}$ excursion that defines the OAE, and the return to pre-OAE values is captured well after the event. Interestingly, the magnitudes of the positive sulfur-isotope excursions among the various stratigraphic sections suggest a regional trend, with the UK sites showing lower $\delta^{34}S_{CAS}$ values relative to the other sections. Specifically, the average shifts are ~2‰ in the UK, whereas sections, the section at Raia Del Pedale shows a ~5‰ shift, similar to $\delta^{34}S_{CAS}$ excursion from the WIS and the Italian pelagic deep-sea section that contains the Bonarelli Level (Adams et al., 2010; Ohkouchi et al., 1999).

Modeling C and S

The observed carbon- and sulfur-isotope trends demand dramatic perturbations to the geochemical cycles of both elements during OAE2. To elucidate the coupled dynamics of the carbon and sulfur cycles, we constructed a forward box model. In our model, we prescribed the initial boundary conditions for the two cycles and then perturbed the fluxes until we were able to recreate the observed isotopic excursions, similar to previous studies (Adams et al., 2010; Gill et al., 2011a; Gill et al., 2011b; Kurtz et al., 2003). The initial

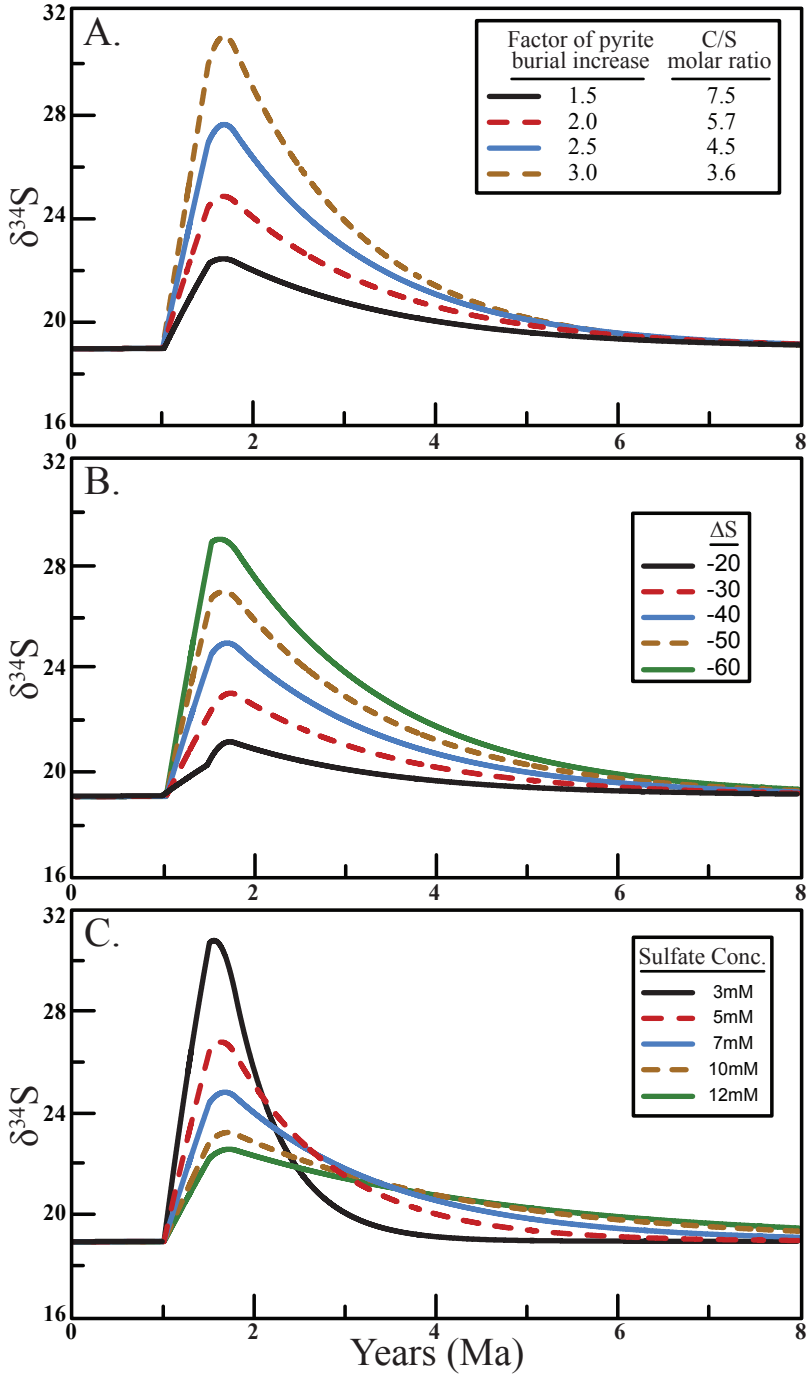

Figure 2.4: Sensitivity tests for the modeled sulfur cycle. Here we simulated variations (A) in increased pyrite burial and the corresponding C/S ratio, (B) increased isotope fractionation during microbial sulfate reduction ($\Delta^{34}S$) and (C) initial marine sulfate concentrations. Key parameters were treated the same in each simulation: initial marine sulfate concentration of 7mM, a 2-fold increase in pyrite burial and a change in $\Delta^{34}S$ from -30 (non-OAE) to -40‰ during the OAE unless the impact of varying a specific parameter was explored in the simulation.

boundary parameters for the model are given in the supplemental information Table 1.S1. Important but poorly constrained parameters were explored through sensitivity tests (Fig. 2.4). These influential factors include the magnitude of pyrite fractionation during microbial sulfate reduction ($\Delta^{34}S$), increasing pyrite burial and initial marine sulfate concentrations. In this model we do not explicitly delineate burial of organic sulfur, which does increase during OAE2 (Hetzel et al., 2009); however, since it represents a reduced sulfur phase, it is lumped with pyrite burial. The difference between pyrite-S and organic-S fractionation relative to the parent sulfate could be a source of some error; however, this assumption does not change our results significantly.

Our model confirms that recreating the observed C- and S-isotope trends can be generated through increasing OC and pyrite burial (Fig 2.5.). An increase of 1.6-times the modern OC flux is necessary to simulate a C-isotope excursion of ~3.5‰ (the approximate average of all published OAE2 excursions, which range from 2 to 6‰, was used for all

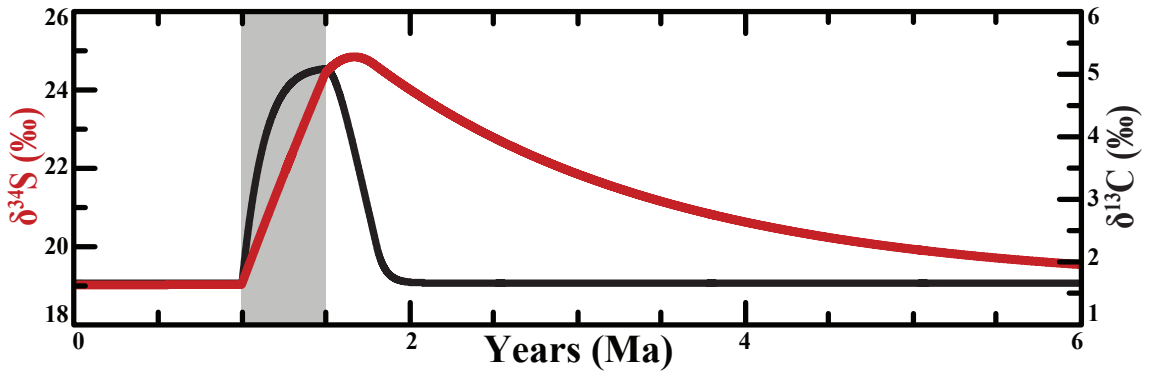

Figure 2.5: Modeling of the positive carbon- (black) and sulfur- (red) isotope excursion, with the gray bar indicating OAE2 as delineated by the characteristic C-isotope profile. In this model the initial marine sulfate concentrations was 7 mM, $\Delta^{34}S$ was increased to -40‰, pyrite burial was doubled, and OC burial was increased 1.6-fold during the OAE. The burial of OC and pyrite were decreased progressively, and $\Delta^{34}S$ was immediately returned to -30‰ for 300 ka after the OAE.

models). A two-fold increase in the total pyrite buried is required to simulate a sulfur-isotope excursion of 5‰. The duration of OAE2 has been shown to be ~0.5 Ma (Kuhnt et al., 2005), a time interval that we adopt for all model runs. The magnitude of the excursions can be dampened or amplified by changing the magnitude of OC and pyrite burial, the initial sulfate concentration and the assumed $\Delta^{34}S$. It should be noted that these modeling results are not unique solutions because of the high degrees of freedom in key assumptions; they do, however, represent the most plausible circumstances for the generation of the observed geochemical records based on sensitivity tests and observations from the geologic record.

Figure 2.4 shows the sensitivity of the model to transient changes in pyrite burial, $\Delta^{34}S$ and initial marine sulfate concentrations. The magnitude of pyrite burial has a large influence on the magnitude of the sulfate isotope excursion captured by $\delta^{34}S_{CAS}$. For example, a 1.5-fold increase in pyrite produces an excursion of ~3‰, while a 3-fold increase generates a 12‰ excursion (Fig. 2.4A) using an initial sulfate concentration of 7 mM and a $\Delta^{34}S$ of -40‰ during the OAE. We modeled a range of $\Delta^{34}S$ values (-20‰ to -60‰) with a two-fold increase in pyrite burial and initial marine sulfate of 7 mM, which predicts a range in the $\delta^{34}S$ excursion of 2 to 10‰ for seawater sulfate, respectively (Fig. 2.4B). As expected, varying the initial marine sulfate reservoir has an effect on the magnitude of the S-isotope excursion, with 3 mM and 12 mM yielding excursions of 12‰ and 3‰, respectively, based on a two-fold increase in pyrite burial and a $\Delta^{34}S$ of -40‰ (Fig. 2.4C).

We also used the model to simulate the observed offset in the C- and S-isotope records. To replicate the observed trends most successfully, we adopt a doubling of pyrite burial during the OAE, a $\Delta^{34}S$ of -40‰ and an initial marine sulfate concentration of 7 mM as our boundary conditions. The value for $\Delta^{34}S$ was chosen based on the global mean $\Delta^{34}S$ defined by an average pre-OAE marine $\delta^{34}S_{sulfate}$ of ~+20‰ [from average CAS and the barite values of Paytan et al. (Paytan et al., 2004)] and an adjusted average pyrite $\delta^{34}S$ of

-20‰. In fact, the average pyrite $\delta^{34}S$ value during OAE2 is ~-30‰ (Adams et al., 2010; Hetzel et al., 2009), but this average is exclusively from euxinic localities. Pyrite formation in euxinic settings generally has larger fractionations that have the potential to exaggerate the global $\Delta^{34}S$ average (Kurtz et al., 2003), and the inclusion of organic sulfur would also reduce the global fractionation. Therefore, we use a value of -20‰ for reduced sulfur or, specifically, a $\Delta^{34}S$ of ~-40‰, reflecting some balance between oxic and euxinic deposition and the importance of organic-S burial during the OAE. The sulfate concentration was chosen based on our model runs—specifically, the length of time for the isotope record to recover to the pre-OAE baseline (see discussion below), and the amount of pyrite buried was determined by reproducing a ~5‰ excursion.

Global implication from the sulfur cycle

We used a geochemical box model to simulate the observed C- and S-isotope excursions, using sensitivity tests (Fig. 2.4) to inform the unconstrained variables in the sulfur cycle. This exercise sheds light on the ocean redox evolution during OAE2. In the modern ocean, euxinic settings cover only ~0.15% of the seafloor [similar to (Reinhard et al., 2013)] and bury reduced sulfur at a rate of ~3.1×10^{16} moles of sulfur/Ma—mostly in the Black Sea (Neretin et al., 2001). For OAE2, the entire transient increase in pyrite burial is attributed to increased euxinic deposition, which yields a burial rate of ~4.7×10^{17} to 9.3×10^{17} moles of sulfur/Ma during OAE2 (representing the observed $\delta^{34}S_{CAS}$ excursions of 3 to 6‰, respectively, with all other parameters held constant as in Fig. 2.4A). These rates equate to 15 to 30 times the modern global flux of euxinic pyrite burial. Assuming conditions during Cretaceous deposition were comparable to those of modern euxinic sites, including mass accumulation rates and Fe availability, our model predicts that roughly 15 to 30 times more

of the seafloor was overlain by euxinia during OAE2. Relative to the 0.15% of euxinic seafloor today, this equates to ~2.5 to 5% euxinic deposition during OAE2. This prediction assumes pyrite burial under oxic and/or oxygen-deficient but non-euxinic environments remained constant throughout the event. In other words, we assume that the entire increase in pyrite burial occurred only within euxinic settings. This assumption is undoubtedly an oversimplification, and any concomitant increase in pyrite burial in oxic and other non-euxinic environments would decrease the estimated extent of euxinia during OAE2, thus our estimate represents a maximum. Consistent with the possibility of overestimating the extent of euxinia, the negative S-isotope excursions seen in the Eastbourne profile and in the Raia del Pedale profiles close to the onset of the positive carbon-isotope excursion correspond in time with the Plenus Cold Event/Benthic Oxic Event (Gale and Christensen, 1996), which affected at least the northern hemisphere. This event would have oxidized water-column sulfide where present and marine pyrite, transiently returning isotopically light sulfur to the oceans (see Supplementary Information).

Observations have shown that the southern portion of the North Atlantic was euxinic for much of the event, and the northern portion of the Atlantic appears to show a periodic development of euxinia (as reviewed in Jenkyns, 2010). Although redox conditions in the Pacific Ocean during the OAE are poorly known, three equatorial sites are documented with increased OC burial (Schlanger et al., 1987). Overall, the possibility of transient global expansion of oxygen minimum zones (OMZs) alone could account for the increased areal extent of euxinia during OAE2 and correlates well with observed OC burial patterns. While our modeled estimate of area of euxinic deposition is much larger than that seen in the modern ocean, the implication is that the majority of the ocean was either oxygen-deficient (but not euxinic) or oxic. Our result, once we also consider the WIS, suggests that euxinia in the Pacific may have been limited to equatorial regions characterized by high primary

productivity and vigorous upwelling and perhaps other regions of coastal upwelling. This reconstruction is much like the modern ocean but likely with overall lower levels of oxygen and far more euxinia spread more broadly across productive regions during OAE2.

Various factors suggest that our estimate of the increased extent of euxinic deposition might be somewhat conservative. Increases of continental weathering and runoff have been invoked as a mechanism for the enhanced primary production that catalyzed the initiation of OAE2 (Blättler et al., 2011; Jones and Jenkyns, 2001). Enhanced runoff would also increase the flux of ^{34}S-depleted sulfate to the marine reservoir, and as our model sensitivity test shows (Fig. 2.4c), would thus act to dampen the positive isotope shift caused by increased burial of pyrite. For example, a doubling of continental weathering, while holding all other parameters the same, would require a 2.5-fold increase of pyrite-S to replicate a comparable ~6‰ $\delta^{34}S$ excursion. Using a similar calculation to the one above, such a shift would require ~7% of the seafloor to have been euxinic, which is not substantially different than our initial estimate of 2.5 to 5%.

The observed offset between the $\delta^{13}C$ and $\delta^{34}S_{CAS}$ positive excursions is a pronounced feature of OAE2. Previously published sulfate-S data for OAE2 show a similar pattern (Adams et al., 2010; Ohkouchi et al., 1999). On a related note, a more subtle offset is also observed during the Toarcian OAE (Gill et al., 2011a). Only two variables in the model that can reproduce this observation: [1] an increased in $\Delta^{34}S$ fractionation during pyrite burial post-OAE or [2] a slow, simultaneous decrease of OC and pyrite burial. There is evidence, albeit scant, for a $\Delta^{34}S$ change during the OAE (Adams et al., 2010; Hetzel et al., 2009), but there is no evidence for a persistence of higher $\Delta^{34}S$ post-OAE; a more likely prediction would be a decrease in $\Delta^{34}S$ in the face of lower amounts of euxinic pyrite formation. Therefore, we prescribe a transient increase in $\Delta^{34}S$ (-40‰) during the OAE but an immediate return to pre-OAE baseline values following the event (-30‰). More

importantly, however, even if $\Delta^{34}S$ is held at the OAE value (-40‰) while decreasing OC and pyrite burial (300 ka post-OAE), the model generates a slightly larger offset (~20 ka). In order to reproduce the observed offset in the isotope records, the OC and pyrite sulfur burial must be decreased slowly for ~300 ka after the OAE (from 1.5 to 1.8 Ma in the model) (Fig. 2.5). The simultaneous waning of OC and pyrite burial has a more immediate effect on the carbon cycle due to its shorter residence time compared with that of sulfur. The starting reservoirs for each element are relatively similar, 3.3×10^{18} moles of inorganic C and 3.16×10^{18} moles (7 mM sulfate) of S, but the input flux for C (25×10^{18} moles/Ma) is an order of magnitude greater than sulfur's (1.50×10^{18} moles/Ma). Using our pre-OAE fluxes and initial marine reservoir concentrations yields C and S residence times of ~150 ka and ~2 Ma, respectively. In other words, decreasing extents of euxinia continue to drive the S-isotope excursion heavy, while the marine C-isotope compositions rebound faster because the input-to-reservoir ratio is dramatically larger relative to sulfur. The model predicts a small drawdown of sulfate during the OAE, namely a 1 mM decrease based on an initial concentration of 7 mM and doubling of pyrite burial—and so the resulting effect on the residence time of sulfate would be small (Fig. 2.S1). In sum, the most plausible driver for the observed offset between carbon- and sulfur-isotope ratios are parallel, incremental decreases in OC and pyrite burial after the OAE in the face of very different residence time relationships (see Supplementary Information for more details).

Additionally, the time it takes the $\delta^{34}S$ for sulfate to return to pre-OAE values is strongly tied to the size of the sulfate reservoir. Figure 2.4C demonstrates that the lower the sulfate concentration the more rapid the return to the pre-OAE baseline. The Raia del Pedale section is the only location with enough stratigraphic coverage to record the full return to the S -isotope baseline after the OAE, which appears to take ~3 to 5 Ma. Modeling suggests that a protracted recovery of this duration demands an initial pre-OAE sulfate

reservoir of ~7 mM. This concentration is at the lower limits estimated for marine sulfate for the late Cretaceous based on fluid inclusions from marine halite (Lowenstein et al., 2003) but is above the upper limit of 2.1-4mM suggested by Adams et al. (Adams et al., 2010) for the WIS.

The model predicts a global mean C/S burial ratio of 5.7 (molar ratio) using the 1.6-fold increase in OC burial and two-fold increase in pyrite burial. The modern 'normal' (oxic) marine C/S ratio is ~7.5, while modern euxinic settings exhibit both very low [<2] and high [>10] C/S ratios, where the high C/S ratio is indicative of euxinic settings where pyrite formation is severely limited by the supply of reactive Fe in combination with high organic-matter availability (Lyons and Berner, 1992). The average modeled C/S ratio of 5.7 is consistent with a global expansion of euxinic pyrite burial with comparatively significant inputs of reactive Fe on a global scale. However, at the local/regional scale, there is appreciable spatial variability in measured C/S ratios, suggesting heterogeneity in reactive Fe inputs (euxinic pyrite formation, by definition, is Fe-limited, and so the amount of pyrite largely reflects the delivery of Fe to the site of deposition). For example, Demerara Rise in the western equatorial Atlantic records an average C/S ratio of ~12 (Hetzel et al., 2009; Kraal et al., 2009), which suggests that pyrite-S burial was strongly limited by reactive Fe inputs relative to high burial of OC. In contrast, the WIS records an average C/S ratio of ~2 (Dean and Arthur, 1989), suggesting, at least locally, somewhat low OC availability and relatively high fluxes of reactive iron, possibly due to increased hydrothermal activity (Meyers, 2007; Snow et al., 2005). Our calculated mean C/S ratio thus captures the balance between these extremes across the spatial landscape of varying organic production and Fe delivery.

Conclusions

Paired C- and S-isotope records illuminate the timing of environmental change and spatial expansion and contraction of euxinia during OAE2. Our measurements show that the inter-site magnitude of the positive S-isotope excursion during OAE2 varies from 2 to 7‰, while the magnitude of the C-isotope excursion varies from 2 to 5‰. Modeling of the isotope records suggests that the excursions were driven by increased burial of pyrite and OC. Although generally coupled, these C- and S-isotope excursions show a pronounced offset between peak magnitudes. The observed offset between these isotope signatures may not be unique in the geologic record but is certainly a pronounced characteristic of OAE2. Our modeling links this relationship to continued euxinic burial of OC and pyrite-S after the OAE proper, but at decreasing rates, with carbon rebounding at a faster rate due to its shorter residence time compared to that of sulfur. The spatial variability in the excursion magnitudes could be due to local watermass differences and/or varying riverine fluxes to an ocean with substantially lower than modern sulfate concentrations, an effect noted also for the Toarcian OAE (Newton et al., 2011).

The spatial extent of euxinia predicted during OAE2 is also estimated through our modeling. In order to reproduce the observed geochemical signatures, the model demands a 15 to 30 fold increase in the area of euxinic deposition during the event: equivalent to ~2.5 to 5% of the seafloor. Importantly, this estimate is still relatively small and implies that much of the ocean was devoid of hydrogen sulfide in the water column and was predominantly anoxic (but non-sulfidic), suboxic and/or oxic. Parallel modeling of trace-metal and isotopic geochemistry could help resolve the global extent of oxygen-deficient settings with sulfide limited to the pore waters *and* sea-floor oxic deposition during the event. Nevertheless, this spatial increase in euxinia during OAE2 would likely have major implications for other biogeochemical elements, such as Fe and Mo, which could

eventually limit primary production and thus trigger the termination of the OAE through feedback processes.

Methods

We used a CAS extraction method similar to traditional approaches. In summary, 20 g of powdered sample were treated with NaCl and bleach solutions, followed by distilled water rinses. The intent was to remove any sulfate and organic-sulfur compounds that might otherwise be incorporated into the extracted CAS record. The samples were then dissolved with 4 N HCl and filtered to isolate the CAS-bearing solute from the insoluble fraction within one hour. Through addition of BaCl, the extracted sulfate precipitated as barite, which was then analyzed through on-line combustion using a Thermo Finnigan Delta V Plus continuous-flow stable isotope ratio mass spectrometer at the University of California, Riverside. Further discussion on methods and samples is available in the supplementary information.

References

Adams, D.D., Hurtgen, M.T., Sageman, B.B., 2010. Volcanic triggering of a biogeochemical cascade during Oceanic Anoxic Event 2. Nature Geoscience 3, 201–204.

Arthur, M.A., Dean, W.E., Pratt, L.M., 1988. Geochemical and climatic effects of increased marine organic carbon burial at the Cenomanian/Turonian boundary. Nature 335, 714–717.

Berner, R.A., 2006. GEOCARBSULF: A combined model for Phanerozoic atmospheric O_2 and CO_2. Geochimica et Cosmochimica Acta: A Special Issue Dedicated to Robert A. Berner 70, 5653–5664.

Blättler, C.L., Jenkyns, H.C., Reynard, L.M., Henderson, G.M., 2011. Significant increases in global weathering during Oceanic Anoxic Events 1a and 2 indicated by calcium isotopes. Earth and Planetary Science Letters 309, 77–88.

Bottrell, S.H., Newton, R.J., 2006. Reconstruction of changes in global sulfur cycling from marine sulfate isotopes. Earth-Science Reviews 75, 59–83.

Canfield, D.E., Farquhar, J., Zerkle, A.L., 2010. High isotope fractionations during sulfate reduction in a low-sulfate euxinic ocean analog. Geology 38, 415–418.

Dean, W.E., Arthur, M.A., 1989. Iron-sulfur-carbon relationships in organic-carbon-rich sequences; I, Cretaceous Western Interior Seaway. American Journal of Science 289, 708–743.

Forster, A., Kuypers, M.M.M., Turgeon, S.C., Brumsack, H.-J., Petrizzo, M.R., Sinninghe Damsté, J.S., 2008. The Cenomanian/Turonian oceanic anoxic event in the South Atlantic: New insights from a geochemical study of DSDP Site 530A. Palaeogeography, Palaeoclimatology, Palaeoecology 267, 256–283.

Frijia, G., Parente, M., 2008. Strontium isotope stratigraphy in the upper Cenomanian shallow-water carbonates of the southern Apennines: Short-term perturbations of marine $^{87}Sr/^{86}Sr$ during the oceanic anoxic event 2. Palaeogeography, Palaeoclimatology, Palaeoecology 261, 15–29.

Gale, A.S., Christensen, W.K., 1996. Occurrence of the belemnite *Actinocamax plenus* in the Cenomanian of SE France and its significance. Bulletin of the Geological Society of Denmark 43, 68–77.

Gale, A.S., Jenkyns, H.C., Kennedy, W.J., Corfield, R.M., 1993. Chemostratigraphy versus biostratigraphy: data from around the Cenomanian-Turonian boundary. Journal of the Geological Society 150, 29–32.

Gill, B.C., Lyons, T.W., Jenkyns, H.C., 2011a. A global perturbation to the sulfur cycle during the Toarcian Oceanic Anoxic Event. Earth and Planetary Science Letters 312, 484–496.

Gill, B.C., Lyons, T.W., Young, S.A., Kump, L.R., Knoll, A.H., Saltzman, M.R., 2011b. Geochemical evidence for widespread euxinia in the Later Cambrian ocean. Nature 469, 80–83.

Hasegawa, T., Crampton, J.S., Schiøler, P., Field, B., Fukushi, K., Kakizaki, Y., 2013. Carbon isotope stratigraphy and depositional oxia through Cenomanian/Turonian boundary sequences (Upper Cretaceous) in New Zealand. Cretaceous Research 40, 61–80.

Hetzel, A., Böttcher, M.E., Wortmann, U.G., Brumsack, H.-J., 2009. Paleo-redox conditions during OAE2 reflected in Demerara Rise sediment geochemistry (ODP Leg 207). Palaeogeography, Palaeoclimatology, Palaeoecology 273, 302–328.

Huber, B.T., Hodell, D.A., Hamilton, C.P., 1995. Middle-Late Cretaceous climate of the southern high latitudes: Stable isotopic evidence for minimal equator-to-pole thermal gradients. Geological Society of America Bulletin 107, 1164–1191.

Hurtgen, M.T., Arthur, M.A., Suits, N.S., Kaufman, A.J., 2002. The sulfur isotopic composition of Neoproterozoic seawater sulfate: implications for a snowball Earth? Earth and Planetary Science Letters 203, 413–429.

Jarvis, I., Gale, A.S., Jenkyns, H.C., Pearce, M.A., 2006. Secular variation in Late Cretaceous carbon isotopes: a new Campanian (99.6-70.6 Ma). Geological Magazine 143, 561–608.

Jarvis, I., Lignum, J.S., Gröcke, D.R., Jenkyns, H.C., Pearce, M.A., 2011. Black shale deposition, atmospheric CO_2 drawdown, and cooling during the Cenomanian-Turonian Oceanic Anoxic Event. Paleoceanography 26, PA3201.

Jenkyns, H.C., 2010. Geochemistry of oceanic anoxic events. Geochemistry, Geophysics, Geosystems 11, Q03004.

Jenkyns, H.C., Forster, A., Schouten, S., Sinninghe Damsté, J.S., 2004. High temperatures in the Late Cretaceous Arctic Ocean. Nature 432, 888–892.

Jenkyns, H.C., Matthews, A., Tsikos, H., Erel, Y., 2007. Nitrate reduction, sulfate reduction, and sedimentary iron isotope evolution during the Cenomanian-Turonian oceanic anoxic event. Paleoceanography 22, PA3208.

Jenkyns, H.C., Schouten-Huibers, L., Schouten, S., Sinninghe Damsté, J.S., 2012. Warm Middle Jurassic–Early Cretaceous high-latitude sea-surface temperatures from the Southern Ocean. Climate of the Past 8, 215–226.

Jones, C.E., Jenkyns, H.C., 2001. Seawater Strontium Isotopes, Oceanic Anoxic Events, and Seafloor Hydrothermal Activity in the Jurassic and Cretaceous. American Journal of Science 301, 112–149.

Kraal, P., Slomp, C.P., Forster, A., Kuypers, M.M.M., 2010. Phosphorus cycling from the margin to abyssal depths in the proto-Atlantic during oceanic anoxic event 2. Palaeogeography, Palaeoclimatology, Palaeoecology 295, 42–54.

Kraal, P., Slomp, C.P., Forster, A., Kuypers, M.M.M., Sluijs, A., 2009. Pyrite oxidation during sample storage determines phosphorus fractionation in carbonate-poor anoxic sediments. Geochimica et Cosmochimica Acta 73, 3277–3290.

Kuhnt, W., Luderer, F., Nederbragt, S., Thurow, J., Wagner, T., 2005. Orbital-scale record of the late Cenomanian-Turonian oceanic anoxic event (OAE-2) in the Tarfaya Basin (Morocco). International Journal of Earth Sciences 94, 147–159.

Kurtz, A.C., Kump, L.R., Arthur, M.A., Zachos, J.C., Paytan, A., 2003. Early Cenozoic decoupling of the global carbon and sulfur cycles. Paleoceanography 18, 1090.

Lowenstein, T.K., Hardie, L.A., Timofeeff, M.N., Demicco, R.V., 2003. Secular variation in seawater chemistry and the origin of calcium chloride basinal brines. Geology 31, 857–860.

Lu, Z., Jenkyns, H.C., Rickaby, R.E.M., 2010. Iodine to calcium ratios in marine carbonate as a paleo-redox proxy during oceanic anoxic events. Geology 38, 1107–1110.

Lyons, T.W., Berner, R.B., 1992. Carbon-sulfur-iron systematics of the upper-most deep-water sediments of the Black Sea. Chemical Geology 99, 1–27.

MacLeod, K.G., Martin, E.E., Blair, S.W., 2008. Nd isotopic excursion across Cretaceous ocean anoxic event 2 (Cenomanian-Turonian) in the tropical North Atlantic. Geology 36, 811–814.

Meyer, K.M., Kump, L.R., 2008. Oceanic Euxinia in Earth History: Causes and Consequences. Annual Review of Earth and Planetary Sciences 36, 251–288.

Meyers, S.R., 2007. Production and preservation of organic matter: The significance of iron. Paleoceanography 22, PA4211.

Monteiro, F.M., Pancost, R.D., Ridgwell, A., Donnadieu, Y., 2012. Nutrients as the dominant control on the spread of anoxia and euxinia across the Cenomanian-Turonian oceanic anoxic event (OAE2): Model-data comparison. Paleoceanography 27, PA4209.

Neretin, L.N., Volkov, I.I., Böttcher, M.E., Grinenko, V.A., 2001. A sulfur budget for the Black Sea anoxic zone. Deep Sea Research Part I: Oceanographic Research Papers 48, 2569–2593.

Newton, R.J., Reeves, E.P., Kafousia, N., Wignall, P.B., Bottrell, S.H., Sha, J.-G., 2011. Low marine sulfate concentrations and the isolation of the European epicontinental sea during the Early Jurassic. Geology 39, 7–10.

Ohkouchi, N., Kawamura, K., Kajiwara, Y., Wada, E., Okada, M., Kanamatsu, T., Taira, A., 1999. Sulfur isotope records around Livello Bonarelli (northern Apennines, Italy) black shale at the Cenomanian-Turonian boundary. Geology 27, 535–538.

Owens, J.D., Lyons, T.W., Li, X., Macleod, K.G., Gordon, G., Kuypers, M.M.M., Anbar, A., Kuhnt, W., Severmann, S., 2012. Iron isotope and trace metal records of iron cycling in the proto-North Atlantic during the Cenomanian-Turonian oceanic anoxic event (OAE-2). Paleoceanography 27, PA3223.

Ozaki, K., Tajima, S., Tajika, E., 2011. Conditions required for oceanic anoxia/euxinia: Constraints from a one-dimensional ocean biogeochemical cycle model. Earth and Planetary Science Letters 304, 270–279.

Paytan, A., Kastner, M., Campbell, D., Thiemens, M.H., 2004. Seawater sulfur isotope fluctuations in the Cretaceous. Science 304, 1663–1665.

Pearce, M.A., Jarvis, I., Tocher, B.A., 2009. The Cenomanian-Turonian boundary event, OAE2 and palaeoenvironmental change in epicontinental seas: New insights from the dinocyst and geochemical records. Palaeogeography, Palaeoclimatology, Palaeoecology 280, 207–234.

Raab, M., Spiro, B., 1991. Sulfur isotopic variations during seawater evaporation with fractional crystallization. Chemical Geology: Isotope Geoscience section 86, 323–333.

Reinhard, C.T., Planavsky, N.J., Robbins, L.J., Partin, C.A., Gill, B.C., Lalonde, S.V., Bekker, A., Konhauser, K.O., Lyons, T.W., 2013. Proterozoic ocean redox and biogeochemical stasis. Proceedings of the National Academy of Sciences.

Sageman, B.B., Meyers, S.R., Arthur, M.A., 2006. Orbital time scale and new C-isotope record for Cenomanian-Turonian boundary stratotype. Geology 34, 125–128.

Schlanger, S.O., Arthur, M.A., Jenkyns, H.C., Scholle, P.A., 1987. The Cenomanian-Turonian Oceanic Anoxic Event, I. Stratigraphy and distribution of organic carbon-rich beds and the marine $\delta^{13}C$ excursion, in *Marine Petroleum Source Rocks*, edited by J. Brooks and A. J. Fleet. Geological Society, London, Special Publications 26, 371–399.

Schlanger, S.O., Jenkyns, H.C., 1976. Cretaceous anoxic events: causes and consequences. Geologie en Mijnbouw 55, 179–184.

Scholle, P.A., Arthur, M.A., 1980. Carbon isotope fluctuations in Cretaceous pelagic limestones; potential stratigraphic and petroleum exploration tool. AAPG Bulletin 64, 67–87.

Snow, L.J., Duncan, R.A., Bralower, T.J., 2005. Trace element abundances in the Rock Canyon Anticline, Pueblo, Colorado, marine sedimentary section and their relationship to Caribbean plateau construction and oxygen anoxic event 2. Paleoceanography 20, PA3005.

Takashima, R., Nishi, H., Huber, B.T., Leckie, M., 2006. Greenhouse World and the Mesozoic Ocean. Oceanography 19, 82–92.

Takashima, R., Nishi, H., Yamanaka, T., Tomosugi, T., Fernando, A.G., Tanabe, K., Moriya, K., Kawabe, F., Hayashi, K., 2011. Prevailing oxic environments in the Pacific Ocean during the mid-Cretaceous Oceanic Anoxic Event 2. Nature Communications 2, 234.

Tsikos, H., Jenkyns, H.C., Walsworth-Bell, B., Petrizzo, M.R., Forster, A., Kolonic, S., Erba, E., Premoli Silva, I., Baas, M., Wagner, T., Sinninghe Damsté, J.S., 2004. Carbon-isotope stratigraphy recorded by the Cenomanian–Turonian Oceanic Anoxic Event: correlation and implications based on three key localities. Journal of the Geological Society 161, 711–719.

van Bentum, E.C., Reichart, G.-J., Forster, A., Sinninghe Damsté, J.S., 2012. Latitudinal differences in the amplitude of the OAE-2 carbon isotopic excursion: pCO_2 and paleo productivity. Biogeosciences 9, 717–731.

Van Cappellen, P., Ingall, E.D., 1994. Benthic phosphorus regeneration, net primary production, and ocean anoxia: A model of the coupled marine biogeochemical cycles of carbon and phosphorus. Paleoceanography 9, 677–692.

Voigt, S., Erbacher, J., Mutterlose, J., Weiss, W., Westerhold, T., Wiese, F., Wilmsen, M., Wonik, T., 2008. The Cenomanian Turonian of the Wunstorf section (North Germany): global stratigraphic reference section and new orbital time scale for Oceanic Anoxic Event 2. Newsletters on Stratigraphy 43, 65–89.

Wortmann, U.G., Paytan, A., 2012. Rapid Variability of Seawater Chemistry Over the Past 130 Million Years. Science 337, 334–336.

Zheng, X.-Y., Jenkyns, H.C., Gale, A.S., Ward, D.J., Henderson, G.M., 2013. Changing ocean circulation and hydrothermal inputs during Ocean Anoxic Event 2 (Cenomanian-Turonian): Evidence from Nd-isotopes in the European shelf sea. Earth and Planetary Science Letters 375, 338–348.

Supplemental Information

Materials and methods

We present results from four-localities in Europe spanning intervals before, during and after OAE2. The sample locations were selected with an eye toward sites that had direct connection to the open ocean and a spatial distribution that encompasses multiple marine basins (Fig. 2.1). All sample sites have been previously documented to record the OAE2 interval by means of biostratigraphy, chemostratigraphy (Sr- and C-isotopes) or a combination of both (Jarvis et al., 2006; Jenkyns et al., 2007; Parente et al., 2008; Schlanger et al., 1987; Tsikos et al., 2004). A comprehensive discussion of the sedimentology, age relationships and tectonic settings of the sampled localities is already available (Gale et al., 1993; Parente et al., 2008; Schlanger et al., 1987; Wood et al., 1994). All of the sections are dominated by carbonate lithologies with abundant microfossils, along with some macrofossils and are characterized by low OC contents (Gale et al., 1993; Parente et al., 2008; Schlanger et al., 1987; Wood et al., 1994), with one exception. The section at South Ferriby contains a 10-cm-thick organic-rich interval deposited during OAE2 (Jenkyns et al., 2007; Schlanger et al., 1987), which was avoided for CAS analysis. We chose these carbonate sites because they can capture evolving global seawater chemistry, which tracks ocean-scale redox processes. Importantly, because organic-lean sites typically provide lithologic uniformity before, during and after the OAE, they potentially represent the best isotopic archives of *global* marine conditions. Briefly, three of the four localities (Eastbourne cliff section, South Ferriby Quarry and the Trunch borehole: all UK) illustrate poorly lithified pelagic foraminiferal-nannofossil-rich chalk facies with similar diagenetic histories and consistently good carbonate preservation. The fourth sample site, Raia del Pedale, is a - well-lithified platform-carbonate section in southern Italy, rich in rudist fragments and benthic foraminifera and formerly located on the margin of the Tethys Ocean

(Fig. 2.1). In figure 2.2, lithostratigraphic sections and carbon isotopes for South Ferriby from Jenkyns et al. (Jenkyns et al., 2007), stratigraphy for Trunch borehole from Jarvis et al. (Jarvis et al., 2006) (note $\delta^{13}C$ from bulk pelagic carbonate) and stratigraphic data and carbon isotopes for the Eastbourne section from Tsikos et al. (Tsikos et al., 2004).

All samples analyzed for the $\delta^{34}S_{CAS}$ were dominated by high carbonate contents (60 to 80 wt%). We followed a standard procedure extracting CAS from the carbonate-rich samples (Gill et al., 2011a; Gill et al., 2011b). Briefly, the samples were trimmed to eliminate weathered surfaces, including surficial Fe oxidation. Then, 10-20 g of powdered sample were treated with NaCl and NaOCl solutions and rinsed with multiple deionized rinses to prevent the incorporation of any non-CAS sulfur-bearing phases. The samples were then dissolved using 4 M HCl and vacuum-filtered less than 1 hour later to minimize the pyrite oxidation, which was further limited in the samples by low pyrite and ferric iron concentrations. A $BaCl_2$ solution was added to precipitate sulfate as $BaSO_4$.

The precipitated and homogenized $BaSO_4$ from each sample was loaded into tin capsules with excess V_2O_5 and analyzed for its $^{34}S/^{32}S$ ratio at the University of California, Riverside. Sulfur-isotope ratios were measured using a Thermo Delta V gas-source isotope-ratio mass spectrometer coupled to a Costech 4010 ECS for on-line sample combustion and analysis. All sulfur-isotope compositions are reported in standard delta notation as per mil (‰) deviation relative to Vienna Canyon Diablo Troilite (V-CDT) and were corrected to a suite of international reference materials using a linear regression (e.g. Gill et al., 2011a; Gill et al., 2011b) based on replicate analyses of international standards (IAEA SO-5 [0.49], IAEA SO-6 [-34.05], and NBS 127 [21.1]) agreed to within 0.2‰ of their published values.

C and S modeling

The values used in the coupled carbon and sulfur model were based on the combination of available geochemical data and on the sensitivity tests (Fig. 2.4) to help constrain unknown parameters for the sulfur cycle. As previously stated, there are several possibilities to replicate the observed trends by 'mixing and matching' unconstrained parameters but we have attempted to bracket a few of these factors using data in combination with estimates for these values in the modern cycles. For instance, the $\Delta^{34}S$ used in the model during non-OAE intervals is close to the modern value and was necessary to achieve steady state with the inputs, while the ΔS during the OAE itself was chosen based on the known starting sulfate value (~+20‰; Paytan et al., 2004) and an average pyrite value of -20‰ [the average pyrite value during the OAE based on the available data is ~-30‰ (Adams et al., 2010; Böttcher et al., 2006; Gautier, 1987; van Bentum et al., 2009) but this is exclusively from euxinic settings and we assume a global average closer to -20‰], which provides a $\Delta^{34}S$ of -40‰. Consequently, the $\Delta^{34}S$ is transiently shifted in the model from -30‰ to -40‰ and back to -30‰ for the intervals prior, during and after the OAE, respectively. The starting sulfate concentration was based on the length of time it takes for the S-isotope profile of the Raia del Pedale section to indicate recovery to the pre-OAE baseline and seems to fit best with values between 5 to 9 mM and thus we used the average of 7 mM. The values for continental weathering were held constant with the exception of the enhanced weathering scenario (discussed previously), which would only dampen the positive excursion. Therefore, the only parameter to further 'adjust' is the amount of pyrite burial, which can have dramatic effects on the magnitude of the excursion.

To model the carbon isotope excursion in the modeling exercises all parameters are held constant in the carbon cycle and the burial of organic carbon is increased to1.6-

times the pre-excursion rate. For the sulfur cycle portion of the model, we used the values discussed above and increased the pyrite burial rate to 2-times the starting rate because it best replicated a 5 to 6‰ excursion, however adjusting this value does not affect the offset between the carbon and sulfur isotope excursions. Replicating this offset requires a waning of the carbon and sulfur burial rates (shown in Fig. 2.S1). The longer the transient decay back to the pre-OAE baseline burial rates, the larger the offset because of the differences of sizes of DIC and sulfate reservoirs and relative magnitude of the fluxes in the cycles as compared to this reservoir size. Consequently the peak carbon-isotope values occur closer to the time of maximum organic-carbon burial (i.e. near the end of the OAE), but the sulfur excursion continues to rise until the return to 'normal' pyrite burial as seen in Figure 2.S1.

Eastbourne sulfur geochemical preservation

The $\delta^{34}S_{CAS}$ at this site shows several negative shifts during the first half of the OAE, although the overall trend of the data shows progressively more positive values. This is the only documented site to clearly show these small negative excursions within the OAE, although the Raia del Pedale section seems to indicate similar features. These negative excursions in the Eastbourne section seem to be correlated with the most positive $\delta^{13}C_{carb}$ values prior to the slight decreases in carbon-isotope values. It is difficult to pin-point the exact origin of the negative excursions at Eastbourne but there are three possibilities to explain the observed phenomena: (1) later pyrite oxidation skewing the primary CAS signal (2) enhanced delivery of sulfate or (3) a paleoceanographic circulation change.

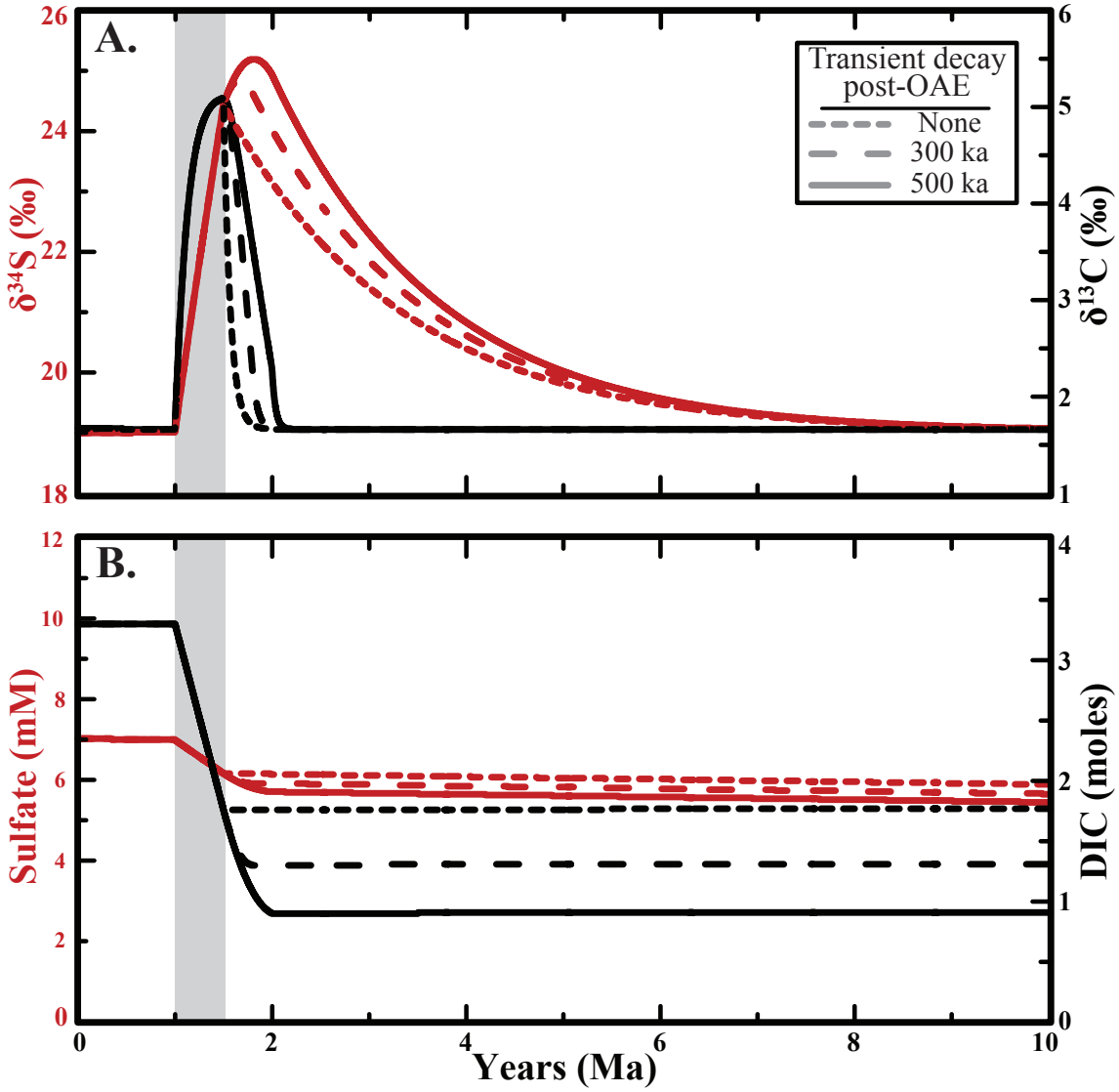

Figure 2.S1: Sensitivity test for the modeled offset of the coupled carbon and sulfur cycle by varying the amount of time it takes to return to pre-OAE values. This model shows the sensitivity of a waning carbon burial with an increase in the offset of the carbon and sulfur cycles. An increase in time allows for a greater offset and a larger magnitude sulfur-isotope excursion (A) while having very little effect on the sulfate concentration (B). The black lines represent all of the carbon models and blue represents the sulfur models, and the dashes for A and B are shown in the legend on A. The models use a 2-fold increase in pyrite burial, ΔS of -40 during the OAE and a starting marine concentration of 7 mM.

A concern for the validity of the data for CAS has been the oxidation of pyrite either during the burial of the rock, outcrop weathering or during the chemical extraction of CAS (Marenco et al., 2008; Mazumdar et al., 2008). Due to the slight decrease in carbonate concentration leading into the OAE (on average 83 wt% in OAE chalk sediment and ~91 wt%, in non-OAE chalk sediment) this could be a concern. With this in mind, we measured the amount of pyrite in most samples post-filtration of the CAS dissolution step and performed a standard chromium chloride extraction (Canfield et al., 1986). The low amounts of pyrite measured for all sections (Fig. 2.S2) with Eastbourne having the highest values, but relatively low when compared to previously published CAS data sets (Fike and Grotzinger, 2008; Fike et al., 2006; Gill et al., 2011a; Gill et al., 2011b; Loyd et al., 2012; Wotte et al., 2012) suggest this effect played a limited role during the extraction procedure. In addition, cross-plots of sulfate isotopes and sulfate concentrations against the pyrite concentration show no trends for individual sections (Fig. 2.S2) or all samples combined. Also, CAS isotope *vs.* pyrite concentration for Eastbourne shows no linear correlation or obvious trends. Linear correlations with pyrite would imply a mixed signal of primary CAS and pyrite-contaminated sulfate (Gill et al., 2011b; Marenco et al., 2008; Mazumdar et al., 2008); therefore, we believe this signal is a primary $\delta^{34}S_{CAS}$ signal.

Geochemical proxies suggest there was an increase of continental weathering during the OAE (Blättler et al., 2011; Frijia and Parente, 2008; Pogge von Strandmann et al., 2013) or increased volcanic activity (Adams et al., 2010), phenomena which could have delivered isotopically depleted sulfur to the marine reservoir. This model seems unlikely, because a simple mass-balance calculation would suggest that a massive delivery of sulfate would have had to enter the system to account for the isotopic shift.

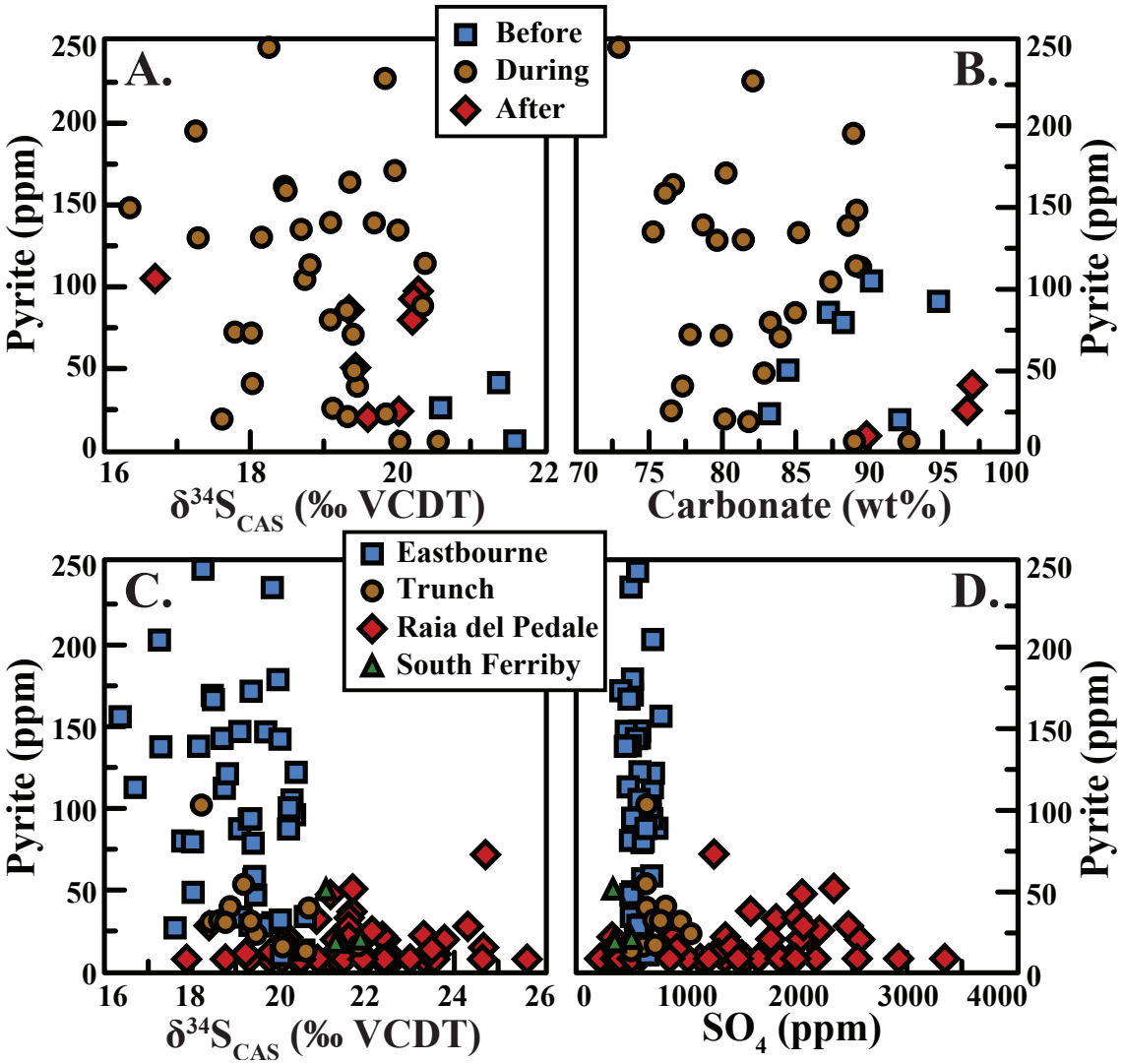

Figure 2.S2: Cross-plots of geochemical data for Eastbourne (A and B) and all four sections analyzed in this study (C and D). In A and B, pyrite concentrations vs $\delta^{34}S_{CAS}$ (A) and carbonate contents (B) shows no correlation, indicating that pyrite concentrations have not systematically affected the $\delta^{34}S_{CAS}$ values at Eastbourne. Similarly, figure C and D show no correlation for pyrite concentration and $\delta^{34}S_{CAS}$ (C) or sulfate concentration (D).

Furthermore, there is no evidence for increased marine sulfate concentrations during the OAE that would necessarily have affected all localities equally.

The third possibility for the $\delta^{34}S_{CAS}$ record that the negative excursions observed at Eastbourne are changes in the paleoceanographic circulation patterns due to climatic

processes. There is mounting evidence for a cooling episode during the early part of the OAE, not only due to silicate weathering but also to the global burial of organic carbon, thus decreasing atmospheric CO_2 (Arthur et al., 1988; Barclay et al., 2010; Jarvis et al., 2011; van Bentum et al., 2012). The fall in temperature is documented by the paleotemperature proxy TEX_{86} (Forster et al., 2007; Sinninghe Damsté et al., 2010) in the Northern proto-Atlantic and by invasion of boreal faunas (the so-called Plenus Cold Event) in the north European Chalk Sea (Gale and Christensen, 1996), both accompanied by excursions in Nd-isotope ratios, suggesting introduction of watermasses of possible Arctic derivation (MacLeod et al., 2008; Martin et al., 2012; Zheng et al., 2013). In the proto-Atlantic region and the Western Interior Seaway the invasion of cooler more oxygenated waters during the same time interval was characterized by population of the seafloor by benthic foraminifera: the so-called Benthic Oxic Event (Friedrich et al., 2006; Keller et al., 2004). Such oxygenated waters as these would have oxidized sub-sea-floor surficial pyrite and introduced isotopically depleted sulfate into the water column and thus lowered the S-isotope composition of ambient seawater.

	Carbon Conconcentration	$\delta^{13}C$ (‰)	Sulfur Conconcentration	$\delta^{34}S$ (‰)
Starting marine reservoir	3.3	+1.8	1.35 to 5.4	+19
Weathering flux	25	-4	0.52[a] and 0.98[b]	+5.5
Organic burial	5	-28	-	-
Inorganic burial	20	-	0.67[c] and 0.83[d]	-11[c] and -[d]

Table 2.S1: Initial parameters for the C and S model. All fluxes are in 10^{18} moles/Ma, while the reservoir sizes are 10^{18} moles. The 'weathering flux' for both cycles combines both the fluxes from volcanic (a) and continental weathering (b). The isotopic composition of the 'weathering flux' was calculated through isotopic mass balance. The inorganic flux for carbon is based on the burial of carbonates, while the sulfur burial portion of the model includes pyrite (c) and evaporite minerals (d). The dashes indicate phases that do not impart a major fractionation on the isotope reservoirs (40), and the $\delta^{34}S$ value for pyrite gives a $\Delta^{34}S$ of -30‰.

References

Adams, D.D., Hurtgen, M.T., Sageman, B.B., 2010. Volcanic triggering of a biogeochemical cascade during Oceanic Anoxic Event 2. Nature Geoscience 3, 201–204.

Arthur, M.A., Dean, W.E., Pratt, L.M., 1988. Geochemical and climatic effects of increased marine organic carbon burial at the Cenomanian/Turonian boundary. Nature 335, 714–717.

Barclay, R.S., McElwain, J.C., Sageman, B.B., 2010. Carbon sequestration activated by a volcanic CO_2 pulse during Ocean Anoxic Event 2. Nature Geoscience 3, 205–208.

Blättler, C.L., Jenkyns, H.C., Reynard, L.M., Henderson, G.M., 2011. Significant increases in global weathering during Oceanic Anoxic Events 1a and 2 indicated by calcium isotopes. Earth and Planetary Science Letters 309, 77–88.

Böttcher, M.E., Hetzel, A., Brumsack, H.J., Schipper, A., 2006. Sulfur–iron–carbon geochemistry in sediments of the Demerara Rise. In: Mosher, D.C., Erbacher, J., Malone, M.J. (Eds.), Proceedings of the Ocean Drilling Program. Scientific Results, vol. 207. Ocean Drilling Program, College Station, TX, 1–23.

Canfield, D.E., Raiswell, R., Westrich, J.T., Reaves, C.M., Berner, R.A., 1986. The use of chromium reduction in the analysis of reduced inorganic sulfur in sediments and shales. Chemical Geology 54, 149-155.

Fike, D.A., Grotzinger, J.P., 2008. A paired sulfate-pyrite $\delta^{34}S$ approach to understanding the evolution of the Ediacaran-Cambrian sulfur cycle. Geochimica et Cosmochimica Acta 72, 2636–2648.

Fike, D.A., Grotzinger, J.P., Pratt, L.M., Summons, R.E., 2006. Oxidation of the Ediacaran ocean. Nature 444, 744–747.

Forster, A., Schouten, S., Moriya, K., Wilson, P.A., Sinninghe Damsté, J.S., 2007. Tropical warming and intermittent cooling during the Cenomanian/Turonian oceanic anoxic event 2: Sea surface temperature records from the equatorial Atlantic. Paleoceanography 22, PA1219.

Friedrich, O., Erbacher, J., Mutterlose, J., 2006. Paleoenvironmental changes across the Cenomanian/Turonian Boundary Event (Oceanic Anoxic Event 2) as indicated by benthic foraminifera from the Demerara Rise (ODP Leg 207). Revue de Micropaléontologie 49, 121–139.

Frijia, G., Parente, M., 2008. Strontium isotope stratigraphy in the upper Cenomanian shallow-water carbonates of the southern Apennines: Short-term perturbations

of marine $^{87}Sr/^{86}Sr$ during the oceanic anoxic event 2. Palaeogeography, Palaeoclimatology, Palaeoecology 261, 15–29.

Gale, A.S., Christensen, W.K., 1996. Occurrence of the belemnite *Actinocamax plenus* in the Cenomanian of SE France and its significance. Bulletin of the Geological Society of Denmark 43, 68–77.

Gale, A.S., Jenkyns, H.C., Kennedy, W.J., Corfield, R.M., 1993. Chemostratigraphy versus biostratigraphy: data from around the Cenomanian-Turonian boundary. Journal of the Geological Society 150, 29–32.

Gautier, D.L., 1987. Isotopic composition of pyrite: Relationship to organic matter type and iron availability in some North American Cretaceous shales. Chemical Geology: Isotope Geoscience section 65, 293–303.

Gill, B.C., Lyons, T.W., Jenkyns, H.C., 2011a. A global perturbation to the sulfur cycle during the Toarcian Oceanic Anoxic Event. Earth and Planetary Science Letters 312, 484–496.

Gill, B.C., Lyons, T.W., Young, S.A., Kump, L.R., Knoll, A.H., Saltzman, M.R., 2011b. Geochemical evidence for widespread euxinia in the Later Cambrian ocean. Nature 469, 80–83.

Jarvis, I., Gale, A.S., Jenkyns, H.C., Pearce, M.A., 2006. Secular variation in Late Cretaceous carbon isotopes: a new Campanian (99.6-70.6 Ma). Geological Magazine 143, 561–608.

Jarvis, I., Lignum, J.S., Gröcke, D.R., Jenkyns, H.C., Pearce, M.A., 2011. Black shale deposition, atmospheric CO_2 drawdown, and cooling during the Cenomanian-Turonian Oceanic Anoxic Event. Paleoceanography 26, PA3201.

Jenkyns, H.C., Matthews, A., Tsikos, H., Erel, Y., 2007. Nitrate reduction, sulfate reduction, and sedimentary iron isotope evolution during the Cenomanian-Turonian oceanic anoxic event. Paleoceanography 22, PA3208.

Keller, G., Berner, Z., Adatte, T., Stueben, D., 2004. Cenomanian–Turonian and $\delta^{13}C$, and $\delta^{18}O$, sea level and salinity variations at Pueblo, Colorado. Palaeogeography, Palaeoclimatology, Palaeoecology 211, 19–43.

Kurtz, A.C., Kump, L.R., Arthur, M.A., Zachos, J.C., Paytan, A., 2003. Early Cenozoic decoupling of the global carbon and sulfur cycles. Paleoceanography 18, 1090.

Loyd, S.J., Marenco, P.J., Hagadorn, J.W., Lyons, T.W., Kaufman, A.J., Sour-Tovar, F., Corsetti, F.A., 2012. Sustained low marine sulfate concentrations from the Neoproterozoic to the Cambrian: Insights from carbonates of northwestern Mexico and eastern California. Earth and Planetary Science Letters 339-340, 79–94.

MacLeod, K.G., Martin, E.E., Blair, S.W., 2008. Nd isotopic excursion across Cretaceous ocean anoxic event 2 (Cenomanian-Turonian) in the tropical North Atlantic. Geology 36, 811–814.

Marenco, P.J., Corsetti, F.A., Kaufman, A.J., Bottjer, D.J., 2008. Environmental and diagenetic variations in carbonate associated sulfate: An investigation of CAS in the Lower Triassic of the western USA. Geochimica et Cosmochimica Acta 72, 1570–1582.

Martin, E.E., MacLeod, K.G., Jiménez Berrocoso, A., Bourbon, E., 2012. Water mass circulation on Demerara Rise during the Late Cretaceous based on Nd isotopes. Earth and Planetary Science Letters 327-328, 111–120.

Mazumdar, A., Goldberg, T., Strauss, H., 2008. Abiotic oxidation of pyrite by Fe(III) in acidic media and its implications for sulfur isotope measurements of lattice-bound sulfate in sediments. Chemical Geology 253, 30–37.

Parente, M., Frijia, G., Di Lucia, M., Jenkyns, H.C., Woodfine, R.G., Baroncini, F., 2008. Stepwise extinction of larger foraminifers at the Cenomanian-Turonian boundary: A shallow-water perspective on nutrient fluctuations during Oceanic Anoxic Event 2 (Bonarelli Event). Geology 36, 715–718.

Paytan, A., Kastner, M., Campbell, D., Thiemens, M.H., 2004. Seawater sulfur isotope fluctuations in the Cretaceous. Science 304, 1663–1665.

Pogge von Strandmann, P.A.E., Jenkyns, H.C., Woodfine, R.G., 2013. Lithium isotope evidence for enhanced weathering during Oceanic Anoxic Event 2. Nature Geoscience 6, 668-672.

Schlanger, S.O., Arthur, M.A., Jenkyns, H.C., Scholle, P.A., 1987. The Cenomanian-Turonian Oceanic Anoxic Event, I. Stratigraphy and distribution of organic carbon-rich beds and the marine $\delta^{13}C$ excursion, in *Marine Petroleum Source Rocks*, edited by J. Brooks and A. J. Fleet. Geological Society, London, Special Publications 26, 371–399.

Sinninghe Damsté, J.S., van Bentum, E.C., Reichart, G.-J., Pross, J., Schouten, S., 2010. A CO_2 decrease-driven cooling and increased latitudinal temperature gradient during the mid-Cretaceous Oceanic Anoxic Event 2. Earth and Planetary Science Letters 293, 97–103.

Tsikos, H., Jenkyns, H.C., Walsworth-Bell, B., Petrizzo, M.R., Forster, A., Kolonic, S., Erba, E., Premoli Silva, I., Baas, M., Wagner, T., Sinninghe Damsté, J.S., 2004. Carbon-isotope stratigraphy recorded by the Cenomanian–Turonian Oceanic Anoxic Event: correlation and implications based on three key localities. Journal of the Geological Society 161, 711–719.

van Bentum, E.C., Hetzel, A., Brumsack, H.-J., Forster, A., Reichart, G.-J., Sinninghe Damsté, J.S., 2009. Reconstruction of water column anoxia in the equatorial Atlantic during the Cenomania-Turonian oceanic anoxic event using biomarker and trace metal proxies. Palaeogeography, Palaeoclimatology, Palaeoecology 280, 489–498.

van Bentum, E.C., Reichart, G.-J., Forster, A., Sinninghe Damsté, J.S., 2012. Latitudinal differences in the amplitude of the OAE-2 carbon isotopic excursion: pCO_2 and paleo productivity. Biogeosciences 9, 717–731.

Wood, C.J., Morter, A.A., Gallois, R.W., 1994. Upper Cretaceous stratigraphy of the Trunch borehole. In Geology of the Country around Great Yarmouth Memoir for 1:50,000 Sheet 162 (England and Wales) with an Appendix on the Trunch Borehole by Wood and Morter (eds R. S. Arthurton, S. J. Booth, A. N. Morigi, M. A. W. Abbott and C. J. Wood), 105–10. London: HMSO.

Wotte, T., Strauss, H., Fugmann, A., Garbe-Schönberg, D., 2012. Paired $\delta^{34}S$ data from carbonate-associated sulfate and chromium-reducible sulfur across the traditional Lower–Middle Cambrian boundary of W-Gondwana. Geochimica et Cosmochimica Acta 85, 228–253.

Zheng, X.-Y., Jenkyns, H.C., Gale, A.S., Ward, D.J., Henderson, G.M., 2013. Changing ocean circulation and hydrothermal inputs during Ocean Anoxic Event 2 (Cenomanian-Turonian): Evidence from Nd-isotopes in the European shelf sea. Earth and Planetary Science Letters 375, 338–348.

Table 2.S2: Geochemical data from Raia del Pedale.

Depth (m)	$\delta^{13}C_{inorg}$ (‰)	$\delta^{34}C_{CAS}$ (‰)	C_{inorg} (wt%)	$\frac{^{87}Sr}{^{86}Sr}$
318.00	-2.72			
317.00	-2.86			0.708
316.00	-2.62	19.90	75.56	
315.00	-1.67			
314.00	-1.95			
313.00	-2.37			
312.00	-2.68			
311.00	-2.47			
310.00	-2.58			
309.00	-1.98			
308.00	-1.71			
307.00	-2.55			
306.00	-2.52	17.88	91.72	
305.00	-2.62			
304.00	-1.45			
303.00	1.22			0.708
302.00	-3.52			
301.00	1.21			0.707
300.00	-0.88	19.78	70.86	
299.00	-3.31			
298.00	1.15			
297.00	-2.38			
295.00	-2.54			
294.00	-0.79			
293.00	1.50	18.76	75.57	0.708
292.00	-1.00			
291.00	-2.57			
290.00	-2.61			
289.00	-2.83	19.31	77.13	
288.00	-1.10			
287.00	-3.42			0.708
286.00	-0.67			
285.00	-2.32			
284.00	-2.66			
283.00	-2.90			
282.00	-1.84			
281.00	-2.77			
280.00	-1.76	19.23	72.42	
279.00	-3.59			
278.00	-3.54			
277.00	-2.88			
276.00	-3.15			
275.00	-2.50			
274.00	-3.18			
273.00	-3.36			
272.00	-2.53			
271.00	1.85	20.07	74.72	0.708
270.00	-1.22			
269.00	-2.30	18.39	79.54	0.707
268.00	-1.95			
267.00	-2.50			
266.00	-2.21			
265.00	1.28			0.707
264.00	-2.11			
263.00	-2.51			
262.00	-2.66			
261.00	0.89			0.707
260.00	-1.33	20.19	78.13	
259.00	1.68			0.708
258.00	-0.59			
257.00	1.27			
256.00	-0.84			
255.00	2.12	21.12	79.86	
254.00	2.23			
253.00	1.93			0.707
252.00	-1.19			
251.00	0.74			
249.00	1.37			0.707
248.00	-0.07	19.82	76.28	
247.00	1.71			
246.00	0.71			
245.00	1.85			0.707
244.00	-0.56			
243.00	-0.66			
242.00	-0.62	20.53	73.45	
241.00	0.24			
240.00	1.10			
239.00	0.24			
238.00	0.09			
237.00	2.87			0.707
236.00	0.41	20.41	69.53	
235.00	0.82			
233.00	0.20			0.707
232.00	1.20			
231.00	2.29			
230.00	1.31			
229.00	-0.99			
228.00	0.69	21.31	47.28	
227.00	2.83			
226.00	1.57			
225.00	3.03			
224.00	2.40			
223.00	1.19	21.16	51.35	0.707
222.00	0.82			
221.00	1.47			
220.00	2.19			
219.00	0.99			
218.00	0.64			
217.00	-1.31	20.19	70.49	0.707
216.00	1.34			
215.00	3.01			
214.00	0.55			
213.00	-0.01			
212.00	0.82			
211.00	-0.57			

Table 2.S2: *continued*

Depth (m)	$\delta^{13}C_{inorg}$ (‰)	$\delta^{34}C_{CAS}$ (‰)	C_{inorg} (wt%)	$\frac{^{87}Sr}{^{86}Sr}$
210.00	0.98			
209.00	2.83			
208.00	2.73			
207.00	2.52			
206.00	2.82			
205.00	-2.20	21.66	72.79	0.707
204.00	1.11			
203.00	1.75			
201.00	2.41			0.707
200.00	2.10			
199.00	0.50			0.707
198.00	1.94	20.85	75.94	
197.00	2.53			
196.00	1.99			
195.00	2.35			
194.00	2.81			
193.00	2.04			
192.00	2.58			
191.00	3.00			
190.00	2.06	21.28	73.46	
189.00	1.92			0.707
187.00	2.98			
185.00	0.88	20.30	72.14	
184.00	1.48			
183.00	0.57			
182.00	2.80	21.60	74.24	
181.00	1.45			0.707
180.60	1.02			
180.00	2.23	20.48	99.56	
179.00	-0.62			
178.00	2.06			
177.00	-2.63	21.58	70.56	
176.00	0.78			0.707
175.00	-3.06			
174.00	1.49			
173.00	1.05			
172.00	1.08			
171.00	-3.14			
170.00	3.09			0.707
169.00	0.16			
168.00	1.61			
167.00	0.30			
166.00	0.80			0.707
165.00	1.22			
164.00	1.47			
163.00	0.25			
162.00	1.59			
161.00	0.15			
160.00	1.17			
159.00	0.94	21.68	83.51	
158.00	1.94			
157.00	-1.80			
156.00	1.04			
155.00	0.79			
154.00	1.19			
153.00	1.55	22.43	77.23	
152.00	2.12			
151.00	0.68			
150.00	0.61			0.707
149.00	1.10	22.35	68.46	
148.00	1.37			0.707
147.00	2.03			
146.00	0.55			
145.00	1.93			
144.00	1.07			
143.00	1.49	22.12	80.83	
142.00	0.62			0.707
141.00	-0.46			
140.00	0.33			
139.00	2.48			
138.00	1.58			
137.00	2.08	21.59	69.67	
136.00	1.47			0.707
135.00	-2.88			
134.00	1.24			
133.00	1.96			
132.00	1.80			0.707
131.00	-2.76			
130.00	2.23			
129.00	2.63			
128.00	1.59			
127.00	-1.68			
126.00	3.88			
125.00	2.02			
124.00	1.45			0.707
123.00	-1.17			
122.00	1.15			
121.00	0.13	22.62	82.58	
120.00	1.52			
119.00	0.39			
118.00	1.09	22.99	94.68	0.707
117.00	1.48			
116.00	0.54			
115.00	-0.46			
114.00	0.38			
113.00	1.31	23.58	79.26	
112.00	2.76			0.707
111.00	1.07			
110.00	0.74			
109.00	-0.22			
108.00	1.02			0.707
106.00	0.97	22.47	85.30	0.707
105.00	0.76			
104.00	1.08			
103.00	1.00			
102.00	0.36			
101.00	0.90			
99.00	0.23			

Table 2.S2: *continued*

Depth (m)	$\delta^{13}C_{inorg}$ (‰)	$\delta^{34}C_{CAS}$ (‰)	C_{inorg} (wt%)	$\frac{^{87}Sr}{^{86}Sr}$	Depth (m)	$\delta^{13}C_{inorg}$ (‰)	$\delta^{34}C_{CAS}$ (‰)	C_{inorg} (wt%)	$\frac{^{87}Sr}{^{86}Sr}$	Depth (m)	$\delta^{13}C_{inorg}$ (‰)	$\delta^{34}C_{CAS}$ (‰)	C_{inorg} (wt%)	$\frac{^{87}Sr}{^{86}Sr}$
98.00	-3.05	22.48	72.47		78.25	-0.76				68.75	2.59			
97.00	0.04				77.75	-1.07				68.50	2.50			
96.00	-1.43				77.50	-0.33				68.25	1.32	23.54	87.74	
95.00	1.84				77.25	-0.75				68.00	2.37			0.707
93.00	3.20				77.00	-1.36	24.67	69.45		67.75	2.69			
92.00	0.54	22.00	81.76		76.75	-1.82				67.50	2.98			
91.50	0.21				76.50	-3.12				67.25	2.49			
91.40	-0.81	22.31	90.57		76.25	-1.81				67.00	2.43			
91.00	0.50				76.00	-0.43			0.707	66.75	1.79			
90.00	-0.78				75.75	1.82				66.50	1.99			
89.00	-2.11	23.30	92.99		75.50	2.18				66.25	1.83			
88.00	-0.70			0.707	75.25	-3.00				66.00	1.50			0.707
87.00	-1.27				75.00	0.03				65.75	1.85			
86.00	0.57	25.66	85.48		74.75	-3.24				65.50	0.63			
85.75	1.47				74.50	-3.59				65.25	0.72			
85.50	-3.06				74.25	-3.37				65.00	0.50			
85.25	-3.52				74.00	-0.95	24.31	70.98	0.707	64.75	0.55			
85.00	-1.01				73.75	0.77				64.50	0.73			
84.75	-0.55				73.50	-1.58				64.25	0.89			
82.75	0.99				73.50	1.79				64.00	1.37	23.30	73.92	
82.50	-0.78				73.00	3.42				63.75	1.45			
82.25	-0.40	24.71	72.91		72.50	-1.02				63.50	2.13			
82.00	-1.70				72.25	-0.83				63.25	2.44			
81.75	-0.10				72.00	-0.73			0.707	63.00	2.24			
81.25	0.73				71.75	0.02				62.75	1.94			
81.00	-2.17				71.30	0.47				62.50	2.41			
80.75	-0.61				71.25	1.19				62.25	2.08			
80.50	-0.31				71.00	0.94				62.00	3.02	22.99	74.83	
80.25	-0.54				70.75	1.54				61.75	1.92			
80.00	-0.29	23.77	71.98	0.707	70.50	0.03				61.50	1.95			
79.75	-0.75				70.25	0.97				61.25	2.95			
79.50	-0.59				70.00	1.39	22.40	76.29	0.707	61.00	3.20			0.707
79.25	-0.66				69.75	1.92				60.75	3.89			
79.00	-0.74				69.50	1.94				60.50	3.31			
78.75	0.53				69.25	1.96				60.25	3.29			
78.50	-0.96				69.00	2.20				60.00	3.30			0.708

Table 2.S2: *continued*

Depth (m)	$\delta^{13}C_{inorg}$ (‰)	$\delta^{34}C_{CAS}$ (‰)	C_{inorg} (wt%)	$\frac{^{87}Sr}{^{86}Sr}$	Depth (m)	$\delta^{13}C_{inorg}$ (‰)	$\delta^{34}C_{CAS}$ (‰)	C_{inorg} (wt%)	$\frac{^{87}Sr}{^{86}Sr}$	Depth (m)	$\delta^{13}C_{inorg}$ (‰)	$\delta^{34}C_{CAS}$ (‰)	C_{inorg} (wt%)	$\frac{^{87}Sr}{^{86}Sr}$
59.75	3.62				51.25	2.80				42.25	3.17			
59.50	3.41				51.00	4.02				42.00	3.26	20.87	88.88	
59.25	3.93	23.54	90.94		50.75	4.46				41.75	3.47			
59.00	3.28			0.707	50.50	4.54				41.50	2.95			
58.75	1.70				50.25	4.34				41.25	3.06			
58.50	3.29				50.00	4.55			0.707	41.00	2.72			0.707
58.25	2.99				49.75	4.65				40.75	2.95			
58.00	3.49			0.707	49.50	4.34				40.50	2.72			
57.75	3.71				49.25	4.44				40.25	3.14			
57.50	3.12				49.00	3.84			0.707	40.00	3.34	21.48	83.49	
57.25	3.58				48.75	3.77				39.75	2.67			
57.00	4.22				48.50	4.50				39.50	3.27			
56.75	2.95				48.25	3.81				39.25	0.07			
56.50	1.92				48.00	3.03			0.707	39.00	2.75			
56.25	4.86				47.75	2.70				38.50	2.92			
56.00	3.84	22.40	96.15		47.50	3.30				38.25	2.98			
55.75	2.44				47.25	3.91				38.00	2.68	21.91	93.02	
55.50	2.93				47.00	4.18	23.49	68.72	0.707	37.75	3.42			
55.25	3.68				46.75	4.49				37.50	2.59			
55.00	2.96			0.707	46.50	3.91				37.25	2.59			
54.75	3.71				46.25	3.99				37.00	2.02			0.708
54.50	3.80				46.00	3.67				36.75	2.03			
54.25	3.43				45.75	3.24				36.25	1.83			
54.00	3.07			0.707	45.50	4.25				36.00	2.19			
53.75	4.86				45.25	4.19				35.25	1.36			
53.50	4.69				45.00	3.59			0.707	35.00	1.21			
53.25	4.83				44.75	3.94				34.75	1.87			
53.00	3.75				44.50	4.51				34.50	2.12			
52.75	3.83				44.25	3.94				34.00	2.09			
52.50	3.74				44.00	3.74	21.49	91.09		33.75	2.36			
52.25	2.35				43.75	4.15				33.50	2.21			
52.20	1.69				43.50	3.27				33.00	2.04			0.707
52.00	3.60			0.707	43.25	3.25				32.75	2.29			
51.75	3.92				43.00	3.42			0.707	32.50	2.64			
51.65	3.31	24.64	88.02		42.75	3.98				32.00	2.67	20.49	93.40	
51.50	4.01				42.50	3.57				31.75	2.94			

Table 2.S2: *continued*

Depth (m)	$\delta^{13}C_{inorg}$ (‰)	$\delta^{34}C_{CAS}$ (‰)	C_{inorg} (wt%)	$\frac{^{87}Sr}{^{86}Sr}$
31.25	2.73			
31.00	2.57			
30.75	2.64			
30.50	3.19			
30.00	1.49			
29.75	1.77			
29.50	2.46			
29.25	3.16			
29.00	2.63			
28.75	3.16			
28.50	1.97			
28.25	2.38			
28.00	2.13	21.18	72.44	
27.75	2.02			
27.50	2.07			
27.25	1.67			
27.00	1.27			0.708
26.75	-0.29			
26.50	-0.21			
26.25	0.04			
26.00	0.24	21.31	71.71	
25.75	0.15			
25.25	0.52			
25.00	-0.26			0.708
24.75	0.84			
24.50	0.60			
24.25	0.16			
24.00	-0.20			
23.75	0.59			
23.50	1.31			
23.25	0.51			
23.00	-0.15			0.707
22.75	0.13			
22.50	-1.27			
22.25	0.41			
22.00	0.24			
21.75	-0.72			
21.25	0.10			
21.00	0.27			0.707
20.75	-0.81			
20.50	-0.83			
20.25	-0.00			
20.00	0.31	22.25	76.95	
19.75	-0.32			
19.50	0.10			
19.25	-1.05			
19.00	-0.72			0.708
18.75	-0.59			
18.50	-0.37			
18.25	0.11			
18.00	-0.68			
17.75	-0.26			
17.50	-0.05			
17.25	-0.63			
17.00	0.94			
16.75	-0.04			
16.50	-0.06			
16.25	0.65			
16.00	0.19	19.98	49.86	
15.00	-0.70			
14.00	-0.41			
13.00	-0.58			
12.00	1.00			
11.00	0.20	20.48	51.35	
10.00	0.51	23.52	89.51	
9.00	-1.21	20.00	56.03	
8.00	0.15	21.55	53.22	
7.00	0.85			
6.00	0.43	20.40	51.55	
5.20	-2.38			
5.00	0.16			
4.00	-3.57			
3.00	-1.60	22.56	72.46	
2.00	-1.47			
1.00	0.15			
0.00	-0.42			

Table 2.S3: Geochemical data from Trunch.

Depth (m)	$\delta^{13}C_{inorg}$ (‰)	$\delta^{34}C_{CAS}$ (‰)	C_{inorg} (wt%)
481.50	2.50		97.24
483.33	2.42	20.07	100.24
484.50	2.68	20.88	95.51
486.50	2.70	20.76	96.36
487.80	2.73	20.92	96.94
489.50	3.04	21.41	96.26
491.50	3.44	21.57	96.05
493.50	3.60	21.43	97.06
495.64	3.51	21.80	93.58
496.50	3.41	21.25	97.54
498.55	3.45	20.74	97.08
499.79	3.50	21.03	96.43
500.14		20.61	
500.75	3.03	20.67	94.45
501.18	2.89	20.38	90.61
502.05	2.80	19.85	92.82
502.66	2.75	20.18	93.34
503.50	2.56	19.91	89.91
504.50	2.40	19.18	85.66
505.50	2.34	18.43	85.81
506.05	2.44	19.47	84.84
506.65	2.00	18.87	90.06
507.05	1.91	18.21	91.13
507.89	1.98	18.63	93.08
508.41	1.99	18.86	88.21
509.05	1.84	19.34	91.77
510.50	1.61	18.77	88.95

Table 2.S4: Geochemical data from South Ferriby.

Depth (cm)	$\delta^{13}C_{inorg}$ (‰)	$\delta^{34}C_{CAS}$ (‰)	C_{inorg} (wt%)
200	3.32	21.49	56.23
150	3.36	21.08	55.49
100	3.34	21.83	48.56
95	3.28	22.03	58.62
90	3.19	21.57	67.92
85	3.21	21.85	43.25
80	3.23	21.54	43.66
75	3.20	21.63	41.47
70	3.27	21.77	50.11
65	3.17	21.86	39.70
60	3.24	21.99	37.30
55	3.16	21.95	44.84
50	3.34	22.07	37.58
45	3.31	22.00	75.47
40	3.31	21.94	37.48
35	3.40	21.65	42.08
30	3.34	21.38	41.62
25	3.48	21.06	37.58
20	3.62	21.29	28.71
-5	4.40	21.06	25.19
-10	4.51	20.82	29.53
-15	3.34	20.96	46.88
-20	3.28	20.90	48.49
-25	3.40	20.70	53.87
-30	3.26	21.02	46.18
-35	3.32	20.78	44.40
-40	3.24	20.79	47.08
-45	3.22	20.86	50.56
-50	3.24	20.86	53.25
-55	3.26	20.57	58.40
-60	3.25	20.74	55.00
-65	3.08	20.56	50.85
-70	3.16	20.47	54.70
-75	3.20	20.45	43.23
-80	3.08	20.91	49.39
-85	3.08	20.66	5.43
-90	3.10	20.89	50.52
-95	3.08	20.51	55.95
-100	3.16	20.48	54.53

Table 2.S5: Geochemical data from Eastbourne.

Depth (cm)	$\delta^{13}C_{inorg}$ (‰)	$\delta^{34}C_{CAS}$ (‰)	C_{inorg} (wt%)	Depth (cm)	$\delta^{13}C_{inorg}$ (‰)	$\delta^{34}C_{CAS}$ (‰)	C_{inorg} (wt%)	Depth (cm)	$\delta^{13}C_{inorg}$ (‰)	$\delta^{34}C_{CAS}$ (‰)	C_{inorg} (wt%)
2690	3.53	21.11	93.80	1990	4.55	21.35	91.61	1360	4.96	17.26	88.92
2670	3.50	21.60	89.81	1970	4.61			1340	4.87	18.74	87.37
2650	3.51	21.83	92.22	1950	4.50			1320	4.78	16.36	89.15
2630	3.58			1930	4.54	20.52	91.89	1300	4.70	18.81	89.41
2610	3.69	21.25	94.02	1910	4.61			1260	4.48	18.46	
2590	3.76			1890	4.61			1240	4.54	20.38	89.10
2570	3.67			1870	4.66			1140	4.28	18.69	75.28
2550	3.67	21.38	97.03	1850	4.76	21.53	92.10	1120	4.48	19.09	78.68
2530	3.42			1840		20.59	96.67	1100	4.63	19.97	80.24
2510	3.61	21.61	95.23	1830	4.73			1080	4.67	19.69	88.57
2490	3.87			1810	4.81			1040	4.77	20.01	85.19
2470	3.76	21.62	95.79	1790	4.92	20.76	89.70	1020	4.70	19.85	
2450	3.78			1770	4.74			1000	4.74	19.40	83.94
2430	3.78			1770	4.78	20.64	92.76	980	4.67		
2410	3.73	21.47	92.31	1730	4.75			960	4.54	19.84	82.07
2390	3.79			1710	4.89			940	4.41	18.15	81.43
2370	3.66	21.47	94.76	1670	4.86			930		19.31	84.96
2350	3.77			1650	4.67	20.95	93.63	900	4.15	17.29	79.63
2330	3.72			1630	4.72			880	3.89	18.25	72.94
2310	3.76	21.16	93.21	1610	4.70			860	3.87	17.61	81.80
2290	3.75			1590	4.63	20.56	88.99	840	3.45	17.79	77.79
2270	3.74			1570	4.84			820	3.52		
2250	3.82			1550	4.95			800	3.52	18.02	79.92
2230	3.90	21.57	93.69	1540		20.79	91.50	760	3.48	19.12	76.52
2210	4.11	21.40	93.94	1530	4.82			740	3.43	18.03	77.29
2190	3.91	21.35	93.39	1510	4.84			730			77.16
2170	3.71			1490	4.80	20.35		720	3.43	19.46	
2150	3.77	21.35	94.50	1470	4.85			700	3.50	19.35	76.66
2130	3.87			1450	4.98			680	3.31	18.49	76.10
2110	3.89			1440	4.94	19.65	91.66	660	3.24	19.33	80.16
2090	3.87	21.56	92.35	1430	5.16			640	3.22	19.41	82.83
2070	4.09			1410	5.38			600	2.74	19.34	87.22
2050	4.20	21.25	94.33	1400	5.34	20.04	92.70	580	2.73	20.18	89.13
2030	4.29			1390	5.18			560	2.70	16.70	90.15
2010	4.33	20.98	93.46	1380	5.07	19.09	83.26	540	2.64	20.11	89.94

Table 2.S5: *continued*

Depth (cm)	$\delta^{13}C_{inorg}$ (‰)	$\delta^{34}C_{CAS}$ (‰)	C_{inorg} (wt%)
520	2.67	20.20	89.99
500	2.75	19.96	
480	2.71	19.01	94.40
460	2.66	20.29	
440	2.67	19.54	89.02
420	2.60	20.49	93.73
400	2.68	18.29	89.82
380	2.74	20.19	91.25
360	2.74	20.44	89.93
340	2.77	20.20	85.91
320	2.81	19.96	84.14
300	2.78	20.44	93.13
260	2.82	20.45	92.20
240	2.80	20.19	91.14
220	2.89	20.35	89.28
200	2.84	19.60	92.08
180	2.83	20.10	89.33
160	2.79	20.23	94.72
140	2.86	19.05	
120	2.88	19.48	92.37
100	2.89	20.23	87.81
80	2.90	19.43	84.46
60	2.90	20.02	83.20
40	2.89		
20	2.94	20.21	88.23
0	2.95	21.00	90.46

Chapter 3

Marine trace-metal drawdown during the Cenomanian-Turonian Boundary Event (OAE2): implication for global redox and biological perturbation

Introduction

Understanding the global redox state of the oceans and its cause-and-effect relationship with periods of widespread organic-carbon deposition is vital to understanding Earth's climatic and biotic feedbacks during Mesozoic periods of expanded oxygen deficiency and by extension analogous events throughout Earth's history. Among these 'oceanic anoxic events' [OAEs (Jenkyns, 2010)], the Cenomanian-Turonian boundary event (OAE2, ~93.9 Ma) is the most well-documented episode of widespread carbon burial in Earth history and is characterized by a large coeval positive carbon isotope excursion (3 to 7‰). Here, we present a compilation of data from an organic-rich locality within the proto-North Atlantic that shows a dramatic drawdown of redox-sensitive trace elements. New iron geochemical data independently suggest euxinic deposition (i.e., anoxic and sulfidic bottom waters) for the entire section, thus confirming its potential as a global metal inventories archive. In particular, depleted molybdenum (Mo; Reinhard et al., 2013; Scott et al., 2008) and vanadium (V; Algeo, 2004) concentrations effectively record the global expansion of euxinia and oxygen-deficient but non-sulfidic waters, respectively. The V drawdown precedes the OAE, thus fingerprinting an expansion of oxygen deficiency as a precursor to expanded euxinia. Molybdenum drawdown coincides with the onset of OAE2. Parallel lipid biomarkers analyses provide compelling evidence for significant and progressive reorganization of marine microbial ecology through the OAE, with the contributions to total primary production from eukaryotes compared to bacteria being lowest during metal depleted intervals. Geochemical box modelling of Mo suggests euxinia was restricted to <11% of the ocean. Because of their roles as micronutrients, the drawdown of Mo and V could have had profound effects on the nitrogen cycle (Anbar and Knoll, 2002; Bellenger et al., 2011; Glass et al., 2009; Glass et al., 2010). At the same time, the environmental

challenge presented by low dissolved oxygen and euxinia coincide with increased extinction rates of radiolarian and calcareous nannofossils, followed by planktonic foraminifera (Leckie et al., 2002), suggesting that the temporal patterns of anoxia/euxinia and associated nutrient limitations may explain the fabric of OAE2-related extinction.

Main Article

Despite the presence of a well-oxygenated atmosphere (Berner, 2006), multiple geochemical proxies record anoxic and/or euxinic conditions during OAE2, a short-lived event [~500 thousand years, ka (Jenkyns, 2010)], and on occasion, dissolved hydrogen sulfide appears to have penetrated the photic zone (Jenkyns, 2010). However, despite the apparent extremes in oxygen deficiency, marked also by the widespread deposition of organic-rich shales, direct geochemical evidence for local bottom-water anoxia/euxinia has been restricted to the Atlantic and Tethys Oceans, while redox conditions in the Pacific, Indian and Arctic Oceans remain unconstrained. Nevertheless, despite recent estimates of 40-50% (Monteiro et al., 2012; Montoya-Pino et al., 2010) ocean anoxia, and sulfur isotope systematics suggesting ~7% euxinia (Owens et al., in review), further geochemical estimates are needed that more specifically delineate the redox structure of the ocean and its links to nutrient availability, with attendant consequences for life. OAE2 marks the eighth largest extinction since the beginning of the Mesozoic (Raup and Sepkoski, 1986) which has been causally linked to an expansion of anoxia and/or euxinia (Leckie et al., 2002), with implications for the widespread oceanic oxygen deficiency that may lie in our future (Falkowski et al., 2011).

Increased organic carbon burial during an OAE can, in principle, be attributed to enhanced productivity and/or increased preservation (Jenkyns, 2010). However,

the maintenance of enhanced productivity and export on a global scale would require exceptional availability of major nutrients and bio-essential trace metals within the ocean. Nutrient delivery and/or recycling mechanisms include increased hydrothermal activity (Jenkyns, 2010), continental weathering (Blättler et al., 2011; Jenkyns, 2010) and recycling of phosphorus from sediments due to more pervasive anoxia (Kraal et al., 2010; Van Cappellen and Ingall, 1994). Marine trace elements are important micronutrients for a range of catalytic metabolisms such as nitrogen fixation (Anbar and Knoll, 2002; Bellenger et al., 2011; Glass et al., 2009), which may control globally integrated rates of primary production. In this light, we combine trace element datasets (Hetzel et al., 2009; Owens et al., 2012), lipid biomarkers and geochemical modelling to explore the spatiotemporal distribution during and proximal to OAE2, with the specific goal of providing novel insight into the extent and timing of ocean redox conditions and its possible impacts on marine ecosystems.

We first explore the speciation of reactive iron minerals to independently constrain the local depositional redox chemistry from a continuous organic-rich black shale sequence from Ocean Drilling Program site 1258. Such independent constraint on local redox, which does not rely on the systematics of redox-sensitive trace elements, is essential for the accurate assessment of this setting as an archive for changes in global trace metal inventories. This extraction method differentiates separate labile mineral phases of highly reactive iron (Poulton and Canfield, 2009) (Fe_{HR}), which is traditionally defined as the sum of pyrite-Fe (Fe_{py}) and remaining Fe phases that are reactive to sulfide on short timescales. Such phases include carbonates (Fe_{carb}), ferric oxides (Fe_{ox}) and magnetite [Fe_{mag} (see Supplemental Information)]. Modern marine siliciclastic muds deposited beneath oxic waters record a range of Fe_{HR}/Fe_{T} (total Fe) values (0.06 to 0.38), where values above this oxic baseline suggest Fe scavenging in an anoxic water column (Poulton and Canfield, 2009). High

Fe_{HR}/Fe_T ratios, in combination with elevated Fe_{py}/Fe_{HR} (>0.7) values, suggest deposition under euxinic conditions because nearly all of the reactive Fe has been converted to pyrite (Poulton and Canfield, 2009). In other words, sulfidic (euxinic) depositional settings are Fe-limited (Raiswell and Berner, 1986). Importantly, site 1258 maintains relatively stable and elevated Fe_{HR}/Fe_T and Fe_{py}/Fe_{HR} ratios throughout the section—with averages of 0.82±0.12 and 0.76±0.09, respectively—consistent with local euxinia before, during and following OAE2 (Fig. 3.1; see Supplemental Information) and is supported by persistently laminated sediments throughout this interval. This independent environmental context provides the ideal platform for using site 1258 as a window to the global marine redox and nutrient landscape during OAE2 by minimizing the effect of local redox shifts as a driver of trace element systematics, with stratigraphic trends in metal enrichment reflective of the seawater inventory rather than local redox controls.

Trace-metal enrichments recorded in black shales are an effective tracer of local redox conditions (Lyons et al., 2009) and often, such as site 1258, can track the size of the marine reservoir and thus the global redox state of the ocean through the specific enrichment magnitude for continuously euxinic environments (Emerson and Huested, 1991; Reinhard et al., 2013; Scott et al., 2008). The relationship between sedimentary enrichments and dissolved marine concentrations is well known for modern euxinic basins (Lyons et al., 2009). Observed enrichments of Mo, V, and Zn are several orders of magnitude greater than those observed in oxic environments, and their stratigraphic enrichment patterns are explained by their different redox behaviors. Molybdenum is the most abundant transition metal in the well-oxygenated modern ocean due to its high solubility as MoO_4^{2-} [~107 nM (Fischer et al., 2009)] and long residence time [~450 ka (Miller et al., 2011)]. The dominant removal of Mo in the modern ocean is through Mn-oxide phases; however, Mo is most efficiently buried in the presence of free sulfide, such as reducing and euxinic environments.

The greatest Mo enrichments occur in euxinic environments (Scott and Lyons, 2012). Importantly, reducing environments for Mo are defined as sulfidic pore fluids often beneath low-O_2 bottom waters similar to modern oxygen minimum zones environments (Helz et al., 1996). In the modern oxic ocean V exhibits a relatively short residence time [~50 to 100 ka (Algeo, 2004; Morford and Emerson, 1999)] due to a smaller dissolved marine reservoir [35 to 45 nM (Emerson and Huested, 1991; Morford and Emerson, 1999)], removal of vanadate oxyanions (HVO_4^{2-} and HVO_4^-) associated with Mn- and Fe-oxides, with efficient burial in low oxygen settings. Sequestration of sedimentary V, in contrast, starts in low oxygen environments and continues through euxinic conditions (Algeo, 2004; Morford and Emerson, 1999). Therefore, reductive enrichment of V in marine sediments can be independent of sulfide and we are using V as an indicator of low oxygen and anoxic conditions, providing an important contrast to Mo.

The observed trace metal drawdown during OAE2 (Fig. 3.1) suggests a dramatic and widespread perturbation to the marine geochemical redox system that impacted global metal inventories. Again, the persistence of local euxinia throughout the section confirms that shifting local redox is not controlling the observed metal enrichment pattern, and we can think of no reasonable local inventory control that would assert itself differentially over the entire interval of interest. The depletion of V enrichments precedes the OAE and associated Mo depletion by ~0.65 m or ~100 ka assuming a linear sedimentation rate (Fig. 3.1 and 3.S3). Carbonate-free V concentrations prior to the OAE (including the decline) and post-OAE2 are 2,407±1,008 and 1,757±1,140 ppm, respectively, while during OAE2 V concentrations drop to an average of 960±384 ppm. The non-OAE Mo average baseline (carbonate-free) at this locality is 183±91 ppm, while the average Mo concentration during the OAE drops to 56±38 ppm. Significantly, a ~3 m mid-portion of the OAE [422.99 to 425.92 mcd] preserves very low enrichments of both elements. At the nadir [423.86 to

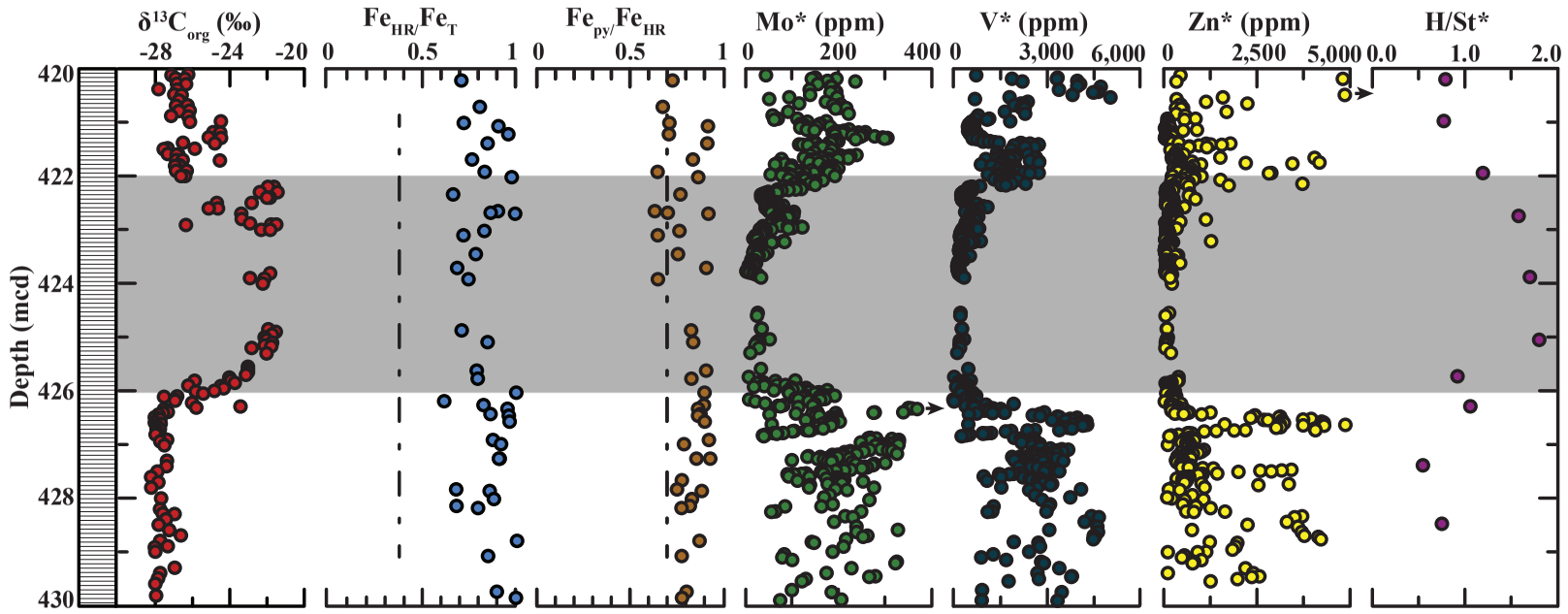

Figure 3.1: Stratigraphic geochemical trends of the paleoredox elements Mo and V where OAE2 is marked by the grey box which is delineated by the positive carbon isotope excursion. The * denotes that these plots are corrected for carbonate contents (Supplemental Information Fig. S2). The Fe_{HR}/Fe_T and Fe_{py}/Fe_{HR} samples do not include ferric oxides (see supplemental information for further discussion). There are 4 data points for Mo* not plotted that are above the axis maximum (see appendix data; from 426.35 to 426.37 mcd with values up to 796 ppm. The H/St* is from free and bound kerogen representing hopane/(sterane + sterene).

423.26 mcd], Mo and V enrichments approach crustal averages [~2 ppm Mo and ~180 ppm V (Taylor and McLennan, 1995)]—with values of 18±9 and 263±79 ppm, respectively. The very rapid Mo decrease (~25 ka) despite its long residence time—starting at high enrichments near the onset of the OAE (150 ppm at 426.08 mcd) followed by an abrupt drop to concentrations below 50 ppm (425.88 mcd)—indicates that the ~100 ka offset between the drawdown of V and Mo is unlikely to have been driven by residence time differences. In addition, other trace metals with sensitivity to low oxygen conditions, such as zinc (see supplemental information) and chromium (Hetzel et al., 2009), illustrate a drawdown coincident with V despite very different residence times in the ocean. Thus, this offset is most easily explained by dramatic increases in metal uptake via large-scale expansion of anoxia, followed by subsequent expansion of euxinic conditions.

The relatively well constrained modern Mo mass balance (Emerson and Huested, 1991; Morford and Emerson, 1999; Reinhard et al., 2013) shows that reducing (sulfidic pore waters) and euxinic environments effectively sequester 65% and 6.5% of the Mo delivered annually to the ocean, respectively, but occupy relatively small areas of the modern seafloor (Table 3.S1). It follows that the global burial of redox-sensitive trace elements during OAEs should increase dramatically (Reinhard et al., 2013) and would likely reduce the seawater inventories of many redox-sensitive elements. In general, muted Mo enrichments in shales deposited under euxinic conditions suggest that the marine reservoir was diminished by large-scale burial (Reinhard et al., 2013; Scott et al., 2008), thus providing a mechanism to estimate the extent of those conditions and a window to overall Mo availability in the ocean and its biological implications. To this end, a time-dependent forward first-order mass balance model was constructed to replicate the observed stratigraphic Mo trends, which simulates the geochemical cycle of Mo using modern fluxes and burial rates (Supplemental Information) and thereby quantitatively predicts the global extents of euxinia and reducing

environments. The model demands that all increases in euxinic and/or reducing burial occur at the expense of oxic seafloor. It is important to note that we are modelling the oceanic Mo reservoir concentration and not the sedimentary record, but the first-order model directly correlates sedimentary enrichments to the dissolved marine reservoir.

Importantly, the model quantitatively estimates the global extent of euxinia and reducing environments. Site 1258 shows 30% decrease from non-OAE to OAE average carbonate corrected Mo enrichments—and at the extreme a ~90% decrease. Using a strictly first-order approach, where a 90% sedimentary depletion equates to a 90% dissolved Mo depletion (or a seawater Mo concentration of ~10.7 nM relative to ~107 nM in modern seawater), this would require a ~100-fold increase (~10.8% seafloor area) of euxinic deposition relative to the modern areal extent of such conditions. Alternatively, a ~20-fold increase (~38.4% seafloor area) of reducing deposition would also result in the same ~10 nM seawater concentration (Fig. 3.2), and it may be reasonable to assume increases in both euxinic and reducing deposition (Fig. 3.S7); therefore the maximum extent of euxinia is ~11% but this would decrease with an increase in reducing deposition. Importantly, currently available data indicate a pronounced change in growth status and nitrogen fixation rates once ambient Mo concentrations drop below ~10nM (Glass et al., 2010). Using this first-order model assumes a linear relationship between seawater concentration and burial enrichment; however, this may be an oversimplification—thus allowing for lower predicted Mo concentrations in seawater[3] which is consistent with the observed Mo-to-TOC ratios (see Supplemental Information).

The geochemical, stratigraphic and modelling evidence for OAE2 suggest that euxinia was restricted to <11% of the seafloor, and reducing conditions covered <20%, but we could explain the data equally well with even less euxinia and a greater extent of

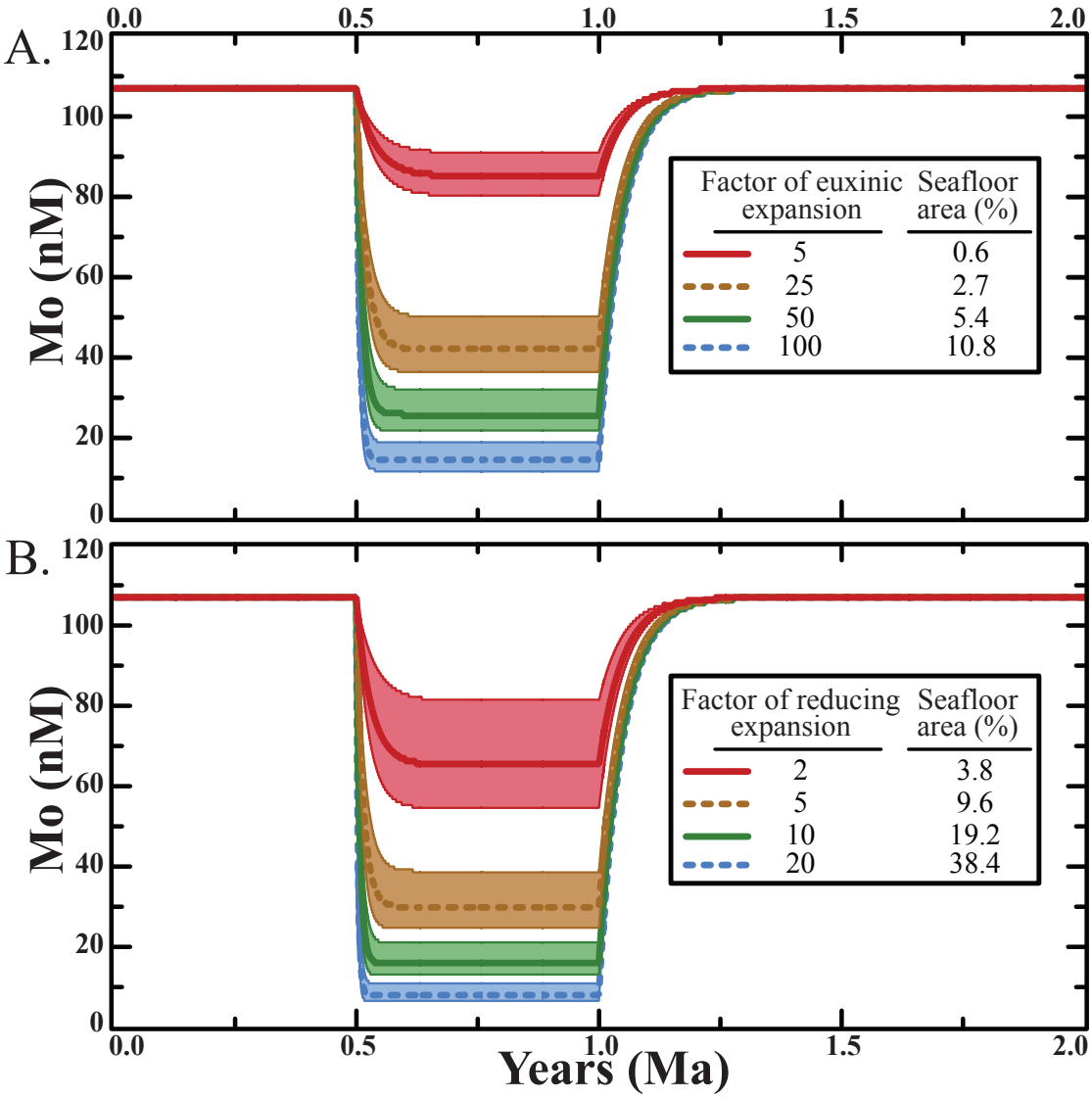

Figure 3.2: Modeled sensitivity test for Mo reservoir drawdown. Part A demonstrates an expansion of euxinic seafloor while B represents an expansion of reducing seafloor. The upper and lower dashed lines in both A and 3 represent 0.75% and 1.25% modern accumulation rates, respectively.

reducing conditions. Based on these predictions, the major regions of oxygen deficiency could have been restricted to the proto-North Atlantic, plus productive margins outside the North Atlantic, epicontinental seaways and/or equatorial upwelling regions. Importantly, widespread euxinia is not demanded for the Pacific. These estimates agree well with the global distribution of known black shales during OAE2 (Jenkyns, 2010) and allow for a mostly non-euxinic ocean. Consistent with the idea of widespread oxygen deficiency, the observed pre-event decline in V enrichment suggests an expansion of low-oxygen/anoxic conditions without sufficient sulfide accumulation prior to the initiation of OAE2. Importantly, this pre-event decline in marine oxygen roughly correlates with increased extinction rates for oxygen-demanding radiolarians (Leckie et al., 2002). Of equal significance, the predicted increased seafloor expansion of reducing conditions, as defined by Mo, at the onset of OAE2 correlates well with increased extinction rates for calcareous nannofossils and benthic and planktonic foraminifera (Leckie et al., 2002).

An important and related observation coincident with the OAE and trace metal drawdown is a systematic increase in hopane/sterane (H/St) biomarker ratio (Fig. 3.1; Supplementary Information), and is driven by both an increase in hopanes and a sterane decrease, most likely arising from diminishing eukaryotic contributions to sedimentary organic matter during OAE (Table 3.S2). The local lipid biomarker record provides compelling evidence for a significant and progressive reorganization of marine microbial ecology that must be related to more pervasive environmental changes—since the local setting was persistently productive and euxinic before, during and after the event. Subsequent to the OAE, H/St ratios return immediately to near pre-OAE values locally (Fig. 3.1). Site 1258 was characterized by strong upwelling, delivering ammonium, phosphorus, and other nutrients from the deep ocean thereby maintaining the high total organic carbon (TOC) content observed which would reduce the local impact of nutrient- and trace metal-stress

on eukaryotes such as microalgae (Higgins et al., 2012). Fixed nitrogen was unlikely to be limiting due to delivery of ammonium but low Zn concentrations could preferentially inhibit eukaryotic primary production (Scott et al., 2013). It is expected that open-ocean H/St ratios could record higher values, reflecting oligotrophic growth conditions for eukaryotes to depleted trace metal concentrations thus limiting the availability of fixed nitrogen. Similar oceanographic H/St results have been recorded in the Late Ordovician with high H/St ratios for nitrogen-limited epeiric seaways (Rohrssen et al., 2012). The expansion of oxygen deficiency, including euxinia, may have challenged life and perturbed the ecology in the ocean immediately before and during OAE2. This condition was compounded by limitations in bioessential trace metals, such as Mo and V, which are required by cyanobacteria enzymes and other N_2-fixing bacteria to replenish the fixed nitrogen pool and sustain marine productivity.

The observed positive carbon-isotope excursion dictates an increased global carbon burial during OAE2 demands either higher productivity or enhanced preservation. The depleted trace metals during the event demands a shift to preservational controls on the amount of TOC buried globally because global primary production would be hampered at the onset of the event. Increased sedimentation rates and reducing/euxinic deposition likely increased preservational controls as the dominate burial of OC during OAE2 is in marginal marine settings. Low oxygen marine conditions in the Phanerozoic are often short lived discrete events which are likely tied to high atmospheric O_2 which is the ultimate feedback controlling bioessential metal cycles, primary production, preservation through redox and sedimentation, and the extent and duration of OAEs.

References

Algeo, T.J., 2004. Can marine anoxic events draw down the trace element inventory of seawater? Geology 32, 1057–1060.

Anbar, A.D., Knoll, A.H., 2002. Proterozoic ocean chemistry and evolution: A bioinorganic bridge? Nature 297, 1137-1142.

Bellenger, J.P., Wichard, T., Xu, Y., Kraepiel, A.M.L., 2011. Essential metals for nitrogen fixation in a free-living N2-fixing bacterium: chelation, homeostasis and high use efficiency. Environmental Microbiology 13, 1395–1411.

Berner, R.A., 2006. GEOCARBSULF: A combined model for Phanerozoic atmospheric O_2 and CO_2. Geochimica et Cosmochimica Acta: A Special Issue Dedicated to Robert A. Berner 70, 5653–5664.

Blättler, C.L., Jenkyns, H.C., Reynard, L.M., Henderson, G.M., 2011. Significant increases in global weathering during Oceanic Anoxic Events 1a and 2 indicated by calcium isotopes. Earth and Planetary Science Letters 309, 77–88.

Emerson, S.R., Huested, S.S., 1991. Ocean anoxia and the concentrations of molybdenum and vanadium in seawater. Marine Chemistry 34, 177–196.

Falkowski, P.G., Algeo, T., Codispoti, L., Deutsch, C., Emerson, S., Hales, B., Huey, R.B., Jenkins, W.J., Kump, L.R., Levin, L.A., Lyons, T.W., Nelson, N.B., Schofield, O.S., Summons, R., Talley, L.D., Thomas, E., Whitney, F., Pilcher, C.B., 2011. Ocean deoxygenation: Past, present, and future. EOS, Transactions American Geophysical Union 92, 409–410.

Fischer, J.P., Ferdelman, T.G., D'Hondt, S., Røy, H., Wenzhöfer, F., 2009. Oxygen penetration deep into the sediment of the South Pacific gyre. Biogeosciences 6, 1467–1478.

Glass, J.B., Wolfe-Simon, F., Anbar, A.D., 2009. Coevolution of metal availability and nitrogen assimilation in cyanobacteria and algae. Geobiology 7, 100–123.

Glass, J.B., Wolfe-Simon, F., Elser, J.J., Anbar, A.D., 2010. Molybdenum-nitrogen co-limitation in freshwater and coastal heterocystous cyanobacteria. Limnology Oceanography 55, 667–676.

Helz, G.R., Miller, C.V., Charnock, J.M., Mosselmans, J.F.W., Pattrick, R.A.D., Garner, C.D., Vaughan, D.J., 1996. Mechanism of molybdenum removal from the sea and its concentration in black shales: EXAFS evidence. Geochimica et Cosmochimica Acta 60, 3631–3642.

Hetzel, A., Böttcher, M.E., Wortmann, U.G., Brumsack, H.-J., 2009. Paleo-redox conditions during OAE 2 reflected in Demerara Rise sediment geochemistry (ODP Leg 207). Palaeogeography, Palaeoclimatology, Palaeoecology 273, 302–328.

Higgins, M.B., Robinson, R.S., Husson, J.M., Carter, S.J., Pearson, A., 2012. Dominant eukaryotic export production during ocean anoxic events reflects the importance of recycled NH_4^+. Proceedings of the National Academy of Sciences 109, 2269–2274.

Jenkyns, H.C., 2010. Geochemistry of oceanic anoxic events. Geochemistry, Geophysics, Geosystems 11, Q03004.

Kraal, P., Slomp, C.P., Forster, A., Kuypers, M.M.M., 2010. Phosphorus cycling from the margin to abyssal depths in the proto-Atlantic during oceanic anoxic event 2. Palaeogeography, Palaeoclimatology, Palaeoecology 295, 42–54.

Leckie, R.M., Bralower, T.J., Cashman, R., 2002. Oceanic anoxic events and plankton evolution: Biotic response to tectonic forcing during the mid-Cretaceous. Paleoceanography 17, PA000623.

Lyons, T.W., Anbar, A.D., Severmann, S., Scott, C., Gill, B.C., 2009. Tracking Euxinia in the Ancient Ocean: A Multiproxy Perspective and Proterozoic Case Study. Annual Review of Earth and Planetary Sciences 37.

Miller, C.A., Peucker-Ehrenbrink, B., Walker, B.D., Marcantonio, F., 2011. Re-assessing the surface cycling of molybdenum and rhenium. Geochimica et Cosmochimica Acta 75, 7146–7179.

Monteiro, F.M., Pancost, R.D., Ridgwell, A., Donnadieu, Y., 2012. Nutrients as the dominant control on the spread of anoxia and euxinia across the Cenomanian-Turonian oceanic anoxic event (OAE2): Model-data comparison. Paleoceanography 27, PA4209.

Montoya-Pino, C., Weyer, S., Anbar, A.D., Pross, J., Oschmann, W., van de Schootbrugge, B., Arz, H.W., 2010. Global enhancement of ocean anoxia during Oceanic Anoxic Event 2: A quantitative approach using U isotopes. Geology 38, 315–318.

Morford, J.L., Emerson, S., 1999. The geochemistry of redox sensitive trace metals in sediments. Geochimica et Cosmochimica Acta 63, 1735–1750.

Owens, J.D., Gill, B.C., Jenkyns, H.C., Bates, S.M., Severmann, S., Kuypers, M.M.M., Woodfine, R.G., Lyons, T.W., in review. Sulfur isotopes track the global extent and dynamics of euxinia during Cretaceous Oceanic Anoxic Event 2 Proceedings of the National Academy of Sciences.

Owens, J.D., Lyons, T.W., Li, X., Macleod, K.G., Gordon, G., Kuypers, M.M.M., Anbar, A., Kuhnt, W., Severmann, S., 2012. Iron isotope and trace metal records of iron cycling in the proto-North Atlantic during the Cenomanian-Turonian oceanic anoxic event (OAE-2). Paleoceanography 27, PA3223.

Poulton, S.W., Canfield, D.E., 2009. Ferruginous Conditions: A Dominant Feature of the Ocean through Earth's History. Elements 7, 107–112.

Raiswell, R., Berner, R.A., 1986. Pyrite and organic matter in Phanerozoic normal marine shales. Geochimica et Cosmochimica Acta 50, 1967–1976.

Raup, D.M., Sepkoski, J.J., 1986. Periodic extinction of families and genera. Science 231, 833-836.

Reinhard, C.T., Planavsky, N.J., Robbins, L.J., Partin, C.A., Gill, B.C., Lalonde, S.V., Bekker, A., Konhauser, K.O., Lyons, T.W., 2013. Proterozoic ocean redox and biogeochemical stasis. Proceedings of the National Academy of Sciences.

Rohrssen, M., Love, G.D., Fischer, W., Finnegan, S., Fike, D.A., 2012. Lipid biomarkers record fundamental changes in the microbial community structure of tropical seas during the Late Ordovician Hirnantian glaciation. Geology 41, 127–130.

Scott, C., Lyons, T.W., 2012. Contrasting molybdenum cycling and isotopic properties in euxinic versus non-euxinic sediments and sedimentary rocks: Refining the paleoproxies. Chemical Geology 324-325, 19–27.

Scott, C., Lyons, T.W., Bekker, A., Shen, Y., Poulton, S.W., Chu, X., Anbar, A.D., 2008. Tracing the stepwise oxygenation of the Proterozoic ocean. Nature 452, 456–459.

Scott, C., Planavsky, N.J., Dupont, C.L., Kendall, B., Gill, B.C., Robbins, L.J., Husband, K.F., Arnold, G.L., Wing, B.A., Poulton, S.W., Bekker, A., Anbar, A.D., Konhauser, K.O., Lyons, T.W., 2013. Bioavailability of zinc in marine systems through time. Nature Geoscience 6, 125–128.

Taylor, S.R., McLennan, S.M., 1995. The Geochemical Evolution of the Continental Crust. Reviews of Geophysics 33, 241–265.

Van Cappellen, P., Ingall, E.D., 1994. Benthic Phosphorus Regeneration, Net Primary Production, and Ocean Anoxia: A Model of the Coupled Marine Biogeochemical Cycles of Carbon and Phosphorus. Paleoceanography 9, 677–692.

Supplemental information

Sample locality and geologic setting

We present high-resolution spliced data for Demerara Rise, Ocean Drilling Project (ODP) site 1258, which includes holes 1258A, 1258B and 1258C. Site 1258 was drilled at a water depth of 3192.2 meters, the deepest of all the holes drilled during the Demerara Rise transect (Shipboard Scientific Party, 2004) which includes ODP 1257, 1259 and 1260, located on the continental slope of Suriname (Fig. 3.S1). The core depths [specifically meter core depth (mcd) below seafloor] for the new data presented here were adjusted to correlate with the carbon isotope stratigraphy (Erbacher et al., 2005) as described previously (Hetzel et al., 2009; MacLeod et al., 2008; Owens et al., 2012). Previously published data (Hetzel et al., 2009; Owens et al., 2012) used in this compilation were corrected during publication; consequently, no additional correction was applied to these samples. This unique section is marked by a continuous record of finely laminated organic-rich sedimentary deposition preceding and subsequent to the OAE, which is unique as there are only two other localities with a similar sedimentary record. Site 1260, drilled near 1258, has a similar geochemical record although this site has not been as extensively studied; therefore, it lacks the same data resolution. Similarly, site 367, an organic-rich shale before and during the OAE (Owens et al., 2012) from a similar latitude but off-shore from Cape Verde (Fig. 3.S1) but there was significant core loss during the OAE (Kuypers et al., 2002). Ocean drilling program site 1258 is also marked by high carbonate contents throughout the analyzed portion of the core. This 10 m compilation documents organic carbon contents ranging from 0.5 to 30 wt% and carbonate contents ranging from 0 to 95 wt%. [Fig. 3.S2 (Erbacher et al., 2005; Hetzel et al., 2009; Owens et al., 2012)]. Interestingly, local TOC contents, on a carbonate-free basis, show very small enrichments (Fig 3.S2) during the OAE. The recorded TOC

values on a carbonate free basis are 18.8 wt% for non-OAE intervals and 21.9 wt% during the OAE which is only a 3 wt% increase during the OAE.

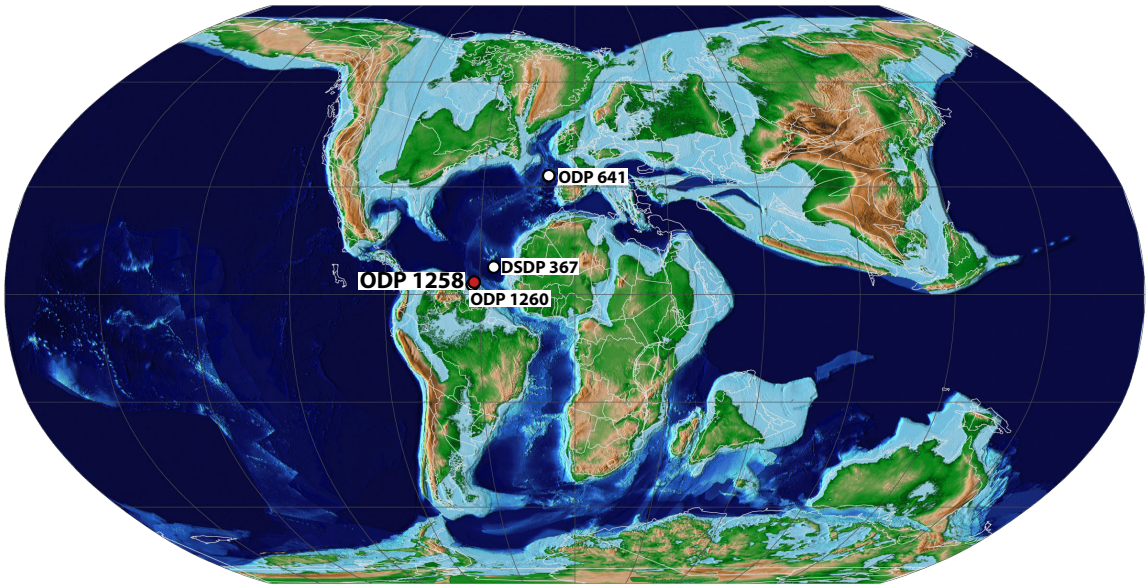

Figure 3.S1: Paleogeographical reconstruction for OAE2 with all localities discussed with ODP 1258 highlighted in red. The dark blue indicates deep sea settings, the light blue represents shallow-marine settings, and green and brown designate the continental land masses for 94 Ma (Scotese, 2008).

Inorganic geochemistry

Methods

All samples were examined for any possible signs of chemical oxidation prior to analysis and were powdered in a ceramic trace metal clean ball mill. For trace element analysis ~100 mg of dry powder was heated for ~12 hours at 450°C to volatilize organic material, and was subsequently weighed after cooling to determine the loss on ignition (LOI). Samples were weighed into trace metal clean vials and completely dissolved using a standard sequential acid (HNO_3/HCl/HF) protocol at ~150°C, then dried down and reconstituted in 2% HNO_3 for major and trace element analysis. All acids used in this study

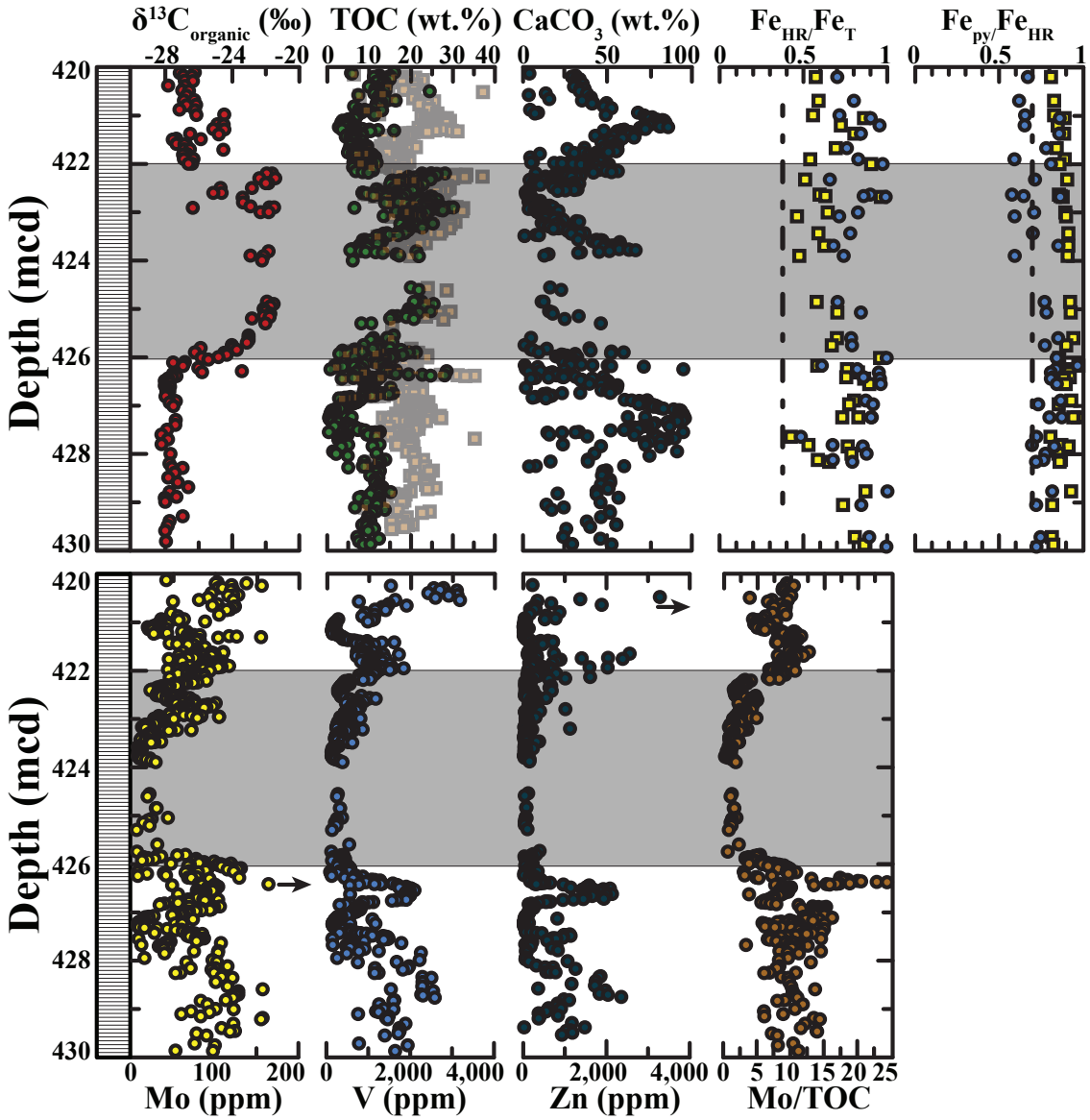

Figure 3.S2: Stratigraphic geochemical trends with OAE2 marked by the grey box. The squares (■) on the TOC plot are carbonate free TOC values. The circles (●) in Fe_{HR}/Fe_T and Fe_{py}/Fe_{HR} plots denoting samples that were calculated with Fe_{ox} and the squares (■) were calculated without Fe_{ox} phase. The dashed lines for Fe_{HR}/Fe_T represents the modern oxic marine average (0.38) and the dashed line for Fe_{py}/Fe_{HR} represents the low cutoff for euxinic deposition (0.7). The arrow denotes there are additional data points above the axis not plotted for Mo and Zn.

were Aristar/trace metal grade. Elemental concentrations (Al, Mo and V) were measured through inductively coupled plasma mass spectrometry (ICP-MS) on an Agilent 7500ce at the University of California, Riverside. Standard reference materials (SDO-1 shales) were digested along with samples and analyzed with each set of digestion extractions and in all cases were within the accepted analytical error for all elements with procedural blanks below detection limits.

Highly reactive iron (Fe_{HR}) was calculated by summing Fe_{pyrite} (Fe_{py}), $Fe_{carbonate}$ (Fe_{carb}), Fe_{oxides} (Fe_{ox}), and $Fe_{magnitite}$ (Fe_{mag}), where Fe_{py} was quantified by assuming a stoichiometry of FeS_2 from the pyrite sulfur content as measured through conventional techniques (Canfield et al., 1986). Briefly, a 100 mg sample was weighed into a 15 ml centrifuge tube to isolate Fe by a series of sequential chemical extractions (Poulton and Canfield, 2005a). First, carbonate-associated iron (Fe_{carb}) was extracted using a sodium acetate solution at pH of 4.5 for 24 hours with constant shaking. The extract was decanted, and the sample was then treated with a buffered sodium dithionite solution (pH 4.8) for 2 hours while shaking to mobilized oxide iron (Fe_{ox}). Finally, magnetite iron (Fe_{mag}) was extracted from the remaining residue using an ammonium oxalate and oxalic acid solution buffered to a pH of 3.2 for 6 hours. All solutions were then diluted in 2% HNO_3 and analyzed for Fe concentrations using an ICP-MS as described above for trace and major element analysis.

Determination of new data for total inorganic carbon (TIC) and total carbon (TC) was performed on an Eltra CS-500 carbon-sulfur analyzer. Total carbon was combusted using a high- temperature (1400°C) continuous O_2 flow furnace to CO_2 that was subsequently analyzed by a series of infrared (IR) absorption cells. Total inorganic carbon was measured using an acidification module that volatilizes inorganic carbon and combines with the

continuous O_2 flow which is carried to the IR analyzer as CO_2. Total organic carbon (TOC) is calculated by difference (TOC=TC-TIC).

Fe speciation discussion

We analyzed 43 samples that span the entire 10 m of section. Importantly, due to the high carbonate and organic contents for this section, Fe speciation was only analyzed on samples with total Fe values >0.5 wt%. We used this cutoff because the initial calibration of the sequential Fe extraction method was performed on fine-grained marine siliciclastic sediments which generally have a high abundance of total Fe [~4 wt% (Poulton and Raiswell, 2002; Poulton and Canfield, 2005b)]. Additionally, this method has a reproducibility of ~5% associated with each extraction (Poulton and Canfield, 2005b) on 'typical' siliciclastic sediments, and as a result samples that contain lower amounts of detrital material, Fe or are diluted by organic or inorganic carbon must be interpreted with caution.

Due to the considerable amount of time between drilling and Fe extraction analysis (~10 years) we have also calculated the Fe ratios without Fe_{ox} because an initial but low resolution dataset documents minimal amount of Fe_{ox} (Böttcher et al., 2006). It is likely that the samples have experienced some post-drilling pyrite oxidation. Post-drilling pyrite oxidation would lead to "double counting" of pyrite in this calculation: (1) chromium reduction analyses all reduced sulfur species which would extract elemental sulfur – the oxidized form of pyrite where the Fe is then stoichiometrically calculated; (2) Fe_{ox} is then extracted via a dithionite solution which would extract any oxidized pyrite as ferric-oxides. Therefore, we do not include the Fe_{ox} portion in the calculations which accounts for nearly all of the non-pyrite Fe (generally less than 0.2 wt%). The highest concentrations of Fe_{ox} were found in sediments with low carbonate contents. These low carbonate samples lack

the buffering capacity which would oxidize pyrite to Fe_{ox} during storage (Kraal et al., 2009). Importantly, including Fe_{ox} values affects only a few samples and requires negligible modification of our interpretations. Including Fe_{ox} values in the Fe_{HR}/Fe_T ratio increases the highly reactive concentration which pushes the ratio to greater values or more enriched than typical oxic marine sediments [0.38 (Poulton and Canfield, 2005b)] – the section average with Fe_{ox} was 0.82 ± 0.12 compared to 0.71 ± 0.14 without Fe_{ox}. Initially the Fe_{py}/Fe_{HR} lower limit for euxinic deposition was considered to be 0.8 (Anderson and Raiswell, 2004) but, subsequently, has been suggested to be lower [0.7 (Poulton and Canfield, 2009)]

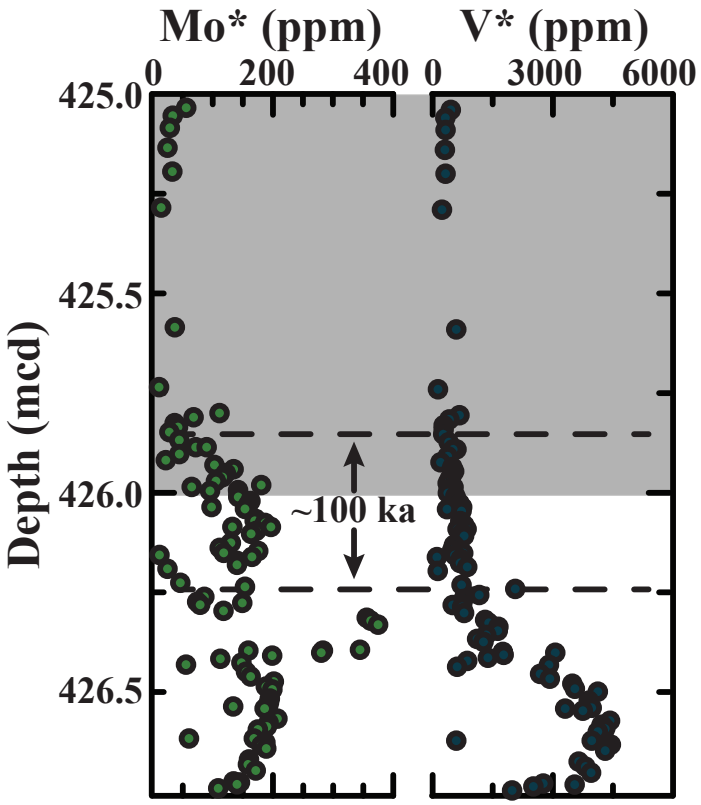

Figure 3.S3: An in-depth view of the stratigraphic plots for Mo and V for site 1258 (grey box represents OAE2). Note the drawdown of V prior to the OAE while the low value of Mo is achieved until after the onset of the OAE. The lower dashed line indicates the initial drawdown of V and the upper line delineates the start of the muted Mo enrichments which is separated by ~100 ka. Similar to Figure 1 there are 4 data points not included on the plot in-order to view the temporal shifts succinctly.

and the inclusion of Fe_{ox} does lower the average from 0.89 ± 0.04 to 0.76 ± 0.09 with a range of 0.81 to 1.01 without Fe_{ox} and 0.58 to 0.76 with Fe_{ox}. Therefore, including Fe_{ox} does decrease the Fe_{py}/Fe_{HR} ratio but most of the samples (33 of 43) still remain above 0.7, therefore excluding Fe_{ox} does not alter our overall interpretation of the Fe systematics throughout the studied interval (Fig. 3.S2).

Trace-metal results

The magnitude of the trace metal enrichments can be influenced by carbonate dilution, so we plot both the carbonate normalized (denoted *) and non-normalized values for Mo and V. Importantly, the stratigraphic drawdown trends for carbonate corrected Mo and V content are only exacerbated because the overall carbonate contents decrease going into the OAE which is comparable to the trace metal trends (Fig. 3.S2 and 3.S3). In other words, Mo, V and carbonate values are greater outside the OAE while during the OAE the values decrease nearly simultaneously; therefore, the carbonate correction has a greater

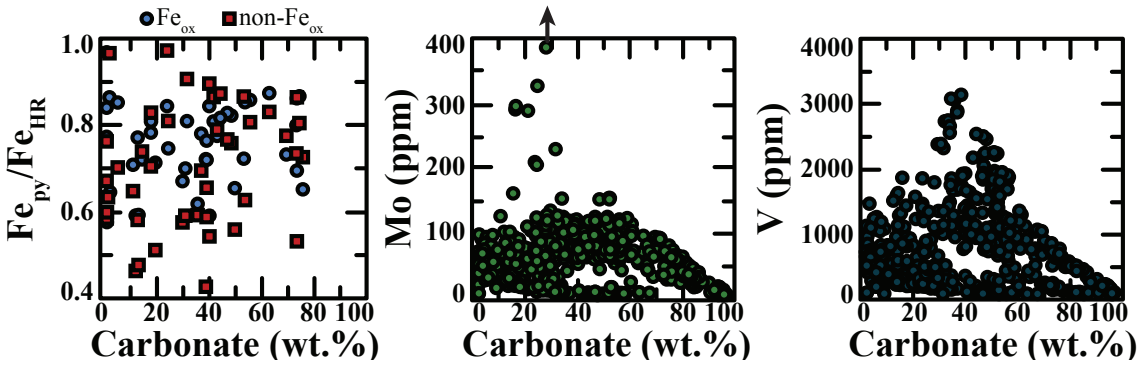

Figure 3.S4: Iron geochemistry and trace-metal proxies vs. carbonate contents. These plots show that the ratio [Fe_{py}/Fe_{HR} and Fe_{HR}/Fe_T (not shown)] and concentration (Mo and V) is not dependent on the carbonate contents and are recording changes in the global trace-metal inventory or the local redox stability (Fe geochemistry).

influence on non-OAE samples. It is important to note that there is no correlation between carbonate content and Mo, V or Fe_{py}/Fe_{HR} with or without Fe_{ox} included (Fig. 3.S5) which suggests that carbonate burial is not dictating the overall observed stratigraphic trends.

It has been previously noted that the trace element drawdown seen at site 1258 during the OAE is recorded at other sites including two other Demerara Rise sections (1257 and 1260 (Hetzel et al., 2009; van Bentum et al., 2009)) and Deep Sea Drilling Program site 367 which records similar depositional conditions before and during the onset of the OAE. However, due to coring loss during the event it is impossible to fully resolve the trace metal drawdown in the latter core. However, the data seem to suggest similar trends (Owens et al., 2012) for both trace metals recording a drawdown during the event. The observed stratigraphic enrichment trends at ODP 1258 for Mo and V show a significant decrease in absolute and normalized concentrations nearly coincident with the onset of the OAE. It is also important to point out that there is at least one site, ODP 641 [a deep abyssal North-Atlantic site located near the modern Spanish continental shelf with high TOC (Thurow, 1988)] that exhibits large enrichments in Mo (average of 1,700 ppm) during the thin 30 cm thick OAE with decreasing concentrations within the OAE. This is primarily due to the very slow sedimentation rates which allow for greater trace-metal enrichments and might be indicative of a deep sea abyssal enrichment. However, the overall Mo mass accumulation rate is lower here than at ODP 1258 due to the low sedimentation rate during the OAE which are explored through sensitivity tests (discussed below).

Zinc is not well constrained but it exhibits a relatively short residence time [~51 ka (Bruland et al., 1994)] with a small dissolved marine reservoir [~5.4 nM (Bruland et al., 1994)] as Zn^{2+} or $ZnCl^{+}$ (Calvert and Pedersen, 1993). Sequestration of sedimentary Zn starts in low oxygen environments and continues through euxinic conditions (Algeo and Maynard, 2004). Carbonate-free Zn concentrations prior to the OAE (including the

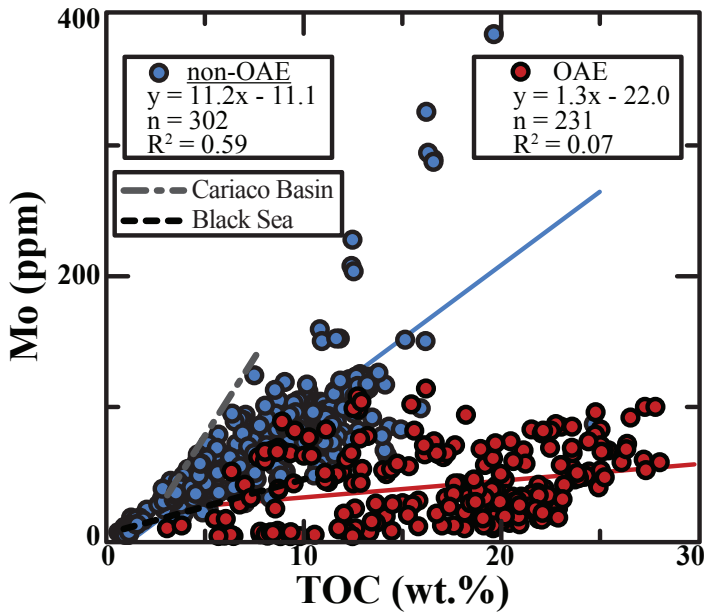

Figure 3.S5: Molybdenum concentration vs. TOC contents during OAE2 (●) and non-OAE2 intervals (●). The black dashed line represents the modern Black Sea – a restricted euxinic basin and the grey dashed line represents the modern Cariaco Basin – an open ocean euxinic site. Note the relatively good correlation for non-OAE2 samples (similar to the Cariaco basin) and the poor correlation for OAE2 samples. The OAE compilation includes some high concentration samples from the beginning and end of the OAE.

decline) and post-OAE2 are 1,196±1,153 and 1,353±2,480 ppm, respectively, while during OAE2 Zn concentrations drop to near crustal values [~78 ppm (Taylor and McLennan, 1995)] with an average of 211±321 ppm. Importantly, Zn has been documented to be essential for eukaryotic evolution through protein-DNA interactions (Dupont et al., 2006). The values during OAE2 are lower than the Precambrian which has been suggested to have stifled eukaryotic evolution but Scott and Lyons (2012) demonstrated Zn values were high enough to support eukaryotes during the Precambrian.

Mo-TOC relationship

One of the intriguing findings is the similarity between modern euxinic basins and OAE data with respect to Mo-TOC relationships (Algeo and Rowe, 2011). In the modern ocean, it is well documented that Mo co-varies with TOC (Algeo and Lyons, 2006; Lyons et al., 2009) where the modern euxinic Black Sea records low Mo vs. TOC values due to the relatively low bottom water Mo concentration [5 nM (Lyons et al., 2009)] resulting from its restricted circulation with the Mo replete open ocean, while the euxinic Cariaco Basin [and other euxinic basins (Algeo and Lyons, 2006; Lyons et al., 2009)] records higher Mo vs.TOC values because of the open connection with the ocean with high Mo concentrations [107 nM (Fischer et al., 2009)]. Therefore, the Mo vs. TOC relationship in modern euxinic basins is highly dependent on the Mo concentration in the water column.

ODP 1258 shows a similar Mo vs. TOC relationship (Fig. 3.S3) with two distinct populations where the non-OAE (pre- and post-OAE) samples plot similarly to the Cariaco Basin and samples from the OAE are similar to the Black Sea. The non-OAE samples have a correlation similar to the Cariaco Basin [non-OAE R^2 of 0.59, Cariaco Basin R^2 of 0.58 and 0.62 (Lyons et al., 2009)]. However, the Black Sea exhibits a very good correlation (R^2 of 0.92) and correlation between Mo and TOC burial at ODP 1258 during the OAE is non-existent (R^2 of 0.07). The low Mo/TOC ratio recorded during the OAE (average of 2.8) is lower than that of the modern Black Sea [average Mo/TOC of ~4.5 (Algeo and Lyons, 2006)] while the non-OAE average is much higher (9.5), more similar to modern open ocean euxinia.

Mo mass balance modeling

A geochemical Mo box model was constructed to quantitatively explore the redox landscape of the ocean using a conventional mass balance formulation (Borchers et al., 2005), where we treat the ocean as a well-mixed single reservoir (an assumption traditionally used for elements with long marine residence times such as Mo). A similar model was constructed to investigate the Precambrian (Reinhard et al., 2013), but the scope and interpretational framework of this study was very different from that presented here, and the short duration of this event made it necessary to implement a steady-state analysis of a time-dependent model using STELLA™ software. We use a conventional forward model, where we prescribe the initial boundary conditions and perturb the system to recreate the observed stratigraphic trends.

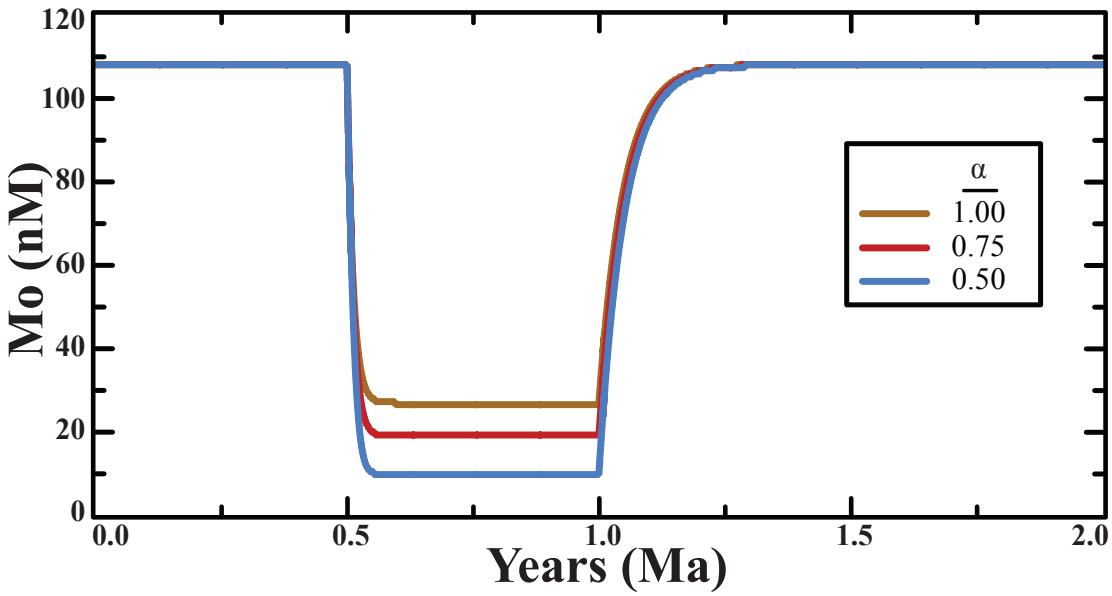

Figure 3.S6: Modeled sensitivity test for varying α for euxinic burial of 50 fold increase or 5.4% seafloor area. An α of 1 for this model depletes the Mo reservoir to ~30 nM and an α of 0.50 reduces the Mo reservoir to ~10nM while holding all other parameters constant.

	Flux (moles/Ma)	Burial rate ($\mu g/cm^2 \cdot Ma$)	Area (km^2)	Area (%)
Input	$30.0 \cdot 10^{13}$	-	-	-
Oxic burial	$8.66 \cdot 10^{13}$	$2.75 \cdot 10^{3}$	$3.02 \cdot 10^{8}$	83.89
Reducing burial	$19.4 \cdot 10^{13}$	$0.27 \cdot 10^{6}$	$6.90 \cdot 10^{6}$	1.92
Sulfidic burial	$1.94 \cdot 10^{13}$	$0.48 \cdot 10^{6}$	$3.87 \cdot 10^{5}$	0.11
Neutral burial	-	-	$5.07 \cdot 10^{7}$	14.08

Table 3.S1: Initial parameters for the Mo model with a starting Mo concentration of 107 nM.

Changes in the size of the Mo reservoir are due to imbalances in the input and output (burial) fluxes over geologic time, where increased burial (F_{out}) depletes the system and increased delivery (F_{in}) enriches the reservoir. The general equation for the globally averaged seawater concentration of Mo is given as:

$$\frac{d}{dt}\int_{v}[Mo]dv = F_{in} - F_{out} \qquad \text{(Equation 3.S1)}$$

where [*Mo*] represents the seawater concentration, integrated over ocean volume. The input flux, which has recently been updated (Miller et al., 2011), is largely dominated by riverine input through continental weathering of sulfides and organics hosted in shales and igneous rocks which has recently been updated with more modern riverine fluxes for dissolved MoO_4^{2-} (Miller et al., 2011). Importantly, we suggest that changes in the marine reservoir of Mo are most likely to be controlled by variations in the burial fluxes, rather than F_{in} during the Phanerozoic, given relatively high pO_2 and the sensitivity of sulfide weathering at relatively low O_2 levels (Anbar et al., 2007; Canfield et al., 2000; Reinhard et al., 2009). We note, however, that significant changes in global uplift/denudation rates or changes in the bulk composition of the weatherable shell at Earth's surface (the balance between igneous and sedimentary lithologies available for weathering, etc.) may well lead to changes in redox sensitive trace element fluxes during Phanerozoic time, and that exploring this possibility should be a priority of future research. The output flux includes

three permanent removal mechanisms from the marine reservoir: burial in oxic sediments, burial in reducing sediments and euxinic sedimentary removal. Therefore, we consider it likely that any major perturbation to the Mo seawater reservoir will be dictated by the redox structure of the ocean.

A simplified burial flux for a given environment is calculated as:

$$F_i = A_i b_i \left[\frac{[Mo]_t}{[Mo]_M} \right]^{\alpha} \qquad \text{(Equation 3.S2)}$$

where A_i is seafloor area of the environment (oxic, reducing or euxinic), b_i is the globally averaged burial rate for the environment, $[Mo]_t$ represents the average marine concentration at a given time, $[Mo]_M$ is the modern marine Mo concentration and the term $\alpha = 1.0$ for a strictly first-order mass balance model. However, we explore the sensitivity of this term in figure 3.S6. The basic idea behind this model formulation is that the burial of Mo generally scales linearly with the overlying seawater concentration (Algeo and Lyons, 2006; Rosenthal et al., 1995); therefore, the burial enrichments of Mo are dependent largely on the ambient marine concentration (Emerson and Huested, 1991). In principle, this allows for the magnitude of trace element burial to speak to the size of the marine reservoir because it should scale in some fashion with the ambient reservoir size, a pattern which has been documented for modern euxinic basins (Algeo and Lyons, 2006; Lyons et al., 2009).

The modern ocean is dominated by oxic bottom water conditions which are generally ineffective at burying Mo – oxic environments constitute ~83.9% of seafloor area but remove only ~28.9% of the Mo input to the ocean [Table 3.S1 (Reinhard et al., 2013)]. Euxinic conditions, which represent ~0.1 to 0.2% seafloor area but account for ~6.5% of Mo burial on a global scale, and reducing sediments (sulfide limited to the centimeter or less of the sediment column), which may represent ~1.9% of seafloor area and bury ~64.7% of the annual Mo flux to the ocean, make up the remainder of the removal flux. It

is important to point out that the latter term has been solved for assuming a modern steady-state Mo mass balance, and thus although the mass flux is reasonably well constrained the seafloor area through which it is removed depends on the assumed globally averaged burial rate. In addition, there is a non-trivial portion of the modern seafloor that is effectively Mo neutral and therefore does not bury an appreciable amount of Mo (Anbar et al., 2005; Morford and Emerson, 1999; Scott and Lyons, 2012) which is held constant throughout all models.

Modeling results

As a result of the dependence of the seawater Mo budget on the marine redox landscape, the burial of Mo should dramatically increase during periods of more prevalent reducing conditions, particularly euxinia. A decrease in the Mo reservoir, expressed as a decrease in the scale of enrichment within sedimentary rocks of the requisite depositional redox as constrained by independent methods, can track the global expansion of reducing sediments and/or euxinic conditions due to their effective Mo removal. In other words, large Mo enrichments in a sedimentary rock deposited under euxinic conditions suggest that the marine Mo reservoir was robust, in turn suggesting relatively limited removal into those settings that efficiently bury Mo (reducing sediments and euxinic environments) on a global scale.

The observed trend in Mo concentrations suggests a dramatic perturbation to geochemical redox evolution of the ocean during OAE2. In our model, we prescribe the initial boundary conditions (modern conditions and fluxes; table 3.S1) and instantaneously perturb these fluxes to recreate the primary features of our observed stratigraphic Mo trends. It is important to note that we are modelling the oceanic Mo reservoir concentration

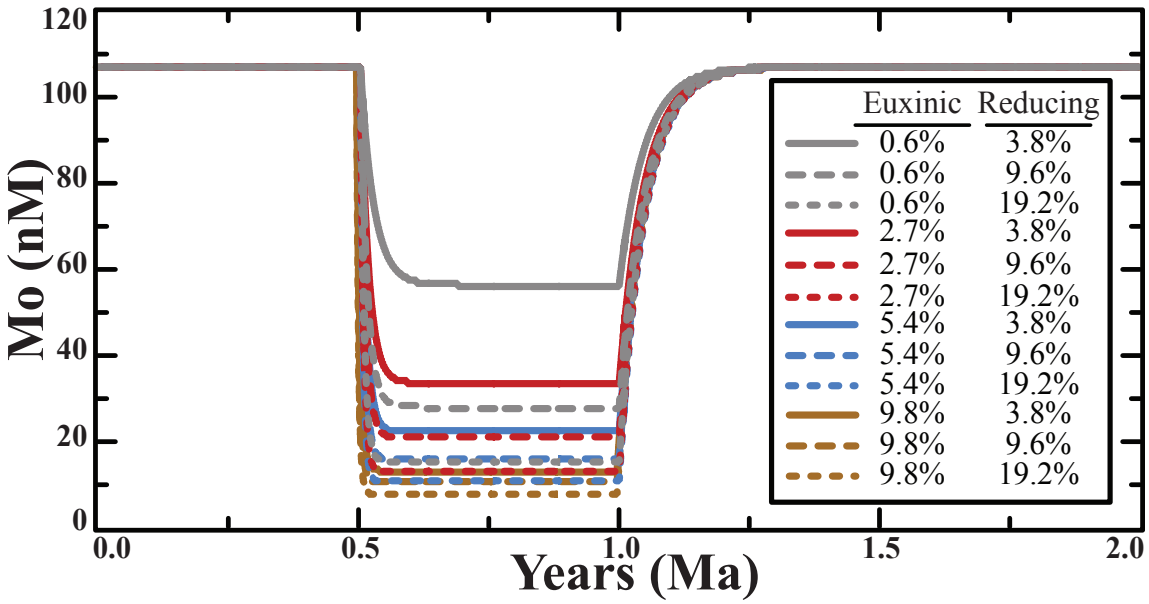

Figure 3.S7: Modeled sensitivity test of Mo reservoir drawdown using both euxinic and reducing burial.

and not the sedimentary record but, notably, the size of the sedimentary enrichment to some extent scales with the reservoir size (e.g. the Black Sea vs. Cariaco Basin). In other words, the model indicates Mo reservoir changes that would be expected to directly affect the sedimentary record.

We performed individual sensitivity test on several parameters, including increased euxinia and reducing sediment burial, Mo accumulation rate, combined increases of euxinia and reducing burial, and the linear scaling factor α (Fig. 3.3, 3.S6 and 3.S7). This time-dependent model requires the system to be in steady state prior to any perturbation, so we use modern burial rates including a global euxinic Mo burial of 0.48 $\mu g \cdot cm^{-2} \cdot y^{-1}$. However, this area-weighted average is greatly biased toward the restricted Black Sea which is much lower than the open ocean euxinic basins and the globally averaged non-Black Sea euxinic burial rate is 1.53 $\mu g \cdot cm^{-2} \cdot y^{-1}$ as discussed by Reinhard et al. (2013). Incorporating the

Mo burial rate in the model which includes the Black Sea lowers the globally averaged burial rate and consequently requires a greater amount of euxinic burial during the OAE to achieve a given Mo drawdown. However, this value has no effect on the burial rate of reducing settings. The average Mo burial rate for ODP site 1258 during the non-OAE period is ~0.65 $\mu g \cdot cm^{-2} \cdot y^{-1}$. Also, the model demands that all increases in euxinic and/or reducing burial are at the expense of oxic deposition while Mo-neutral deposition remains constant throughout all model runs. This assumption thus requires a greater expansion of a given environment than if it were expanding at the expense of Mo-neutral regions, because it replaces a region of the ocean which is already burying Mo. Therefore, an expansion of euxinic conditions at the expense of Mo-neutral environments would require less area than that of oxic settings.

The burial rate of Mo depends on the sedimentary enrichment of Mo and the sediment accumulation rate. The model explores several values for each environmental condition, and these are shown to have a relatively minor effect. The upper dashed lines for Figures 3.2A and 3.2B represents 0.75% and the lower dashed line represents 1.25% of the modern Mo accumulation rate for each environment. Exploring a range of accumulation rates for Mo burial is an important test because this incorporates sediment burial rates along with Mo concentrations. Therefore, exploring Mo accumulation rates inherently tests changes in the global bulk sediment mass accumulation rate and metal enrichments although it does not test these parameters independently. Variation in Mo burial rates is important for the mass balance of Mo but this does not alter the primary conclusions. Also, a strictly first-order model uses an α of 1.0 but it has been shown that the modern euxinic basins may not follow this trend (Reinhard et al., 2013). Changes in α have substantial effects within the model where a lowering of α increases the overall burial of Mo (Reinhard

et al., 2013), and thus ultimately the reservoir is decreased to much lower concentration for a given perturbation (Fig. 3.S6).

Here we use 0.5 Ma for all runs due to the estimated duration of the OAE by cyclostratigraphy (Kuhnt et al., 1997; Sageman et al., 2006; Veizer et al., 1999). The magnitude of the Mo depletion can be amplified or dampened by changing the aerial extent of reducing or euxinic burial (Fig. 3.2). Increasing both reducing and euxinic sinks may not be mutually exclusive; therefore, we model the increase of settings simultaneously. We modelled several but not all possible combinations with numerous combinations that sufficiently deplete the Mo reservoir. Figure 3.S7 shows a range of combined euxinic and reducing expansion scenarios which in combination require a smaller extent of each burial to achieve the same drawdown. The model predicts a Mo drawdown to ~10 nM with a fifty-fold increase (5.4% seafloor area) in euxinia combined with a ten-fold increase in reducing (19.2% seafloor area) or a hundred-fold euxinic increase (9.8% seafloor area) with a five-fold increase in reducing (9.6% seafloor area). However this does not include any changes in α and incorporates the burial rate which incorporates the low values of the Black Sea, so these estimates could be overestimating the extent of euxinia and/or reducing burial environments. In this model we do not account for a large removal of Mo in environments with slow bulk sediment flux (e.g. abyssal plains) which would require a greater portion of the sediments deposited globally be exposed to reducing and/or euxinic conditions (Dahl et al., 2011; Reinhard et al., 2013). The model predicts that the observed Mo drawdown can be driven by less than ~20% of the seafloor being characterized by reducing and/or euxinic sedimentation which we are assuming is restricted to marginal marine settings due to the high TOC fluxes in the modern ocean (Dunne et al., 2007; Jahnke, 1996).With limited mass balance constraints on other redox sensitive elements it is difficult to deconstruct the distribution and extent of various bottom water conditions although this method does

generally inform the maximum values for each bottom water condition. The use of an informed mass balance model for V would be useful to distinguish the extent of low oxygen conditions prior to the OAE, but the current knowledge of V fluxes is poorly constrained and the construction of such a model would be have limited utility at present.

It should also be pointed out that this estimate of increased reducing deposition is likely conservative. The model is run with static input fluxes while only manipulating the seafloor redox condition but increases in continental weathering have also been documented during OAE2 (Blättler et al., 2011; Jones and Jenkyns, 2001; Pogge von Strandmann et al., 2013), which could also influence sedimentation rates and trace element input rates to the ocean. An increased input flux from continental weathering, the dominant input mechanism of Mo (Reinhard et al., 2013), could possibly increase the reservoir size and dampen the Mo drawdown effect. Understanding how trace-metal fluxes increase with continental weathering is relatively unexplored but here we are going to assume a linear correlation. In other words, a doubling of continental weathering, while holding all other parameters constant, would require a near doubling of the seafloor area for a given environment to account for the same seawater Mo drawdown.

Organic geochemistry

Methods

The outer surfaces of sediment core and larger cuttings fragments as available were cleaned sequentially by ultrasonication in distilled water, then methanol, then dichloromethane, and finally *n*-hexane for ~20 seconds per step prior to extraction. Cleaned core fragments and cuttings were then crushed to a fine powder using an alumina ceramic puck mill housed in a SPEX 8515 shatterbox. Between samples, the puck mill was cleaned

by crushing annealed sand three times for 2-minute periods each followed by washing with the same cleaning solvent sequence described above.

Powdered samples were extracted in a Microwave Accelerated Reaction System (CEM corp.) with dichloromethane and methanol (9:1 v/v) at 100ºC for 15 minutes. Extracted sediments were impregnated with an aqueous methanol solution of ammonium dioxydithiomolybdate [$(NH_4)_2MoO_2S_2$] to give a give a nominal loading of 5 wt% molybdenum after evaporation to dryness. Ammonium dioxydithiomolybdate reductively decomposes *in situ* under catalytic hydropyrolysis (HyPy) conditions above 250ºC to form a catalytically-active molybdenum sulphide (MoS_2) phase. HyPy was conducted using a continuous flow catalytic hydropyrolysis rig as described previously (Love et al., 1995), at 15.0 MPa H_2 pressure, with a H_2 flow rate of 6 dm^3 min^{-1} and a temperature program ramping from room temperature to 250ºC at 100ºC/min, followed by a ramp to 480ºC at 8ºC/min, and final hold time of 1 minute. Products were trapped on dry ice-cooled 35-70 mesh silica and added directly to the top of a silica gel chromatography column. Hydropyrolysis products and total lipid extracts were separated by sequential elution with hexane, hexane:dichloromethane (1:1 v/v), and dichloromethane:methanol (3:1 v/v) to yield aliphatic hydrocarbons, aromatic hydrocarbons, and polar (N, S, and O-containing) compound fractions, respectively. Elemental sulfur was removed from the total lipid extract and hydrocarbon fraction of hyropyrolysis products with HCl-activated, solvent washed copper pellets.

Gas chromatography-mass spectrometry (GC-MS) analyses of saturated and aromatic hydrocarbons were conducted with an Agilent 7890A, equipped with a DB-1MS capillary column (60 m x 0.32 mm, 0.25µm film) and run with He as carrier gas. The temperature program for GC-MS full scan and selected ion monitoring (SIM) was 60ºC (2 min), heated to 250ºC at 20ºC/min, then to 325ºC at 2ºC/min, and held at 325ºC for

20 min. Hopane, hopene, sterane and sterene diastereoisomer compounds were identified based on retention time of known compounds and their mass spectra, and quantified in SIM mode. Quantification was accomplished by comparison with a deuterated C_{29} sterane internal standard (d_4-ααα-24-ethylcholestane (20R), Chiron Laboratories, AS) which gives a characteristic m/z 221 mass fragment, assuming equal response factors between sample compounds and the internal standard. Hopane/sterane ratios were calculated as the sum of C_{27-35} hopanes/enes (m/z 191) divided by the sum of C_{27-29} steranes (m/z 217) and sterenes (m/z 215). Average uncertainties in the hopanoid/steroid ratios were estimated as within ±8% of the absolute values from multiple analysis of a saturated hydrocarbon fraction from a standard oil (n = 30). Procedural blanks were conducted to ensure very low levels of background biomarker compounds for both extractions and hydropyrolysis products.

Lipid biomarker discussion

In this investigation, we monitored the stratigraphic occurrence and total abundance of the hopanes plus hopenes (C_{27}-C_{35}) relative to the steranes plus sterenes (C_{27}-C_{29}) in 10 rock extracts and extracted sediment hydropyrolysates from sediments taken from the ODP Site 1258 core to assess the relative source contributions from bacteria versus eukaryotes. Hopanoids and steroids are polycyclic lipids, with similarly high preservation potentials for survival in the geological record, synthesized by diverse groups of bacteria and eukaryotes, respectively. Major shifts in hopanoid/steroid ratios largely record changes in the balance of bacterial versus algal primary production. The sample coverage was chosen to capture the interval characterized by a strong positive C isotopic excursion (here recorded as $\delta^{13}C_{org}$) and variable Mo/V contents, as well as encompassing the pre- and post- OAE baselines for the site.

For immature sulphur-rich sedimentary rocks, the potential exists for lipid biomarker signal bias (Kohnen et al., 1992) if only the extractable (free) hydrocarbon are analyzed since a high proportion of the total biomarker pool is often found covalently-linked into geomacromolecules in immature rocks, aided by natural vulcanization processes during early diagenesis in the water column and shallow sediments in euxinic depositional environments. Thus, we also analyzed the quantitatively important kerogen-bound biomarker pool using the technique of continuous-flow catalytic hydropyrolysis or HyPy (Love et al., 1995). HyPy is a proven analytical pyrolysis technique for generating high yields of soluble products from kerogens whilst retaining the important structural and stereochemical features in biomarker hydrocarbon products. Being covalently-bound, these biomarker structures are also immobile and therefore are most assuredly genuine. Table 3.S2 indicates that for each sample >85% of the total hopanoid and steroid biomarkers considered here were generated from cleaving covalent-linkages within the kerogen -- a high proportion of the total signal as expected. The same stratigraphic trends are observed for hopanoid/steroid for both the free hydrocarbons and the kerogen hydropyrolysates, although absolute values are different due to selective biomarker partitioning in immature S_{org}-rich rocks (Kohnen et al., 1992), so we focus on the total (free plus bound) hopanoid/steroid ratio to get the quantitatively most accurate picture of the magnitude of the changes in this ratio observed through OAE2 at site 1258.

A systematic increase in the balance of bacterial to eukaryotic primary production is observed at Site 1258 during the peak of OAE2, coincident with the lowest sedimentary Mo and V concentrations and hence the greatest oceanic drawdown of these metals. A substantial, three-fold increase in the total hopanoid/steroid biomarker ratio (from 0.55 pre-excursion up to 1.80 during peak excursion, see Table 3.S2) is observed for core sediments from Site 1258 traversing through the positive carbon isotope excursion maximum.

This increase in H/St is driven by both an increase in hopanoid yields and a decrease in steroid biomarker yields, most likely arising from diminishing eukaryotic contributions to sedimentary organic matter during OAE (see Table 3.S2), particularly during the peak of the OAE when metal concentrations are lowest (Fig. 3.1). The total (free hydrocarbon + kerogen-bound) hopanoid/steroid ratios return again to lower values (0.77 and 0.79) between 420 and 421 m depth, post-dating the positive carbon isotopic excursion (Fig. 3.1) and in the upper interval where Mo and V contents increase again. The Phanerozoic average for hopane/sterane ratios for organic-rich source rocks and oils lies typically in the range of 0.5-2.0 (Cao et al., 2009), so the highest values for total hopanoid/steroid reported here (1.70 and 1.80) remain within this range though close to the upper limits. Site 1258 was characterized by strong upwelling, delivering ammonium, phosphorus, and other nutrients from the deep ocean thereby maintaining the high total organic carbon (TOC) content observed at the site. It is expected that, in locations unaffected by upwelling, similar relative stratigraphic trends in hopanoid/steroid ratios would be observed across OAE2. Absolute values of hopanoid/steroid, however, would be higher, reflecting oligotrophic growth conditions for eukaryotes, particularly with respect to fixed nitrogen availability.

The aliphatic hydrocarbon products generated from HyPy of extracted sediments yielded profiles as expected from thermally immature Cretaceous sediments on full scan GC-MS analysis, with a noticeable even-over-odd carbon number preference of straight-chain hydrocarbons extending up to C_{36} and beyond, abundant hopanoids and steroids with immature stereochemical configurations [mainly17β,21β(H)- for hopanes/enes and ααα20R or βααR for steranes/enes], as well as a strong hydrocarbon signal generated from lipids produced by pelagic thaumarchaetoa as evidenced by abundant bi- and tricyclic biphytanes (C_{40} isoprenoidal hydrocarbons) derived from kerogen-bound crenarchaeol (Pancost et al., 2008).

References

Algeo, T.J., Lyons, T.W., 2006. Mo–total organic carbon covariation in modern anoxic marine environments: Implications for analysis of paleoredox and paleohydrographic conditions. Paleoceanography 21, PA1016.

Algeo, T.J., Maynard, J.B., 2004. Trace-element behavior and redox facies in core shales of Upper Pennsylvanian Kansas-type cyclothems. Chemical Geology; Geochemistry of Organic-Rich Shales: New Perspectives 206, 289–318.

Algeo, T.J., Rowe, H., 2011. Paleoceanographic applications of trace-metal concentration data. Chemical Geology 324-325, 6–18.

Anbar, A.D., Arnold, G.L., Lyons, T.W., Barling, J., 2005. Response to Comment on "Molybdenum Isotope Evidence for Widespread Anoxia in Mid-Proterozoic Oceans". Science 309, 1017.

Anbar, A.D., Duan, Y., Lyons, T.W., Arnold, G.L., Kendall, B., Creaser, R.A., Kaufman, A.J., Gordon, G.W., Scott, C., Garvin, J., Buick, R., 2007. A Whiff of Oxygen Before the Great Oxidation Event? Science 317, 1903–1906.

Anderson, T.F., Raiswell, R., 2004. Sources and mechanisms for the enrichment of highly reactive iron in euxinic Black Sea sediments. American Journal of Science 304, 203–233.

Blättler, C.L., Jenkyns, H.C., Reynard, L.M., Henderson, G.M., 2011. Significant increases in global weathering during Oceanic Anoxic Events 1a and 2 indicated by calcium isotopes. Earth and Planetary Science Letters 309, 77–88.

Borchers, S.L., Schnetger, B., Böning, P., Brumsack, H.J., 2005. Geochemical signatures of the Namibian diatom belt: Perennial upwelling and intermittent anoxia. Geochemistry, Geophysics, Geosystems 6, Q06006.

Böttcher, M.E., Hetzel, A., Brumsack, H.J., Schipper, A., 2006. Sulfur–iron–carbon geochemistry in sediments of the Demerara Rise. In: Mosher, D.C., Erbacher, J., Malone, M.J. (Eds.), Proceedings of the Ocean Drilling Program. Scientific Results, vol. 207. Ocean Drilling Program, College Station, TX, pp. 1–23.

Bruland, K.W., Orians, K.J., Cowen, J.P., 1994. Reactive trace metals in the stratified central North Pacific. Geochimica et Cosmochimica Acta 58, 3171–3182.

Calvert, S.E., Pedersen, T.F., 1993. Geochemistry of Recent oxic and anoxic marine sediments: Implications for the geological record. Marine Geology: Marine Sediments, Burial, Pore Water Chemistry, Microbiology and Diagenesis 113, 67–88.

Canfield, D.E., Habicht, K.S., Thamdrup, B., 2000. The Archean sulfur cycle and the early history of atmospheric oxygen. Science 288, 658–661.

Canfield, D.E., Raiswell, R., Westrich, J.T., Reaves, C.M., Berner, R.A., 1986. The use of chromium reduction in the analysis of reduced inorganic sulfur in sediments and shales. Chemical Geology 54, 149–155.

Cao, C., Love, G.D., Hays, L.E., Wang, W., Shen, S., Summons, R.E., 2009. Biogeochemical evidence for euxinic oceans and ecological disturbance presaging the end-Permian mass extinction event. Earth and Planetary Science Letters 281, 188–201.

Dahl, T.W., Canfield, D.E., Rosing, M.T., Frei, R.E., Gordon, G.W., Knoll, A.H., Anbar, A.D., 2011. Molybdenum evidence for expansive sulfidic water masses in ~ 750 Ma oceans. Earth and Planetary Science Letters 311, 264–274.

Dunne, J.P., Sarmiento, J.L., Gnanadesikan, A., 2007. A synthesis of global particle export from the surface ocean and cycling through the ocean interior and on the seafloor. Global Biogeochemical Cycles 21, GB4006.

Dupont, C.L., Yang, S., Palenik, B., Bourne, P.E., 2006. Modern proteomes contain putative imprints of ancient shifts in trace metal geochemistry. Proceedings of the National Academy of Sciences 103, 17822–17827.

Emerson, S.R., Huested, S.S., 1991. Ocean anoxia and the concentrations of molybdenum and vanadium in seawater. Marine Chemistry 34, 177–196.

Erbacher, J., Friedrich, O., Wilson, P.A., Birch, H., Mutterlose, J., 2005. Stable organic carbon isotope stratigraphy across Oceanic Anoxic Event 2 of Demerara Rise, western tropical Atlantic. Geochemistry, Geophysics, Geosystems 6, Q06010.

Fischer, J.P., Ferdelman, T.G., D'Hondt, S., Røy, H., Wenzhöfer, F., 2009. Oxygen penetration deep into the sediment of the South Pacific gyre. Biogeosciences 6, 1467–1478.

Hetzel, A., Böttcher, M.E., Wortmann, U.G., Brumsack, H.-J., 2009. Paleo-redox conditions during OAE 2 reflected in Demerara Rise sediment geochemistry (ODP Leg 207). Palaeogeography, Palaeoclimatology, Palaeoecology 273, 302–328.

Jahnke, R.A., 1996. The global ocean flux of particulate organic carbon: Areal distribution and magnitude. Global Biogeochemical Cycles 10, 71–88.

Jones, C.E., Jenkyns, H.C., 2001. Seawater Strontium Isotopes, Oceanic Anoxic Events, and Seafloor Hydrothermal Activity in the Jurassic and Cretaceous. American Journal of Science 301, 112–149.

Kohnen, M.E.L., Schouten, S., Damsté, J.S.S., de Leeuw, J.W., Merritt, D.A., Hayes, J.M., 1992. Recognition of Paleobiochemicals by a Combined Molecular Sulfur and Isotope Geochemical Approach. Science 256, 358–362.

Kraal, P., Slomp, C.P., Forster, A., Kuypers, M.M.M., Sluijs, A., 2009. Pyrite oxidation during sample storage determines phosphorus fractionation in carbonate-poor anoxic sediments. Geochimica et Cosmochimica Acta 73, 3277–3290.

Kuhnt, W., Nederbragt, A., Leine, L., 1997. Cyclicity of Cenomanian-Turonian organic-carbon-rich sediments in the Tarfaya Atlantic Coastal Basin (Morocco). Cretaceous Research 18, 587-601.

Kuypers, M.M.M., Pancost, R.D., Nijenhuis, I.A., Sinninghe Damsté, J.S., 2002. Enhanced productivity led to increased organic carbon burial in the euxinic North Atlantic basin during the late Cenomanian oceanic anoxic event. Paleoceanography 17.

Love, G.D., Snape, C.E., Carr, A.D., Houghton, R.C., 1995. Release of covalently-bound alkane biomarkers in high yields from kerogen via catalytic hydropyrolysis. Organic Geochemistry 23, 981–986.

Lyons, T.W., Anbar, A.D., Severmann, S., Scott, C., Gill, B.C., 2009. Tracking Euxinia in the Ancient Ocean: A Multiproxy Perspective and Proterozoic Case Study. Annual Review of Earth and Planetary Sciences 37.

MacLeod, K.G., Martin, E.E., Blair, S.W., 2008. Nd isotopic excursion across Cretaceous ocean anoxic event 2 (Cenomanian-Turonian) in the tropical North Atlantic. Geology 36, 811–814.

Miller, C.A., Peucker-Ehrenbrink, B., Walker, B.D., Marcantonio, F., 2011. Re-assessing the surface cycling of molybdenum and rhenium. Geochimica et Cosmochimica Acta 75, 7146–7179.

Morford, J.L., Emerson, S., 1999. The geochemistry of redox sensitive trace metals in sediments. Geochimica et Cosmochimica Acta 63, 1735–1750.

Owens, J.D., Lyons, T.W., Li, X., Macleod, K.G., Gordon, G., Kuypers, M.M.M., Anbar, A., Kuhnt, W., Severmann, S., 2012. Iron isotope and trace metal records of iron cycling in the proto-North Atlantic during the Cenomanian-Turonian oceanic anoxic event (OAE-2). Paleoceanography 27, PA3223.

Pancost, R.D., Coleman, J.M., Love, G.D., Chatzi, A., Bouloubassi, I., Snape, C.E., 2008. Kerogen-bound glycerol dialkyl tetraether lipids released by hydropyrolysis of marine sediments: A bias against incorporation of sedimentary organisms? Organic Geochemistry 39, 1359–1371.

Pogge von Strandmann, P.A.E., Jenkyns, H.C., Woodfine, R.G., 2013. Lithium isotope evidence for enhanced weathering during Oceanic Anoxic Event 2. Nature Geoscience 6, 668–672.

Poulton, S., Canfield, D., 2005a. Development of a sequential extraction procedure for iron: implications for iron partitioning in continentally-derived particulates. Chem Geol 214, 209–221.

Poulton, S., Raiswell, R., 2002. The low-temperature geochemical cycle of iron: from continental fluxes to marine sediment deposition. Am J Sci 302, 774–805.

Poulton, S.W., Canfield, D.E., 2005b. Development of a sequential extraction procedure for iron: implications for iron partitioning in continentally derived particulates. Chemical Geology 214, 209–221.

Poulton, S.W., Canfield, D.E., 2009. Ferruginous Conditions: A Dominant Feature of the Ocean through Earth's History. Elements 7, 107-112.

Reinhard, C.T., Planavsky, N.J., Robbins, L.J., Partin, C.A., Gill, B.C., Lalonde, S.V., Bekker, A., Konhauser, K.O., Lyons, T.W., 2013. Proterozoic ocean redox and biogeochemical stasis. Proceedings of the National Academy of Sciences.

Reinhard, C.T., Raiswell, R., Scott, C., Anbar, A.D., Lyons, T.W., 2009. A Late Archean Sulfidic Sea Stimulated by Early Oxidative Weathering of the Continents. Science 326, 713–716.

Rosenthal, Y., Boyle, E.A., Labeyrie, L., Oppo, D., 1995. Glacial enrichments of authigenic Cd And U in subantarctic sediments: A climatic control on the elements' oceanic budget? Paleoceanography 10, 395–413.

Sageman, B.B., Meyers, S.R., Arthur, M.A., 2006. Orbital time scale and new C-isotope record for Cenomanian-Turonian boundary stratotype. Geology 34, 125–128.

Scott, C., Lyons, T.W., 2012. Contrasting molybdenum cycling and isotopic properties in euxinic versus non-euxinic sediments and sedimentary rocks: Refining the paleoproxies. Chemical Geology 324-325, 19–27.

Shipboard Scientific Party, 2004. Leg 207 summary, in Erbacher, J., Mosher, D.C., Malone, M.J., et al., *Proc. ODP, Init. Repts*., 207: College Station, TX (Ocean Drilling Program). 1-89.

Taylor, S.R., McLennan, S.M., 1995. The Geochemical Evolution of the Continental Crust. Reviews of Geophysics 33, 241–265.

Thurow, J., 1988. Cretaceous radiolarians of the North Atlantic Ocean: ODP Leg 103

(Sites 638, 640, and 641) and DSDP Legs 93 (Site 603) and 47B (Site 398), in Boillot, G., Winterer, E.L., et al., *Proc. ODP, Sci. Results*, 103: College Station, TX (Ocean Drilling Program), 379–418.

van Bentum, E.C., Hetzel, A., Brumsack, H.-J., Forster, A., Reichart, G.-J., Sinninghe Damsté, J.S., 2009. Reconstruction of water column anoxia in the equatorial Atlantic during the Cenomania-Turonian oceanic anoxic event using biomarker and trace metal proxies. Palaeogeography, Palaeoclimatology, Palaeoecology 280, 489–498.

Veizer, J., Ala, D., Azmy, K., Bruckschen, P., Buhl, D., Bruhn, F., Carden, G.A.F., Diener, A., Ebneth, S., Godderis, Y., Jasper, T., Korte, C., Pawellek, F., Podlaha, O.G., Strauss, H., 1999. $^{87}Sr/^{86}Sr$, $\delta^{13}C$ and $\delta^{18}O$ evolution of Phanerozoic seawater. Chemical Geology 161, 59–88.

Table 3.S2: Selected lipid biomarker ratios and absolute yields of hopanes/enes and steranes/enes. H/St*[1] is the hopanoid/steroid ratio calculated for the free hydrocarbon and the kerogen-bound biomarker pools. C_{27-35} hopanes/enes were analyzed and quantified in m/z 191 ion chromatograms while C_{27-29} (steranes+sterenes) were analyzed using m/z 217 and m/z 215 ion chromatograms. The combined (free hydrocarbon+kerogen-bound) H/St was used for Fig. 3.1.

Sample (207-1258-x)	Depth (mcd)	TOC (wt %)	Free (Extracted)				Bound (Hydropyrolysis Products)				Free + Bound				
			Hopanes (µg/g TOC)	Steranes (µg/g TOC)	Sterenes (µg/g TOC)	H/ St*1	Hopanes (µg/g TOC)	Steranes (µg/g TOC)	Sterenes (µg/g TOC)	H/ St*	Hopanes (µg/g TOC)	Steranes (µg/g TOC)	Sterenes (µg/g TOC)	H/ St*	Free/ Bound (%)
B 45-R 3, 1-2	420.19	14.7	16.6	6.0	5.9	1.40	115.4	92.7	62.6	0.74	132.0	98.7	68.6	0.79	9.5
B 45-R 3 80-81	420.98	11.3	20.5	6.7	9.7	1.25	206.2	190.5	86.7	0.74	226.7	197.2	96.4	0.77	7.1
A 42-6 47-49	421.95	6.4	4.8	1.5	1.3	1.70	169.1	105.3	37.5	1.18	173.9	106.7	38.8	1.19	2.4
A 42-6 127-129	422.75	20.9	18.7	2.3	2.2	4.17	328.7	141.3	73.9	1.53	347.4	143.5	76.1	1.58	4.1
A 42-7 100-101	423.89	17.3	23.0	3.7	3.5	3.17	145.6	80.7	11.1	1.59	168.6	84.5	14.6	1.70	11.3
C 17R-1 27-28	425.06	22.0	27.5	3.0	2.8	4.69	498.9	168.6	117.4	1.74	526.5	171.7	120.2	1.80	4.1
C 17R-1 95-96	425.74	12.4	28.1	5.1	5.1	2.74	104.7	94.4	39.6	0.78	132.8	99.6	44.7	0.92	13.8
C 17R-2 12-13	426.30	7.1	26.0	24.4	4.3	0.91	238.0	181.9	38.5	1.08	264.0	206.3	42.8	1.06	10.7
C 17R-3 4-5	427.40	1.8	43.4	48.0	11.7	0.73	256.5	465.8	23.5	0.52	299.9	513.8	35.2	0.55	12.1
A 43-2 73-75	428.49	10.8	23.6	6.4	6.2	1.88	197.2	218.2	63.1	0.70	220.9	224.7	69.2	0.75	7.0

Table 3.S3: Geochemical data for Demerara Rise ODP site 1258. Italicized meter core depth (mcd) was adjusted according to MacLeod et al. (2008). Compilation of data from Erbacher et al. (2005), Hetzel et al. (2009), Owens et al. (2012) and new data from this study. Carbonate corrected values denoted by *.

Sample ID	Depth	$\delta^{13}C_{carb}$	C_{org}	C_{inorg}	Al	Fe_T	V	V*	Zn	Zn*	Mo	Mo*	with Fe_{ox}		without Fe_{ox}	
(Leg 207-1258)	(mcd)	(‰)	(wt%)	(wt%)	(wt%)	(wt%)	(ppm)	(ppm)	(ppm)	(ppm)	(ppm)	(ppm)	$\frac{Fe_{py}}{Fe_T}$	$\frac{Fe_{py}}{Fe_{HR}}$	$\frac{Fe_{py}}{Fe_T}$	$\frac{Fe_{py}}{Fe_{HR}}$
A 42-4 130-131	420.10	-26.21	16.1													
A 42-4 140-141	420.11	-27.1	5.8													
A 42-4 141-141.5	420.12		6.0	4.1	1.95	0.76	744	776	431	449	40	42				
A 42-4 145.5-146	420.17		12.7	31.7	2.65	1.35	2322	3398	4912	7188	101	148				
A 42-5 0-1	420.17	-26.89	12.3													
B 45-3 0-1	420.18	-26.38	15.1													
A 42-5 1.5-2	420.19		11.2	29.4	3.14	1.34	2381	3373	3476	4925	99	140				
B 45-3 1-2	420.19		14.7	29.7	2.97	1.45	1357	1930	4689	6671	136	193	0.70	0.67	0.58	0.81
A 42-5 5.5-6	420.23		13.0	32.2	3.05	1.36	2734	4030	5206	7675	118	174				
B 45-3 20-22	420.24		15.0	34.1	3.08	1.48	1492	2263	223	338	154	234				
A 42-5 10-11	420.27	-26.81	12.5													
B 45-3 10-11	420.28	-26.32	13.5													
A 42-5 11.5-12	420.29		11.9	33.4	3.08	1.27	2748	4127	4288	6440	102	153				
A 42-5 12-15	420.29				2.68	1.09	2518	2518	5103	5103	107	107				
B 45-3 29.5-30	420.33		14.0	34.1	3.11	1.43	2660	4035	6187	9386	120	182				
A 42-5 16.5-17	420.34		13.2	35.9	2.90	1.20	3068	4788	7508	11716	117	183				
A 42-5 20-21	420.37	-27.8	10.5													
B 45-3 20-21	420.38	-26.8	14.1													
A 42-5 22-22.5	420.39		10.1	30.7	2.13	0.95	2386	3441	5540	7990	94	136				
B 45-3 39-41	420.43		13.2	34.6	3.23	1.40	3082	4711	6667	10192	126	193				
A 42-5 26.5-27	420.44		12.9	36.9	2.66	1.14	2895	4589	7001	11098	120	190				
B 45-3 41-41.5	420.44		11.5	36.8	3.20	1.36	2871	4545	4537	7183	114	180				
A 42-5 30-31	420.47	-26.96	12.0													

Table 3.S3: *continued*

Sample ID (Leg 207-1258)	Depth (mcd)	$\delta^{13}C_{carb}$ (‰)	C_{org} (wt%)	C_{inorg} (wt%)	Al (wt%)	Fe_T (wt%)	V (ppm)	V* (ppm)	Zn (ppm)	Zn* (ppm)	Mo (ppm)	Mo* (ppm)	with Fe_{ox}		without Fe_{ox}	
													$\frac{Fe_{py}}{Fe_T}$	$\frac{Fe_{py}}{Fe_{HR}}$	$\frac{Fe_{py}}{Fe_T}$	$\frac{Fe_{py}}{Fe_{HR}}$
B 45-3 30-31	420.48	-26.56	14.0													
A 42-5 31.5-32	420.49		24.6	34.1	2.96	1.17	2557	3879	3282	4979	90	137				
A 42-5 36-36.5	420.53		11.3	13.8	3.11	1.18	1595	1851	1369	1589	79	92				
B 45-3 50.5-51	420.54		12.8	38.4	2.90	1.21	3141	5100	7177	11654	120	195				
A 42-5 39.5-40	420.57		7.5	1.3	2.04	0.73	726	736	341	346	48	49				
B 45-3 40-41	420.58	-26.7	13.6													
A 42-5 44.5-45	420.62		12.2	40.8	2.53	1.25	1443	2435	672	1134	101	170				
B 45-3 61-63	420.65		13.4	15.9	3.59	1.36	1867	2220	1886	2243	95	113				
A 42-5 49.5-50	420.67		13.5	39.7	2.68	1.20	1400	2320	274	454	122	202				
A 42-5 50-51	420.67	-26.24	12.8													
B 45-3 50-51	420.68	-26.86	14.4													
A 42-5 51-53	420.68		16.5	35.5	2.53	1.24	1289	1997	268	415	120	186	0.80	0.62	0.59	0.83
B 45-3 69-71	420.73		13.1	42.3	2.59	1.16	1341	2322	298	516	116	201				
A 42-5 56-56.5	420.73		11.9	50.1	2.02	0.97	1112	2228	162	325	107	214				
B 45-3 71-71.5	420.74		12.9	41.5	2.67	1.17	1368	2338	273	467	112	191				
A 42-5 60-61	420.77	-26.13	12.6													
B 45-3 60-61	420.78	-26.7	12.5													
A 42-5 63-63.5	420.80		6.5	48.5	1.47	0.61	876	1701	868	1685	46	89				
B 45-3 80.5-81	420.84		11.4	53.1	2.01	0.99	1103	2351	155	330	103	220				
A 42-5 70-71	420.87	-27.12	7.7													
A 42-5 70-70.5	420.87		9.0	3.3	2.90	1.19	810	838	554	573	54	56				
B 45-3 80-71	420.88	-26.2	13.2													
A 42-5 76-76.5	420.93		8.2	68.8	1.10	0.69	236	757	30	96	34	109				
B 45-3 90-90.5	420.93		10.9	9.2	3.80	1.49	1087	1197	775	854	61	67				
B 45-3 91-93	420.95		11.4	7.4	4.23	1.70	1050	1134	517	558	55	59				

Table 3.S3: *continued*

Sample ID (Leg 207-1258)	Depth (mcd)	$\delta^{13}C_{carb}$ (‰)	C_{org} (wt%)	C_{inorg} (wt%)	Al (wt%)	Fe_T (wt%)	V (ppm)	V* (ppm)	Zn (ppm)	Zn* (ppm)	Mo (ppm)	Mo* (ppm)	with Fe_{ox}		without Fe_{ox}	
													$\frac{Fe_{py}}{Fe_T}$	$\frac{Fe_{py}}{Fe_{HR}}$	$\frac{Fe_{py}}{Fe_T}$	$\frac{Fe_{py}}{Fe_{HR}}$
A 42-5 80-81	420.97	-24.45	7.4													
B 45-3 80-81	420.98	-26.11	11.3	49.7	1.78	0.91	943	1874	69	136	86	171	0.71	0.65	0.56	0.83
A 42-5 81.5-82	420.99		7.2	72.5	0.95	0.59	171	622	26	95	36	131				
A 42-5 85.5-86	421.03		6.5	77.3	0.77	0.52	128	565	24	106	36	159				
B 45-3 99-101	421.03		7.0	74.1	0.93	0.58	186	718	22	85	30	116				
A 42-5 87-88	421.04		6.3	73.3	0.79	0.54	143	537	28	106	42	156	0.90	0.86	0.86	0.89
B 45-3 101-103	421.05		6.7	75.8	0.91	0.57	165	680	20	82	30	124				
B 45-3 103-105	421.07		5.1	79.3	0.75	0.47	134	646	21	101	25	120				
A 42-5 91-91.5	421.08		5.3	80.5	0.61	0.43	100	513	11	56	35	179				
B 45-3 105-106	421.09		4.9	83.4	0.61	0.41	116	699	18	109	25	151				
B 45-3 106-107	421.10		3.7	84.4	0.56	0.34	103	661	27	173	18	116				
B 45-3 107-108	421.11		4.8	83.2	0.51	0.37	96	570	5	30	23	137				
A 42-5 96-96.5	421.13		5.1	81.8	0.57	0.42	104	572	13	72	40	220				
B 45-3 110-111.5	421.14		3.5	85.3	0.60	0.34	97	661	131	893	19	130				
B 45-3 111.5-112.5	421.15		3.9	84.3	0.59	0.38	93	590	82	521	23	146				
B 45-3 112.5-113	421.16		3.9	85.2	0.50	0.36	82	553	14	94	31	209				
B 45-3 113-113.5	421.16		4.2	82.3	0.65	0.41	91	515	26	147	34	192				
A 42-5 100-101	421.17	-24.86	5.7													
B 45-3 113.5-115.5	421.18		4.0	84.2	0.56	0.36	93	587	16	101	32	202				
B 45-3 100-101	421.18	-24.49	6.4													
A 42-5 101-101.5	421.18		6.3	74.9	0.91	0.56	155	618	23	92	64	255				
B 45-3 115.5-116.5	421.19		3.4	85.6	0.50	0.33	92	638	12	83	29	201				
A 42-5 102-103	421.19		5.7	75.6	1.10	0.68	194	795	37	151	59	241	0.95	0.65	0.73	0.85
B 45-3 116.5-117.5	421.20		3.7	84.3	0.58	0.36	100	638	14	89	29	185				
B 45-3 117.5-118.5	421.21		4.6	81.6	0.64	0.38	105	570	17	92	38	206				

Table 3.S3: *continued*

Sample ID (Leg 207-1258)	Depth (mcd)	$\delta^{13}C_{carb}$ (‰)	C_{org} (wt%)	C_{inorg} (wt%)	Al (wt%)	Fe_T (wt%)	V (ppm)	V* (ppm)	Zn (ppm)	Zn* (ppm)	Mo (ppm)	Mo* (ppm)	with Fe_{ox}		without Fe_{ox}	
													$\frac{Fe_{py}}{Fe_T}$	$\frac{Fe_{py}}{Fe_{HR}}$	$\frac{Fe_{py}}{Fe_T}$	$\frac{Fe_{py}}{Fe_{HR}}$
B 45-3 118.5-119.5	421.22		4.6	82.3	0.64	0.41	112	631	12	68	41	231				
B 45-3 119.5-120.5	421.23		2.9	86.8	0.47	0.29	106	805	14	106	25	190				
A 42-5 106.5-107	421.24		6.2	73.3	1.05	0.66	206	773	16	60	67	251				
B 45-3 120.5-122.5	421.25		6.9	70.1	1.21	0.72	219	732	21	70	68	227				
B 45-3 122.5-123	421.26		6.8	70.3	1.24	0.78	255	860	68	229	73	246				
B 45-3 123-123.5	421.26		8.0	70.9	1.03	0.68	226	777	13	45	80	275				
A 42-5 110-111	421.27	-25.1	8.5													
B 45-3 123.5-124.5	421.27		6.7	73.3	1.06	0.65	253	947	19	69	65	244				
B 45-3 110-111	421.28	-24.44	3.6													
A 42-5 111-111.5	421.28		10.1	60.7	1.37	0.94	291	740	18	46	115	292				
B 45-3 125.5-126.5	421.29		12.2	59.0	1.34	1.00	315	768	12	29	124	302				
B 45-3 126.5-128	421.30		16.1	48.4	1.72	1.29	343	665	28	54	153	297				
B 45-3 128-129	421.32		10.4	56.5	1.68	1.07	352	809	35	80	102	234				
B 45-3 129-131	421.33		7.4	63.8	1.53	0.92	382	1056	55	152	70	194				
A 42-5 117-117.5	421.34		6.6	64.6	1.47	0.88	344	971	52	147	66	186				
B 45-3 131-131.5	421.34		6.6	66.6	1.42	0.89	372	1113	58	174	65	195				
B 45-3 131.5-132.5	421.35		6.6	64.0	1.68	1.00	439	1219	77	214	71	197				
A 42-5 119-121	421.36		8.4	55.5	1.49	0.88	446	1003	108	243	65	146	0.84	0.86	0.81	0.89
B 45-3 132.5-133.5	421.36		7.6	58.7	1.82	1.12	488	1181	81	196	79	191				
A 42-5 120-121	421.37	-26.49	6.9													
B 45-3 133.5-134.5	421.37		7.7	56.4	1.95	1.17	595	1365	98	225	80	184				
B 45-3 134.5-135	421.38		8.4	56.2	1.91	1.05	659	1503	102	233	78	178				
B 45-3 120-121	421.38	-24.77	5.8													
B 45-3 135-136	421.39		7.6	58.1	1.91	0.84	924	2204	168	401	76	181				
A 42-5 122-122.5	421.39		4.9	67.0	1.22	0.52	743	2252	590	1788	45	136				

Table 3.S3: *continued*

Sample ID (Leg 207-1258)	Depth (mcd)	$\delta^{13}C_{carb}$ (‰)	C_{org} (wt%)	C_{inorg} (wt%)	Al (wt%)	Fe_T (wt%)	V (ppm)	V* (ppm)	Zn (ppm)	Zn* (ppm)	Mo (ppm)	Mo* (ppm)	with Fe_{ox} $\frac{Fe_{py}}{Fe_T}$	with Fe_{ox} $\frac{Fe_{py}}{Fe_{HR}}$	without Fe_{ox} $\frac{Fe_{py}}{Fe_T}$	without Fe_{ox} $\frac{Fe_{py}}{Fe_{HR}}$
B 45-3 136-137.5	421.40		5.7	63.3	1.72	0.69	922	2509	417	1135	55	150				
B 45-3 137.5-138.5	421.41		8.4	43.4	2.73	1.16	1573	2780	714	1262	64	113				
B 45-3 138.5-139	421.42		7.1	54.3	2.01	0.92	1276	2789	712	1556	55	120				
B 45-3 139-141	421.43		4.5	66.8	1.02	0.55	665	1998	314	943	44	132				
B 45-3 141-142.5	421.45		5.6	66.5	1.34	0.69	782	2334	230	687	53	158				
B 45-3 142.5-143	421.46		7.3	59.0	2.07	0.96	1091	2661	276	673	72	176				
A 42-5 129-129.5	421.46		6.4	59.7	1.60	0.83	952	2360	466	1155	66	164				
A 42-5 130-131	421.47	-27.31	6.9													
B 45-3 130-131	421.48	-25.85	6.9													
A 42-6 0-1	421.49	-27.52	6.7													
A 42-6 2-4	421.51				2.07	0.95	847	847	180	180	81	81				
A 42-6 2-2.5	421.51		8.4	53.0	2.07	0.96	897	1909	181	385	86	183				
A 42-6 6.5-7	421.56		7.3	47.2	1.68	0.84	766	1450	172	326	77	146				
B 45-3 140-141	421.58	-27.3	5.9													
A 42-6 10-11	421.59	-26.73	7.6													
B 45-4 0-1	421.59	-26.83	7.2													
B 45-4 0-1	421.60		8.1	56.7	2.07	0.94	1059	2444	232	535	77	178				
A 42-6 11.5-12	421.61		5.6	56.1	1.23	0.66	678	1544	129	294	60	137				
B 45-4 1-2.5	421.61		8.6	54.3	2.16	1.13	925	2022	167	365	108	236				
B 45-4 2.5-3	421.62		8.2	54.1	1.96	1.02	857	1866	147	320	93	203				
B 45-4 3-4	421.63		9.6	51.6	2.09	1.09	889	1836	127	262	108	223				
B 45-4 3-5	421.63		9.3	55.8	1.95	0.99	847	1918	124	281	96	217				
B 45-4 4-5	421.64		8.8	53.0	2.03	1.01	878	1868	135	287	94	200				
B 45-4 5-7	421.65		7.3	48.8	1.73	0.86	740	1444	109	213	81	158				
A 42-6 16-16.5	421.65		7.5	51.4	1.98	0.85	1314	2705	738	1519	80	165				

Table 3.S3: *continued*

Sample ID (Leg 207-1258)	Depth (mcd)	$\delta^{13}C_{carb}$ (‰)	C_{org} (wt%)	C_{inorg} (wt%)	Al (wt%)	Fe_T (wt%)	V (ppm)	V* (ppm)	Zn (ppm)	Zn* (ppm)	Mo (ppm)	Mo* (ppm)	with Fe_{ox} $\frac{Fe_{py}}{Fe_T}$	with Fe_{ox} $\frac{Fe_{py}}{Fe_{HR}}$	without Fe_{ox} $\frac{Fe_{py}}{Fe_T}$	without Fe_{ox} $\frac{Fe_{py}}{Fe_{HR}}$
A 42-6 17-18	421.66		7.8	36.9	2.15	0.91	1685	2669	2556	4049	78	123	0.75	0.78	0.70	0.85
B 45-4 7-7.5	421.66		8.2	49.2	1.91	0.92	857	1686	188	370	82	161				
B 45-4 7.5-8.5	421.67		8.5	55.2	1.94	1.04	907	2023	115	257	98	219				
B 45-4 8.5-9.5	421.68		8.6	51.7	1.82	0.92	882	1825	176	364	86	178				
A 42-6 19-19.5	421.68		7.0	26.8	1.79	0.78	796	1087	325	444	55	75				
B 45-4 9.5-10	421.69		8.0	52.2	1.69	0.90	818	1710	108	226	94	197				
A 42-6 20-21	421.69	-26.84	8.2													
B 45-4 10-11	421.69	-26.5	7.6													
B 45-4 10-10.5	421.69		6.3	52.4	1.32	0.70	675	1419	145	305	66	139				
A 42-5 90-91	421.70	-24.5	5.3													
B 45-4 10.5-11.5	421.70		6.1	56.7	1.46	0.70	814	1878	131	302	65	150				
B 45-4 11.5-13	421.71		7.7	56.3	1.91	0.82	1098	2510	172	393	76	174				
B 45-4 13-15.5	421.73		7.4	55.8	1.95	0.85	1240	2808	335	758	73	165				
B 45-4 15.5-16	421.75		7.0	51.3	1.88	0.78	1363	2796	2037	4178	66	135				
B 45-4 16-17	421.76		5.0	36.1	1.29	0.53	955	1494	1406	2200	43	67				
A 42-6 26.5-27	421.76		9.8	44.1	2.42	1.15	959	1715	200	358	87	156				
B 45-4 17-18.5	421.77		6.2	30.8	1.66	0.64	1110	1605	2388	3453	57	82				
B 45-4 18.5-20	421.78		6.4	10.3	1.96	0.72	833	929	895	998	55	61				
A 42-6 30-31	421.79	-26.67	10.6													
B 45-4 20-21	421.79	-26.69	7.9													
B 45-3 90-91	421.80	-26.91	10.9													
B 45-4 21-22	421.81		7.0	39.3	1.78	0.79	775	1276	252	415	59	97				
A 42-6 31.5-32	421.81		10.5	42.9	2.67	1.29	1154	2022	187	328	107	187				
A 42-6 32-34	421.81				2.49	1.14	1293	1293	800	800	89	89				
B 45-4 22-25	421.83		10.3	44.0	2.23	1.11	943	1684	202	361	97	173				

Table 3.S3: *continued*

Sample ID (Leg 207-1258)	Depth (mcd)	$\delta^{13}C_{carb}$ (‰)	C_{org} (wt%)	C_{inorg} (wt%)	Al (wt%)	Fe_T (wt%)	V (ppm)	V* (ppm)	Zn (ppm)	Zn* (ppm)	Mo (ppm)	Mo* (ppm)	with Fe_{ox} $\frac{Fe_{py}}{Fe_T}$	with Fe_{ox} $\frac{Fe_{py}}{Fe_{HR}}$	without Fe_{ox} $\frac{Fe_{py}}{Fe_T}$	without Fe_{ox} $\frac{Fe_{py}}{Fe_{HR}}$
B 45-4 25-25.5	421.84		10.1	44.5	2.48	1.34	1049	1890	283	510	101	182				
B 45-4 25.5-26	421.85		10.2	44.7	2.46	1.20	1061	1917	308	557	96	173				
B 45-4 26-27	421.86		10.5	45.8	2.34	1.21	934	1722	144	265	107	197				
A 42-6 36.5-37	421.86		11.6	3.4	4.03	1.51	1470	1522	702	727	92	95				
B 45-4 27-28	421.87		10.2	45.1	2.46	1.23	964	1755	246	448	98	178				
B 45-4 28-29	421.88		10.1	42.8	2.73	1.36	1068	1868	199	348	99	173				
B 45-4 29-30.5	421.89		10.8	41.8	2.83	1.38	1146	1970	331	569	107	184				
A 42-6 40-41	421.89	-26.86	8.7													
B 45-4 30-31	421.89	-26.29	10.4	40.0	2.39	1.18	1004	1673	315	525	84	139	0.82	0.59	0.54	0.89
B 45-4 30.5-31.5	421.90		11.5	39.3	2.80	1.37	1122	1847	209	344	115	189				
A 42-6 41-41.5	421.90		7.3	42.9	1.67	0.95	1095	1918	380	666	68	119				
B 45-4 31.5-32	421.91		10.5	39.5	2.87	1.38	1198	1980	222	367	100	165				
B 45-4 32-32.5	421.91		11.0	41.4	2.74	1.34	1168	1994	208	355	101	172				
B 45-4 32.5-33.5	421.92		10.9	41.5	2.82	1.38	1242	2123	224	383	106	181				
B 45-4 33.5-34.5	421.93		11.2	42.5	2.74	1.26	1337	2325	447	777	102	177				
B 45-4 34.5-35.5	421.94		9.8	44.8	2.60	1.10	1542	2791	1594	2885	80	145				
B 45-4 35.5-36	421.95		11.3	28.2	3.65	1.45	1797	2502	2028	2823	90	125				
A 42-6 46-46.5	421.95		6.4	46.4	1.40	0.71	1004	1874	496	926	61	114				
A 42-6 47-49	421.95		6.4	43.6	1.51	0.62	1087	1926	503	892	51	90				
B 45-4 36-36.5	421.95		11.2	6.2	3.84	1.51	1265	1348	644	686	82	87				
B 45-4 36.5-38	421.96		11.9	5.2	4.15	1.66	1241	1309	638	673	84	89				
B 45-4 37-39	421.97		8.4	22.5	2.33	1.11	1246	1608	626	808	59	76				
B 45-4 38-38.5	421.97		6.4	18.8	1.91	0.95	936	1153	475	585	42	52				
B 45-4 38.5-39.5	421.98		10.6	23.6	2.67	1.20	1467	1920	693	907	74	97				
A 42-6 50-51	421.99	-26.37	9.7													

Table 3.S3: *continued*

Sample ID (Leg 207-1258)	Depth (mcd)	$\delta^{13}C_{carb}$ (‰)	C_{org} (wt%)	C_{inorg} (wt%)	Al (wt%)	Fe_T (wt%)	V (ppm)	V* (ppm)	Zn (ppm)	Zn* (ppm)	Mo (ppm)	Mo* (ppm)	with Fe_{ox}		without Fe_{ox}	
													$\frac{Fe_{py}}{Fe_T}$	$\frac{Fe_{py}}{Fe_{HR}}$	$\frac{Fe_{py}}{Fe_T}$	$\frac{Fe_{py}}{Fe_{HR}}$
B 45-4 40-41	421.99	-26.59	8.4	31.5	1.69	0.90	1006	1468	584	852	57	84	0.97	0.81	0.91	0.86
B 45-4 39.5-40.5	421.99		7.5	29.9	1.93	0.85	1100	1570	620	885	53	76				
A 42-6 50.5-51	422.00		8.8	51.6	1.97	1.08	862	1780	116	240	92	190				
B 45-4 40.5-42	422.00		8.0	34.8	1.86	0.86	1132	1737	661	1014	62	95				
B 45-4 42-43	422.02		8.6	40.3	1.89	1.01	1161	1943	493	825	72	121				
B 45-4 43-45	422.03		8.0	43.8	1.82	0.92	1138	2023	365	649	69	123				
A 42-6 56-57	422.06		7.6	49.5	1.64	0.86	852	1687	250	495	65	129				
A 42-6 57-57.5	422.06		6.3	40.3	1.50	0.78	811	1357	479	802	54	90				
A 42-6 57.5-58.5	422.07		8.0	48.2	1.95	0.95	1098	2118	788	1520	65	125				
A 42-6 58.5-59.5	422.08		9.5	48.2	2.28	1.38	804	1551	173	334	85	164				
A 42-6 60-62	422.09				2.18	1.07	812	812	398	398	76	76				
A 42-6 59.5-60.5	422.09		8.3	52.7	2.06	1.24	735	1553	97	205	70	148				
A 42-6 62-63	422.12		10.2	45.7	2.38	1.35	936	1723	363	668	80	147				
A 42-6 63-64	422.13		11.0	41.5	2.55	1.38	976	1668	210	359	86	147				
A 42-6 64-65	422.14		9.2	49.8	2.18	1.18	962	1918	296	590	68	136				
A 42-6 65-65.5	422.14		6.9	56.8	1.57	0.68	1022	2368	1606	3720	44	102				
B 45-4 57-57.5	422.16		8.6	53.2	2.14	1.27	743	1586	124	265	69	147				
B 45-4 57.5-59	422.17		9.9	42.3	2.36	1.21	999	1730	1007	1744	66	114				
B 45-4 59-60.5	422.19		24.9	7.8	2.59	1.85	832	903	619	672	74	80				
A 42-6 70-71	422.19	-21.6	28.2													
B 45-4 60-61	422.19	-21.92	22.7													
B 45-4 60.5-61.5	422.20		26.2	20.9	2.18	2.30	497	628	203	257	75	95				
A 42-6 71-71.5	422.20		22.9	25.3	2.34	2.06	497	665	91	122	88	118				
B 45-4 61.5-62.5	422.21		25.0	25.0	2.09	2.18	402	536	127	169	69	92				
B 45-4 62.5-63.5	422.22		26.2	19.3	2.18	2.45	422	523	164	203	71	88				

Table 3.S3: *continued*

Sample ID (Leg 207-1258)	Depth (mcd)	$\delta^{13}C_{carb}$ (‰)	C_{org} (wt%)	C_{inorg} (wt%)	Al (wt%)	Fe_T (wt%)	V (ppm)	V* (ppm)	Zn (ppm)	Zn* (ppm)	Mo (ppm)	Mo* (ppm)	with Fe_{ox} $\frac{Fe_{py}}{Fe_T}$	with Fe_{ox} $\frac{Fe_{py}}{Fe_{HR}}$	without Fe_{ox} $\frac{Fe_{py}}{Fe_T}$	without Fe_{ox} $\frac{Fe_{py}}{Fe_{HR}}$
B 45-4 63.5-64.5	422.23		23.5	26.8	2.14	2.22	420	573	90	123	72	98				
B 45-4 64.5-65.5	422.24		24.3	34.6	1.63	2.01	368	563	43	66	77	118				
B 45-4 65.5-66.5	422.25		22.4	32.0	1.97	1.87	407	599	78	115	72	106				
A 42-6 76-76.5	422.25		23.4	13.8	3.30	2.97	491	569	66	77	57	66				
A 42-6 77-79	422.26				3.11	3.25	357	357	120	120	49	49				
B 45-4 66.5-67.5	422.26		19.5	29.2	2.28	1.60	419	592	178	251	64	90				
B 45-4 67.5-68.5	422.27		21.1	20.0	2.93	2.34	512	640	108	135	60	75				
B 45-4 68.5-69	422.28		24.9	17.2	2.87	2.51	476	575	67	81	55	66				
B 45-4 69-70	422.29		23.7	14.5	3.11	3.15	406	475	75	88	53	62				
A 42-6 80-81	422.29	-22.36	19.2													
B 45-4 70-71	422.29	-21.41	24.1													
B 45-4 70-71	422.30		19.6	15.0	3.21	2.80	317	373	64	75	40	47				
B 45-4 71-72	422.31		19.4	12.5	3.36	2.95	311	355	72	82	40	46				
A 42-6 82-83	422.31		19.9	19.4	2.47	2.50	318	394	38	47	52	65	0.65	0.71	0.51	0.91
A 42-6 82-82.5	422.31		24.8	4.9	3.37	3.18	325	342	57	60	44	46				
B 45-4 72-73	422.32		18.2	12.6	3.39	2.92	305	349	138	158	35	40				
B 45-4 73-74	422.33		17.5	4.2	3.32	5.63	288	301	670	699	37	39				
B 45-4 74-75	422.34		15.7	8.6	3.81	2.91	391	428	79	86	32	35				
B 45-4 75-76	422.35		15.4	7.6	4.13	3.51	355	384	92	100	29	31				
B 45-4 76-76.5	422.35		21.7	12.3	2.93	3.99	261	298	97	111	38	43				
A 42-6 87-87.5	422.36		22.1	6.8	3.58	2.10	338	362	630	676	41	44				
B 45-4 76.5-78	422.36		20.9	16.8	2.85	2.52	256	308	144	173	35	42				
B 45-4 78-79	422.38		21.1	18.6	3.02	2.56	256	314	72	88	32	39				
B 45-4 79-80	422.39		18.0	30.5	2.65	2.04	234	337	48	69	23	33				
A 42-6 90-91	422.39	-21.82	21.7													

Table 3.S3: *continued*

Sample ID (Leg 207-1258)	Depth (mcd)	$\delta^{13}C_{carb}$ (‰)	C_{org} (wt%)	C_{inorg} (wt%)	Al (wt%)	Fe_T (wt%)	V (ppm)	V* (ppm)	Zn (ppm)	Zn* (ppm)	Mo (ppm)	Mo* (ppm)	with Fe_{ox} $\frac{Fe_{py}}{Fe_T}$	with Fe_{ox} $\frac{Fe_{py}}{Fe_{HR}}$	without Fe_{ox} $\frac{Fe_{py}}{Fe_T}$	without Fe_{ox} $\frac{Fe_{py}}{Fe_{HR}}$
B 45-4 80-81	422.39	-21.97	17.9													
B 45-4 80-82	422.40		15.2	33.8	2.79	1.78	289	437	138	209	21	32				
B 45-4 82-83	422.42		22.2	7.2	3.37	2.34	296	319	141	152	36	39				
B 45-4 82-83	422.42		23.0	9.4	3.28	2.24	277	306	234	258	33	36				
B 45-4 83-83.5	422.42		21.4	10.5	3.47	2.06	292	326	196	219	37	41				
B 45-4 83.5-84	422.43		21.2	19.8	2.97	1.82	277	345	685	854	34	42				
B 45-4 84-85	422.44		20.8	26.3	2.56	1.76	234	317	90	122	30	41				
A 42-6 94.5-95	422.44		19.7	31.3	2.44	1.74	294	428	69	100	35	51				
B 45-4 85-86	422.45		20.9	26.8	2.66	1.97	246	336	59	81	34	46				
B 45-4 86-86.5	422.45		20.9	26.3	2.58	2.04	248	336	73	99	31	42				
B 45-4 86.5-87.5	422.46		21.2	27.7	2.59	1.88	261	361	45	62	30	41				
B 45-4 87.5-88.5	422.47		19.8	25.3	2.82	2.19	284	380	65	87	31	42				
B 45-4 88.5-89.5	422.48		21.0	18.4	3.21	2.48	331	406	143	175	34	42				
A 42-6 99-99.5	422.48		17.8	29.7	2.79	1.97	345	491	52	74	45	64				
B 45-4 89.5-90	422.49		21.8	25.3	2.70	2.00	316	423	76	102	36	48				
A 42-6 100-101	422.49	-24.67	16.0													
B 45-4 90-91	422.49	-22.8	21.3													
B 45-4 90-90.5	422.49		20.7	27.7	2.69	1.92	298	412	54	75	32	44				
B 45-4 90.5-91.5	422.50		18.8	29.5	2.72	1.75	306	434	63	89	28	40				
B 45-4 91.5-92.5	422.51		18.3	28.6	2.79	1.67	313	438	85	119	30	42				
A 42-6 102.5-103	422.52		11.9	2.5	3.15	1.73	785	805	296	304	54	55				
B 45-4 92.5-93.5	422.52		19.1	32.8	2.46	1.86	294	437	41	61	34	51				
B 45-4 93.5-94.5	422.53		18.7	30.8	2.59	1.94	307	444	39	56	40	58				
B 45-4 94.5-95.5	422.54		18.5	25.6	2.92	2.32	357	480	149	200	48	65				
B 45-4 95.5-96.5	422.55		20.5	21.0	2.99	2.30	405	513	80	101	62	78				

Table 3.S3: *continued*

Sample ID (Leg 207-1258)	Depth (mcd)	$\delta^{13}C_{carb}$ (‰)	C_{org} (wt%)	C_{inorg} (wt%)	Al (wt%)	Fe_T (wt%)	V (ppm)	V* (ppm)	Zn (ppm)	Zn* (ppm)	Mo (ppm)	Mo* (ppm)	with Fe_{ox}		without Fe_{ox}	
													$\frac{Fe_{py}}{Fe_T}$	$\frac{Fe_{py}}{Fe_{HR}}$	$\frac{Fe_{py}}{Fe_T}$	$\frac{Fe_{py}}{Fe_{HR}}$
B 45-4 96.5-98	422.56		16.6	2.5	4.44	2.64	981	1006	341	350	68	70				
A 42-6 108-108.5	422.57		12.9	1.8	4.14	2.01	964	982	319	325	56	57				
B 45-4 98-99	422.58		14.3	0.7	4.32	2.08	1129	1137	548	552	56	56				
B 45-4 99-100	422.59		8.6	2.5	2.23	1.28	516	529	256	263	41	42				
A 42-6 110-111	422.59	-24.61	13.0													
B 45-4 100-101	422.59	-25.1	8.5													
B 45-4 100-101	422.60		8.6	2.9	2.21	1.40	509	524	203	209	40	41				
B 45-4 101-102	422.61		9.4	2.5	2.51	1.60	537	551	215	221	45	46				
B 45-4 102-103	422.62		11.6	3.4	3.26	2.00	682	706	296	306	52	54				
A 42-6 113-114	422.62		18.8	0.9	3.78	2.41	764	771	254	257	71	72	0.89	0.58	0.60	0.86
A 42-6 113-113.5	422.62		16.5	2.2	3.67	2.50	734	750	253	259	73	75				
B 45-4 103-104.5	422.63		12.4	1.9	3.74	1.90	853	870	299	305	45	46				
B 45-4 104.4-105.5	422.64		11.2	2.5	3.15	1.78	661	678	240	246	46	47				
B 45-4 106-107	422.65		14.6	2.1	3.14	2.12	659	673	227	232	60	61	0.86	0.65	0.63	0.87
B 45-4 105.5-107	422.65		11.0	3.0	3.08	1.75	645	665	227	234	47	48				
A 42-6 117.5-118	422.67		24.7	2.5	3.19	3.28	709	727	189	194	99	102				
B 45-4 107-108.5	422.67		16.0	3.8	3.29	2.30	668	695	219	228	67	70				
A 42-6 118-119	422.67		25.1	1.9	1.87	1.70	416	424	347	354	50	51	0.99	0.86	0.97	0.88
B 45-4 108.5-109.5	422.68		14.1	2.4	3.28	1.91	738	756	329	337	52	53				
B 45-4 109.5-110	422.69		17.6	4.2	3.81	2.64	762	795	259	270	74	77				
B 45-4 110-111	422.69	-23.36	18.0													
B 45-4 110-111	422.70		22.6	5.6	3.42	3.55	677	717	128	136	90	95				
A 42-6 121.5-122	422.71		16.7	3.3	2.68	1.76	564	583	156	161	67	69				
B 45-4 111-112.5	422.71		21.4	4.4	3.44	3.48	753	788	220	230	86	90				
B 45-4 112.5-114	422.72		21.9	4.3	3.23	3.26	710	742	177	185	83	87				

Table 3.S3: *continued*

Sample ID (Leg 207-1258)	Depth (mcd)	$\delta^{13}C_{carb}$ (‰)	C_{org} (wt%)	C_{inorg} (wt%)	Al (wt%)	Fe_T (wt%)	V (ppm)	V* (ppm)	Zn (ppm)	Zn* (ppm)	Mo (ppm)	Mo* (ppm)	with Fe_{ox} $\frac{Fe_{py}}{Fe_T}$	with Fe_{ox} $\frac{Fe_{py}}{Fe_{HR}}$	without Fe_{ox} $\frac{Fe_{py}}{Fe_T}$	without Fe_{ox} $\frac{Fe_{py}}{Fe_{HR}}$
B 45-4 113-115	422.73		22.4	6.9	3.28	3.44	727	781	175	188	85	91				
B 45-4 114-115	422.74		26.4	5.4	2.93	3.52	689	728	304	321	95	100				
B 45-4 115-116	422.75		24.9	4.4	3.07	2.74	672	703	228	239	86	90				
B 45-4 116-117	422.76		23.5	6.0	3.03	2.80	649	690	214	228	88	94				
A 42-6 126.5-127	422.76		15.2	10.6	3.91	2.13	754	843	157	176	58	65				
B 45-4 117-118	422.77		22.0	4.6	2.99	2.43	692	725	222	233	85	89				
A 42-6 127-129	422.78		20.9	7.9	3.55	2.47	590	641	115	124	67	73				
B 45-4 118-119	422.78		17.0	3.6	2.69	1.80	573	594	138	143	65	67				
B 45-4 119-120	422.79		17.1	4.5	2.76	1.87	570	597	132	138	68	71				
B 45-4 120-121	422.79	-23.33	14.5													
B 45-4 120-122	422.80		13.9	4.8	3.17	1.81	650	682	161	169	55	58				
A 42-6 131.5-132	422.81		24.3	10.3	3.33	2.66	464	517	1012	1129	54	60				
B 45-4 122-123	422.82		19.1	8.4	3.68	2.64	672	734	150	164	59	64				
B 45-4 123-124	422.83		23.5	6.5	3.27	4.01	532	569	95	102	68	73				
B 45-4 124-125	422.84		22.9	5.2	3.30	4.04	478	504	315	332	59	62				
B 45-4 125-126	422.85		24.1	9.4	3.27	3.01	461	509	402	444	50	55				
B 45-4 126-127	422.86		23.6	16.2	2.92	2.82	406	484	49	58	48	57				
A 42-6 137-137.5	422.86		27.1	9.1	3.09	2.31	429	472	41	45	63	69				
B 45-4 127-127.5	422.86		25.0	14.2	2.85	2.76	392	457	38	44	51	59				
A 42-6 138-140	422.87	-22.89	26.4													
B 45-4 127.5-128.5	422.87		27.2	12.0	2.81	2.76	387	440	55	63	55	63				
B 45-4 128.5-129.5	422.88		24.2	13.0	3.14	2.62	484	556	73	84	51	59				
B 45-4 129.5-130	422.89		23.1	18.2	3.11	2.31	533	651	54	66	44	54				
A 42-7 0-1	422.89	-21.76	20.3													
B 45-4 130-131	422.89	-21.48	29.2													

Table 3.S3: *continued*

Sample ID (Leg 207-1258)	Depth (mcd)	$\delta^{13}C_{carb}$ (‰)	C_{org} (wt%)	C_{inorg} (wt%)	Al (wt%)	Fe_T (wt%)	V (ppm)	V* (ppm)	Zn (ppm)	Zn* (ppm)	Mo (ppm)	Mo* (ppm)	with Fe_{ox}		without Fe_{ox}	
													$\frac{Fe_{py}}{Fe_T}$	$\frac{Fe_{py}}{Fe_{HR}}$	$\frac{Fe_{py}}{Fe_T}$	$\frac{Fe_{py}}{Fe_{HR}}$
B 45-4 130-131	422.90		30.2	7.2	2.78	2.81	482	519	63	68	72	78				
A 42-6 60-61	422.90	-26.33	6.6													
B 45-4 131-132	422.91		27.9	7.9	3.10	2.56	444	482	53	58	61	66				
A 42-7 1.5-2	422.91		21.8	9.3	3.66	2.57	443	489	68	75	44	49				
B 45-4 132-133	422.92		26.0	5.9	3.12	2.35	447	475	97	103	61	65				
B 45-4 133-134	422.93		25.1	3.7	3.26	2.65	486	504	169	175	70	73				
A 42-7 4-4.5	422.93		19.7	12.3	3.59	2.38	384	438	79	90	31	35				
B 45-4 134-135	422.94		24.6	7.1	2.99	2.62	497	535	161	173	82	88				
B 45-4 135-136	422.95		27.1	12.1	2.79	2.29	548	623	179	204	103	117				
B 45-4 136-137	422.96		27.7	14.3	2.62	2.31	524	611	140	163	103	120				
A 42-7 6.5-7	422.96		19.5	12.6	3.47	2.34	333	381	81	93	31	35				
A 42-7 7-9	422.96				3.32	2.16	283	283	80	80	31	31				
B 45-4 137-138	422.97		20.4	21.4	3.01	1.84	648	825	159	202	77	98				
B 45-4 138-139	422.98		16.5	14.1	3.66	4.07	748	871	295	343	77	90				
B 45-4 139-140	422.99		20.1	8.6	4.16	2.52	765	837	87	95	48	53				
A 42-7 9.5-10	422.99		18.4	15.2	3.44	2.25	305	360	96	113	28	33				
A 42-7 10-11	422.99	-22.29	21.6	10.8	3.10	2.14	292	327	89	100	25	29	0.82	0.71	0.65	0.90
B 45-4 140-141	422.99	-21.8	24.2													
B 45-4 140-140.5	422.99		23.8	9.3	3.56	2.50	451	497	55	61	49	54				
B 45-4 140.5-141.5	423.00		19.0	9.9	3.77	2.57	433	481	95	105	35	39				
B 45-4 141.5-142.5	423.01		20.1	11.3	3.55	2.52	403	455	83	94	37	42				
B 45-4 142.5-143.5	423.02		20.5	12.2	3.47	2.44	376	428	87	99	35	40				
A 42-7 13-13.5	423.02		22.5	12.2	3.30	2.67	268	305	62	71	34	39				
B 45-4 143.5-144.5	423.03		20.5	11.8	3.35	2.24	334	379	76	86	31	35				
B 45-4 144.5-145.5	423.04		19.2	11.3	3.56	2.34	330	372	97	109	31	35				

Table 3.S3: *continued*

Sample ID (Leg 207-1258)	Depth (mcd)	$\delta^{13}C_{carb}$ (‰)	C_{org} (wt%)	C_{inorg} (wt%)	Al (wt%)	Fe_T (wt%)	V (ppm)	V* (ppm)	Zn (ppm)	Zn* (ppm)	Mo (ppm)	Mo* (ppm)	with Fe_{ox}		without Fe_{ox}	
													$\frac{Fe_{py}}{Fe_T}$	$\frac{Fe_{py}}{Fe_{HR}}$	$\frac{Fe_{py}}{Fe_T}$	$\frac{Fe_{py}}{Fe_{HR}}$
B 45-4 145-147	423.05		20.5	14.1	3.43	2.34	304	354	73	85	30	35				
B 45-4 145.5-147	423.05		20.4	12.2	3.42	2.34	303	345	72	82	27	31				
A 42-7 16.5-17	423.06		22.1	16.8	3.05	2.37	228	274	128	154	27	32				
B 45-4 147-148	423.07		19.8	12.9	3.35	2.43	278	319	87	100	30	34				
B 45-4 148-149	423.07		13.6	11.9	3.17	2.28	277	315	72	82	30	34	0.71	0.59	0.46	0.90
B 45-4 148-149	423.08		20.7	13.1	3.28	2.34	267	307	65	75	28	32				
B 45-4 149-149.5	423.08		21.5	12.3	3.41	2.66	276	315	70	80	29	33				
A 42-7 20-20.5	423.09		22.8	15.1	3.06	2.32	221	260	66	78	26	31				
A 42-7 21.5-22.5	423.11		20.3	21.0	3.12	2.06	215	272	62	78	15	19				
A 42-7 22.5-23.5	423.12		22.6	13.6	3.09	2.30	226	262	55	64	20	23				
A 42-7 23.5-24.5	423.13		21.8	18.9	2.98	2.28	213	263	75	92	18	22				
A 42-7 24.5-25	423.14		19.9	23.7	2.82	2.04	200	262	105	138	16	21				
A 42-7 26.5-28	423.16		19.5	24.4	2.72	1.90	203	269	60	79	11	15				
A 42-7 28-29	423.18		20.8	32.1	2.21	1.73	192	283	25	37	14	21				
A 42-7 29-30	423.19		19.4	33.8	2.36	1.65	199	300	27	41	15	23				
A 42-7 31.5-33	423.21		21.0	11.4	3.72	2.13	819	925	1125	1270	70	79				
A 42-7 33-35	423.22				3.15	1.66	460	460	136	136	53	53				
A 42-7 33-34	423.23		25.3	14.3	3.10	1.85	601	701	214	250	70	82				
A 42-7 34-34.5	423.23		17.5	21.8	3.38	1.85	519	663	156	199	45	58				
A 42-7 34.5-35	423.24		19.6	20.3	3.33	1.76	440	552	97	122	43	54				
A 42-7 36.5-37.5	423.26		20.3	12.8	3.72	2.37	320	367	107	123	27	31				
A 42-7 37.5-38.5	423.27		21.4	15.9	3.30	2.22	283	337	57	68	25	30				
A 42-7 38.5-39.5	423.28		19.7	15.5	3.47	2.16	262	310	113	134	21	25				
A 42-7 39.5-40	423.29		19.7	16.2	3.44	2.21	261	311	106	126	23	27				
A 42-7 41.5-42.5	423.31		22.8	21.8	2.81	2.08	196	251	37	47	19	24				

Table 3.S3: *continued*

Sample ID (Leg 207-1258)	Depth (mcd)	$\delta^{13}C_{carb}$ (‰)	C_{org} (wt%)	C_{inorg} (wt%)	Al (wt%)	Fe_T (wt%)	V (ppm)	V* (ppm)	Zn (ppm)	Zn* (ppm)	Mo (ppm)	Mo* (ppm)	with Fe_{ox} $\frac{Fe_{py}}{Fe_T}$	with Fe_{ox} $\frac{Fe_{py}}{Fe_{HR}}$	without Fe_{ox} $\frac{Fe_{py}}{Fe_T}$	without Fe_{ox} $\frac{Fe_{py}}{Fe_{HR}}$
A 42-7 42.5-43	423.32		19.2	24.1	3.13	2.06	202	266	38	50	18	24				
A 42-7 43-44	423.33		19.6	21.5	3.28	2.20	206	262	32	41	20	25				
A 42-7 44-45	423.34		18.8	18.4	3.51	2.49	208	255	43	53	19	23				
A 42-7 46.5-47.5	423.36		19.5	28.6	2.72	1.85	169	237	104	146	13	18				
A 42-7 47.5-48	423.37		19.1	28.7	2.85	1.83	170	238	22	31	14	20				
A 42-7 48-49	423.38		19.0	26.8	2.88	1.89	167	228	20	27	13	18				
A 42-7 49-50	423.39		18.0	30.7	2.67	1.76	158	228	21	30	11	16				
A 42-7 51.5-52	423.41		17.5	30.8	2.59	1.78	163	236	46	67	13	19				
A 42-7 52-53	423.42		16.9	32.4	2.66	1.62	165	244	24	36	13	19				
A 42-7 53-54	423.42		18.6	30.8	2.09	1.79	178	257	30	43	31	45	0.77	0.70	0.59	0.92
A 42-7 53-54	423.43		14.4	36.9	2.58	1.56	167	265	31	49	9	14				
A 42-7 54-54.5	423.43		13.6	34.2	2.72	1.70	185	281	24	36	15	23				
A 42-7 54.5-55	423.44		14.1	29.1	3.00	1.93	204	288	40	56	20	28				
A 42-7 56.5-57.5	423.46		14.9	8.0	4.87	2.50	353	384	73	79	30	33				
A 42-7 57.5-58	423.47		17.1	9.8	4.59	2.29	331	367	74	82	34	38				
A 42-7 58-59	423.48		12.5	0.0	6.01	3.74	473	473	384	384	26	26				
A 42-7 59-60	423.49		11.9	0.0	6.09	3.77	572	572	315	315	22	22				
A 42-7 66.5-67	423.56		12.8	33.2	3.31	2.10	247	370	35	52	7	10				
A 42-7 67-67.5	423.56		9.2	44.1	2.62	3.68	205	367	100	179	7	13				
A 42-7 67.5-68	423.57		8.6	46.7	2.35	4.05	170	319	137	257	9	17				
A 42-7 68-69	423.58		10.5	47.7	2.40	1.51	151	289	29	55	6	11				
A 42-7 69-70	423.59		13.2	41.7	2.49	1.39	122	209	106	182	8	14				
A 42-7 71.5-72.5	423.61		8.7	58.0	1.78	1.22	93	221	29	69	5	12				
A 42-7 72.5-73	423.62		12.5	46.8	1.88	1.23	99	186	234	439	11	21				
A 42-7 73-74	423.63		11.7	44.1	2.21	1.65	115	206	74	132	10	18				

Table 3.S3: *continued*

Sample ID (Leg 207-1258)	Depth (mcd)	$\delta^{13}C_{carb}$ (‰)	C_{org} (wt%)	C_{inorg} (wt%)	Al (wt%)	Fe_T (wt%)	V (ppm)	V* (ppm)	Zn (ppm)	Zn* (ppm)	Mo (ppm)	Mo* (ppm)	with Fe_{ox} $\frac{Fe_{py}}{Fe_T}$	with Fe_{ox} $\frac{Fe_{py}}{Fe_{HR}}$	without Fe_{ox} $\frac{Fe_{py}}{Fe_T}$	without Fe_{ox} $\frac{Fe_{py}}{Fe_{HR}}$
A 42-7 74-75	423.64		12.1	44.8	1.94	1.58	107	194	57	103	8	14				
A 42-7 76.5-77	423.66		9.2	49.8	2.03	1.52	106	211	44	88	5	10				
A 42-7 77-78	423.67		8.1	58.3	1.62	1.17	88	211	29	70	2	5				
A 42-7 78-79	423.68		8.2	55.6	1.71	1.55	85	191	47	106	3	7				
A 42-7 79-80	423.68		8.4	53.5	1.45	1.22	77	166	36	78	7	16	0.67	0.85	0.63	0.92
A 42-7 79-80	423.69		7.7	56.8	1.77	1.10	94	217	27	62	3	7				
A 42-7 81.5-82.5	423.71		8.2	53.7	1.88	1.27	92	199	46	99	4	9				
A 42-7 82.5-83.5	423.72		9.7	48.1	1.91	1.48	95	183	33	64	5	10				
A 42-7 83.5-85	423.73		7.7	52.8	1.57	2.07	83	176	95	201	5	11				
A 42-7 86.5-87	423.76		5.9	57.7	1.37	1.21	77	182	73	172	2	5				
A 42-7 87-87.5	423.76		6.4	63.3	1.31	0.80	87	237	14	38	0	0				
A 42-7 87.5-88	423.77		6.2	63.6	1.36	0.85	87	239	20	55	1	3				
A 42-7 88-89.5	423.78		5.6	67.5	1.11	0.69	85	262	16	49	0	0				
A 42-7 89.5-91.5	423.80		8.0	51.8	1.82	1.23	103	214	62	129	3	6				
B 45-4 149-150	423.80	-21.81	21.4													
A 42-7 92-94	423.81				2.86	1.74	164	164	133	133	20	20				
A 42-7 91.5-92.5	423.81		9.3	45.7	2.05	1.29	115	212	29	53	8	15				
A 42-7 92.5-93.5	423.82		11.7	34.8	2.58	1.69	151	231	59	90	11	17				
A 42-7 93.5-95	423.83		13.3	33.3	2.72	1.73	168	252	147	220	16	24				
A 42-7 96.5-97.5	423.86		16.6	15.5	4.19	2.50	256	303	152	180	22	26				
A 42-7 100-101	423.89	-22.89	17.3	13.0	3.56	1.95	338	389	149	172	27	31	0.74	0.59	0.48	0.91
A 42-7 20-21	423.90	-22.11	22.0													
A 42-7 110-111	423.99	-22.2	6.2													
C 17-1 10-11.5	424.55		20.1	16.4	3.17	2.48	225	269	120	144	20	24				
C 17-1 15-16.5	424.60		21.9	23.1	2.73	2.09	206	267	36	46	18	23				

Table 3.S3: *continued*

Sample ID (Leg 207-1258)	Depth (mcd)	$\delta^{13}C_{carb}$ (‰)	C_{org} (wt%)	C_{inorg} (wt%)	Al (wt%)	Fe_T (wt%)	V (ppm)	V* (ppm)	Zn (ppm)	Zn* (ppm)	Mo (ppm)	Mo* (ppm)	with Fe_{ox}		without Fe_{ox}	
													$\frac{Fe_{py}}{Fe_T}$	$\frac{Fe_{py}}{Fe_{HR}}$	$\frac{Fe_{py}}{Fe_T}$	$\frac{Fe_{py}}{Fe_{HR}}$
C 17-1 5-6.5	424.84	-21.9	22.6	11.4	3.49	2.61	278	313	68	77	28	31				
C 17-1 5-6	424.84		20.8	12.6	3.40	2.45	279	319	75	86	28	33	0.70	0.77	0.58	0.93
C 17-1 10-11.5	424.89	-21.5	25.5													
C 17-1 15-16.5	424.94	-21.7	23.3													
C 17-1 20-21.5	424.99	-22.1	19.6													
C 17-1 25-26.5	425.04	-22	24.8	15.8	3.05	2.12	326	387	61	72	42	50				
C 17-1 27-28	425.06		22.0	17.6	2.77	1.91	206	251	78	95	23	28	0.84	0.78	0.71	0.93
C 17-1 30-31.5	425.09	-21.7	20.0	18.0	3.35	2.45	211	257	45	55	19	23				
C 17-1 35-36.5	425.14	-22.1	16.8	33.5	2.45	1.59	158	238	37	55	13	19				
B 46-1 0-1	425.16	-21.75	19.0													
C 17-1 40-41.5	425.19	-22.8	15.1													
B 46-1 3-5	425.20		20.8	25.2	2.92	2.02	192	257	34	45	20	27				
C 17-1 50-51.5	425.29	-22	10.6	46.7	1.96	2.77	89	166	102	190	5	8				
C 17-1 75-76.5	425.54	-23	16.0													
C 17-1 80-81.5	425.59	-23	11.1													
C 17-1 80-81	425.59		14.4	5.0	4.65	3.14	496	522	526		29	31	0.78	0.85	0.70	0.95
C 17-1 85-86.5	425.64	-23	10.5													
C 17-1 90-91.5	425.69	-23.1	15.7													
C 17-1 95-96.5	425.74	-24	8.8													
C 17-1 95-96	425.74		12.4	0.0	3.53	2.01	69	69	394	394	5	5	0.79	0.77	0.67	0.90
C 17-1 100-101.5	425.79	-23.9	11.7													
B 46-2 0 -1	425.80	-25.86	15.0													
B 46-2 0-1	425.81		12.1	39.9	2.03	1.59	360	599	239	398	63	105				
B 46-2 1-2	425.82		11.0	14.5	1.89	1.19	300	351	311	364	53	62				
B 46-2 2-4	425.83		6.7	4.9	1.18	0.73	199	209	194	204	29	30				

Table 3.S3: *continued*

Sample ID (Leg 207-1258)	Depth (mcd)	$\delta^{13}C_{carb}$ (‰)	C_{org} (wt%)	C_{inorg} (wt%)	Al (wt%)	Fe_T (wt%)	V (ppm)	V* (ppm)	Zn (ppm)	Zn* (ppm)	Mo (ppm)	Mo* (ppm)	with Fe_{ox} $\frac{Fe_{py}}{Fe_T}$	with Fe_{ox} $\frac{Fe_{py}}{Fe_{HR}}$	without Fe_{ox} $\frac{Fe_{py}}{Fe_T}$	without Fe_{ox} $\frac{Fe_{py}}{Fe_{HR}}$
B 46-2 3-5	425.84		7.2	6.0	1.19	0.76	194	206	194	206	34	36				
C 17-1 105-106.5	425.84	-23.7	17.7													
B 46-2 4-6.5	425.85		3.7	40.6	0.55	0.41	117	197	28	47	13	22				
B 46-2 6.5-8	425.87		6.0	53.1	0.84	0.61	156	333	53	113	18	38				
B 46-2 8-10	425.89		8.5	60.3	1.40	0.96	209	527	38	96	26	66				
C 17-1 110-111.5	425.89	-26.2	21.3	9.6	3.03	2.16	402	444	179	198	76	84				
B 46-2 10-11	425.90	-24.45	4.7													
B 46-2 10-11.5	425.91		5.4	52.8	0.82	0.62	145	307	72	152	18	38				
B 46-2 11.5-13	425.92		3.0	31.4	0.48	0.34	88	128	69	101	11	16				
B 46-2 13-14	425.94		16.0	23.3	2.60	1.57	324	422	102	133	74	96				
C 17-1 115-116.5	425.94	-24.3	15.0													
B 46-2 14-15	425.95		18.1	24.2	2.73	1.65	358	472	93	123	97	128				
B 46-2 15-16	425.96		15.5	26.2	2.38	1.41	306	414	128	173	85	115				
B 46-2 16-17	425.97		13.1	26.3	1.95	1.26	262	356	76	103	81	110				
B 46-2 17-18	425.98		12.8	20.0	1.77	1.22	246	308	187	234	79	99				
B 46-2 18-19	425.99		16.1	32.6	2.03	1.42	307	455	84	125	117	174				
C 17-1 120-121.5	425.99	-24.8	12.8	22.5	2.20	1.38	257	332	90	115	46	59				
B 46-2 19-20.5	426.00		15.3	22.3	2.22	1.48	326	420	116	149	105	135				
B 46-2 20-21	426.00	-25.8	13.9													
C 17-1 121-122	426.00		12.3	23.8	1.63	1.10	240	315	226	297	68	89	0.99	0.84	0.97	0.86
B 46-2 20.5-21	426.01		12.7	25.8	2.42	1.47	371	500	129	174	101	136				
B 46-2 21-22	426.02		12.4	24.8	2.45	1.40	390	519	185	246	102	136				
B 46-2 22-23	426.03		12.6	28.8	2.64	1.51	427	600	170	239	111	156				
B 46-2 23-24	426.04		12.8	29.7	2.72	1.48	469	667	172	245	107	152				
C 17-1 125-126.5	426.04	-25.4	10.3	27.8	1.41	0.96	211	291	47	64	66	91				

Table 3.S3: *continued*

Sample ID (Leg 207-1258)	Depth (mcd)	$\delta^{13}C_{carb}$ (‰)	C_{org} (wt%)	C_{inorg} (wt%)	Al (wt%)	Fe_T (wt%)	V (ppm)	V* (ppm)	Zn (ppm)	Zn* (ppm)	Mo (ppm)	Mo* (ppm)	with Fe_{ox} $\frac{Fe_{py}}{Fe_T}$	with Fe_{ox} $\frac{Fe_{py}}{Fe_{HR}}$	without Fe_{ox} $\frac{Fe_{py}}{Fe_T}$	without Fe_{ox} $\frac{Fe_{py}}{Fe_{HR}}$
B 46-2 24-25	426.05		12.7	27.8	2.77	1.57	469	650	204	283	106	147				
B 46-2 26.5-27.5	426.07		13.1	25.8	2.59	1.43	462	623	174	235	122	164				
B 46-2 27-28	426.08		12.9	28.1	2.61	1.45	465	647	205	285	117	163				
B 46-2 27.5-28.5	426.08		13.7	28.3	2.74	1.51	515	719	212	296	129	180				
C 17-1 130-131.5	426.09	-26.8	12.0	29.0	2.44	1.37	394	555	142	200	90	126				
B 46-2 28.5-29.5	426.09		12.8	32.4	2.70	1.45	524	775	223	330	128	189				
B 46-2 30-31	426.10	-27.5	12.8													
B 46-2 29.5-30.5	426.10		12.9	24.4	2.75	1.48	503	665	226	299	125	165				
B 46-2 30.5-31	426.11		12.2	28.0	2.68	1.37	516	717	222	308	113	157				
B 46-2 32.5-33.5	426.13		9.0	29.5	1.61	0.80	328	465	147	209	87	123				
B 46-2 33.5-35	426.14		6.9	35.2	1.25	0.64	273	421	99	153	68	105				
C 17-1 136-137.5	426.15	-26.9	13.4	28.5	2.75	1.48	497	695	201	281	121	169				
B 46-2 35-36	426.16		6.8	41.8	1.18	0.61	279	479	105	180	65	112				
C 17-1 137-138	426.16		2.0	0.1	3.32	1.40	40	40	347	347	6	6	0.61	0.97	0.59	1.00
B 46-2 36-37	426.17		7.4	50.8	1.27	0.66	310	629	139	282	78	158				
B 46-2 37-38	426.17	-26.91	4.9													
B 46-2 37-38	426.18		6.6	52.8	1.15	0.59	290	615	134	284	63	134				
B 46-2 38-39	426.19		3.8	72.3	0.67	0.33	219	792	79	286	37	134				
B 46-2 39-40	426.20		1.8	9.1	0.30	0.13	58	64	25	27	17	19				
C 17-2 3-4.5	426.21	-26	8.1													
A 42-7 114-115	426.23		13.6	0.8	3.92	1.76	647	653	188	189	40	40	0.82	0.84	0.76	0.90
B 46-2 43-45	426.24		0.9	95.9	0.08	0.07	81	1984	19	465	6	147				
B 46-2 45-46	426.26		16.1	24.8	2.66	2.18	822	1092	157	209	327	435				
A 42-7 116.5-118.5	426.27		16.5	4.4	4.46	2.57	671	702	257	269	76	80				
A 42-7 118.5-119	426.28		14.1	2.7	4.38	2.31	641	659	224	230	66	68				

Table 3.S3: *continued*

Sample ID (Leg 207-1258)	Depth (mcd)	$\delta^{13}C_{carb}$ (‰)	C_{org} (wt%)	C_{inorg} (wt%)	Al (wt%)	Fe_T (wt%)	V (ppm)	V* (ppm)	Zn (ppm)	Zn* (ppm)	Mo (ppm)	Mo* (ppm)	with Fe_{ox}		without Fe_{ox}	
													$\frac{Fe_{py}}{Fe_T}$	$\frac{Fe_{py}}{Fe_{HR}}$	$\frac{Fe_{py}}{Fe_T}$	$\frac{Fe_{py}}{Fe_{HR}}$
B 46-2 47-49	426.28		7.4	10.7	1.35	0.89	389	435	157	176	127	142				
C 17-2 10-11.5	426.28	-23.4	28.6													
A 42-7 119-120	426.29		14.0	3.8	4.20	2.36	642	667	225	234	70	73				
B 46-2 50-51	426.30	-25.77	15.2													
C 17-2 12-13	426.30		7.1	17.7	1.52	0.87	588	715	310	376	92	111	0.94	0.81	0.83	0.92
B 46-2 51.5-52	426.32		16.5	16.3	2.58	1.57	1033	1235	283	338	291	348				
B 46-2 52-53	426.33		16.2	16.5	2.56	1.47	1107	1326	365	437	296	354				
C 17-2 15-16.5	426.33	-27.5	9.0													
B 46-2 53-54	426.34		16.5	21.2	2.71	1.52	1235	1567	424	538	289	367				
B 46-2 54-55	426.35		19.5	28.1	2.80	1.78	1114	1549	285	396	386	537				
B 46-2 55-56	426.36		22.8	26.9	2.64	2.01	921	1260	249	341	462	632				
B 46-2 56-57	426.37		28.1	20.2	2.27	2.33	830	1040	163	204	636	797				
B 46-2 57-57.5	426.37		24.8	25.0	2.45	2.37	898	1197	273	364	598	797				
C 17-2 20-21.5	426.38	-27.3	6.2													
B 46-2 59.5-60	426.40		12.4	31.7	2.89	1.66	1146	1677	422	618	230	337				
B 46-2 60-61	426.40	-27.56	12.8													
C 17-2 22-23	426.40		9.7	48.3	1.99	1.01	1537	2975	647	1252	79	152	0.85	0.82	0.76	0.93
B 46-2 59-61	426.40		12.3	23.8	2.89	1.51	1276	1673	516	677	210	275				
B 46-2 60-61	426.41		12.4	24.5	2.87	1.50	1281	1697	475	629	206	273				
A 42-7 132-135	426.41				3.17	1.79	1250	1250	366	366	308	308				
B 46-2 61-61.5	426.41		10.7	15.5	2.40	1.35	1100	1302	418	495	162	192				
B 46-2 61.5-62.5	426.42		6.3	7.7	1.43	0.90	731	792	273	296	98	106				
C 17-2 25-26	426.43		11.0	41.6	1.98	0.97	1646	2817	312	535	82	141	0.95	0.81	0.86	0.89
C 17-2 25-26.5	426.43	-27.8	9.2													
B 46-2 62.5-64.5	426.44		3.6	5.1	0.62	0.29	513	540	964	1016	47	50				

Table 3.S3: *continued*

Sample ID (Leg 207-1258)	Depth (mcd)	$\delta^{13}C_{carb}$ (‰)	C_{org} (wt%)	C_{inorg} (wt%)	Al (wt%)	Fe_T (wt%)	V (ppm)	V* (ppm)	Zn (ppm)	Zn* (ppm)	Mo (ppm)	Mo* (ppm)	with Fe_{ox} $\frac{Fe_{py}}{Fe_T}$	with Fe_{ox} $\frac{Fe_{py}}{Fe_{HR}}$	without Fe_{ox} $\frac{Fe_{py}}{Fe_T}$	without Fe_{ox} $\frac{Fe_{py}}{Fe_{HR}}$
B 46-2 64.5-66	426.45		11.2	35.3	2.41	1.19	1681	2599	1582	2446	96	148				
B 46-2 66-67	426.47		11.9	34.7	2.61	1.22	1856	2841	1590	2434	102	156				
B 46-2 67-68.5	426.48		9.9	50.1	2.18	1.09	1696	3398	1560	3125	97	194				
C 17-2 30-31.5	426.48	-28	10.6													
B 46-2 68.5-69.5	426.49		9.2	50.9	2.05	1.01	1699	3461	1519	3095	89	181				
B 46-2 69.5-70	426.50		9.8	51.1	2.42	1.20	1970	4027	1139	2328	94	192				
B 46-2 70-71	426.50	-27.82	8.9													
B 46-2 71.5-72.5	426.52		10.7	47.3	2.27	1.08	2002	3801	2084	3957	99	188				
C 17-2 34-35.5	426.52	-27.7	9.1													
B 46-2 72.5-73.5	426.53		10.4	48.5	2.21	1.04	1965	3816	1925	3738	96	186				
B 46-2 73.5-74	426.54		10.5	47.0	2.36	1.13	2054	3875	1425	2689	98	185				
A 42-CCW 4-5	426.54		9.4	39.9	1.88	0.93	1935	3220	1680	2796	77	127	0.96	0.84	0.90	0.90
B 46-2 74-75	426.55		11.0	46.9	2.27	1.07	1941	3657	1688	3180	95	179				
B 46-2 76.5-77.5	426.57		9.2	56.6	1.93	0.96	1879	4328	1839	4236	87	200				
B 46-2 77.5-78.5	426.58		9.7	53.7	2.04	0.97	1909	4120	1453	3136	86	186				
C 17-2 40-41.5	426.58	-28	10.7													
B 46-2 78.5-79.5	426.59		9.6	56.3	1.89	0.91	1843	4213	1879	4295	80	183				
B 46-2 79.5-80	426.60		9.2	51.8	2.14	1.00	1944	4029	1557	3227	81	168				
B 46-2 80-81	426.60	-27.69	10.7													
A 43-1 14-15	426.62		15.2	0.8	0.88	0.44	519	523	1623	1636	54	54				
B 46-2 81.5-82.5	426.62		9.1	52.9	2.03	0.94	1824	3874	1468	3118	76	161				
C 17X2 45-46.5	426.63	-27.9	9.3													
B 46-2 82.5-83.5	426.63		9.5	56.3	1.96	0.94	1904	4352	2133	4875	79	181				
B 46-2 83.5-84	426.64		10.2	54.0	2.06	0.95	1952	4243	1723	3746	80	174				
B 46-2 84-85	426.65		10.5	53.8	2.10	0.99	1945	4213	1987	4304	84	182				

Table 3.S3: *continued*

Sample ID (Leg 207-1258)	Depth (mcd)	$\delta^{13}C_{carb}$ (‰)	C_{org} (wt%)	C_{inorg} (wt%)	Al (wt%)	Fe_T (wt%)	V (ppm)	V* (ppm)	Zn (ppm)	Zn* (ppm)	Mo (ppm)	Mo* (ppm)	with Fe_{ox} $\frac{Fe_{py}}{Fe_T}$	with Fe_{ox} $\frac{Fe_{py}}{Fe_{HR}}$	without Fe_{ox} $\frac{Fe_{py}}{Fe_T}$	without Fe_{ox} $\frac{Fe_{py}}{Fe_{HR}}$
B 46-2 86.5-88	426.67		11.1	47.2	2.27	1.04	1876	3551	1656	3134	81	153				
C 17-2 50-51.5	426.68	-27.9	8.9													
B 46-2 88-89	426.69		10.6	50.5	2.21	0.99	1841	3719	1494	3018	75	152				
B 46-2 90-91	426.70	-27.73	11.4													
B 46-2 89-91	426.70		10.6	53.2	2.04	0.94	1809	3863	1897	4051	77	164				
B 46-2 92.5-93	426.73		13.0	34.4	2.79	1.24	1757	2679	1438	2193	84	128				
C 17-2 55-56.5	426.73	-27.9	9.4	52.4	2.00	0.93	1645	3454	1939	4070	66	139				
B 46-2 93-94	426.74		15.8	23.6	3.16	1.42	1859	2433	1445	1891	102	133				
B 46-2 94-95	426.75		14.2	14.3	3.04	1.36	1632	1905	1207	1409	88	103				
B 46-2 95-95.5	426.75		14.8	12.5	2.94	1.31	1515	1731	952	1088	86	98				
C 17-2 60-61.5	426.78	-27.9	11.0													
B 46-2 98-98.5	426.78		11.5	14.8	2.40	1.08	1071	1256	576	676	67	79				
B 46-2 98-99	426.79		8.6	17.6	1.82	0.82	813	986	526	638	48	58				
B 46-2 98.5-99	426.79		10.6	13.7	2.16	1.01	959	1111	651	754	57	66				
B 46-2 99-100.5	426.80		8.9	16.5	1.89	0.85	834	999	545	653	54	65				
B 46-2 100-101	426.80	-27.96	8.4													
B 46-2 100.5-102	426.81		5.6	7.6	1.13	0.53	521	564	364	394	38	41				
B 46-2 102-103.5	426.83		4.3	6.0	0.85	0.41	416	443	191	203	33	35				
B 46-2 103.5-105	426.84		2.9	13.9	0.48	0.27	267	310	129	150	32	37				
B 46-2 106.5-108	426.87		8.0	60.9	1.19	0.74	780	1996	267	683	104	266				
C 17-2 70-71.5	426.88	-27.5	4.8													
C 17-2 70-71	426.88		4.5	74.3	1.11	0.58	679	2643	208	810	67	262	0.87	0.87	0.80	0.93
B 46-2 108-109	426.89		7.0	65.2	1.17	0.66	770	2211	198	568	97	278				
B 46-2 109-109.5	426.89		6.5	69.6	1.21	0.68	777	2555	215	707	95	312				
B 46-2 110-111	426.90	-27.34	6.8													

Table 3.S3: *continued*

Sample ID (Leg 207-1258)	Depth (mcd)	$\delta^{13}C_{carb}$ (‰)	C_{org} (wt%)	C_{inorg} (wt%)	Al (wt%)	Fe_T (wt%)	V (ppm)	V* (ppm)	Zn (ppm)	Zn* (ppm)	Mo (ppm)	Mo* (ppm)	with Fe_{ox} $\frac{Fe_{py}}{Fe_T}$	with Fe_{ox} $\frac{Fe_{py}}{Fe_{HR}}$	without Fe_{ox} $\frac{Fe_{py}}{Fe_T}$	without Fe_{ox} $\frac{Fe_{py}}{Fe_{HR}}$
B 46-2 111-111.5	426.91		6.9	71.6	1.12	0.60	732	2576	180	633	93	327				
B 46-2 111.5-112.5	426.92		7.2	69.2	1.11	0.62	701	2278	251	816	82	266				
C 17-2 75-76.5	426.93	-27.7	4.0													
B 46-2 112.5-114	426.93		6.7	71.2	1.22	0.69	764	2650	185	642	94	326				
B 46-2 114-115	426.95		6.4	71.5	1.27	0.67	740	2596	191	670	92	323				
B 46-2 115-115.5	426.95		5.6	74.9	1.10	0.59	670	2671	160	638	82	327				
A 43-1 41-42	426.96		5.8	69.3	1.06	0.60	687	2239	146	477	75	245	0.91	0.73	0.78	0.86
B 46-2 117-117.5	426.97		5.1	76.3	1.01	0.53	641	2708	143	604	75	317				
B 46-2 117.5-118	426.98		5.1	78.1	0.88	0.48	573	2614	135	616	67	306				
B 46-2 118-119	426.99		4.6	76.7	1.07	0.55	658	2820	146	626	67	287				
B 46-2 119-120	427.00		4.5	79.4	0.92	0.48	582	2828	144	700	61	296				
B 46-2 120-121	427.00	-27.49	4.6													
B 46-2 120-121	427.01		4.6	80.1	0.87	0.47	550	2762	144	723	65	326				
B 46-2 121-122	427.02		4.5	78.3	0.92	0.48	561	2589	135	623	60	277				
B 46-2 122-124	427.03		4.1	81.4	0.86	0.45	525	2825	128	689	56	301				
B 46-2 124-125	427.05		3.8	82.8	0.82	0.41	492	2852	111	643	51	296				
B 46-2 125-126	427.06		3.2	84.1	0.74	0.38	453	2846	118	741	47	295				
B 46-2 126-128	427.07		2.0	90.2	0.46	0.24	311	3163	75	763	25	254				
B 46-2 128-129	427.09		1.6	93.4	0.33	0.19	233	3539	57	866	19	289				
B 46-2 129-130	427.10		1.3	94.3	0.28	0.15	212	3741	61	1076	15	265				
B 46-2 130-131	427.11		1.2	93.8	0.30	0.17	212	3392	54	864	19	304				
B 46-2 131-131.5	427.11		1.4	94.3	0.27	0.15	202	3513	40	696	18	313				
B 46-2 131.5-132.5	427.12		1.1	94.2	0.26	0.15	194	3326	47	806	13	223				
B 46-2 132.5-133.5	427.13		1.1	94.8	0.29	0.15	184	3561	52	1006	13	252				
A 43-1 66-68	427.14				2.43	1.02	1050	1050	817	817	72	72				

Table 3.S3: *continued*

Sample ID (Leg 207-1258)	Depth (mcd)	$\delta^{13}C_{carb}$ (‰)	C_{org} (wt%)	C_{inorg} (wt%)	Al (wt%)	Fe_T (wt%)	V (ppm)	V* (ppm)	Zn (ppm)	Zn* (ppm)	Mo (ppm)	Mo* (ppm)	with Fe_{ox}		without Fe_{ox}	
													$\frac{Fe_{py}}{Fe_T}$	$\frac{Fe_{py}}{Fe_{HR}}$	$\frac{Fe_{py}}{Fe_T}$	$\frac{Fe_{py}}{Fe_{HR}}$
B 46-2 133.5-134.5	427.14		1.1	93.8	0.23	0.13	161	2611	29	470	13	211				
B 46-2 134.5-135.5	427.15		0.9	94.8	0.23	0.13	157	3014	48	922	12	230				
B 46-2 135.5-136.5	427.16		1.4	94.2	0.23	0.13	149	2554	37	634	13	223				
B 46-2 136.5-137.5	427.17		1.1	95.7	0.22	0.13	146	3369	34	785	14	323				
B 46-2 137.5-138.5	427.18		1.2	94.9	0.23	0.15	144	2833	28	551	12	236				
B 46-2 138.5-139	427.19		1.0	95.9	0.21	0.17	126	3086	28	686	8	196				
B 46-2 138-140	427.19		0.8	95.7	0.20	0.17	126	2908	27	623	8	185				
B 46-2 139-140	427.20		1.2	95.7	0.19	0.16	118	2750	22	513	9	210				
B 46-2 140-141	427.21		0.9	95.6	0.17	0.16	115	2604	25	566	9	204				
B 46-2 141-142	427.22		1.1	95.5	0.16	0.22	100	2222	17	378	6	133				
B 46-2 142-143	427.23		1.0	95.4	0.15	0.15	107	2335	17	371	6	131				
A 43-1 75-76.5	427.23		4.5	73.2	0.94	0.51	520	1938	122	455	50	188	0.90	0.80	0.73	0.98
C 17-2 105-106	427.23		5.9	62.8	1.55	0.79	1124	3022	136	366	59	159	0.90	0.87	0.83	0.95
B 46-2 143-144	427.24		0.5	95.9	0.16	0.19	100	2449	22	539	8	196				
B 46-2 144-145	427.25		0.9	96.6	0.15	0.13	99	2898	19	556	6	176				
B 46-2 145-146	427.26		0.6	96.8	0.16	0.13	107	3379	23	726	7	221				
B 46-2 146-147	427.27		0.7	95.4	0.16	0.14	110	2400	19	415	7	153				
B 46-2 147-148.5	427.28		0.8	94.6	0.19	0.24	120	2215	23	425	9	166				
B 46-2 148.5-149	427.29		1.0	93.8	0.19	0.10	124	2011	20	324	6	97				
B 46-3 0-1	427.29	-27.35	1.3													
B 46-3 0-1	427.30		1.1	95.1	0.19	0.12	134	2725	26	529	9	183				
B 46-3 1-2	427.31		1.1	95.4	0.22	0.12	164	3578	23	502	8	175				
B 46-3 2-3	427.32		1.4	92.3	0.32	0.18	225	2935	33	430	14	183				
B 46-3 3-4	427.33		2.6	87.3	0.47	0.25	299	2345	45	353	29	227				
B 46-3 4-6	427.34		2.8	86.3	0.58	0.32	351	2553	66	480	41	298				

Table 3.S3: *continued*

Sample ID (Leg 207-1258)	Depth (mcd)	$\delta^{13}C_{carb}$ (‰)	C_{org} (wt%)	C_{inorg} (wt%)	Al (wt%)	Fe_T (wt%)	V (ppm)	V* (ppm)	Zn (ppm)	Zn* (ppm)	Mo (ppm)	Mo* (ppm)	with Fe_{ox} $\frac{Fe_{py}}{Fe_T}$	with Fe_{ox} $\frac{Fe_{py}}{Fe_{HR}}$	without Fe_{ox} $\frac{Fe_{py}}{Fe_T}$	without Fe_{ox} $\frac{Fe_{py}}{Fe_{HR}}$
B 46-3 6-7	427.36		4.6	78.8	0.96	0.51	508	2400	97	458	58	274				
B 46-3 7-8	427.37		4.6	78.3	0.96	0.48	499	2294	102	469	51	234				
B 46-3 8-9	427.38		4.7	78.0	1.05	0.54	565	2568	131	595	60	273				
B 46-3 9-10	427.39		4.7	77.8	0.97	0.50	549	2467	161	724	60	270				
B 46-3 10-11	427.39	-27.37	5.6													
B 46-3 11.5-12.5	427.41		5.1	74.3	1.13	0.59	640	2494	149	581	65	253				
B 46-3 12.5-13	427.42		5.5	73.3	1.25	0.64	681	2554	165	619	67	251				
C 17-3 4-5	427.42		1.8	87.7	0.67	0.33	264	2153	59	478	26	211				
B 46-3 13-14	427.43		5.5	72.2	1.30	0.66	767	2756	186	668	72	259				
B 46-3 14-15	427.44		6.5	70.1	1.37	0.68	902	3015	312	1043	75	251				
B 46-3 15-15.5	427.44		6.8	66.5	1.56	0.76	1039	3101	446	1331	83	248				
B 46-3 16.5-18.5	427.47		7.1	67.4	1.32	0.65	1069	3281	1117	3428	73	224				
B 46-3 18.5-19	427.48		6.2	69.1	1.31	0.66	1047	3387	978	3163	65	210				
B 46-3 19-20	427.49		8.0	61.4	1.84	0.90	1300	3369	1000	2592	74	192				
B 46-3 20-21	427.49	-27.86	7.3													
B 463 20-21	427.50		7.4	60.6	1.93	0.93	1361	3453	1138	2887	68	173				
B 463 21-22	427.51		9.1	52.5	2.16	1.00	1408	2964	953	2006	76	160				
B 463 23.5-25.5	427.54		12.7	33.7	3.03	1.38	1437	2166	952	1435	85	128				
A 43-1 106-107	427.54		0.5	95.9	0.19	0.12	94	2278			7	165				
B 46-3 25-25.5	427.54		11.6	31.6	3.22	1.48	1352	1976	714	1044	81	118				
B 46-3 25-27	427.55		10.9	14.8	3.40	1.66	1289	1512	793	930	75	88				
B 46-3 25.5-26.5	427.55		12.3	23.6	3.52	1.62	1413	1849	751	983	78	102				
B 46-3 26.5-28	427.56		11.4	15.4	3.46	1.71	1322	1563	785	928	76	90				
B 46-3 30-31	427.59	-28.2	9.6													
B 46-3 29.5-30.5	427.59		9.9	16.0	2.59	1.29	856	1019	573	682	76	90				

Table 3.S3: *continued*

Sample ID (Leg 207-1258)	Depth (mcd)	$\delta^{13}C_{carb}$ (‰)	C_{org} (wt%)	C_{inorg} (wt%)	Al (wt%)	Fe_T (wt%)	V (ppm)	V* (ppm)	Zn (ppm)	Zn* (ppm)	Mo (ppm)	Mo* (ppm)	with Fe_{ox}		without Fe_{ox}	
													$\frac{Fe_{py}}{Fe_T}$	$\frac{Fe_{py}}{Fe_{HR}}$	$\frac{Fe_{py}}{Fe_T}$	$\frac{Fe_{py}}{Fe_{HR}}$
B 46-3 30.5-31.5	427.60		5.0	66.7	1.13	0.61	526	1578	207	621	45	135				
B 46-3 31.5-32.5	427.61		4.3	77.9	0.99	0.62	506	2291	112	507	43	195				
B 46-3 32.5-33.5	427.62		4.0	79.6	0.99	0.56	529	2591	121	593	39	191				
C 17-3 25-26	427.63		11.7	38.6	2.72	1.28	1742	2839	214	349	105	171	0.48	0.72	0.43	0.81
B 46-3 33.5-34.5	427.63		3.8	80.6	0.89	0.48	490	2524	98	505	39	201				
B 46-3 34.5-35.5	427.64		3.9	78.7	1.02	0.53	533	2498	118	553	43	202				
B 46-3 35.5-36.5	427.65		3.7	80.0	0.92	0.50	513	2565	125	625	42	210				
A 43-1 119-120	427.67		3.3	90.7	0.22	0.28	105	1126	46	494	10	110				
B 46-3 38.5-39	427.68		3.4	83.3	0.75	0.39	458	2748	86	516	32	192				
B 46-3 39-40	427.69		2.8	86.4	0.66	0.35	417	3070	81	596	34	250				
B 46-3 40-41	427.69	-27.81	3.2													
B 46-3 40-41	427.70		2.8	84.9	0.79	0.41	463	3070	84	557	31	206				
B 46-3 41-42.5	427.71		3.3	83.3	0.79	0.41	468	2808	93	558	33	198				
B 46-3 42.5-43.5	427.72		3.4	82.4	0.91	0.48	517	2940	178	1012	36	205				
B 46-3 43.5-45	427.73		4.2	75.9	1.19	0.58	776	3222	808	3355	42	174				
B 46-3 45-47	427.75		4.5	72.8	1.42	0.66	862	3173	690	2540	37	136				
B 46-3 50-51	427.79	-28.19	12.2													
B 46-3 50-51	427.80		12.6	24.1	3.51	1.62	1202	1584	831	1095	102	134				
A 43-2 4-5	427.80		5.1	73.3	1.16	0.65	730	2738	64	240	73	274	0.67	0.70	0.53	0.87
C 17-3 45-46	427.83		10.9	46.8	1.99	0.98	2208	4152	72	135	102	191	0.85	0.83	0.77	0.92
B 46-3 55-55.5	427.84		3.5	82.4	0.78	0.50	437	2485	76	432	38	216				
B 46-3 64.5-65	427.94		1.5	92.2	0.33	0.18	209	2668	60	766	14	179				
C 17-CC 2-3	427.98		11.9	42.9	2.10	1.05	2176	3810	52	91	95	166	0.87	0.78	0.79	0.86
B 46-3 70-71	427.99	-27.66	2.2													

Table 3.S3: *continued*

Sample ID (Leg 207-1258)	Depth (mcd)	$\delta^{13}C_{carb}$ (‰)	C_{org} (wt%)	C_{inorg} (wt%)	Al (wt%)	Fe_T (wt%)	V (ppm)	V* (ppm)	Zn (ppm)	Zn* (ppm)	Mo (ppm)	Mo* (ppm)	with Fe_{ox} $\frac{Fe_{py}}{Fe_T}$	with Fe_{ox} $\frac{Fe_{py}}{Fe_{HR}}$	without Fe_{ox} $\frac{Fe_{py}}{Fe_T}$	without Fe_{ox} $\frac{Fe_{py}}{Fe_{HR}}$
A 43-2 26-28	428.02				2.80	1.23	1632	1632	1064	1064	100	100				
B 46-3 73.5-74	428.03		5.0	75.8	1.23	0.64	702	2895	136	561	64	264				
C 17-CC 15-16	428.11		14.0	38.9	1.80	1.05	1927	3156	313	512	113	185	0.67	0.76	0.59	0.87
A 43-2 39-41	428.15		12.9	38.9	2.40	1.09	1898	3109	526	861	98	161	0.79	0.72	0.66	0.86
B 46-3 85-87	428.15		8.9	16.7	2.12	0.97	1112	1334	716	859	69	83				
A 43-2 42-44	428.18				2.63	1.15	1776	1776	1255	1255	94	94				
B 46-3 90-91	428.19	-27.72	12.4													
B 46-3 95-95.5	428.24		8.6	7.9	1.98	0.87	1191	1293	554	602	57	62				
C 18-1 3-4	428.25		9.2	60.6	1.83	0.98	1198	3039	648	1644	97	246				
B 46-3 95-97	428.25		8.8	3.9	1.67	0.78	1102	1147	777	809	51	53				
B 46-3 98-99	428.27	-27.57	5.1													
B 46-4 0-1	428.28	-26.94	12.3													
B 46-4 4-6	428.33		12.6	50.0	1.96	0.92	2245	4490	1857	3714	106	212				
B 46-4 6-8	428.35		12.6	48.0	2.13	1.01	2459	4729	1827	3513	119	229				
B 46-4 10-11	428.38	-27.4	11.7													
B 46-4 15.5-16	428.44		10.4	47.4	2.02	0.99	2247	4273	1738	3305	99	188				
B 46-4 20-21	428.48	-27.79	12.3													
A 43-2 100-105	428.49		10.7	48.4	2.07	0.94	2177	4217	1160	2247	99	193				
B 46-4 24.5-25	428.53		11.4	52.2	2.06	0.99	2239	4681	1721	3598	113	236				
B 46-4 30-31	428.58	-27.23	11.7													
C 18-1 37-38	428.59		11.6	52.3	2.16	1.17	1493	3132	360	755	155	325				
B 46-4 34.5-35	428.63		12.5	46.8	2.39	1.17	2502	4699	1973	3705	126	237				
B 46-4 40-41	428.68	-26.6	13.3													
B 46-4 41-42	428.70		12.6	51.4	1.96	0.93	2217	4563	1833	3773	126	259				
B 46-4 42.5-44.4	428.71		11.8	50.9	2.07	1.01	2259	4602	2036	4148	123	251				

Table 3.S3: *continued*

Sample ID (Leg 207-1258)	Depth (mcd)	$\delta^{13}C_{carb}$ (‰)	C_{org} (wt%)	C_{inorg} (wt%)	Al (wt%)	Fe_T (wt%)	V (ppm)	V* (ppm)	Zn (ppm)	Zn* (ppm)	Mo (ppm)	Mo* (ppm)	with Fe_{ox}		without Fe_{ox}	
													$\frac{Fe_{py}}{Fe_T}$	$\frac{Fe_{py}}{Fe_{HR}}$	$\frac{Fe_{py}}{Fe_T}$	$\frac{Fe_{py}}{Fe_{HR}}$
A 43-2 100-105	428.76		11.1	44.2	2.30	1.21	2540	4552	2354	4218	119	214	1.00	0.82	0.87	0.93
B 46-4 50-51	428.78	-27.71	15.2													
B 46-4 52-54	428.81		12.5	20.8	2.89	1.34	1575	1989	977	1234	111	140				
C 18-1 61-62	428.83		10.4	44.2	2.45	1.17	1553	2781	1103	1976	81	145				
B 46-4 60-61	428.88	-27.3	8.2													
B 46-4 61.5-62	428.90		7.7	57.3	2.00	1.09	1212	2835	826	1932	89	208				
B 46-3 80-81	428.90	-28	12.5													
A 43-2 119-121	428.95		7.9	57.0	1.95	0.95	1386	3225	792	1844	103	240				
B 46-4 70-71	428.98	-27.97	12.5													
B 46-4 71-71.5	428.99		9.5	46.5	2.43	1.19	1330	2486	610	1140	99	185				
A 43-2 124-126	429.00				3.10	1.44	1555	1555	907	907	120	120				
A 43-3 2-3	429.04		12.0	14.3	2.68	1.27	1137	1327			70	81	0.84	0.72	0.74	0.82
A 43-3 4-7	429.06				3.19	1.49	1201	1201	550	550	92	92				
B 46-4 81-82.5	429.10		6.7	24.6	1.64	0.77	709	940	368	488	58	77				
C 18-1 93-94	429.15		13.9	17.4	3.91	1.79	1441	1745	836	1012	81	98				
B 46-4 90-91	429.18		10.6													
B 46-4 89-91	429.18		11.7	52.0	1.95	1.04	1378	2871	391	815	155	323				
B 46-4 92.5-93	429.21		10.8	52.2	2.05	1.11	1414	2956	370	774	153	320				
B 46-4 100-101	429.28	-26.93	9.9													
B 46-4 101.5-102	429.30		10.1	46.8	2.42	1.16	1840	3455	1167	2192	120	225				
B 46-4 110-111	429.38	-27.71	10.4													
B 46-4 110.5-111	429.39		9.4	38.3	2.46	1.15	1695	2749	1479	2398	106	172				
A 43-3 37-39	429.39		3.3	81.5	0.71	0.33	528	2849	20	110	37	202				
B 46-4 116-118	429.45		9.0	55.9	2.13	1.05	1701	3859	1130	2563	122	277				

Table 3.S3: *continued*

Sample ID (Leg 207-1258)	Depth (mcd)	$\delta^{13}C_{carb}$ (‰)	C_{org} (wt%)	C_{inorg} (wt%)	Al (wt%)	Fe_T (wt%)	V (ppm)	V* (ppm)	Zn (ppm)	Zn* (ppm)	Mo (ppm)	Mo* (ppm)	with Fe_{ox}		without Fe_{ox}	
													$\frac{Fe_{py}}{Fe_T}$	$\frac{Fe_{py}}{Fe_{HR}}$	$\frac{Fe_{py}}{Fe_T}$	$\frac{Fe_{py}}{Fe_{HR}}$
B 46-4 117-119	429.46		8.5	56.0	2.15	1.08	1690	3841	1038	2359	116	264				
B 46-4 120-121	429.48	-27.83	9.5													
C 18-1 129-130	429.50		10.9	40.3	2.17	1.04	1670	2799	1180	1978	76	127				
B 46-4 126-126.5	429.54		11.3	26.1	3.36	1.55	1347	1822	929	1257	88	119				
B 46-4 130-131	429.58	-27.97	9.8													
A 43-3 68.5-70	429.71		7.3	24.3	1.47	0.78	730	964	441	582	74	97	0.89	0.75	0.81	0.82
C 18-2 22-23	429.75		12.5	46.4	2.36	1.16	1892	3531	1540	2874	98	183				
B 46-4 80-81	429.80	-27.93	7.7													
A 43-3 88.5-90	429.91		8.7	53.1	1.49	0.76	1593	3396	1043	2225	96	204	0.99	0.72	0.87	0.83
C 18-2 45-47	429.98		10.4	29.6	2.60	1.31	673	956	450	639	51	72				

Chapter 4

Observed global distributions of organic carbon burial versus carbon-isotope-based model estimates during OAE2: Quantifying the missing sink

Abstract

The Cretaceous experienced numerous global and local perturbations to the ocean-atmosphere system, especially during periods of widespread organic-carbon burial known as oceanic anoxic events (OAEs). The best documented OAE in the geologic record is the Cenomanian-Turonian boundary event (~93.9 Ma), or OAE2, which has the widest global distribution known for an OAE—with reports from ~120 sections. Despite the large number of locations, the majority are found within the proto-Atlantic and Tethyan oceans and interior seaways. The pervasive increase in organic carbon (OC) burial during OAE2 drove carbon isotope values more positive (2 to 7‰) due to the low $\delta^{13}C$ values of the OC. Because these isotope data allow us to constrain the global mass of OC burial, even for unstudied portions of the global ocean, we can solve for any 'missing' OC sinks by comparing our model estimates with the known distribution of OAE2 sediments and their organic contents. Specifically, we compared the known spatial extent of OC burial with our results from a forward carbon-isotope box model. Our mapping of OC burial requires knowledge of the average total organic carbon (TOC) contents during the OAE *and* sedimentation rate for each locality in-order to calculate OC mass accumulation rate (MAR). Importantly, localities with high TOC but relatively slow sedimentation rates record low OC MAR and vice versa. Using the known OC distribution and reasonably extrapolating to analogous settings lacking data allows us to account for only ~13% of the total seafloor, mostly marginal marine settings. This 'mapped' distribution accounts for 4.04×10^{19} g of C or an isotope excursion of ~2‰ using modern fluxes, which means that 13% of the OAE2 seafloor buried more OC than the entire modern ocean combined. Additionally, conservatively adding the modern OC MAR, for appropriate deposition settings, to the unknown portions of the OAE2 seafloor, mostly deep abyssal plain, can minimally accounts 5.02×10^{19} g of C or 4‰ excursion

using modern fluxes. Therefore, the OC MAR estimated using known localities and estimated OC burial for unknown portions of the ocean can account for a 4‰ excursion using modern carbon fluxes, similar to the observed carbonate carbon isotope excursion. This suggests the mapping distribution can account for nearly all of the OC buried during OAE2 unless carbon fluxes were dramatically different during this event.

Introduction

Extensive deposition of organic-rich facies was common throughout the Mesozoic era; highlighted in the Cretaceous, these time intervals have aptly been named oceanic anoxic events (OAEs) (Schlanger and Jenkyns, 1976). The Cenomanian-Turonian boundary event (93.9 million years: Ma), or OAE2, is the most extensively studied of these events, with reports of elevated organic carbon (OC) deposition in multiple ocean basins (Indian, Pacific, Atlantic and Tethys oceans) and under various paleo-water depths, paleolatitudes and depositional conditions (Arthur et al., 1987; Jenkyns, 2010; Kuroda and Ohkouchi, 2006; Schlanger et al., 1987; Takashima et al., 2006). Due to the enhanced burial of organic matter, which preferentially buries isotopically light carbon during these OAEs, there is a coeval positive carbon isotope excursion (Arthur et al., 1988; Schlanger et al., 1987; Scholle and Arthur, 1980). Importantly, the positive carbon isotope excursion is observed in all carbon phases: organic-C, carbonate-C and terrestrial OM (Hasegawa, 1997; Jarvis et al., 2006; Jenkyns, 2010; Scholle and Arthur, 1980). The magnitude of this excursion ranges between 4 to 7‰, with the average carbonate hosts recording an excursion of ~4‰, and organic-C records showing larger excursions (Erbacher et al., 2005; Forster et al., 2007; Jarvis et al., 2006; Jenkyns et al., 1994; Kuypers et al., 2002; Schlanger et al., 1987; Tsikos et al., 2004). The latter is interpreted to reflect a changing

net fractionation between organic matter and inorganic C over the course of the event due to declining atmospheric *p*CO2, although varying this parameter only does not perfectly reproduce the observed $\delta^{13}C$ trends (Kump and Arthur, 1999). Also, much of the $\delta^{13}C_{organic}$ variation recorded globally can be corrected for with paleolatitudinal sea surface temperatures due to increased fractionation at lower latitudes (van Bentum et al., 2012). This pervasive OC burial during OAE2 is thought to be the result of einither enhanced productivity, increased anoxia or a combination of these two factors (Barron, 1983; Kuypers et al., 2002; Schlanger et al., 1987; Schlanger and Jenkyns, 1976).

OAE2 is characterized by an overall warm climate recorded in proxy records for elevated temperatures (Huber et al., 1995; Jarvis et al., 2011; Jenkyns et al., 2004; Jenkyns et al., 2012), as well as high pCO_2 (estimated to be 2-8 times higher) (Barclay et al., 2010; Berner, 2006; Takashima et al., 2006) and increasing sea level (Haq et al., 1987; Jarvis et al., 2001). However, the evidence points to some climatic cooling during the OAE, which has been attributed to the widespread burial of OC and a concomitant decrease in atmospheric pCO_2 (Arthur et al., 1988; Barclay et al., 2010; Jarvis et al., 2011; van Bentum et al., 2012). Sustaining enhanced productivity, export and burial of organic carbon throughout the ~500 thousand year (ka) event (Kuhnt et al., 2005; Sageman et al., 2006; Voigt et al., 2008) requires increased delivery of nutrients (e.g., N and P) and bio-essential metals (e.g., Fe) to the surface ocean. Increased seafloor spreading rates, increased weathering (Blättler et al., 2011; Blumenberg and Wiese, 2012; Flögel et al., 2011; Jones and Jenkyns, 2001) and/or enhanced phosphorus regeneration under oxygen-deficient marine conditions (Kraal et al., 2010; Mort et al., 2008; Nederbragt and Fiorentino, 1999; Ozaki et al., 2011; Van Cappellen and Ingall, 1994) have all been implicated to explain enhanced nutrient delivery. Estimates suggest that the Cretaceous did experience elevated seafloor spreading rates and generally increased

volcanism (e.g. Kerr, 1998; Snow et al., 2005; Turgeon and Creaser, 2008), which could explain the evidence for high *p*CO2 concentrations (Barclay et al., 2010; Berner, 2006; Takashima et al., 2006) and may have fostered high delivery of bio-essential metals to seawater, such as iron. An important consideration, however, is the difficulty in moving large amounts of dissolved and other bioreactive forms of iron under both oxic and anoxic-sulfidic (euxinic) conditions (Owens et al., 2012). Modeling suggests increased phosphorus delivery from rising sea level over the course of the Cretaceous and peaking during OAE2, but this effect cannot account for the enhanced carbon burial during this excursion (Bjerrum et al., 2006).

Traditionally, the widespread distribution of organic-rich sediments has been used to infer regional and even global extents of anoxic deposition, which can enhance organic preservation (Kuroda and Ohkouchi, 2006; Monteiro et al., 2012; Schlanger et al., 1987; Takashima et al., 2006). Numerous geochemical proxies have also been applied to OAEs to independently constrain local anoxia and/or euxinia, such as Mn/Ca and I/Ca ratios and trace metal geochemistry (Brumsack, 2006; Hetzel et al., 2011; Lu et al., 2010; Owens et al., 2012; Pearce et al., 2009; Turgeon and Brumsack, 2006; van Bentum et al., 2009), including evidence for photic zone euxinia based on organic biomarker data (Kuypers et al., 2002; Pancost et al., 2004; Sinninghe Damsté and Köster, 1998; van Bentum et al., 2009). Nevertheless, during OAE2 the documented global evidence for local redox conditions remains poor—especially in the Pacific, Indian and Arctic oceans. Modeling of OAE2 using available geochemical data suggests the global extent of anoxia was up to ~50% (by volume) of the ocean, which implies the maximum possible extent of euxinia was ~50% by volume (Monteiro et al., 2012). Uranium isotopes suggest a 3-fold increase (up to 40% of the seafloor) in reducing (anoxic/euxinic) environments (Montoya-Pino et al., 2010), while S isotopes suggest ~5% of the seafloor was euxinic (Owens et al., in

review-a). The global pervasiveness of reducing conditions has a dramatic effect on the trace metals availability (Reinhard et al., 2013), with decreasing values documented at several localities during OAE2 (Hetzel et al., 2009; Owens et al., in review-a; Owens et al., 2012; Turgeon and Brumsack, 2006; van Bentum et al., 2009). These lower metal concentrations may directly affect the nitrogen cycle (Anbar and Knoll, 2002; Bellenger et al., 2011; Reinhard et al., 2013) and thus levels of primary production. Importantly, organic carbon preservation is also tightly coupled to sedimentation rates (Henrichs and Reeburgh, 1987). For example, the modern ocean buries ~90% of the organic carbon on continental shelves, which have higher sedimentation rates yet represent only 17% of the seafloor (Berner and Canfield, 1989; Burdige, 2007), although other factors also contribute to this relationship.

Understanding the global extent of carbon burial throughout the Phanerozoic has important implications for time-varying levels of atmospheric O_2 and CO_2 (Berner and Canfield, (1989). While estimates are traditionally tied to C isotope trends for seawater and associated modeling (Gill et al., 2011b; Kump and Arthur, 1999; Kuroda and Ohkouchi, 2006; Kurtz et al., 2003; Owens et al., in review-a; Wortmann and Chernyavsky, 2007), Berner and Canfield (1989) took a different approach, which is similar to the method employed here. Specifically, they estimated carbon burial based on average TOC contents and abundances for each sedimentary rock type for given time interval (e.g. Ronov, 1976). This method allowed them to reproduce the results modeled from the long-term carbon isotope curve. Because their focus was long-term estimates for atmospheric composition, they ignored short-term episodes such as OAEs—our emphasis. We have constructed a global map of known OC MAR during OAE2 based on extensive literature reports of the sediments spanning this interval. We then extrapolate these data across unknown portions of the ocean proximal to the available data and of

similar depositional setting to estimate the carbon burial across this event contributed from these settings (similar to the modern study of Jahnke, 1996). By comparing our isotope model and the mapped distributions of TOC in OAE2 sediments we can predict the magnitude of enhanced organic burial required elsewhere in the ocean to explain the observed carbon isotope excursion.

Methods

Estimating global carbon burial from known sediment distributions

To calculate the global carbon burial during a perturbation we must first calculate the average OC mass accumulation rate (MAR; g/cm^2*ka) for given locations. This requires an understanding of the local sedimentation rate (cm/ka) and the rock density (g/cm^3), as well as average total organic carbon content (wt% TOC). Mean sedimentation rate over the duration of the event was calculated from the reported thickness of the section during the OAE and using an estimated duration of 500 ka for OAE2 (Kuhnt et al., 2005; Sageman et al., 2006; Voigt et al., 2008). Any errors in our estimated duration of the OAE will not change our conclusions because we use the same estimate in our isotope modeling approach. For each section, the sediment thickness of the OAE was determined using the positive $\delta^{13}C$ excursion expressed at each location in organic and/or inorganic carbon (both data types are not always available). The initiation and termination of the event are defined by the initial rise above pre-event baseline values and the subsequent return, respectively. The calculation assumes a constant rock density (g/cm^3) of 2.4, rather than the ~2.7 value of common silicate and carbonate minerals, to account for the generally high TOC contents of OAE2 sediments. This difference will have a minimal effect on our final results. Unfortunately, numerous OAE2 sections were

excluded from our compilation because they lacked either TOC data and/or the $\delta^{13}C$ data needed to determine the thickness of the interval. It is important to note the average TOC values may include land-derived terrigenous OM. We did not discriminate among organic types because of our overall goal to quantify the total amount of organic carbon burial during the event and its relationship to the carbon isotope excursion.

To best reproduce the global distribution of sites documented to contain OAE2, we used PaleoAtlas® for ArcGIS® and PointTracker® to reconstruct the most accurate paleo-locations (latitude and longitude), which converts modern GPS locations (some estimated using Google® Maps) to ancient locations through know plate movements over 90 Ma (Scotese, 2008). The average TOC, sediment thickness for the OAE, sedimentation rates and OC MARs for each polygon can be found in Table 4.1. Polygon estimates are the average for a given area based on individual data within that area extrapolated to define broader depositional areas around those points, as dictated by similar paleo-water depths. Therefore, the polygons represent areas with inferred similar depositional environments. For example, numerous sites located in marginal marine settings with similar OC accumulation were lumped together to define a polygon average and were then extrapolated to similar environments, but the extrapolations did not extend to the deep ocean (with the exception of two polygons [discussed below]).

Carbon isotope model

A forward box model of the global carbon cycle was constructed to explore the dynamics of the carbon isotope excursion and specifically to quantify the inferred changes. Initial boundary conditions were prescribed, and individual parameters were perturbed to recreate the observed isotopic trends.

The following time-dependent expression was used to model the isotopic composition (see Gill et al., 2011b; Kump and Arthur, 1999; Kurtz et al., 2003 for additional details):

$$\frac{\partial \delta_0}{\partial t} = \frac{F_W(\delta_W - \delta_0) - F_{org}\Delta C}{M_0} \qquad \text{(Equation 4.1)}$$

where M_0 is the initial concentration of carbon in the marine reservoir (DIC), and δ_0 is the initial isotopic composition. The input to the ocean is the combined fluxes delivered from continental weathering and volcanic emissions, F_w. These input fluxes can be combined because their isotopic compositions are similar—defined as δ_w. The output flux, which isotopically fractionates carbon, is the burial of organic carbon (F_{org}), and ΔC is the isotopic fractionation (isotopic difference between organic carbon and the starting reservoir of dissolved inorganic carbon [DIC]).

The starting reservoir concentration, isotopic estimates and fluxes were based on previously reported values and are relatively similar to modern values, which can be used in modeling studies for the Cenozoic and Cretaceous (Kurtz et al., 2003; Wortmann and Chernyavsky, 2007). We also explore the sensitivity of these assumptions by using an increased DIC pool based on a CO_2-rich Cretaceous world (similar to Kump and Arthur, 1999; Kuroda and Ohkouchi, 2006) shown in Table 4.2. In all the simulations, the models start with a constant C reservoir (3.96×10^{19} g of C), isotope value (1.8‰), weathering flux of DIC (30.1×10^{19} g of C per Ma), carbon isotope value for DIC (-4.0‰), OC burial flux (6.02×10^{19} g of C per Ma) and carbonate burial flux (24.0×10^{19} g of C per Ma), and the OC fractionation is held constant at -28‰ (the estimated fraction for the Cretaceous; Hayes et al., 1999). Using the model we tested the sensitivity of several parameters to our assumptions: OC burial (F_{org}), starting marine concentration (M_0), OC fractionation (ΔC) and weathering flux (F_w). For example, we transiently increased the

Polygon ID	Average Thickness (m)	Average TOC (wt %)	Sedimetation rate (cm/ka)	OC MAR (g/cm^2 ka)	Area (km^2)	OC burial during OAE (10^{19} g)
0	33.00	3.45	6.60	0.55	321832.39	0.09
1	265.00	1.25	53.00	1.59	828253.33	0.66
2	5.33	1.75	1.07	0.04	3456907.59	0.06
3	0.40	3.00	0.08	0.01	2343545.64	0.01
4	142.00	0.50	28.40	0.34	556974.70	0.09
5	12.00	5.40	2.40	0.31	578957.58	0.09
6	3.92	3.83	0.78	0.07	850267.65	0.03
7	0.85	7.04	0.17	0.03	738146.22	0.01
8	1.20	22.00	0.24	0.13	359953.07	0.02
9	0.60	1.60	0.12	0.00	599027.90	0.00
10	10.10	3.00	2.02	0.15	930590.49	0.03
11	2.50	1.00	0.50	0.01	1668936.37	0.01
12	0.40	9.00	0.08	0.02	627837.91	0.01
13	0.50	10.00	0.10	0.02	197177.14	0.00
14	21.00	1.13	4.20	0.11	415475.31	0.02
15	1.50	1.20	0.30	0.01	889736.40	0.00
16	1.67	6.37	0.33	0.05	658047.25	0.01
17	3.50	1.00	0.70	0.02	6876749.12	0.06
18	0.50	5.80	0.10	0.01	1125386.03	0.01
19	0.27	4.93	0.05	0.01	1985945.90	0.01
20	1.15	8.45	0.23	0.05	274292.96	0.01
21	2.43	24.37	0.49	0.28	631721.01	0.07
22	31.75	8.13	6.35	1.24	295526.35	0.18
23	4.95	5.44	0.99	0.13	247139.57	0.01
24	35.00	3.50	7.00	0.59	674864.42	0.20
25	7.00	1.25	1.40	0.04	2332860.87	0.05
26	15.00	0.50	3.00	0.04	935546.60	0.02
27	124.00	4.00	24.80	2.38	1708641.18	1.84
28	0.25	9.60	0.05	0.01	4161175.74	0.02
29	5.00	2.50	1.00	0.06	826139.47	0.02
30	2.85	14.75	0.57	0.20	649103.89	0.07
31	6.00	3.03	1.20	0.09	577676.89	0.03
32	40.00	1.00	8.00	0.19	241822.89	0.02
33	6.50	11.61	1.30	0.36	802059.90	0.15
34	0.15	10.50	0.03	0.01	3528997.29	0.01
35	4.10	4.38	0.82	0.09	1242232.36	0.05
36	30.00	0.40	6.00	0.06	1943409.14	0.06

Table 4.1: Relevant data for each polygon from Figure 4.4 which includes the literature compiled thickness, average TOC. The calculated sedimentation rate and OC MAR were calculated as discussed in the text. The Area for each polygon was calculated using ArcGIS and amount of OC buried for each polygon was calculated by multiplying the area and the OC MAR average for the polygon.

burial of OC for 0.5 Ma (representing the OAE) with an immediate return to pre-OAE fluxes to generate an isotopic excursion, while holding all other variables constant.

Results

Global carbon burial estimates from sediment distributions

The global distribution of OAE2 sites (Fig. 4.1) is dominated by the Tethys and proto-North Atlantic oceans, with most outcrop samples coming from Europe and northern Africa complemented by many ocean drilling sites. Our map is similar to other compilations (Kuroda et al., 2007; Takashima et al., 2006; Trabucho Alexandre et al., 2010)—with the same intrinsic sample biases. Of these sites, there are 72 localities with published TOC values and stratigraphic thicknesses for OAE2, which were used to calculate average TOC and sedimentation rate. Nearly all of these localities (59 sections) were deposited on the continental margins. The Pacific Ocean is constrained by only five sections, with three of the sites located on the continental margins (Hasegawa et al.,

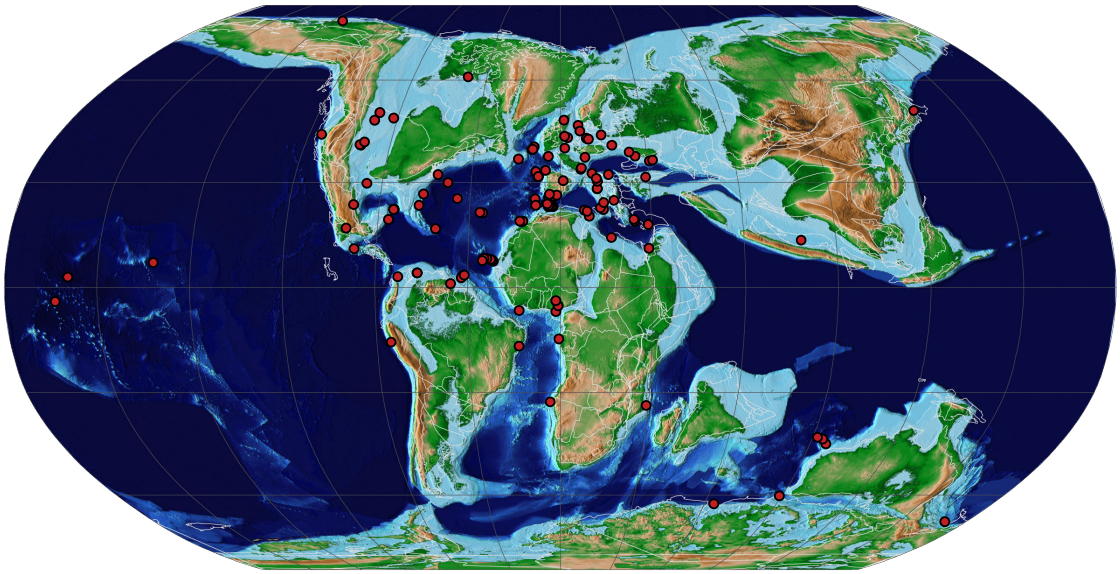

Figure 4.1: Site localities (●) that have been documented to contain sediments from OAE2. This map from adapted from the PALEOMAP Project (Scotese, 2008).

2013; Takashima et al., 2011; Wang et al., 2001) and two from the equatorial region on bathymetric highs (Schlanger et al., 1987; Schlanger and Jenkyns, 1976).

Using ArcGIS® we estimated the total surface area of the ocean to be ~3.62 × 10^8 km^2 during this interval, which is slightly greater than the modern ocean [3.61 × 10^8 km^2 (Charette and Smith, 2010; Menard and Smith, 1966)]. The 36 polygons we generated account for ~0.47 × 10^8 km^2 or 13.0% of the seafloor area. The bulk of the known and estimated seafloor area occurs in marginal marine settings, which is estimated at ~ 0.42 × 10^8 km^2 or ~11.6% of the total area, but there are several sites from deep abyssal settings that account for ~0.05 × 10^8 km^2 or 1.4% of the known OC burial area. Estimates from mapping suggest there is still 0.38 × 10^8 km^2 of marginal marine settings without OC MAR data. This unconstrained area amounts to ~10.5% of seafloor. Therefore, marginal marine settings account for ~0.79 × 10^8 km^2 or 21.8% of the total ocean seafloor, but we

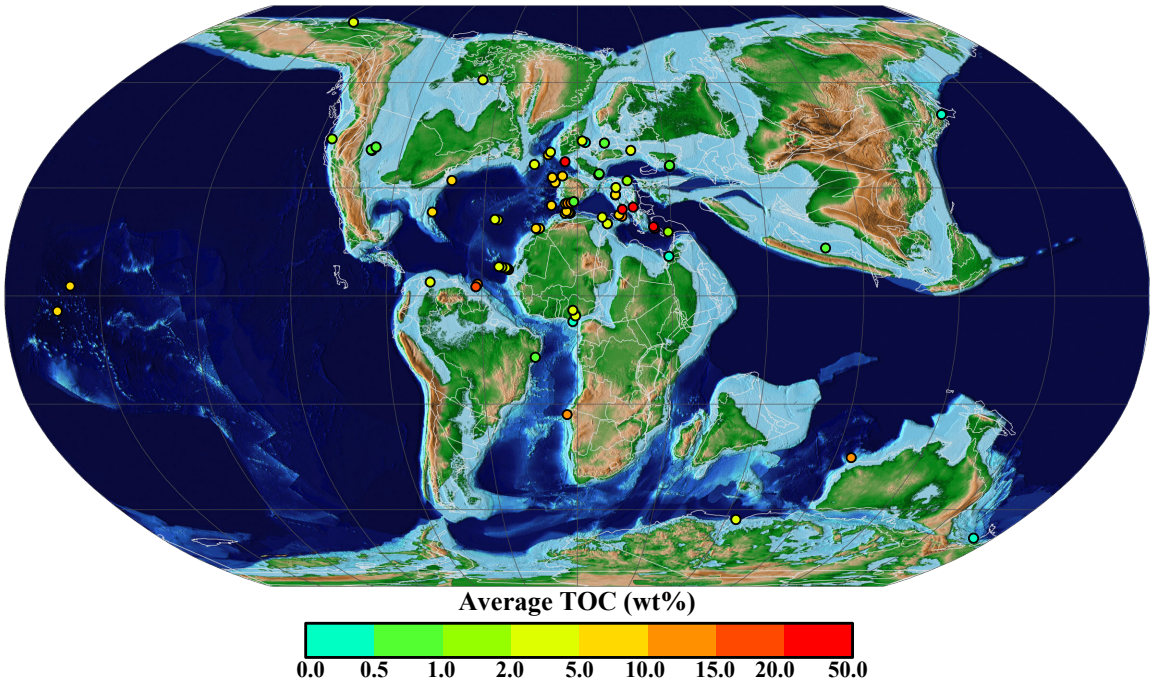

Figure 4.2: The global compilation of all sites with TOC values. This compilation required that the individual sites also contain sedimentation rates. This map from adapted from the PALEOMAP Project (Scotese, 2008).

only have OAE2 OC MAR estimates for ~53% of this area. We have estimated only a very small portion of the deep ocean seafloor due to relatively few locations/data from deep settings. From our model, it is estimated that the deep ocean seafloor represents 2.81 $\times 10^8$ km^2 or 78.2% of the total ocean, and only 0.05 $\times 10^8$ km^2 has been accounted for using the global distribution of available OAE2 data.

As Figure 4.2 shows, 51 localities have average TOC values that are greater than 2 wt%. Average TOC values range from 0.1 wt% to 44 wt% in this compilation, with the highest values coming from Italy, the deep ocean off the coast of Spain and the southern portion of the proto-North Atlantic (Demerara Rise). Figure 4.3 shows calculated sedimentation rates, with nearly all sites plotting within the typical range for modern sedimentation (Sadler, 1981) for their particular depositional settings (e.g., continental margin or abyssal plain localities). This compilation reveals a wide range for average sedimentation rates across the OAE from 0.03 to 53 (cm/ka).

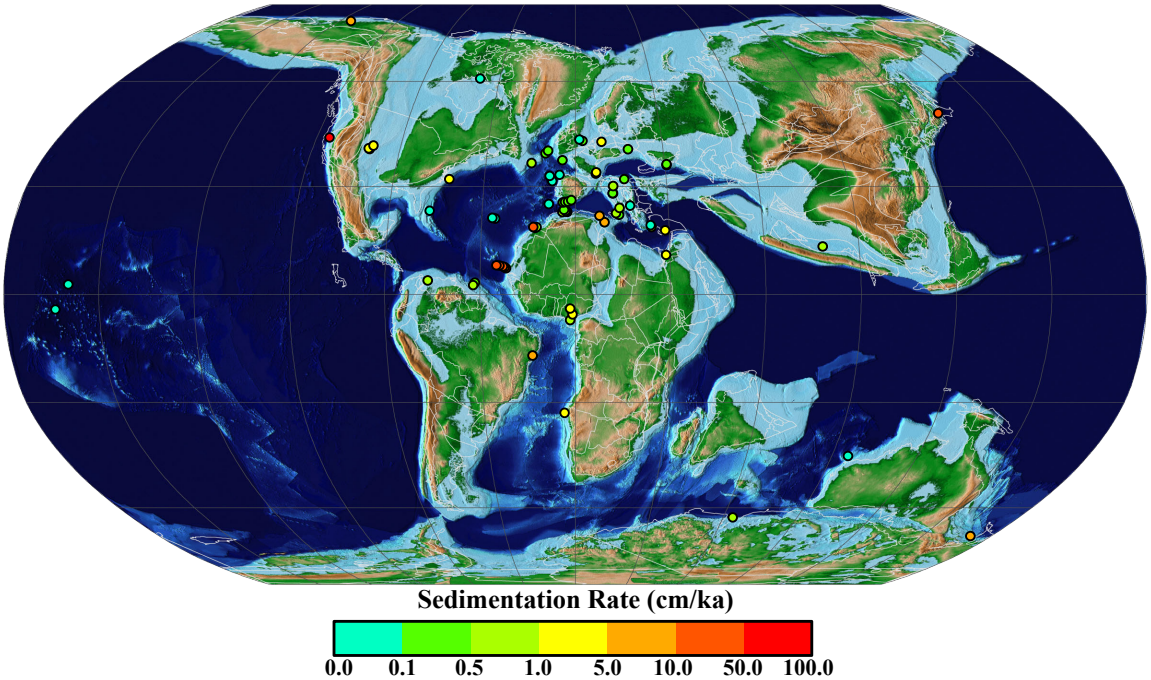

Figure 4.3: Sedimentation rate for the global compilation of all localities which also have TOC values. This map from adapted from the PALEOMAP Project (Scotese, 2008).

The calculated OC MAR values for each site range from 0.001 to 3.3 (g/cm^2*ka), with the abyssal plain sites showing some of the lowest values (Fig. 4.4), while other low values are generally from dominantly carbonate-rich localities with very low TOC contents. Nevertheless, there are several localities with low TOC values but relatively high OC MAR due to high sedimentation rates and concomitant dilution. The colored polygons in Figure 4.4 represent the average OC MAR for a given region, where each polygon provides an area (km^2) for that given depositional environment and an average OC MAR. Generally, each polygon represents either marginal marine or deep abyssal plain environments, with the notable exception of polygons 19 and 27 in the Atlantic Ocean. These two represent transects that include both environments but are lumped together due to the relatively similar OC MAR and the difficulty in accessing the boundary for each environment. Therefore, these two polygons extend from marginal marine and abyssal environments to the relatively close mid-ocean ridge, which could yield a slight overestimation for the OC MAR in these two areas.

The amount of OC buried during the OAE for each polygon can be calculated using the OC MAR, the area for each polygon and the estimated duration of the OAE (~500 ka). The method accounts for a burial of 4.04×10^{19} g of C during the OAE for the known 13% of the seafloor. The unknown 87% of the ocean can conservatively be assigned modern OC MAR (either margin or abyssal depending on the depositional setting) in order to calculate approximate total OC burial during the OAE. This calculation accounts for another $\sim 1 \times 10^{19}$ g of C burial, which leads to a net total of 5.02×10^{19} g of OC buried during the OAE or nearly 2×10^{19} g of C more than modern burial [Tables 4.2 and 4.3; (Burdige, 2007; Kump and Arthur, 1999; Kurtz et al., 2003)].

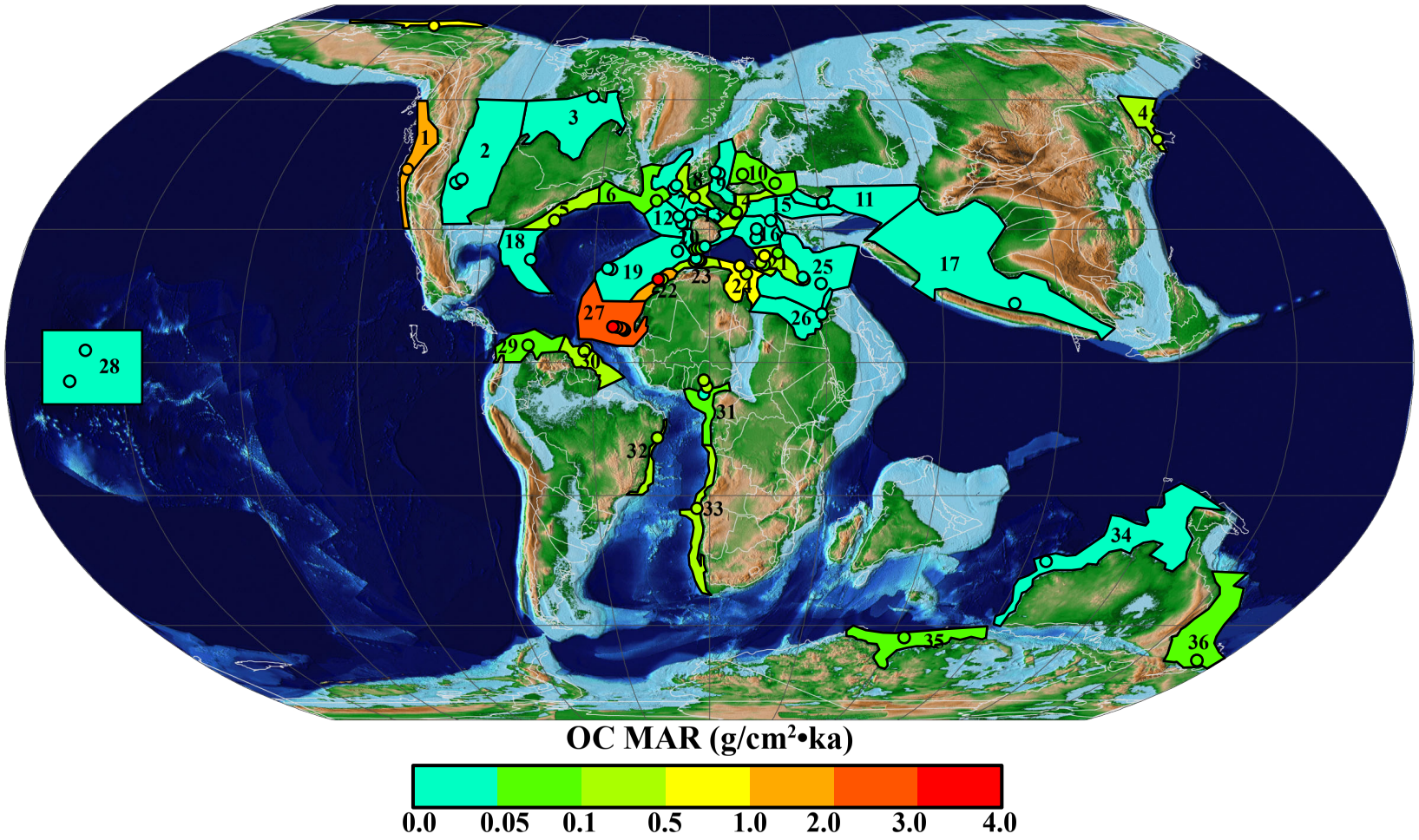

Figure 4.4.: Global distribution of all calculated OC MAR for each locality. Individual symbols represent data for an each locality and the polygons plotted encompass the average OC MAR for all localities within the polygon. The numbers for each polygon corresponds to table 2. This map from adapted from the PALEOMAP Project (Scotese, 2008).

Carbon isotope modeling

The observed carbon-isotope trends demand dramatic perturbations to the carbon cycle during OAE2. To elucidate the magnitude of the carbon isotope excursion, we constructed a forward box model as described above. In our model, we prescribed the initial boundary conditions and perturbed the burial flux of organic carbon to recreate the magnitude of the observed isotopic excursions (2 to 7‰; Fig. 4.5). The magnitude

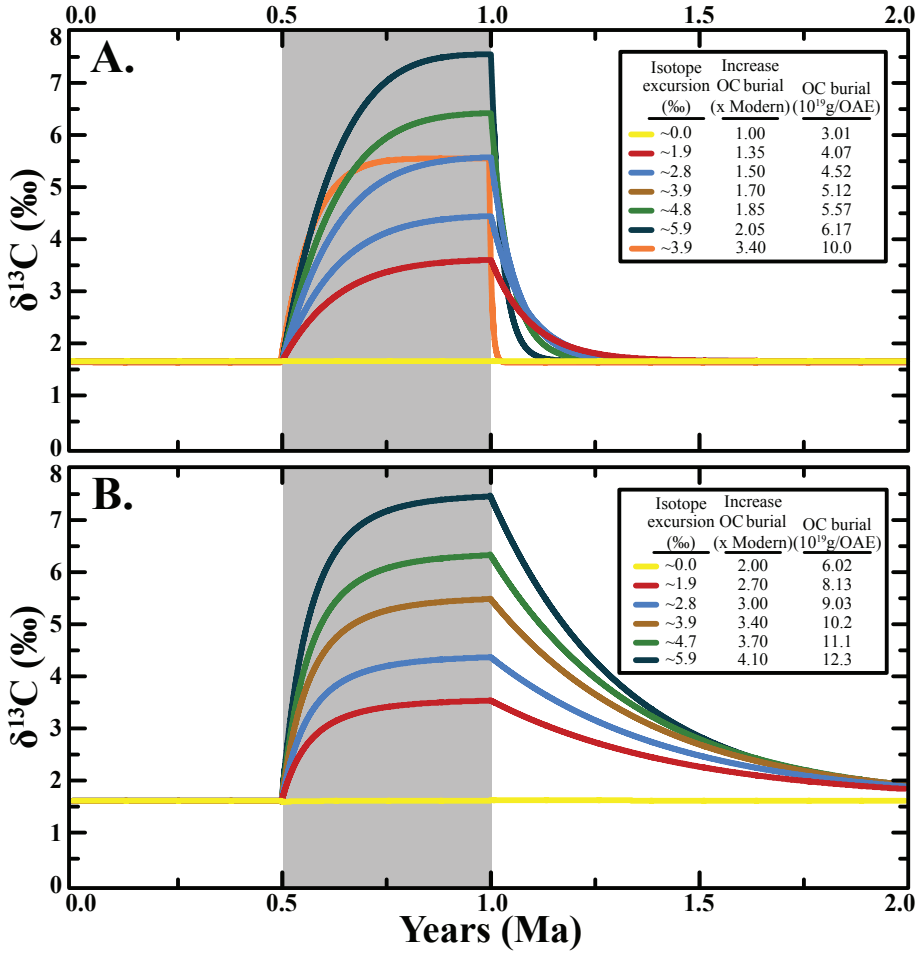

Figure 4.5: Modeled OC sensitivity test for a given positive carbon isotope excursion. Figure 4.5A demonstrates increased organic carbon burial with modern weathering fluxes, and Figure 4.5B represents a doubled weathering scenario which requires increased OC burial in order to replicate similar isotopic magnitudes from Figure 4.5A. Dashed line represents a flux values and DIC concentration from Kump and Arthur (1999) model for a high CO_2 world.

of the excursion is dictated by (1) the amount of OC buried, (2) the OC fractionation [difference between the inorganic carbon pool and the OC value] and to a lesser extent (3) the starting reservoir size (Fig. 4.6). We do not model changes in carbonate burial, as there is only a small fractionation associated with its burial (Gill et al., 2011b; Kump and Arthur, 1999; Kurtz et al., 2003). It is important to note that altering carbonate burial has a minimal affect on the isotope excursion (due to the small fractionation during burial) but does affect the reservoir size and therefore impacts the response of the system

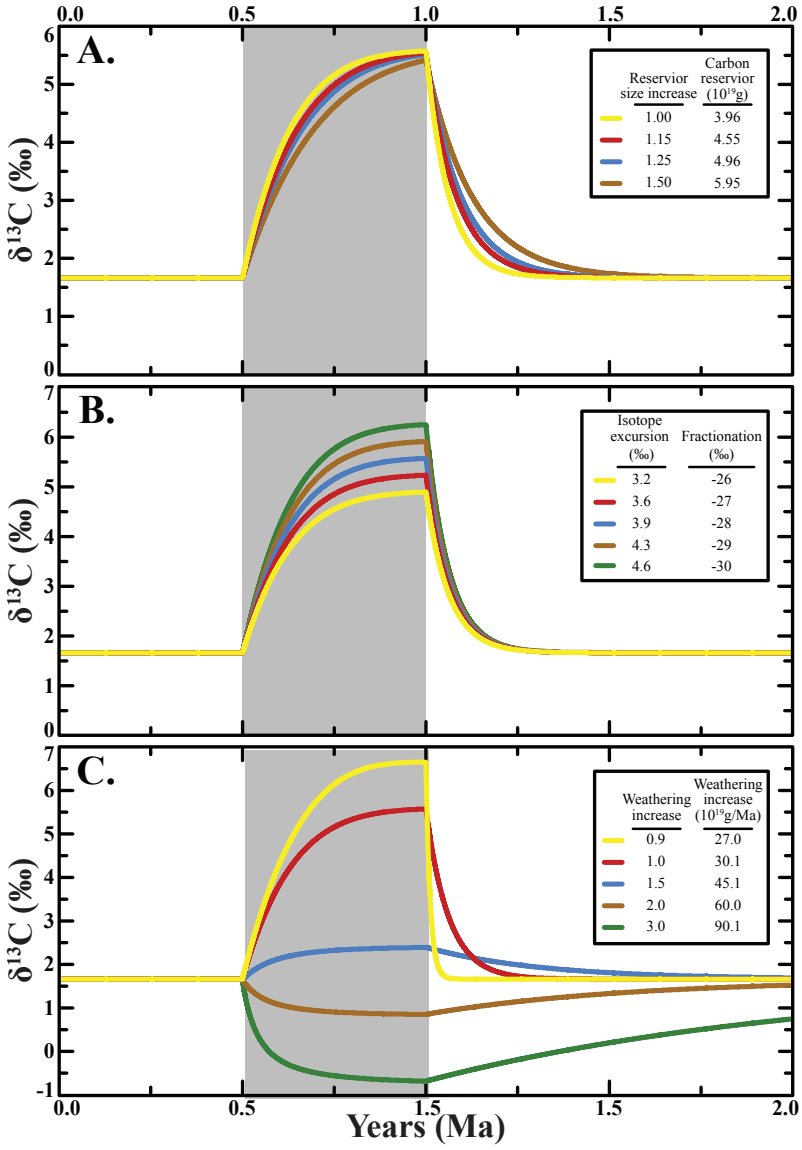

Figure 4.6: Modeled sensitivity simulations for reservoir size, OC fractionation, and weathering flux variations. Figure 4.6A documents the relatively invariant changes in carbon isotopes while increasing the reservoir size. A 4‰ variation in OC fractionation affects the magnitude of the excursion by ~1.4‰ (Fig. 4.6B). Figure 4.6C shows the dramatic affects of varying the weathering flux. Initial parameters (Table 4.1) for all simulations used modern values unless the variable was being tested.

through changing residence time, which can allow OC burial to have a larger impact on the magnitude of the excursion. Therefore, the only variable directly controlling the magnitude of the transient positive excursion is the amount of OC buried—because of its large associated fractionation. In all models presented here the carbonate burial term is held constant for all runs, and there is no fractionation assigned to its burial (similar to Kurtz et al., 2003).

To reproduce the positive excursion with modern weathering input fluxes requires enhanced OC burial. For example, a ~2‰ excursion requires 1.35 times the modern OC flux (3.01×10^{19} g; Kurtz et l., 2003), which equates to 4.07×10^{19} g of carbon burial, whereas as ~6‰ excursion requires 6.17×10^{19} g of carbon burial or 2.05 times the modern OC flux (Fig. 4.5A). Figure 4.5B considers an increased weathering flux scenario during the OAE. Specifically, the model incorporates a doubled weathering flux scenario that coincides with the onset of the OAE. In this case, to reproduce a ~2‰ excursion varying only OC burial requires 2.70 times the modern OC flux, which is 8.13×10^{19} g of

	OC MAR ($g/m^2 \cdot ka$)	Area (10^8 km^2)	OC burial during OAE (10^{19} g)	Area (%)	OC burial (%)
$Total_{accounted}$		0.47	4.04	12.99	80.52
$Margin_{unknown}$	0.030[a]	0.38	0.57	10.41	11.27
$Abyssal_{unknown}$	0.003[a]	2.78	0.41	76.80	8.21
$Total_{unknown}$		3.15	0.98	87.02	19.48
Total		3.62	5.02		
$Margin_{unknown}$	0.1716[b]	0.38	3.23		
$Margin_{modern}$	0.030[a]	0.90	2.71	25.01	90.00
$Abyssal_{modern}$	0.003[a]	2.71	0.30	75.07	10.00
$Total_{modern}$		3.61	3.01		
	[a]modern average	[b]OAE2 weighted average			

Table 4.2: Chart showing the area (km^2 and %) accounted for with the amount of unknown marginal settings and abyssal setting. The statistical data from the distribution can be compared to the modern estimates (Burdige, 2007) which are fairly similar in terms of % OC burial and area.

carbon burial, whereas a ~6‰ excursion requires 12.3 × 10^{19} g of carbon burial or 4.10 times the modern OC flux (Fig. 4.5B). This is due to the increased DIC pool and due to the relatively depleted isotope value for weathering. However, doubling carbonate burial would compensate for the increased DIC reservoir, thus keeping the system in steady-state. However, due to the limited fraction during carbonate burial, these changes have little effect on the carbon isotope excursion. We also ran a model using fluxes, doubled inputs and outputs and starting DIC values of 4.56 × 10^{19} g based on assumed very high levels of atmospheric CO_2 following from Kump and Arthur (1999). To generate the maximum carbonate-C isotope excursion of 4‰ using these fluxes requires 10 × 10^{19} g of carbon burial, which is shown by the dashed line in Figure 4.5.

Sensitivity tests were performed to assess the impact of variations for given parameter (reservoir size, fractionation and weathering flux) using our forward box-model. For all sensitivity simulations, the initial parameters are shown in Table 4.3, with the reservoir size increased at the onset of the simulations, but changes in fractionation and weathering were ascribed to the onset of the OAE. To generate the maximum carbonate-C isotope excursion of 4‰ requires a 1.7-fold increase (5.12 x 10^{19} g) of OC burial at the onset of the OAE, while holding all other parameters steady throughout the run. For all the following sensitivity tests we used a carbon burial value of 5.12 × 10^{19} g and a 1.7-fold increase in OC burial during the OAE; non-OAE intervals are assumed to bury 3.01 × 10^{19} g of carbon, equivalent to modern burial rates. Changing the initial marine reservoir (Fig. 4.6A) has minimal effect on the magnitude of the marine carbon isotope record but does change the shape of the curve. Varying the fractionation during the onset of the OAE affects the magnitude of the excursion: a -26‰ fractionation yields a 3.2‰ excursion, while a -30‰ fractionation equates to a 4.6‰ excursion (Fig 4.6B). Changes in the weathering flux dramatically affects the magnitude and shape of the

carbon isotope excursion, where a 2-fold increase in weathering can cause a 1‰ negative shift, even while burying increased OC during the event, and a decrease in weathering can amplify the positive isotope excursion (Fig. 4.6C). However, if weathering rates decrease to below 0.85 times the modern values, the burial of OC burial will completely deplete the DIC reservoir.

	Initial Marine Reservior	Weathering flux	Organic carbon burial flux	Inorganic carbon burial flux
Concentration (10^{19} g)	3.96 (4.56)	30.1 (60.2)	6.02 (12.04)	24.08 (48.16)
$\delta^{13}C$ (‰)	+1.8	-4.0	-28	-

Table 4.3: Initial parameters for the C box-model. All flux values are for Ma. The isotopic fraction imparted by inorganic carbon is negligible and is not included in this model (similar to Gill et al., 2011b; Kump and Arthur, 1999; Kurtz et al., 2003) values in parenthesis were used in the high CO_2 model for comparison (Kump and Arthur, 1999).

Discussion

Global carbon burial estimates from sediment distributions

The global distribution of TOC contents recorded during the event show a wide range of values, with some of the highest concentrations recorded in the geologic record [in excess of 45 wt% (Kuypers et al., 2002)], but the vast majority of the samples have TOC contents less than 10 wt%. Generally, the highest TOC values are located further offshore but in marginal marine settings, likely to be in upwelling areas. The distribution of sedimentation rates recorded during OAE2 also shows a large range but is consistent with estimates of modern and other ancient sedimentation (Sadler, 1981). Not surprisingly, the sedimentation rates for OAE2 are generally higher in nearshore locations and lower in deep-water abyssal plain settings far removed from riverine detrital sources.

The calculated OC MAR during the OAE is the key parameter in our investigation. Importantly, the rock density used, whether 2.4 or 2.7 g/cm^2, has little affect on the value of the OC MAR. Generally, the highest OC MARs follow the highest sedimentation rates but often with relatively low TOC contents, which suggests that these sites have not experienced low productivity and/or preservation. Instead, the low TOC contents reflect rapid dilution by detrital siliciclastics and pelagic carbonate. Conversely, the enriched TOC localities are generally sections characterized by relatively slow sedimentation, yielding OAE2 intervals that are only a few tens of cm thick, and therefore these sections preserve a relatively small amount of OC on a global scale.

OAE2 has the most extensive documented distribution of any major OC perturbation in geologic history, yet large portions of the oceans are still unknown. The majority of the data are from marginal marine settings, and even those are insufficiently known (Figs 4.2-4.4). By analogy, the modern ocean buries nearly 85% of its OC on continental margins, which are marked by high primary production and rapid sedimentation (Burdige, 2007), as well as riverine inputs of terrigenous OC. This relationship may hold true for OAE2. Importantly, our comparative approach allows us to test this assumption. The estimated OC burial from the known global distribution of OAE2 sediments and their OC contents, along with assumed OC burial using modern values for the unknown marginal marine and deep abyssal settings, equates to 5.02×10^{19} g of OC buried, which is 1.66-fold greater than estimated modern OC burial (Burdige, 2007).

Carbon isotope model

The magnitude of the carbon excursion is tied to the inputs and output. The most important factor is the amount of OC buried, followed by the weathering flux and carbon isotope fractionation linked to photosynthetic production of organic matter from DIC. The sensitivity tests illustrated by Figure 4.6 demonstrate the relative importance of the unconstrained parameters on the carbon isotope excursion—specifically, size of the reservoir, fractionation and changes in weathering inputs. Increasing the starting carbon reservoir size has little effect on the magnitude of the carbon excursion but does have a minor effect on the shape of the curve and the timing of the excursion and its return to pre-OAE values. However, these effects would be very difficult to resolve in the geologic record due to limited sampling localities, chronologic age controls and analytical resolution. The fractionation factor was held constant for Figure 4.4A in order to simplify the model, although this might be an oversimplification. Limited data suggest that the isotopic offset decreases during the event from -28‰ to -26‰ (Arthur et al., 1988; Hayes et al., 1989; Kump and Arthur, 1999). Changes in the fractionation have an effect on the magnitude of the carbon excursion and/or the amount of OC burial to achieve a given magnitude for the excursion. For example, a fractionation of -28‰ yields an excursion of 3.9‰, and a -26‰ fractionation produces a 3.2‰ excursion—while holding all other parameters equal. Any change in the isotope fractionation during the event could be due to decreased atmospheric CO_2 linked to increased OC burial (Arthur et al., 1988) or changes in ecological communities. Ecological shifts could change the global isotope fractionation during the event (Hayes et al., 1989), but it is unclear if and how these changes are expressed during OAE2. A decrease in the fractionation factor would require an increase in OC burial to produce the same magnitude carbon isotope excursion.

Comparison of methods

Our two methods both yield estimates for the amount of OC burial during OAE2. The global estimates of the known/extrapolated OC burial coupled with estimated OC burial for the unknown portions of the ocean can account for 5.02×10^{19} g of C during the OAE. To produce the observed ~4‰ carbonate isotope excursion the model requires 5.12×10^{19} g of C using modern fluxes or 10.0×10^{19} g of C for a high CO_2 world. Therefore, either the 'mapped' distribution accounts for all the OC burial or there could be a 'missing' OC sink. Importantly, the estimated (known and assumed) OC burial distribution may account for the total carbon excursion but depends highly on the modeled fluxes. Increased weathering, changes in fractionation, an increased initial DIC reservoir and increased fluxes (from Kump and Arthur, 1999) would require greater amounts of carbon burial to account for the observed carbon isotopic excursion.

Based on the modeling and our understanding of the OAE localities, it is likely that unknown portions of the OAE2 ocean will have high TOC and possibly high OC MAR, but these environments could be mostly restricted to marginal marine settings and equatorial upwelling regions. If the unknown marginal marine settings buried OC at a similar rate to the known values during the OAE (the known weighted average MAR is 0.17 g/cm^2·ka), then an additional 3.23×10^{19} g of carbon would be buried. This would allow for a total of 7.68×10^{19} g of carbon. Therefore, to attain a 4‰ carbonate-C isotope excursion using the high CO_2 world values, the unknown marginal marine settings could account for a portion of the needed OC burial increase—but cannot account for the entire burial required under an enhanced weathering scenario (or generally high fluxes in a high CO_2 world). If there was an increased DIC reservoir, enhanced weathering or high CO_2, either the abyssal plains would have to bury more OC (from the modern value of 0.003 g/cm^2·ka to 0.015 g/cm^2·ka) or the unknown but highly productive marginal marine settings

would have to be nearly doubled in their area (0.38×10^8 km^2 to 0.70×10^8 km^2) using the known weighted MAR during the OAE. Increasing the marginal marine OC MAR seems more plausible, as there is evidence for high TOC burial in the highly productive regions of the equatorial upwelling zones which is not included in estimated unknown marginal marine settings. An increase in OC MAR may not only be manifested as 'organic-rich shale'—as a function of bulk sedimentation rate.

Conclusions

Understanding the global distribution of OC burial during OAE2, the best documented carbon burial event in Earth's history, is important for many reasons, including insight into the full redox landscape of a greenhouse ocean and associated patterns of primary production in that ocean. Using two methods, sediment mapping and forward box-modeling, has illuminated the known global distributions with reasonable extrapolations and using modern OC burial fluxes for the unknown portion of the ocean during OAE2 can account for most of the OC burial using modern carbon fluxes. While the global distribution only accounts for a small portion of the ocean (~13% area), it can account for 4.04×10^{19} g of carbon burial, and extrapolating the relatively low OC burial rates of the modern ocean for the unknown portion (87% area) of the ocean can account for another 0.98×10^{19} g of carbon, which combined provides a 4‰ excursion. Therefore the 'mapped' distribution and estimated OC burial can account for most of the OC buried during OAE2 provided the weathering fluxes were relatively similar to the modern value. However, an increased weathering flux, which is likely as suggested by multiple proxy data, would require a substantial increase in the OC burial flux to compensate for the isotopic impact of the weathering flux. This consideration inherently includes increased

volcanic CO_2 emissions due to increased seafloor spreading rates because weathering and volcanic fluxes have been lumped together. It is likely that any increase in OC burial for the unknown portions of the oceans was associated with continental margins and possibly the equatorial Pacific, which are highly productive and bury substantial OC in the modern ocean. The modern abyssal equatorial regions are highly productive but ineffective OC sinks due to oxygen exposure time (Hartnett et al., 1998; Jahnke, 1996), but burial there might have been enhanced in the past under lower oxygen conditions.

Our mapping exercise confirms the importance of sedimentation rate. There are several localities with relatively low TOC contents during the OAE but because of their high accumulation rates are burying large quantities of OC. Importantly, our map of high OAE OC MAR roughly mimics the modern patterns of organic production and burial of OC in the ocean, suggesting that OAE2 was an exacerbation of modern controls on these parameters. In the face of enhanced weathering fluxes, our results predict other sites of high OC MAR, such as marginal sites in the Pacific.

Understanding the global dynamics of the OC burial event during OAE2 is key to interpreting the mechanisms that underlie the event, including the global redox state of the ocean and associated nutrient cycles and feedback. For example, increased carbon burial generally facilitates increased burial of reduced sulfur species (pyrite), which has been documented using sulfur isotopes (Adams et al., 2010; Ohkouchi et al., 1999; Owens et al., in review-a). Iodine/calcium ratios show a decrease leading into and during the OAE, which suggest a global increase of anoxic conditions and associated carbon burial, consistent with the $\delta^{13}C$ data (Lu et al., 2010). Further, bio-essential trace-elements (Mo, V, Cr and Zn) are drawn down during the event (Algeo and Rowe, 2011; Hetzel et al., 2009). The spread of low-oxygen, anoxic and euxinic conditions in the ocean and associated burial of organic matter can deplete the marine inventory in these metals, as

has been proposed for OAE2, the Toarcian OAE and the Proterozoic (Algeo, 2004; Algeo and Rowe, 2011; Anbar and Knoll, 2002; Gill et al., 2011a; Gill et al., 2011b; Hetzel et al., 2009; Owens et al., in review-b; Reinhard et al., 2013; Sahoo et al., 2012; Scott et al., 2008), with profound implications for ecological and extinction patterns in those oceans—and possibly in our currently warming ocean.

References

Adams, D.D., Hurtgen, M.T., Sageman, B.B., 2010. Volcanic triggering of a biogeochemical cascade during Oceanic Anoxic Event 2. Nature Geoscience 3, 201–204.

Algeo, T.J., 2004. Can marine anoxic events draw down the trace element inventory of seawater? Geology 32, 1057–1060.

Algeo, T.J., Rowe, H., 2011. Paleoceanographic applications of trace-metal concentration data. Chemical Geology 324-325, 6–18.

Anbar, A.D., Knoll, A.H., 2002. Proterozoic ocean chemistry and evolution: A bioinorganic bridge? Nature 297, 1137–1142.

Arthur, M.A., Dean, W.E., Pratt, L.M., 1988. Geochemical and climatic effects of increased marine organic carbon burial at the Cenomanian/Turonian boundary. Nature 335, 714–717.

Arthur, M.A., Schlanger, S.O., Jenkyns, H.C., 1987. The Cenomanian-Turonian Oceanic Anoxic Event, II. Palaeoceanographic controls on organic-matter production and preservation. Geological Society, London, Special Publications 26, 401–420.

Barclay, R.S., McElwain, J.C., Sageman, B.B., 2010. Carbon sequestration activated by a volcanic CO2 pulse during Ocean Anoxic Event 2. Nature Geoscience 3, 205–208.

Barron, E.J., 1983. A warm, equable Cretaceous: The nature of the problem. Earth-Science Reviews 19, 305–338.

Bellenger, J.P., Wichard, T., Xu, Y., Kraepiel, A.M.L., 2011. Essential metals for nitrogen fixation in a free-living N2-fixing bacterium: chelation, homeostasis and high use efficiency. Environmental Microbiology 13, 1395–1411.

Berner, R.A., 2006. GEOCARBSULF: A combined model for Phanerozoic atmospheric O2 and CO2. Geochimica et Cosmochimica Acta: A Special Issue Dedicated to Robert A. Berner 70, 5653–5664.

Berner, R.A., Canfield, D.E., 1989. A new model for atmospheric oxygen over Phanerozoic time. American Journal of Science 289, 333–361.

Bjerrum, C.J., Bendtsen, J., Legarth, J.J.F., 2006. Modeling organic carbon burial during sea level rise with reference to the Cretaceous. Geochemistry, Geophysics, Geosystems 7, Q05008.

Blättler, C.L., Jenkyns, H.C., Reynard, L.M., Henderson, G.M., 2011. Significant increases in global weathering during Oceanic Anoxic Events 1a and 2 indicated by

calcium isotopes. Earth and Planetary Science Letters 309, 77–88.

Blumenberg, M., Wiese, F., 2012. Imbalanced nutrients as triggers for black shale formation in a shallow shelf setting during the OAE 2 (Wunstorf, Germany). Biogeosciences Discuss 9, 5373–5413.

Brumsack, H.-J., 2006. The trace metal content of recent organic carbon-rich sediments: Implications for Cretaceous black shale formation. Palaeogeography, Palaeoclimatology, Palaeoecology 232, 344–361.

Burdige, D.J., 2007. Preservation of Organic Matter in Marine Sediments: Controls, Mechanisms, and an Imbalance in Sediment Organic Carbon Budgets? Chemical Reviews 107, 467–485.

Charette, M.A., Smith, W.H.F., 2010. The volume of Earth's ocean. Oceanography 23, 112-114.

Erbacher, J., Friedrich, O., Wilson, P.A., Birch, H., Mutterlose, J., 2005. Stable organic carbon isotope stratigraphy across Oceanic Anoxic Event 2 of Demerara Rise, western tropical Atlantic. Geochemistry, Geophysics, Geosystems 6, Q06010.

Flögel, S., Wallmann, K., Poulsen, C.J., Zhou, J., Oschlies, A., Voigt, S., Kuhnt, W., 2011. Simulating the biogeochemical effects of volcanic CO2 degassing on the oxygen-state of the deep ocean during the Cenomanian/Turonian Anoxic Event (OAE2). Earth and Planetary Science Letters 305, 371–384.

Forster, A., Schouten, S., Moriya, K., Wilson, P.A., Sinninghe Damsté, J.S., 2007. Tropical warming and intermittent cooling during the Cenomanian/Turonian oceanic anoxic event 2: Sea surface temperature records from the equatorial Atlantic. Paleoceanography 22, PA1219.

Gill, B.C., Lyons, T.W., Jenkyns, H.C., 2011a. A global perturbation to the sulfur cycle during the Toarcian Oceanic Anoxic Event. Earth and Planetary Science Letters 312, 484–496.

Gill, B.C., Lyons, T.W., Young, S.A., Kump, L.R., Knoll, A.H., Saltzman, M.R., 2011b. Geochemical evidence for widespread euxinia in the Later Cambrian ocean. Nature 469, 80–83.

Haq, B.U., Hardenbol, J.A.N., Vail, P.R., 1987. Chronology of Fluctuating Sea Levels Since the Triassic. Science 235, 1156–1167.

Hartnett, H.E., Keil, R.G., Hedges, J.I., Decvol, A.H., 1998. Influence of oxygen exposure time on organic carbon preservation in continental margin sediments. Nature 391, 572–575.

Hasegawa, T., 1997. Cenomanian-Turonian carbon isotope events recorded in terrestrial organic matter from northern Japan. Palaeogeography, Palaeoclimatology, Palaeoecology 130, 251–273.

Hasegawa, T., Crampton, J.S., Schiøler, P., Field, B., Fukushi, K., Kakizaki, Y., 2013. Carbon isotope stratigraphy and depositional oxia through Cenomanian/Turonian boundary sequences (Upper Cretaceous) in New Zealand. Cretaceous Research 40, 61–80.

Hayes, J.M., Popp, B.N., Takigiku, R., Johnson, M.W., 1989. An isotopic study of biogeochemical relationships between carbonates and organic carbon in the Greenhorn Formation. Geochimica et Cosmochimica Acta 53, 2961-2972.

Hayes, J.M., Strauss, H., Kaufman, A.J., 1999. The abundance of 13C in marine organic matter and isotopic fractionation in the global biogeochemical cycle of carbon during the past 800 Ma. Chemical Geology 161, 103–125.

Henrichs, S.M., Reeburgh, W.S., 1987. Anaerobic mineralization of marine sediment organic matter: Rates and the role of anaerobic processes in the oceanic carbon economy. Geomicrobiology Journal 5, 191–237.

Hetzel, A., Böttcher, M.E., Wortmann, U.G., Brumsack, H.-J., 2009. Paleo-redox conditions during OAE 2 reflected in Demerara Rise sediment geochemistry (ODP Leg 207). Palaeogeography, Palaeoclimatology, Palaeoecology 273, 302–328.

Hetzel, A., März, C., Vogt, C., Brumsack, H.-J., 2011. Geochemical environment of Cenomanian - Turonian black shale deposition at Wunstorf (northern Germany). Cretaceous Research 32, 480–494.

Huber, B.T., Hodell, D.A., Hamilton, C.P., 1995. Middle-Late Cretaceous climate of the southern high latitudes: Stable isotopic evidence for minimal equator-to-pole thermal gradients. Geological Society of America Bulletin 107, 1164–1191.

Jahnke, R.A., 1996. The global ocean flux of particulate organic carbon: Areal distribution and magnitude. Global Biogeochemical Cycles 10, 71–88.

Jarvis, I., Gale, A.S., Jenkyns, H.C., Pearce, M.A., 2006. Secular variation in Late Cretaceous carbon isotopes: a new Campanian (99.6-70.6 Ma). Geological Magazine 143, 561–608.

Jarvis, I., Lignum, J.S., Gröcke, D.R., Jenkyns, H.C., Pearce, M.A., 2011. Black shale deposition, atmospheric CO_2 drawdown, and cooling during the Cenomanian-Turonian Oceanic Anoxic Event. Paleoceanography 26, PA3201.

Jarvis, I.A.N., Murphy, A.M., Gale, A.S., 2001. Geochemistry of pelagic and hemipelagic carbonates: criteria for identifying systems tracts and sea-level change. Journal of the Geological Society 158, 685–696.

Jenkyns, H.C., 2010. Geochemistry of oceanic anoxic events. Geochemistry, Geophysics, Geosystems 11, Q03004.

Jenkyns, H.C., Forster, A., Schouten, S., Sinninghe Damsté, J.S., 2004. High temperatures in the Late Cretaceous Arctic Ocean. Nature 432, 888–892.

Jenkyns, H.C., Gale, A.S., Corfield, R.M., 1994. Carbon- and oxygen-isotope stratigraphy of the English Chalk and Italian Scaglia and its palaeoclimatic significance. Geological Magazine 131, 1–34.

Jenkyns, H.C., Schouten-Huibers, L., Schouten, S., Sinninghe Damsté, J.S., 2012. Warm Middle Jurassic–Early Cretaceous high-latitude sea-surface temperatures from the Southern Ocean. Climate of the Past 8, 215–226.

Jones, C.E., Jenkyns, H.C., 2001. Seawater Strontium Isotopes, Oceanic Anoxic Events, and Seafloor Hydrothermal Activity in the Jurassic and Cretaceous. American Journal of Science 301, 112–149.

Kerr, A.C., 1998. Oceanic plateau formation: a cause of mass extinction and black shale deposition around the Cenomanian-Turonian boundary. J. Geol. Soc. Lond. 155, 619-626.

Kraal, P., Slomp, C.P., Forster, A., Kuypers, M.M.M., 2010. Phosphorus cycling from the margin to abyssal depths in the proto-Atlantic during oceanic anoxic event 2. Palaeogeography, Palaeoclimatology, Palaeoecology 295, 42–54.

Kuhnt, W., Luderer, F., Nederbragt, S., Thurow, J., Wagner, T., 2005. Orbital-scale record of the late Cenomanian-Turonian oceanic anoxic event (OAE-2) in the Tarfaya Basin (Morocco). International Journal of Earth Sciences 94, 147–159.

Kump, L.R., Arthur, M.A., 1999. Interpreting carbon-isotope excursions; carbonates and organic matter. Chemical Geology 161, 181–198.

Kuroda, J., Ogawa, N.O., Tanimizu, M., Coffin, M.F., Tokuyama, H., Kitazato, H., Ohkouchi, N., 2007. Contemporaneous massive subaerial volcanism and late cretaceous Oceanic Anoxic Event 2. Earth and Planetary Science Letters 256, 211–223.

Kuroda, J., Ohkouchi, N., 2006. Implication of spatiotemporal distribution of black shales deposited during the Cretaceous Oceanic Anoxic Event-2. Paleontological Research 10, 345–358.

Kurtz, A.C., Kump, L.R., Arthur, M.A., Zachos, J.C., Paytan, A., 2003. Early Cenozoic decoupling of the global carbon and sulfur cycles. Paleoceanography 18, 1090.

Kuypers, M.M.M., Pancost, R.D., Nijenhuis, I.A., Sinninghe Damsté, J.S., 2002. Enhanced productivity led to increased organic carbon burial in the euxinic North Atlantic basin during the late Cenomanian oceanic anoxic event. Paleoceanography 17.

Lu, Z., Jenkyns, H.C., Rickaby, R.E.M., 2010. Iodine to calcium ratios in marine carbonate as a paleo-redox proxy during oceanic anoxic events. Geology 38, 1107–1110.

Menard, H.W., Smith, S.M., 1966. Hypsometry of ocean basin provinces. Journal of Geophysical Research 71, 4305–4325.

Monteiro, F.M., Pancost, R.D., Ridgwell, A., Donnadieu, Y., 2012. Nutrients as the dominant control on the spread of anoxia and euxinia across the Cenomanian-Turonian oceanic anoxic event (OAE2): Model-data comparison. Paleoceanography 27, PA4209.

Montoya-Pino, C., Weyer, S., Anbar, A.D., Pross, J., Oschmann, W., van de Schootbrugge, B., Arz, H.W., 2010. Global enhancement of ocean anoxia during Oceanic Anoxic Event 2: A quantitative approach using U isotopes. Geology 38, 315–318.

Mort, H.P., Adatte, T., Keller, G., Bartels, D., Föllmi, K.B., Steinmann, P., Berner, Z., Chellai, E.H., 2008. Organic carbon deposition and phosphorus accumulation during Oceanic Anoxic Event 2 in Tarfaya, Morocco. Cretaceous Research 29, 1008–1023.

Nederbragt, A.J., Fiorentino, A., 1999. Stratigraphy and palaeoceanography of the Cenomanian-Turonian Boundary Event in Oued Mellegue, north-western Tunisia. Cretaceous Research 20, 47–62.

Ohkouchi, N., Kawamura, K., Kajiwara, Y., Wada, E., Okada, M., Kanamatsu, T., Taira, A., 1999. Sulfur isotope records around Livello Bonarelli (northern Apennines, Italy) black shale at the Cenomanian-Turonian boundary. Geology 27, 535–538.

Owens, J.D., Gill, B.C., Jenkyns, H.C., Bates, S.M., Severmann, S., Kuypers, M.M.M., Woodfine, R.G., Lyons, T.W., in review-a. Sulfur isotopes track the global extent and dynamics of euxinia during Cretaceous Oceanic Anoxic Event 2 Proceedings of the National Academy of Sciences.

Owens, J.D., Lyons, T.W., Li, X., Macleod, K.G., Gordon, G., Kuypers, M.M.M., Anbar, A., Kuhnt, W., Severmann, S., 2012. Iron isotope and trace metal records of iron cycling in the proto-North Atlantic during the Cenomanian-Turonian oceanic anoxic event (OAE-2). Paleoceanography 27, PA3223.

Owens, J.D., Reinhard, C.T., Rohrssen, M., Love, G.D., Lyons, T.W., in review-b. Marine trace-metal drawdown during the Cenomanian-Turonian Boundary Event (OAE2): implication for global redox and biological perturbation. Nature.

Ozaki, K., Tajima, S., Tajika, E., 2011. Conditions required for oceanic anoxia/euxinia: Constraints from a one-dimensional ocean biogeochemical cycle model. Earth and Planetary Science Letters 304, 270–279.

Pancost, R.D., Crawford, N., Magness, S., Turner, A., Jenkyns, H.C., Maxwell, J.R., 2004. Further evidence for the development of photic-zone euxinic conditions during Mesozoic oceanic anoxic events. Journal of the Geological Society 161, 353–364.

Pearce, M.A., Jarvis, I., Tocher, B.A., 2009. The Cenomanian-Turonian boundary event, OAE2 and palaeoenvironmental change in epicontinental seas: New insights from the dinocyst and geochemical records. Palaeogeography, Palaeoclimatology, Palaeoecology 280, 207–234.

Reinhard, C.T., Planavsky, N.J., Robbins, L.J., Partin, C.A., Gill, B.C., Lalonde, S.V., Bekker, A., Konhauser, K.O., Lyons, T.W., 2013. Proterozoic ocean redox and biogeochemical stasis. Proceedings of the National Academy of Sciences.

Ronov, A.B., 1976. Global carbon geochemistry, volcanism, carbonate accumulation, and life [Translation of Geokhimiya] Geochemistry International 13, 172–195.

Sadler, P.M., 1981. Sediment Accumulation Rates and the Completeness of Stratigraphic Sections. The Journal of Geology 89, 569–584.

Sageman, B.B., Meyers, S.R., Arthur, M.A., 2006. Orbital time scale and new C-isotope record for Cenomanian-Turonian boundary stratotype. Geology 34, 125–128.

Sahoo, S.K., Planavsky, N.J., Kendall, B., Wang, X., Shi, X., Scott, C., Anbar, A.D., Lyons, T.W., Jiang, G., 2012. Ocean oxygenation in the wake of the Marinoan glaciation. Nature 489, 546–549.

Schlanger, S.O., Arthur, M.A., Jenkyns, H.C., Scholle, P.A., 1987. The Cenomanian-Turonian Oceanic Anoxic Event, I. Stratigraphy and distribution of organic carbon-rich beds and the marine δ13C excursion, in Marine Petroleum Source Rocks, edited by J. Brooks and A. J. Fleet. Geological Society, London, Special Publications 26, 371–399.

Schlanger, S.O., Jenkyns, H.C., 1976. Cretaceous anoxic events: causes and consequences. Geologie en Mijnbouw 55, 179–184.

Scholle, P.A., Arthur, M.A., 1980. Carbon isotope fluctuations in Cretaceous pelagic limestones; potential stratigraphic and petroleum exploration tool. AAPG Bulletin 64, 67–87.

Scotese, C.R., 2008. The PALEOMAP Project PaleoAtlas for ArcGIS, Volume 2. Cretaceous Paleogeographic and Plate Rectonic Reconstructions, PALEOMAP Project.

Scott, C., Lyons, T.W., Bekker, A., Shen, Y., Poulton, S.W., Chu, X., Anbar, A.D., 2008. Tracing the stepwise oxygenation of the Proterozoic ocean. Nature 452, 456–459.

Sinninghe Damsté, J.S., Köster, J., 1998. A euxinic southern North Atlantic Ocean during the Cenomanian/Turonian oceanic anoxic event. Earth and Planetary Science Letters 158, 165–173.

Snow, L.J., Duncan, R.A., Bralower, T.J., 2005. Trace element abundances in the Rock Canyon Anticline, Pueblo, Colorado, marine sedimentary section and their relationship to Caribbean plateau construction and oxygen anoxic event 2. Paleoceanography 20, PA3005.

Takashima, R., Nishi, H., Huber, B.T., Leckie, M., 2006. Greenhouse World and the Mesozoic Ocean. Oceanography 19, 82–92.

Takashima, R., Nishi, H., Yamanaka, T., Tomosugi, T., Fernando, A.G., Tanabe, K., Moriya, K., Kawabe, F., Hayashi, K., 2011. Prevailing oxic environments in the Pacific Ocean during the mid-Cretaceous Oceanic Anoxic Event 2. Nature Communications 2, 234.

Trabucho Alexandre, J., Tuenter, E., Henstra, G.A., van der Zwan, K.J., van de Wal, R.S.W., Dijkstra, H.A., de Boer, P.L., 2010. The mid-Cretaceous North Atlantic nutrient trap: Black shales and OAEs. Paleoceanography 25, PA4201.

Tsikos, H., Jenkyns, H.C., Walsworth-Bell, B., Petrizzo, M.R., Forster, A., Kolonic, S., Erba, E., Premoli Silva, I., Baas, M., Wagner, T., Sinninghe Damsté, J.S., 2004. Carbon-isotope stratigraphy recorded by the Cenomanian–Turonian Oceanic Anoxic Event: correlation and implications based on three key localities. Journal of the Geological Society 161, 711–719.

Turgeon, S., Brumsack, H.-J., 2006. Anoxic vs dysoxic events reflected in sediment geochemistry during the Cenomanian-Turonian Boundary Event (Cretaceous) in the Umbria-Marche Basin of central Italy. Chemical Geology 234, 321–339.

Turgeon, S.C., Creaser, R.A., 2008. Cretaceous oceanic anoxic event 2 triggered by a massive magmatic episode. Nature 454, 323–326.

van Bentum, E.C., Hetzel, A., Brumsack, H.-J., Forster, A., Reichart, G.-J., Sinninghe Damsté, J.S., 2009. Reconstruction of water column anoxia in the equatorial Atlantic during the Cenomania-Turonian oceanic anoxic event using biomarker and trace metal proxies. Palaeogeography, Palaeoclimatology, Palaeoecology 280, 489–498.

van Bentum, E.C., Reichart, G.-J., Forster, A., Sinninghe Damsté, J.S., 2012. Latitudinal differences in the amplitude of the OAE-2 carbon isotopic excursion: pCO2 and paleo productivity. Biogeosciences 9, 717–731.

Van Cappellen, P., Ingall, E.D., 1994. Benthic Phosphorus Regeneration, Net Primary Production, and Ocean Anoxia: A Model of the Coupled Marine Biogeochemical Cycles of Carbon and Phosphorus. Paleoceanography 9, 677–692.

Voigt, S., Erbacher, J., Mutterlose, J., Weiss, W., Westerhold, T., Wiese, F., Wilmsen, M., Wonik, T., 2008. The Cenomanian Turonian of the Wunstorf section (North Germany): global stratigraphic reference section and new orbital time scale for Oceanic Anoxic Event 2. Newsletters on Stratigraphy 43, 65–89.

Wang, C.S., Hu, X.M., Jansa, L., Wan, X.Q., Tao, R., 2001. The Cenomanian-Turonian anoxic event in southern Tibet. Cretaceous Research 22, 481–490.

Wortmann, U.G., Chernyavsky, B.M., 2007. Effect of evaporite deposition on Early Cretaceous carbon and sulphur cycling. Nature 446, 654–656.

Chapter 5

Anoxia preceding euxinic condition during the Cenomanian-Turonian Boundary Event (OAE2) in carbonates and shales in central Italy (Furlo)

Abstract

It is important to identify the interplay between climate and biotic feedbacks during periods of widespread organic-carbon deposition by understanding local redox conditions and their relationships with the global redox state of the ocean. We do this by using multiple geochemical proxies distributed among diverse lithofacies. The Mesozoic Era is characterized by numerous episodes of widespread organic-carbon deposition and coeval carbon-isotope excursions, many regarded as oceanic anoxic events (OAEs) due to their ocean-scale if not global extents. The Cenomanian-Turonian boundary event (~93.9 Ma, OAE2) in the Marche-Umbria region of central Italy was the first of these events to be described by Bonarelli (1891), and so it is referred to as 'Livello Bonarelli.' Here we present data from the type Italian locality, Furlo, which shows carbonates and organic-rich levels prior to the organic deposition of the OAE, with carbonate deposition following the OAE. Iron speciation for organic-rich intervals implies a redox shift going into the OAE, with anoxia preceding the OAE leading to euxinia (i.e., anoxic and sulfidic bottom waters) at the onset of the OAE, which is corroborated by the trace metal geochemistry. Enrichments for chromium and vanadium are elevated prior to the OAE, suggesting anoxia, but decrease during the OAE. We attribute the pre-event enrichments to initial expansion of reducing conditions prior to the OAE as a precursor to the event. The greater expanse of anoxia and euxinia during the OAE had the effect of drawing down the marine inventories for both metals. Molybdenum, a reliable euxinic indicator, shows only small enrichments prior to the OAE because of the lack of local euxina and enrichments of up to ~40 ppm during the euxinic interval of the OAE. The Mo enrichments during the OAE are muted compared to many modern and ancient euxinic settings, which is likely due to the enhanced global burial of Mo in widespread euxinic settings during the event. Expanded euxinia during the event is further supported by a ~6‰ isotope excursion recorded in carbonate-associate-

sulfate (CAS) driven by enhanced pyrite burial. However, the observed trend in I/Ca ratio in carbonate lithologies were generally low proceeding the OAE and increase following the OAE which reflects a local oxygen deficient surface ocean. Importantly, values prior to the OAE suggest low but non-zero oxygen and increase post-OAE. Therefore, the geochemical data suggest oscillating anoxic to suboxic conditions preceding the OAE at this locality.

Introduction

The Bonarelli Level or Cenomanian-Turonian boundary event (OAE2) is well exposed at Furlo Gorge in central Italy (Fig. 5.1), with a nearly 20 m-thick succession containing limestone and black shale, including a ~1 m-thick black shale representing the local expression of the OAE. The Cretaceous was punctuated by severe global climatic turbulence marked by numerous widespread episodes of organic-rich deposition (Schlanger and Jenkyns, 1976). These global OAEs record large coeval positive carbon isotope excursions attributed to enhanced burial of organic carbon (Arthur et al., 1988; Schlanger et al., 1987; Scholle and Arthur, 1980). The largest and most widespread of these events is OAE2 (Kuroda and Ohkouchi, 2006; Schlanger et al., 1987; Takashima et al., 2006), marked by elevated temperatures (Huber et al., 1995; Jarvis et al., 2011; Jenkyns et al., 2004; Jenkyns et al., 2012), elevated CO_2 (Berner, 2006; Takashima et al., 2006), high sea level (Haq et al., 1987; Jarvis et al., 2001), enhanced phosphorus regeneration/recycling (Kraal et al., 2010; Mort et al., 2008; Nederbragt and Fiorentino, 1999; Van Cappellen and Ingall, 1994), and high levels of hydrothermal activity (Jones and Jenkyns, 2001; MacLeod et al., 2008; Snow et al., 2005) and continental weathering (Blättler et al., 2011; Blumenberg and Wiese, 2012; Jones and Jenkyns, 2001; Pogge von Strandmann et al., 2013).

Understanding the initiation, duration, and termination mechanism(s) for these short-lived events [500 thousand year; (Kuhnt et al., 2005; Sageman et al., 2006; Voigt et al., 2008)] and similar organic-carbon burial events throughout Earth history has been a major priority toward an understanding of climate forcing and biological feedbacks during biotic extinction events (Raup and Sepkoski, 1986). There is increasing evidence for anoxic and euxinic conditions during OAE2 based on multiple geochemical proxies for local bottom water anoxia and euxinia (Brumsack, 2006; Hetzel et al., 2011; Lu et al., 2010; Owens et al., 2012; Pearce et al., 2009; Turgeon and Brumsack, 2006; van Bentum et al., 2009), as well as evidence for sulfide penetrating into the photic zone (Kuypers et al., 2002; Pancost et al., 2004; Sinninghe Damsté and Köster, 1998; van Bentum et al., 2009). By contrast, the global redox conditions proceeding and subsequent to the OAE remains ambiguous, although the observed extinctions of radiolaria begin prior to the OAE. Similarly, other genera decline during the OAE, which has been attributed to an expansion of anoxic and sulfidic conditions toxic to life (Leckie et al., 2002; Snow et al., 2005).

Recent model estimates suggest 50% (by volume) of the global ocean was anoxic (Monteiro et al., 2012), and a recent sulfur isotope-based estimate places ~5% of the seafloor under euxinic waters (Owens et al., in review-a). Most of the available direct evidence for local bottom water redox conditions has been limited to the proto-Atlantic and Tethys oceans, with the Pacific, Indian, Southern and Arctic Oceans remaining largely unconstrained. Increased organic carbon burial during OAE2 is attributed to enhanced productivity and/or increased preservation under oxygen-deficient conditions (Kuypers et al., 2002). To sustain high levels of productivity and export of organic carbon requires enhanced delivery and/or efficient recycling of major nutrients (e.g., N and P) and other bio-essential elements (Fe and other trace metals) with effective transport

to the surface ocean. Possible delivery mechanisms include increased hydrothermal activity, continental weathering, and phosphorus recycling due to increased anoxia. The availability of marine trace metals are important for nitrogen fixation (Fe, Mo and V; Bellenger et al., 2011) and thus play an integral role in controlling primary production. The dataset presented here combines several geochemical redox proxies from both shales and carbonates to provide insight into the local redox conditions prior to, during, and subsequent to the OAE and to shed light on the global redox landscape during this event.

Materials and methods

Geologic Setting

This study focused on sediments from the Umbria region of Italy near the town of Furlo (Fig. 5.1)—specifically, near a retired quarry located approximately 25 km SE of Urbino. The Bonarelli or OAE2 is punctuated by a 110 cm-thick laminated organic-rich intervals and thin radiolarian sands (Jenkyns et al., 2007; Lanci et al., 2010; Mort et al., 2007; Turgeon and Brumsack, 2006). We sampled carbonates and organic-rich facies extending ~12.5 m below the base of the OAE. Below the OAE, the section consists of rhythmic layers or couplets of alternating light grey micritic limestone, black chert, and black organic-rich shales (Lanci et al., 2010). The samples were collected in the middle of a particular facies to avoid any gradational redox affect associated with the neighboring lithology, but generally the boundaries were sharp and distinct. For this study we avoided the chert-dominated layers, which are not well suited to our proxy approaches. Five carbonate samples were collected above the upper most portion of the organic-rich horizon over an interval of ~4 m organic rich interval. Weathered surfaces

were avoided for all samples collected, especially the carbonate-lean intervals of shale intervals to minimize any post-depositional weathering effects.

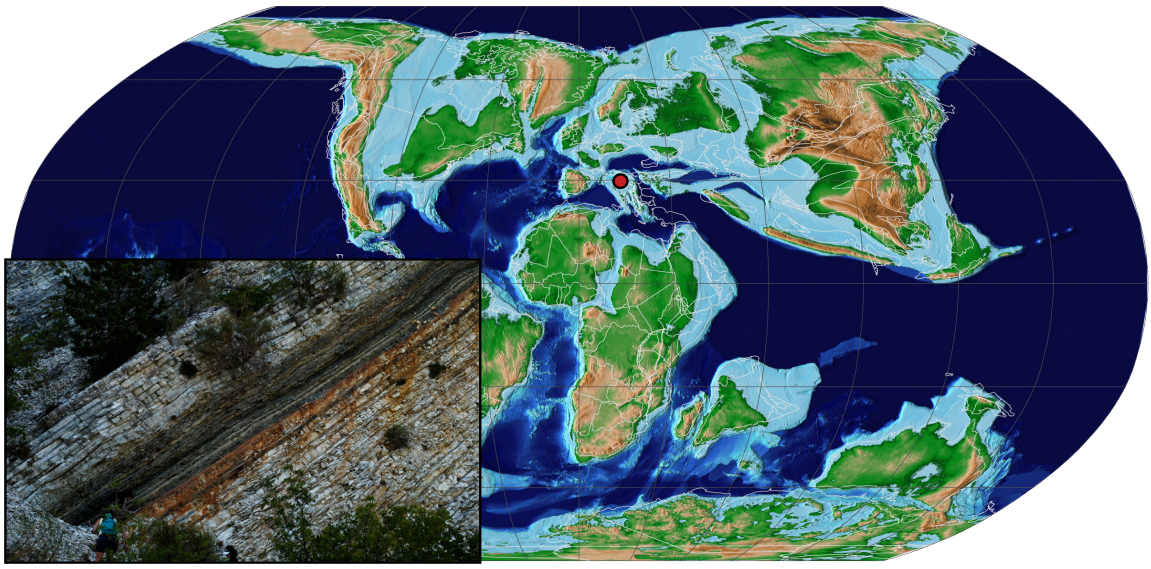

Figure 5.1: Global location of Furlo adapted from the PALEOMAP Project (Scotese, 2008) with an inset photo of the outcrop.

Methods

Samples were collected for whole-rock geochemical analysis of both carbonates and organic-rich shales. All samples were trimmed prior to powdering to ensure that geochemical analyses were performed on the most pristine samples possible. All samples were powdered using a trace metal-clean ball mill. For organic carbon isotopes ($\delta^{13}C_{org}$), all samples were de-carbonated using 4 M hydrochloric acid until effervescence stopped. The samples were then rinsed several times using deionized water and were ultimately combusted by elemental analyzer (EA) coupled, by continuous flow, to a Delta V Thermo IRMS (Isotope Ratio Mass Spectrometer) in the FIRMS (Facility for Isotope Ratio Mass Spectrometry) laboratory at the University of California, Riverside. The isotope ratio ($^{13}C/^{12}C$) was calculated as:

$$\delta^{13}C(‰)=[\frac{^{13}C/^{12}C_{sample}}{^{13}C/^{12}C_{standard}}-1]\bullet 1000 \qquad \text{(Equation 5.1)}$$

All values are presented in the standard delta notation as per mil (‰) deviation from Vienna Pee Dee Belemnite (V-PDB) with replicate analyses yielding a standard deviation of 0.05‰. Total carbon (TC) and total sulfur (TS) were measured by combustion of 100 mg of sample in an Eltra CS-500 carbon/sulfur analyzer with high-temperature furnace (1400°C). Total inorganic carbon (TIC) is measured using an acidification module in combination with the Eltra instrument, and total organic carbon (TOC) is calculated by the difference between TC and TIC.

A standard chromium reduction method was used to quantify pyrite sulfur concentrations (Canfield et al., 1986). Chromium reduction was performed on all bulk samples of organic-rich shale, as well as the residue remaining following the carbonate associated sulfate (CAS) extraction (see below). Specifically, S_{pyrite} was extracted using a 0.5 M hydrochloric acid and chromium chloride solution for 2 hours, which evolves hydrogen sulfide gas. This sulfide is precipitated as zinc sulfide (ZnS) in a trap containing a 1.48 M ammonium hydroxide and 0.03 M zinc acetate solution. The precipitate was quantified by titration, yielding wt.% S_{pyrite}. For isotopic analysis of $\delta^{34}S_{pyrite}$, the hydrogen sulfide is precipitated as silver sulfide using the same chromium chloride method but with a trap containing a 1.48 M ammonium hydroxide and 30 mM silver nitrate solution (Canfield et al., 1986).

All samples analyzed for $\delta^{34}S_{CAS}$ were dominantly carbonates, with carbonate contents of greater than 65 wt% and up to 95 wt%. We followed a standard procedure for extracting CAS (Gellatly and Lyons, 2005; Gill et al., 2011a; Gill et al., 2011b). Briefly, approximately 10 to 20 g of powdered sample were treated with sodium chloride and

sodium hypochlorite solutions and and multiple deionized water rinses to prevent the incorporation of any non-CAS sulfur-bearing phases. The samples were then dissolved using 4 M hydrochloric acid and were then vacuum-filtered less than 1 hour later to minimize any oxidation of pyrite. Pyrite oxidation was further limited by low ferric iron concentrations and generally low pyrite contents. A barium chloride solution was added to precipitate the extracted sulfate as barium sulfate.

The precipitated silver sulfide and barium sulfate was filtered, homogenized, and weighed into pressed tin capsules with excess vanadium pentoxide. The samples were combusted by EA coupled, by continuous flow, to a Delta V Thermo IRMS. The isotope ratio ($^{34}S/^{32}S$) was calculated as:

$$\delta^{34}S(‰)=\left[\frac{^{34}S/^{32}S_{sample}}{^{34}S/^{32}S_{standard}}-1\right]\bullet 1000 \qquad \text{(Equation 5.2)}$$

All sulfur isotope compositions are reported in standard delta notation as ‰ deviation from Vienna Canyon Diablo Troilite (V-CDT) (e.g. Gill et al., 2011a; Gill et al., 2011b). The data were corrected using a series of in-house standards (IAEA S-1, S-2, and S-3) replicate analyses of samples and international standards (IAEA SO-5, IAEA SO-6, and NBS 127) agree within 0.2‰ or better in the Lyons' stable isotope lab at the University of California, Riverside.

Iron speciation data was performed on all of the organic-rich shales, which operationally define highly reactive iron (Fe_{HR}) as pyrite Fe (Fe_{py}), Fe carbonate (Fe_{carb}), Fe oxides (Fe_{ox}), magnetite Fe (Fe_{mag}). All these phases are assumed to be reactive toward hydrogen sulfide on early diagenetic time scales (Poulton and Canfield, 2005; Raiswell and Canfield, 1998). Highly reactive iron is thus calculated as $Fe_{py} + Fe_{carb} + Fe_{ox} + Fe_{mag}$. Pyrite-Fe concentrations are calculated using the CRS method described above and calculating Fe_{py} assuming a stoichiometry of FeS_2. Un-pyritized reactive Fe (Fe_{carb}, Fe_{ox},

and Fe_{mag}) was analyzed using a three-step sequential extraction (Poulton and Canfield, 2005; Poulton and Raiswell, 2005). Briefly, ~100 mg of sample were weighed into a 15 ml centrifuge tube and extracted as follows: (1) 1 M sodium acetate extraction adjusted to a pH of 4.5 with constant shaking for 24 hours to extract Fe_{carb}, (2) the sample residue was extracted for Fe_{ox} using 50 g/L sodium dithionite buffered to a pH of 4.8 for 2 hours with constant shaking, and (3) Fe_{mag} was extracted from the remaining residue using an ammonium oxalate/oxalic acid-buffered solution at a pH of 3.2 for 6 hours. All extracts were analyzed using an inductively coupled plasma mass spectrometry (ICP-MS; see below).

Trace element analysis was performed using ~100 mg of powder weighed into ceramic vials and heated for ~12 hours at 450°C to volatilize all organic material. The samples were subsequently weighed after cooling to determine the loss on ignition. Samples were transferred into trace metal clean Savilex vials and completely dissolved using a standard sequential acid protocol (nitric acid/hydrochloric acid/hydrofluoric acid) at ~150°C. Subsequent to complete dissolution, the samples were dried down and then brought up in 2% HNO_3 for major and trace element analysis. All acids used in this method were Aristar/trace metal grade. Elemental concentrations (Al, Fe, Ti, Mo, V, Cr, and Zn) were measured using the Agilent 7500ce ICP-MS housed in the Lyons' lab at the University of California, Riverside. Standard reference materials (SDO-1 shale) were digested along with the samples and analyzed with each batch of digestions and in all cases were within the accepted analytical error for all elements. Procedural blanks were below detection limits, and sample reproducibility was better than 5% for all elements.

Iodine/calcium ratios (I/Ca) were determined by quadripole ICP-MS (Bruker M90) at Syracuse University. Specifically, measurements of iodine and calcium were determined by dissolving ~1-5 mg of sample in trace metal-clean vials using 0.54 M

nitric acid (Lu et al., 2010). Tetramethlamonium hydroxide was added to all samples and standards to stabilize iodine, as it is volatilized in acidic solutions. The dissolved solutions were analyzed the same day. Standard reference materials (JCP-1 coral) were digested along with the samples and analyzed in parallel, which resulted in an average iodine value of 5.59 ± 0.11 ppm (n = 5), which is similar to previous results of 5.47 ± 0.07 ppm (Lu et al., 2010) and 5.5 ± 0.2 ppm (Chai and Muramatsu, 2007). The sample reproducibility for one sample was better than 5% for both I and Ca.

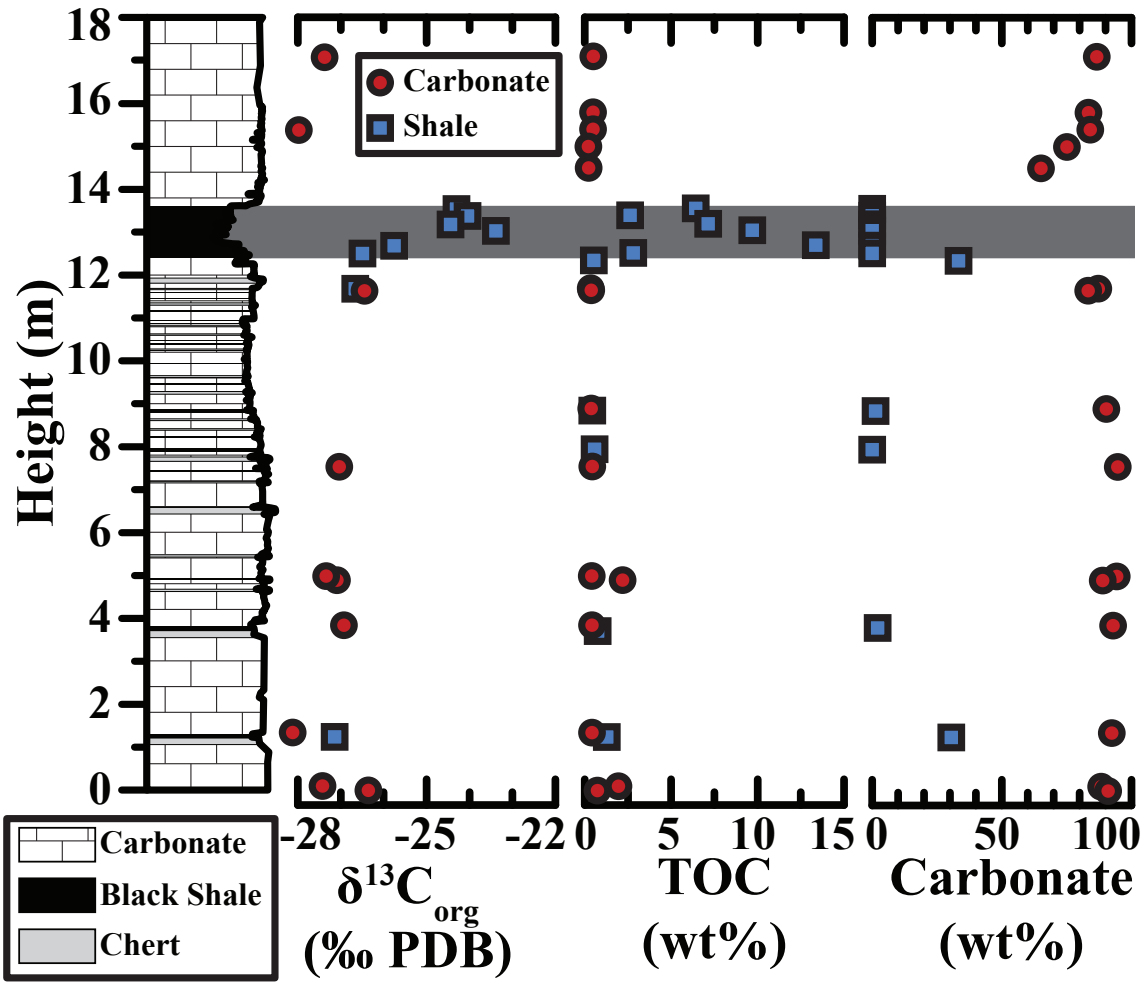

Figure 5.2: Total organic carbon and carbonate data for both the organic-rich shales and carbonates. Total organic carbon is low before the OAE (denoted with the dark grey bar) in both lithologies and increases during the OAE (shales). Stratigraphic column was based on our field campaign but is similar to previous studies (Jenkyns et al., 2007; Mort et al., 2007).

Results

Carbon

The $\delta^{13}C_{org}$ analyses at Furlo reveal a ~4‰ excursion across the roughly 1 m of organic-rich deposition, illustrating the vertical extent of the OAE at this locality. Outside the OAE the values range between -28.1‰ and -26.4‰, with an average of -27.4‰, and during the OAE values range from -26.5‰ and -23.4‰, with an average of -24.8‰ (Fig. 5.2). The TOC values before the OAE (shales and carbonates) and after the OAE (carbonates) are all below 2.2 wt%, and a majority of the samples are near 0.5 wt%. In contrast, the TOC values increase to an average of 7.0 wt% during the OAE, with a maximum value of 13.4 wt %. The TOC values after the OAE are much lower than the average samples prior to the event; however, there are only carbonate lithologies subsequent to the OAE; carbonates would tend to show lower TOC because of dilution effects. The carbonate content in the shales was below 33 wt%, and the carbonates before and after the OAE had averages of 90.7 and 78.7 wt%, respectively. Carbonate contents for the shales during the event were below the detectable limit and are reported as zero.

Fe and trace metal geochemistry

Iron geochemistry was performed on all samples with carbonate contents below 35 wt%, which were all of the organic-rich shales. These samples all had total Fe (Fe_T) contents in excess of 0.5 wt%. Normalizing Fe_T to Al highlights enrichments beyond the detrital average, which for Phanerozoic mudstones and shales is 0.51 (±0.1; Raiswell et al., 2008). Shales from this study have an average ratio prior to the OAE of 0.55, with a range from 0.49 to 0.63. During the OAE the shales have an average of 1.33 and range from 0.63 to 1.83. The ratio of highly reactive Fe (Fe_{HR}) to Fe_T can delineate anoxic

depositional conditions because of the comparatively large proportion of reactive Fe that is typical of those settings (e.g. Poulton et al., 2004). Modern marine muds deposited oxically have an average Fe_{HR}/Fe_T ratio of 0.28 ±0.06 (Raiswell and Canfield, 1998). Our samples prior to the OAE average 0.57, with all samples above 0.50, and during the event average 0.68, with a range of 0.55 and 0.82. The ratio of pyrite Fe (Fe_{py}) to Fe_{HR} is a measure of the amount of the reactive Fe that has been pyritized through exposure to hydrogen sulfide. Values above 0.8 convincingly point to deposition under euxinia, when combined with elevated ratios of Fe_{HR}/Fe_T, while values between 0.7 and 0.8 only suggest euxinic deposition (März et al., 2008). Sample before the onset of the OAE average 0.48, with a range between 0.40 and 0.53, and during the OAE average 0.78, with all values above 0.73 (Fig. 5.3). The average pyrite concentrations before the OAE are 0.33 wt%, and during the OAE the average is 1.49 wt%, with a maximum value of 1.88 wt%.

Trace metal geochemisty at Furlo also assists in our investigation of the depositional redox conditions (Fig. 5.3). Manganese concentrations prior to the OAE (average of 190 ppm) are well below the average shale value of ~850 ppm (Morford and Emerson, 1999; Turgeon and Brumsack, 2006) and drop to 33.5 ppm during the OAE. Vanadium and Cr are both enriched prior to the OAE compared to continental crustal material (125 and 180 ppm with large variability, respectively; Taylor and McLennan, 1995), with averages of 578 ppm and 139 ppm, respectively. Averages for V and Cr during the OAE are 152 ppm and 66 ppm, respectively. Zinc shows enrichments ranging from 314 ppm to 964 ppm (75 ppm; Taylor and McLennan, 1995), with an average of 613 ppm, and during the OAE averages 91 ppm, with a range of 48 ppm to 191 ppm. The samples prior to the OAE have an average Mo value of 6 ppm, with the highest value reaching 9 ppm, and during the OAE average 22 ppm, with a range from 14 ppm to 40 ppm. The average Al values are close to 1 wt% (average of 1.15 wt%) prior to the OAE

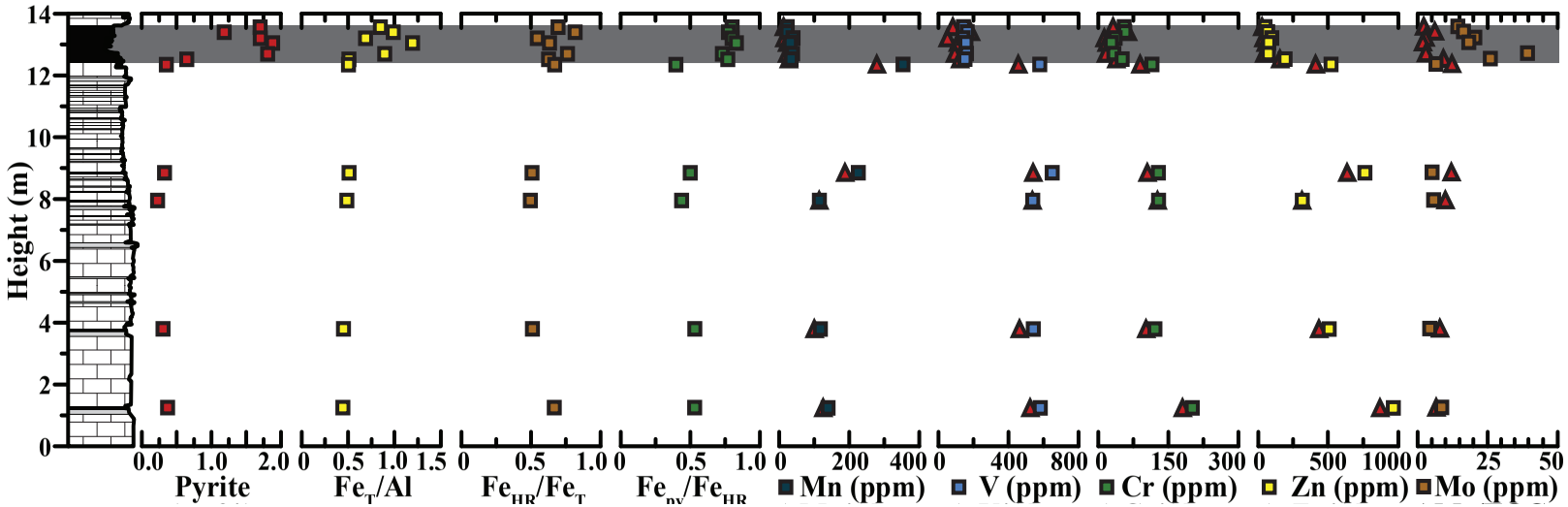

Figure 5.3: Paleoredox geochemical data from the organic-rich lithologies, black shales. The OAE is denoted by the grey bar and nearly all of the parameters show a major perturbation during the OAE with all of the Fe proxies increasing and Mo illustrating a small increase in the concentration. While the low oxygen trace metal proxies, Mn, V, Cr and Zn, all show a significant decline in concentration across the event.

and show a slight increase during the OAE (average of 1.61 wt%). Therefore, the ratios of a given metal to Al ratio do not change the story significantly relative to the absolute concentrations (see Fig. 5.3), although normalization does smooth the trends.

Pyrite isotope data were generated from both shales and carbonates (Fig. 5.4). The carbonate samples yielded pyrite concentrations that were low enough to be within our error and therefore cannot be reported, but we were able to determine isotope values from these samples. Generally, the average $\delta^{34}S_{pyrite}$ values for carbonate and shale are in good agreement, but carbonates show greater variability. Average $\delta^{34}S_{pyrite}$ for non-OAE samples is near -45.0‰, with a range from -34.2‰ to -51.0‰, while the average $\delta^{34}S_{pyrite}$ increased during the OAE to -38. 8‰ and exhibited a narrower range from -36.8‰ to -42.6‰.

Carbonate geochemistry

Again, $\delta^{34}S_{CAS}$ were only generated on the carbonate-rich intervals. From the base of the section to the onset of the OAE the $\delta^{34}S_{CAS}$ are stable with a narrow range from 15.8‰ to 18.3‰ but the two samples prior to the OAE start to trend to more positive values. This trend of increasing $\delta^{34}S_{CAS}$ continues in the carbonate facies following the black shale interval, rising to values near 22‰ 3.5 m above the OAE. The $\Delta^{34}S$, defined as the difference between $\delta^{34}S_{CAS,}$ representing seawater sulfate, and $\delta^{34}S_{pyrite}$ was calculated for six samples where values for both $\delta^{34}S_{CAS}$ and $\delta^{34}S_{pyrite}$ were determined. From these, a trend in $\Delta^{34}S$ is observed, with values rising going into the OAE and falling again after the OAE (Fig. 5.4). The I/Ca ratios showed some scatter, but overall the results reveal a systematic trend most easily described in three stages. The I/Ca ratios are stable at ~0.6 μmol/mol for the first 5 m and decrease to an average of 0.25 μmol/

mol from 5 m to the base of the black shales, and values steadily increase from near 0.25 µmol/mol to > 1 µmol/mol subsequent to the OAE (Fig. 5.4). No iodine data are available for the OAE because of the absence of carbonate.

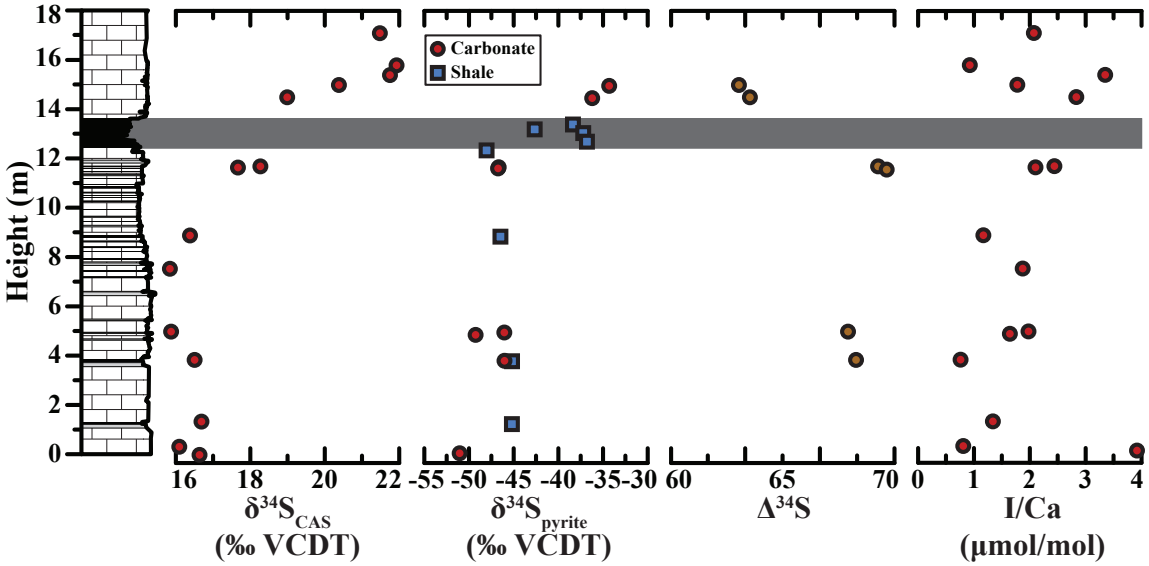

Figure 5.4: Sulfur isotope and carbonate geochemical paleoredox data. The sulfur isotope data shift to more positive values leading into the OAE and increase post OAE although the $\Delta^{34}S$ data actually declines after the OAE. The ratio of I/Ca shows significant scatter but generally throughout the section shows low values indicating deposition in a low oxygen environment.

Discussion

Local geochemical conditions

The trace metal record for this section has been discussed previously but without an independent measure of the local redox conditions (Turgeon and Brumsack, 2006). The Fe speciation results provide an independent constraint on the local redox prior to and during the OAE, allowing a better framework for interpreting the trace metal proxies. Overall, the Fe speciation results—Fe_T/Al, Fe_{HR}/Fe_T, and Fe_{py}/Fe_{HR}—suggest a basin that transitioned

from an anoxic-ferruginous water-column conditions with hydrogen sulfide likely limited to the pore fluids and euxinic conditions persisting for the duration of the OAE. Highly reactive Fe is enriched within anoxic sediments compared to the detrital flux due. One possible explanation is active Fe redox cycling along the chemocline producing an "Fe-shuttle", which leads to preferential iron transport from oxic basin margins to the deeper anoxic waters were it is captured through pyrite formation in the water column in the case of euxinia (Anderson and Raiswell, 2004; Canfield et al., 1996; Lyons, 1997; Wijsman et al., 2001). Hydrothermal inputs can also play a role (Owens et al., 2012). Elevated Fe_{HR}/Fe_T values in the organic-rich levels suggest that these samples have a higher portion of reactive Fe compared to typical oxic modern marine sediments as a result of reducing bottom waters and deposition beneath an anoxic and/or sulfidic water column (Poulton and Canfield, 2011; Raiswell and Canfield, 1998). The samples deposited during the OAE exhibit elevated Fe_{HR}/Fe_T and Fe_{py}/Fe_{HR} (average of 0.78), indicating that a majority of the reactive Fe is pyritized, suggesting at least locally euxinic deposition. Anoxic and euxinc conditions typically enrich Fe relative to Al, but the samples prior to the OAE fall within the crustal average, while the euxinic OAE samples are enriched. This relationship suggests that either a more active "Fe-shuttle" or a larger hydrothermal signal during the OAE proper (Jenkyns et al., 2007).

The previously reported trace metal averages and ranges for the pre-OAE organic-rich bands and the Bonarelli level are similar to those reported here, with Zn being the one exception. Our data are much lower during the OAE, although the trends are similar (Turgeon and Brumsack, 2006). Manganese concentrations in the shales corroborate the Fe speciation results which suggest anoxia prior to the OAE and euxinia during the OAE, with values below the crustal average of 850 ppm (Taylor and McLennan, 1995) prior to the OAE and decreasing during the OAE due to reduction of Mn-oxides under low

oxygen conditions (Turgeon and Brumsack, 2006). Low oxygen, but non-sulfidic trace metal proxies—Cr, V, and Zn (Algeo, 2004; Reinhard et al., 2013; Sahoo et al., 2012; Scott et al., 2013)—show enriched values prior to the OAE, thus agreeing with the Mn and Fe data. However, Cr, V, and Zn crash to near crustal values during the OAE, which should be more reducing locally and should continue to enrich these trace metals. Molybdenum, a reliable euxinic indicator, shows minimal enrichment prior to the OAE and enrichments ($\leq$ ~40 ppm) on the low end of those typical of euxinia during the OAE (Scott and Lyons, 2012). The Mo values prior to the OAE suggest limited or intermittent water column sulfide prior to the OAE or sulfide limited to the upper few centimeters of sediment, and the increased values during the OAE point to euxinia but with somewhat limited Mo uptake. Therefore, all geochemical indicators preceding the OAE are in good agreement, but the trace metal and Fe geochemistry during the OAE are more complicated. Specifically, the Fe geochemistry records local signals, but the trace metal geochemistry can be influenced by global marine inventory controls (see below for further discussion).

I/Ca ratios reflect concentrations of iodate (IO_3^-) in the water column, as IO_3^- is the exclusive iodine species precipitated with carbonates (Lu et al., 2010). Therefore, the simple presence of carbonate-associated iodine at Furlo implies IO_3^- in the local water column, and hence the presence of oxygen, since IO_3^- is limited to oxic water (e.g. Wong and Brewer, 1977). Overall, the I/Ca dataset shows low values throughout the section compared to those presented previously from the Eastbourne, a shallow water locality, OAE2 section (Lu et al., 2010). Lower IO_3^- could be due to differing oceanographic controls at Furlo compared to Eastbourne where increasing distance depth and distance from shore record lower IO_3^- values (Truesdale, 1978, 1994; Truesdale et al., 2000) which is likely lower dissolved oxygen concentrations (Rue et al., 1997). Regardless, outside of generally low values,

the decreasing trend in I/Ca ratios prior to and going into the OAE is likely an indication of deoxygenation at Furlo prior to the carbon isotope excursion, a result also observed at Eastbourne. This is corroborated by the sudden increase in I/Ca ratios post-OAE to values higher than those prior to the OAE, implying increased IO_3^- availability linked to increasing oxygen coming out of the OAE. This may mean that carbonates stratigraphically above and below our sampled section could have much higher I/Ca ratios, perhaps similar to those of Eastbourne (> 2 μmol/mol), and that Furlo captures early deoxygenation. When combined with the Fe speciation and trace metal data in the intercalated shales, this implies that the redox was teetering between low oxygen and anoxic conditions prior to the OAE, which correlate with transitions between carbonate and black shale deposition.

Global implications

The Fe geochemistry suggests that this locality experienced euxinic deposition during the OAE, but the trace metal values are muted. An analogous relationship is observed at another OAE2 locality (Owens et al., in review-b), ODP site 1258 – Demerara Rise, suggesting a global expansion of reducing condition, which depleted the marine reservoir inventory during the OAE (Owens et al., in review-b; Reinhard et al., 2013). Recall that the stratigraphic trend actually reveals an increase in Mo concentrations going into the OAE, but it is subtle, and the Fe data tell us that it is best explained by a local shift from anoxia (non-sulfidic) to euxinia. The euxinic values are muted compared to typical euxinic deposition at times of more limited global extent (Algeo and Lyons, 2006; Lyons et al., 2009) due to global drawdown of the marine Mo reservior (Owens et al., in review-b; Reinhard et al., 2013), which could be mistaken for non-euxinic conditions during the OAE (i.e. Turgeon and Brumsack, 2006).

Additionally, the Mo/TOC ratio drops during the OAE, even when compared to the non-euxinic deposition prior to the OAE, which suggests Mo burial under a highly depleted marine reservoir (Algeo and Lyons, 2006; Lyons et al., 2009). This scenario has been well documented in the modern ocean as TOC and Mo concentrations co-vary, and the mean ratio then tracks the size of the Mo inventory (Algeo and Lyons, 2006) . The non-OAE Mo/TOC values average ~9.8, which is nearly identical to another OAE2 record at IODP site 1258 (Algeo and Rowe, 2011; Hetzel et al., 2009; Owens et al., in review-b), and during the OAE the Mo/TOC averages ~3.2 (slightly higher than the 2.8 observed at site 1258). The Mo/TOC values recorded during the OAE at both Furlo and Demerara Rise are lower than those of the highly restricted, Mo-depleted, modern Black Sea (average of ~4.5), while the more open, Mo-replete Cariaco Basin records Mo/TOC values above ~20 (Algeo and Lyons, 2006), which again suggests that Mo was severely drawn down during the event.

Trace metal limitations have been invoked as a mechanism for retarding the evolution of life during the Proterozoic due to the prevailing redox state of the oceans (Anbar and Knoll, 2002; Dupont et al., 2010; Planavsky et al., 2010; Scott et al., 2008), and similar conditions may have existed for short periods in the Phanerozoic (Gill et al., 2011b; Owens et al., in review-b). Due to widespread reducing conditions limiting the availability of bioessential elements—Mo and V for example, which are linked to the nitrogen cycle as enzymatic co-factors in nitrogen fixation (Bellenger et al., 2011; Glass et al., 2009; Reinhard et al., 2013). Additionally, Zn has been documented to be essential for eukaryotic evolution through protein-DNA interactions (Dupont et al., 2006). Somewhat surprisingly, existing trends suggest that Zn was not limiting in the widely anoxic and euxinic Proterozoic ocean (Scott et al., 2013). However, the values for Zn/Al during the OAE at Furlo and Demerara Rise (Hetzel et al., 2009; Owens et al., in

review-b) average 47 and 62, respectively, which is approaching the crustal average of ~10 (Scott et al., 2013). These values are on the low end of the Precambrian data and may have played an important role ecologically during the OAE, as suggested by a decline in eukaryote abundance relative to bacteria (Owens et al., in review-b). It is difficult to unmix the relative importance of each bioessential trace element, but collectively they are certain to have been important to the ecological and chemical evolution that marked this event.

The sulfur isotope data for both CAS and pyrite show a positive excursion starting at or just prior to the onset of the OAE and extending through and past the OAE. This excursion suggests a global perturbation in the sulfur isotope composition of the ocean due to an increase in pyrite burial, which leaves the marine sulfate reservoir heavy (Owens et al., in review-a). The $\delta^{34}S_{CAS}$ record has now been observed at seven sections worldwide with a consistent presence of $\delta^{34}S_{CAS}$ excursions but of varying magnitudes (2 to 7‰). The timing and lag following the carbon isotope excursion are nearly identical at all localities (Adams et al., 2010; Ohkouchi et al., 1999; Owens et al., in review-a). Our positive $\delta^{34}S_{pyrite}$ excursion of ~12‰ has not been observed at other sites (Adams et al., 2010; Böttcher et al., 2006; Gautier, 1987; Hetzel et al., 2009), and the $\Delta^{34}S$ recorded in this section is the largest known for OAE2, although it is similar to the Western Interior Seaway (Adams et al., 2010) and decreases during and post-OAE (Fig. 5.4).

At both Furlo and Eastbourne, I/Ca ratios increase significantly following the OAE, which suggests a rapid increase in oxygenated waters and less OC burial post-OAE(Lu et al., 2010). The low but non-zero values preceding the OAE suggest low IO_3^- in the water column, consistent with small but limited oxygen concentrations. Organic carbon cycling also plays a role in modulating I/Ca ratios, as iodine is a bioessential

element whose reservoir size is most strongly linked to organic carbon burial and remineralization. The similar trends in I/Ca at both sites provides evidence that a shrinking iodine reservoir was linked to enhanced organic carbon burial during the OAE. Therefore, the iodine data are best viewed in light of a global regulation of the iodine inventory through organic burial in combination with local redox controls. Therefore, the transition between the carbonates and shales preceding the OAE represents local redox vacillations from anoxic-ferrruginous shales to low but present oxygen-containing carbonates.

Conclusions

Paired lithofacies and geochemical proxies illuminate the local and global redox landscape during OAE2. The Fe speciation data suggest the organic-rich facies at Furlo were anoxic (Fe_{HR}/Fe_T above 0.38) but lacked water column euxinia (Fe_{py}/Fe_{HR} well below 0.7) prior to the OAE; however, enriched Fe_{HR}/Fe_T *and* Fe_{py}/Fe_{HR} suggests euxinia during the OAE. The trace metal geochemistry of the black shale layers is consistent with the Fe results. Low oxygen/anoxic indicators—V, Cr, and Zn—are enriched prior to the OAE, while the euxinic proxy, Mo, shows very limited enrichment, suggesting either intermittent euxinia or sulfide limited to pore fluids. During the OAE, Mo values are enriched by up to ~40 ppm, which is similar to the enrichments seen at Demerara Rise during the OAE (Hetzel et al., 2009; Owens et al., 2012). These values are relatively subdued, suggesting deposition under a depleted marine reservoir due to a global expansion of euxinia (Reinhard et al., 2013). Importantly, V, Cr, and Zn associated with the euxinic OAE interval record values close to crustal averages, also suggesting a drawdown of the trace metal marine inventory.

The carbonate proxies show similarities to previous studies (Adams et al., 2010; Lu et al., 2010; Ohkouchi et al., 1999; Owens et al., in review-a). The $\delta^{34}S_{CAS}$ data show a ~6‰ positive excursion starting slightly before the OAE and continuing post-OAE, which suggest continued euxinic burial of pyrite (Owens et al., in review-a). The low I/Ca ratios prior to the OAE point to burial under low oxygen, but not anoxic, surface waters, suggesting oscillating redox conditions prior to the OAE. The data also suggest increasing oxygenation post-OAE (Lu et al., 2010).

The multi-proxy lithofacies approach (carbonates and shales) shows good consistency prior to the OAE, but no comparison can be made during the OAE due to a lack of carbonate deposition—or after due to the lack of organic-rich shales. The rhythmic deposition of sediments is likely tied to climatic and environmental changes (Galeotti et al., 2009), which could also be driving the redox changes for each lithofacies prior to the OAE. This dataset increases the global context for understanding areal extent of euxinia, which was previously modeled to be less than ~10% of the seafloor (Owens et al., in review-a; Owens et al., in review-b), and suggests that this locality experienced low oxygen conditions and even anoxia prior to the OAE—perhaps as a first step toward the more extreme conditions of the OAE.

References

Adams, D.D., Hurtgen, M.T., Sageman, B.B., 2010. Volcanic triggering of a biogeochemical cascade during Oceanic Anoxic Event 2. Nature Geoscience 3, 201–204.

Algeo, T.J., 2004. Can marine anoxic events draw down the trace element inventory of seawater? Geology 32, 1057–1060.

Algeo, T.J., Lyons, T.W., 2006. Mo–total organic carbon covariation in modern anoxic marine environments: Implications for analysis of paleoredox and paleohydrographic conditions. Paleoceanography 21, PA1016.

Algeo, T.J., Rowe, H., 2011. Paleoceanographic applications of trace-metal concentration data. Chemical Geology 324-325, 6–18.

Anbar, A.D., Knoll, A.H., 2002. Proterozoic ocean chemistry and evolution: A bioinorganic bridge? Nature 297, 1137–1142.

Anderson, T.F., Raiswell, R., 2004. Sources and mechanisms for the enrichment of highly reactive iron in euxinic Black Sea sediments. American Journal of Science 304, 203–233.

Arthur, M.A., Dean, W.E., Pratt, L.M., 1988. Geochemical and climatic effects of increased marine organic carbon burial at the Cenomanian/Turonian boundary. Nature 335, 714–717.

Bellenger, J.P., Wichard, T., Xu, Y., Kraepiel, A.M.L., 2011. Essential metals for nitrogen fixation in a free-living N2-fixing bacterium: chelation, homeostasis and high use efficiency. Environmental Microbiology 13, 1395–1411.

Berner, R.A., 2006. GEOCARBSULF: A combined model for Phanerozoic atmospheric O2 and CO2. Geochimica et Cosmochimica Acta: A Special Issue Dedicated to Robert A. Berner 70, 5653–5664.

Blättler, C.L., Jenkyns, H.C., Reynard, L.M., Henderson, G.M., 2011. Significant increases in global weathering during Oceanic Anoxic Events 1a and 2 indicated by calcium isotopes. Earth and Planetary Science Letters 309, 77–88.

Blumenberg, M., Wiese, F., 2012. Imbalanced nutrients as triggers for black shale formation in a shallow shelf setting during the OAE 2 (Wunstorf, Germany). Biogeosciences Discuss 9, 5373–5413.

Böttcher, M.E., Hetzel, A., Brumsack, H.J., Schipper, A., 2006. Sulfur–iron–carbon geochemistry in sediments of the Demerara Rise. In: Mosher, D.C., Erbacher, J.,

Malone, M.J. (Eds.), Proceedings of the Ocean Drilling Program. Scientific Results, vol. 207. Ocean Drilling Program, College Station, TX, pp. 1–23.

Brumsack, H.-J., 2006. The trace metal content of recent organic carbon-rich sediments: Implications for Cretaceous black shale formation. Palaeogeography, Palaeoclimatology, Palaeoecology 232, 344–361.

Canfield, D.E., Lyons, T.W., Raiswell, R., 1996. A model for iron deposition to euxinic Black Sea sediments. American Journal of Science 296, 818–834.

Canfield, D.E., Raiswell, R., Westrich, J.T., Reaves, C.M., Berner, R.A., 1986. The use of chromium reduction in the analysis of reduced inorganic sulfur in sediments and shales. Chemical Geology 54, 149–155.

Chai, J.Y., Muramatsu, Y., 2007. Determination of Bromine and Iodine in Twenty-three Geochemical Reference Materials by ICP-MS. Geostandards and Geoanalytical Research 31, 143–150.

Dupont, C.L., Butcher, A., Valas, R.E., Bourne, P.E., Caetano-Anollés, G., 2010. History of biological metal utilization inferred through phylogenomic analysis of protein structures. Proceedings of the National Academy of Sciences 107, 10567–10572.

Dupont, C.L., Yang, S., Palenik, B., Bourne, P.E., 2006. Modern proteomes contain putative imprints of ancient shifts in trace metal geochemistry. Proceedings of the National Academy of Sciences 103, 17822–17827.

Galeotti, S., Rusciadelli, G., Sprovieri, M., Lanci, L., Gaudio, A., Pekar, S., 2009. Sea-level control on facies architecture in the Cenomanian-Coniacian Apulian margin (Western Tethys): A record of glacio-eustatic fluctuations during the Cretaceous greenhouse? Palaeogeography, Palaeoclimatology, Palaeoecology 276, 196–205.

Gautier, D.L., 1987. Isotopic composition of pyrite: Relationship to organic matter type and iron availability in some North American Cretaceous shales. Chemical Geology: Isotope Geoscience section 65, 293–303.

Gellatly, A.M., Lyons, T.W., 2005. Trace sulfate in mid-Proterozoic carbonates and the sulfur isotope record of biospheric evolution. Geochimica et Cosmochimica Acta 69, 3813–3829.

Gill, B.C., Lyons, T.W., Jenkyns, H.C., 2011a. A global perturbation to the sulfur cycle during the Toarcian Oceanic Anoxic Event. Earth and Planetary Science Letters 312, 484–496.

Gill, B.C., Lyons, T.W., Young, S.A., Kump, L.R., Knoll, A.H., Saltzman, M.R., 2011b. Geochemical evidence for widespread euxinia in the Later Cambrian ocean. Nature 469, 80–83.

Glass, J.B., Wolfe-Simon, F., Anbar, A.D., 2009. Coevolution of metal availability and nitrogen assimilation in cyanobacteria and algae. Geobiology 7, 100–123.

Haq, B.U., Hardenbol, J.A.N., Vail, P.R., 1987. Chronology of Fluctuating Sea Levels Since the Triassic. Science 235, 1156–1167.

Hetzel, A., Böttcher, M.E., Wortmann, U.G., Brumsack, H.-J., 2009. Paleo-redox conditions during OAE 2 reflected in Demerara Rise sediment geochemistry (ODP Leg 207). Palaeogeography, Palaeoclimatology, Palaeoecology 273, 302–328.

Hetzel, A., März, C., Vogt, C., Brumsack, H.-J., 2011. Geochemical environment of Cenomanian - Turonian black shale deposition at Wunstorf (northern Germany). Cretaceous Research 32, 480–494.

Huber, B.T., Hodell, D.A., Hamilton, C.P., 1995. Middle-Late Cretaceous climate of the southern high latitudes: Stable isotopic evidence for minimal equator-to-pole thermal gradients. Geological Society of America Bulletin 107, 1164–1191.

Jarvis, I., Lignum, J.S., Gröcke, D.R., Jenkyns, H.C., Pearce, M.A., 2011. Black shale deposition, atmospheric CO_2 drawdown, and cooling during the Cenomanian-Turonian Oceanic Anoxic Event. Paleoceanography 26, PA3201.

Jarvis, I.A.N., Murphy, A.M., Gale, A.S., 2001. Geochemistry of pelagic and hemipelagic carbonates: criteria for identifying systems tracts and sea-level change. Journal of the Geological Society 158, 685–696.

Jenkyns, H.C., Forster, A., Schouten, S., Sinninghe Damsté, J.S., 2004. High temperatures in the Late Cretaceous Arctic Ocean. Nature 432, 888–892.

Jenkyns, H.C., Matthews, A., Tsikos, H., Erel, Y., 2007. Nitrate reduction, sulfate reduction, and sedimentary iron isotope evolution during the Cenomanian-Turonian oceanic anoxic event. Paleoceanography 22, PA3208.

Jenkyns, H.C., Schouten-Huibers, L., Schouten, S., Sinninghe Damsté, J.S., 2012. Warm Middle Jurassic–Early Cretaceous high-latitude sea-surface temperatures from the Southern Ocean. Climate of the Past 8, 215–226.

Jones, C.E., Jenkyns, H.C., 2001. Seawater Strontium Isotopes, Oceanic Anoxic Events, and Seafloor Hydrothermal Activity in the Jurassic and Cretaceous. American Journal of Science 301, 112–149.

Kraal, P., Slomp, C.P., Forster, A., Kuypers, M.M.M., 2010. Phosphorus cycling from the margin to abyssal depths in the proto-Atlantic during oceanic anoxic event 2. Palaeogeography, Palaeoclimatology, Palaeoecology 295, 42–54.

Kuhnt, W., Luderer, F., Nederbragt, S., Thurow, J., Wagner, T., 2005. Orbital-scale record of the late Cenomanian-Turonian oceanic anoxic event (OAE-2) in the Tarfaya Basin (Morocco). International Journal of Earth Sciences 94, 147–159.

Kuroda, J., Ohkouchi, N., 2006. Implication of spatiotemporal distribution of black shales deposited during the Cretaceous Oceanic Anoxic Event-2. Paleontological Research 10, 345–358.

Kuypers, M.M.M., Pancost, R.D., Nijenhuis, I.A., Sinninghe Damsté, J.S., 2002. Enhanced productivity led to increased organic carbon burial in the euxinic North Atlantic basin during the late Cenomanian oceanic anoxic event. Paleoceanography 17.

Lanci, L., Muttoni, G., Erba, E., 2010. Astronomical tuning of the Cenomanian Scaglia Bianca Formation at Furlo, Italy. Earth and Planetary Science Letters 292, 231-237.

Leckie, R.M., Bralower, T.J., Cashman, R., 2002. Oceanic anoxic events and plankton evolution: Biotic response to tectonic forcing during the mid-Cretaceous. Paleoceanography 17, PA000623.

Lu, Z., Jenkyns, H.C., Rickaby, R.E.M., 2010. Iodine to calcium ratios in marine carbonate as a paleo-redox proxy during oceanic anoxic events. Geology 38, 1107–1110.

Lyons, T.W., 1997. Sulfur isotopic trends and pathways of iron sulfide formation in upper Holocene sediments of the anoxic Black Sea. Geochimica et Cosmochimica Acta 61, 3367–3382.

Lyons, T.W., Anbar, A.D., Severmann, S., Scott, C., Gill, B.C., 2009. Tracking Euxinia in the Ancient Ocean: A Multiproxy Perspective and Proterozoic Case Study. Annual Review of Earth and Planetary Sciences 37.

MacLeod, K.G., Martin, E.E., Blair, S.W., 2008. Nd isotopic excursion across Cretaceous ocean anoxic event 2 (Cenomanian-Turonian) in the tropical North Atlantic. Geology 36, 811–814.

März, C., Poulton, S.W., Beckmann, B., Küster, K., Wagner, T., Kasten, S., 2008. Redox sensitivity of P cycling during marine black shale formation: Dynamics of sulfidic and anoxic, non-sulfidic bottom waters. Geochimica et Cosmochimica Acta 72, 3703–3717.

Monteiro, F.M., Pancost, R.D., Ridgwell, A., Donnadieu, Y., 2012. Nutrients as the dominant control on the spread of anoxia and euxinia across the Cenomanian-Turonian oceanic anoxic event (OAE2): Model-data comparison. Paleoceanography 27, PA4209.

Morford, J.L., Emerson, S., 1999. The geochemistry of redox sensitive trace metals in sediments. Geochimica et Cosmochimica Acta 63, 1735–1750.

Mort, H., Jacquat, O., Adatte, T., Steinmann, P., Föllmi, K., Matera, V., Berner, Z., Stüben, D., 2007. The Cenomanian/Turonian anoxic event at the Bonarelli Level in Italy and Spain: enhanced productivity and/or better preservation? Cretaceous Research 28, 597–612.

Mort, H.P., Adatte, T., Keller, G., Bartels, D., Föllmi, K.B., Steinmann, P., Berner, Z., Chellai, E.H., 2008. Organic carbon deposition and phosphorus accumulation during Oceanic Anoxic Event 2 in Tarfaya, Morocco. Cretaceous Research 29, 1008–1023.

Nederbragt, A.J., Fiorentino, A., 1999. Stratigraphy and palaeoceanography of the Cenomanian-Turonian Boundary Event in Oued Mellegue, north-western Tunisia. Cretaceous Research 20, 47–62.

Ohkouchi, N., Kawamura, K., Kajiwara, Y., Wada, E., Okada, M., Kanamatsu, T., Taira, A., 1999. Sulfur isotope records around Livello Bonarelli (northern Apennines, Italy) black shale at the Cenomanian-Turonian boundary. Geology 27, 535–538.

Owens, J.D., Gill, B.C., Jenkyns, H.C., Bates, S.M., Severmann, S., Kuypers, M.M.M., Woodfine, R.G., Lyons, T.W., in review-a. Sulfur isotopes track the global extent and dynamics of euxinia during Cretaceous Oceanic Anoxic Event 2 Proceedings of the National Academy of Sciences.

Owens, J.D., Lyons, T.W., Li, X., Macleod, K.G., Gordon, G., Kuypers, M.M.M., Anbar, A., Kuhnt, W., Severmann, S., 2012. Iron isotope and trace metal records of iron cycling in the proto-North Atlantic during the Cenomanian-Turonian oceanic anoxic event (OAE-2). Paleoceanography 27, PA3223.

Owens, J.D., Reinhard, C.T., Rohrssen, M., Love, G.D., Lyons, T.W., in review-b. Marine trace-metal drawdown during the Cenomanian-Turonian Boundary Event (OAE2): implication for global redox and biological perturbation. Nature.

Pancost, R.D., Crawford, N., Magness, S., Turner, A., Jenkyns, H.C., Maxwell, J.R., 2004. Further evidence for the development of photic-zone euxinic conditions during Mesozoic oceanic anoxic events. Journal of the Geological Society 161, 353–364.

Pearce, M.A., Jarvis, I., Tocher, B.A., 2009. The Cenomanian-Turonian boundary event, OAE2 and palaeoenvironmental change in epicontinental seas: New insights from the dinocyst and geochemical records. Palaeogeography, Palaeoclimatology, Palaeoecology 280, 207–234.

Planavsky, N.J., Rouxel, O.J., Bekker, A., Lalonde, S.V., Konhauser, K.O., Reinhard, C.T., Lyons, T.W., 2010. The evolution of the marine phosphate reservoir. Nature 467, 1088–1090.

Pogge von Strandmann, P.A.E., Jenkyns, H.C., Woodfine, R.G., 2013. Lithium isotope evidence for enhanced weathering during Oceanic Anoxic Event 2. Nature Geoscience 6, 668–672.

Poulton, S.W., Canfield, D.E., 2005. Development of a sequential extraction procedure for iron: implications for iron partitioning in continentally derived particulates. Chemical Geology 214, 209–221.

Poulton, S.W., Canfield, D.E., 2011. Ferruginous Conditions: A Dominant Feature of the Ocean through Earth's History. Elements 7, 107–112.

Poulton, S.W., Fralick, P.W., Canfield, D.E., 2004. The transition to a sulphidic ocean ~ 1.84 billion years ago. Nature 431, 173–177.

Poulton, S.W., Raiswell, R., 2005. Chemical and physical characteristics of iron oxides in riverine and glacial meltwater sediments. Chemical Geology 218, 203–221.

Raiswell, R., Canfield, D.E., 1998. Sources of iron for pyrite formation in marine sediments. American Journal of Science 298, 219–245.

Raiswell, R., Newton, R., Bottrell, S.H., Coburn, P.M., Briggs, D.E.G., Bond, D.P.G., Poulton, S.W., 2008. Turbidite depositional influences on the diagenesis of Beecher's Trilobite Bed and the Hunsruck Slate; sites of soft tissue pyritization. American Journal of Science 308, 105–129.

Raup, D.M., Sepkoski, J.J., 1986. Periodic extinction of families and genera. Science 231, 833–836.

Reinhard, C.T., Planavsky, N.J., Robbins, L.J., Partin, C.A., Gill, B.C., Lalonde, S.V., Bekker, A., Konhauser, K.O., Lyons, T.W., 2013. Proterozoic ocean redox and biogeochemical stasis. Proceedings of the National Academy of Sciences.

Rue, E.L., Smith, G.J., Cutter, G.A., Bruland, K.W., 1997. The response of trace element redox couples to suboxic conditions in the water column. Deep Sea Research Part I: Oceanographic Research Papers 44, 113–134.

Sageman, B.B., Meyers, S.R., Arthur, M.A., 2006. Orbital time scale and new C-isotope record for Cenomanian-Turonian boundary stratotype. Geology 34, 125–128.

Sahoo, S.K., Planavsky, N.J., Kendall, B., Wang, X., Shi, X., Scott, C., Anbar, A.D., Lyons, T.W., Jiang, G., 2012. Ocean oxygenation in the wake of the Marinoan glaciation. Nature 489, 546–549.

Schlanger, S.O., Arthur, M.A., Jenkyns, H.C., Scholle, P.A., 1987. The Cenomanian-Turonian Oceanic Anoxic Event, I. Stratigraphy and distribution of organic carbon-rich beds and the marine δ13C excursion, in Marine Petroleum Source Rocks, edited by J. Brooks and A. J. Fleet. Geological Society, London, Special Publications 26, 371–399.

Schlanger, S.O., Jenkyns, H.C., 1976. Cretaceous anoxic events: causes and consequences. Geologie en Mijnbouw 55, 179–184.

Scholle, P.A., Arthur, M.A., 1980. Carbon isotope fluctuations in Cretaceous pelagic limestones; potential stratigraphic and petroleum exploration tool. AAPG Bulletin 64, 67–87.

Scott, C., Lyons, T.W., 2012. Contrasting molybdenum cycling and isotopic properties in euxinic versus non-euxinic sediments and sedimentary rocks: Refining the paleoproxies. Chemical Geology 324-325, 19–27.

Scott, C., Lyons, T.W., Bekker, A., Shen, Y., Poulton, S.W., Chu, X., Anbar, A.D., 2008. Tracing the stepwise oxygenation of the Proterozoic ocean. Nature 452, 456-459.

Scott, C., Planavsky, N.J., Dupont, C.L., Kendall, B., Gill, B.C., Robbins, L.J., Husband, K.F., Arnold, G.L., Wing, B.A., Poulton, S.W., Bekker, A., Anbar, A.D., Konhauser, K.O., Lyons, T.W., 2013. Bioavailability of zinc in marine systems through time. Nature Geoscience 6, 125–128.

Sinninghe Damsté, J.S., Köster, J., 1998. A euxinic southern North Atlantic Ocean during the Cenomanian/Turonian oceanic anoxic event. Earth and Planetary Science Letters 158, 165–173.

Snow, L.J., Duncan, R.A., Bralower, T.J., 2005. Trace element abundances in the Rock Canyon Anticline, Pueblo, Colorado, marine sedimentary section and their relationship to Caribbean plateau construction and oxygen anoxic event 2. Paleoceanography 20, PA3005.

Takashima, R., Nishi, H., Huber, B.T., Leckie, M., 2006. Greenhouse World and the Mesozoic Ocean. Oceanography 19, 82–92.

Taylor, S.R., McLennan, S.M., 1995. The Geochemical Evolution of the Continental Crust. Reviews of Geophysics 33, 241–265.

Truesdale, V.W., 1978. Iodine in inshore and off-shore marine waters. Marine Chemistry 6, 1–13.

Truesdale, V.W., 1994. A re-assessment of redfield correlations between dissolved iodine and nutrients in oceanic waters and a strategy for further investigations of iodine. Marine Chemistry 48, 43–56.

Truesdale, V.W., Bale, A.J., Woodward, E.M.S., 2000. The meridional distribution of dissolved iodine in near-surface waters of the Atlantic Ocean. Progress in Oceanography 45, 387–400.

Turgeon, S., Brumsack, H.-J., 2006. Anoxic vs dysoxic events reflected in sediment geochemistry during the Cenomanian-Turonian Boundary Event (Cretaceous) in the Umbria-Marche Basin of central Italy. Chemical Geology 234, 321–339.

van Bentum, E.C., Hetzel, A., Brumsack, H.-J., Forster, A., Reichart, G.-J., Sinninghe Damsté, J.S., 2009. Reconstruction of water column anoxia in the equatorial Atlantic during the Cenomania-Turonian oceanic anoxic event using biomarker and trace metal proxies. Palaeogeography, Palaeoclimatology, Palaeoecology 280, 489–498.

Van Cappellen, P., Ingall, E.D., 1994. Benthic Phosphorus Regeneration, Net Primary Production, and Ocean Anoxia: A Model of the Coupled Marine Biogeochemical Cycles of Carbon and Phosphorus. Paleoceanography 9, 677–692.

Voigt, S., Erbacher, J., Mutterlose, J., Weiss, W., Westerhold, T., Wiese, F., Wilmsen, M., Wonik, T., 2008. The Cenomanian Turonian of the Wunstorf section (North Germany): global stratigraphic reference section and new orbital time scale for Oceanic Anoxic Event 2. Newsletters on Stratigraphy 43, 65–89.

Wijsman, J.W.M., Middelburg, J.J., Heip, C.H.R., 2001. Reactive iron in Black Sea Sediments: implications for iron cycling. Marine Geology 172, 167–180.

Wong, G.T.F., Brewer, P.G., 1977. The marine chemistry of iodine in anoxic basins. Geochimica et Cosmochimica Acta 41, 151–159.

Table 5.1: Geochemical data for Furlo.

Height (m)	$\delta^{13}C_{org}$ (‰)	C_{org} (wt%)	C_{inorg} (wt%)	Al (wt%)	Fe_T (wt%)	V (ppm)	Cr (ppm)	Mn (ppm)	Zn (ppm)	Mo (ppm)	Pyrite (wt%)	$\delta^{34}S_{py}$ (‰)	$\delta^{34}S_{CAS}$ (‰)	$\Delta^{34}S$ (‰)	Fe_{HR} (‰)	$\frac{Fe_{py}}{Fe_T}$	$\frac{Fe_{py}}{Fe_{HR}}$	$\frac{\frac{I}{Ca}}{(m)}$ (µm)
17.10	-27.38	0.49	86.59	NA	NA	NA	NA	NA	NA	NA	NA	NA	NA	NA	NA	NA	NA	1.26
15.80	NA	0.49	83.38	NA	NA	NA	NA	NA	NA	NA	NA	NA	21.9	NA	NA	NA	NA	0.47
15.40	-27.97	0.49	84.06	NA	NA	NA	NA	NA	NA	NA	NA	NA	21.8	NA	NA	NA	NA	0.31
15.00	NA	0.21	75.13	NA	NA	NA	NA	NA	NA	NA	NA	NA	20.4	54.6	NA	NA	NA	0.50
14.50	NA	0.23	65.06	NA	NA	NA	NA	NA	NA	NA	NA	-34.2	19.0	55.3	NA	NA	NA	0.05
13.56	-24.30	6.43	0.00	1.70	1.44	142	56	23	48	14	1.70	NA	NA	NA	1.00	0.69	0.80	NA
13.40	-24.05	2.63	0.00	0.89	0.88	164	57	23	67	16	1.18	-38.4	NA	NA	0.72	0.82	0.77	NA
13.20	-24.44	7.15	0.00	2.70	1.83	141	36	40	96	20	1.70	-42.6	NA	NA	1.00	0.55	0.80	NA
13.05	-23.46	9.69	0.00	1.42	1.68	157	28	32	74	18	1.88	-37.2	NA	NA	1.06	0.63	0.83	NA
12.70	-23.39	13.37	0.00	1.71	1.53	160	33	39	72	39	1.81	-36.8	NA	NA	1.16	0.76	0.73	NA
12.52	-25.76	2.81	0.00	1.22	0.63	151	51	34	191	26	0.65	NA	NA	NA	0.40	0.63	0.77	NA
12.35	-26.50	0.53	33.32	1.27	0.63	579	115	354	519	7	0.35	-48.0	NA	NA	0.42	0.67	0.40	NA
11.70	-26.66	0.35	87.23	NA	NA	NA	NA	NA	NA	NA	NA	-36.4	18.3	63.9	NA	NA	NA	0.01
11.65	-26.45	0.38	83.32	NA	NA	NA	NA	NA	NA	NA	NA	-45.6	17.7	64.5	NA	NA	NA	0.28
8.90	NA	0.38	90.27	NA	NA	NA	NA	NA	NA	NA	NA	-46.8	16.4	NA	NA	NA	NA	0.14
8.85	NA	0.43	1.27	1.20	0.61	650	129	226	761	5	0.33	-46.5	NA	NA	0.31	0.51	0.50	NA
7.95	NA	0.57	0.00	1.00	0.49	538	129	115	314	6	0.23	NA	NA	NA	0.24	0.50	0.44	NA
7.55	-27.03	0.44	94.66	NA	NA	NA	NA	NA	NA	NA	NA	NA	15.8	NA	NA	NA	NA	0.23
5.00	-27.34	0.40	94.33	NA	NA	NA	NA	NA	NA	NA	NA	NA	15.9	62.0	NA	NA	NA	0.25
4.90	-27.09	2.18	88.93	NA	NA	NA	NA	NA	NA	NA	NA	-46.1	NA	NA	NA	NA	NA	0.16
3.85	-26.92	0.42	92.88	NA	NA	NA	NA	NA	NA	NA	NA	-49.2	16.5	62.5	NA	NA	NA	0.67

Table 5.1: *Continued*

Height (m)	$\delta^{13}C_{org}$ (‰)	C_{org} (wt%)	C_{inorg} (wt%)	Al (wt%)	Fe_T (wt%)	V (ppm)	Cr (ppm)	Mn (ppm)	Zn (ppm)	Mo (ppm)	Pyrite (wt%)	$\delta^{34}S_{py}$ (‰)	$\delta^{34}S_{CAS}$ (‰)	$\Delta^{34}S$ (‰)	Fe_{HR} (‰)	$\frac{Fe_{py}}{Fe_T}$	$\frac{Fe_{py}}{Fe_{HR}}$	$\frac{\frac{I}{Ca}\ (\mu m)}{(m)}$
3.80	NA	0.54	2.11	1.17	0.53	541	121	118	506	4	0.30	-45.2	NA	NA	0.27	0.51	0.53	NA
1.35	-28.12	0.42	92.44	NA	NA	NA	NA	NA	NA	NA	NA	-46.0	16.7	NA	NA	NA	NA	0.63
1.25	-27.14	1.28	30.53	1.11	0.49	581	201	140	964	9	0.37	-45.2	NA	NA	0.33	0.67	0.53	NA
0.10	-27.42	1.94	88.32	NA	NA	NA	NA	NA	NA	NA	NA	NA	16.0	NA	NA	NA	NA	0.13
0.00	-26.36	0.74	91.05	NA	NA	NA	NA	NA	NA	NA	NA	-51.0	16.6	NA	NA	NA	NA	0.59

Chapter 6

Iron isotope and trace metal records of iron cycling in the proto-North Atlantic during the Cenomanian-Turonian oceanic anoxic event (OAE-2)

Abstract

The global carbon cycle during the mid-Cretaceous (~125–88 million years ago, Ma) experienced numerous major perturbations linked to increased organic carbon burial under widespread, possibly basin-scale oxygen deficiency and episodes of euxinia (anoxic and H_2S-containing). The largest of these episodes, the Cenomanian-Turonian boundary event (ca. 93.5 Ma), or oceanic anoxic event (OAE) 2, was marked by pervasive deposition of organic-rich, laminated black shales in deep waters and in some cases across continental shelves. This deposition is recorded in a pronounced positive carbon isotope excursion seen ubiquitously in carbonates and organic matter. Enrichments of redox-sensitive, often bioessential trace metals, including Fe and Mo, indicate major shifts in their biogeochemical cycles under reducing conditions that may be linked to changes in primary production. Iron enrichments and bulk Fe isotope compositions track the sources and sinks of Fe in the proto-North Atlantic at seven localities marked by diverse depositional conditions. Included are an ancestral mid-ocean ridge and euxinic, intermittently euxinic, and oxic settings across varying paleodepths throughout the basin. These data yield evidence for a reactive Fe shuttle that likely delivered Fe from the shallow shelf to the deep ocean basin, as well as (1) hydrothermal sources enhanced by accelerated seafloor spreading or emplacement of large igneous province(s) and (2) local-scale Fe remobilization within the sediment column. This study, the first to explore Fe cycling and enrichment patterns on an ocean scale using iron isotope data, demonstrates the complex processes operating on this scale that can mask simple source-sink relationships. The data imply that the proto-North Atlantic received elevated Fe inputs from several sources (e.g., hydrothermal, shuttle and detrital inputs) and that the redox state of the basin was not exclusively euxinic, suggesting previously

unknown heterogeneity in depositional conditions and biogeochemical cycling within those settings during OAE2.

Introduction

The Late Cretaceous greenhouse interval peaked during the late Cenomanian and early Turonian, and the Cenomanian-Turonian boundary coincides with a major perturbation of the global carbon cycle (Arthur et al., 1988; Schlanger et al., 1987; Scholle and Arthur, 1980) reflected in extensive deposition of laminated black shales. These perturbations resulted from either increased primary production (Schlanger and Jenkyns, 1976), enhanced organic matter preservation under oxygen-deficient depositional conditions (Barron, 1983; Schlanger et al., 1987), or some combination of both. Associated with elevated temperatures (Huber et al., 1995) and thus lower oxygen solubility, along with enhanced carbon delivery, the environmental conditions of the basinal proto-North Atlantic became anoxic and euxinic (with free H_2S in the water column) at a scale large enough to be termed an oceanic anoxic event or OAE (Schlanger and Jenkyns, 1976; Jiménez Berrocoso et al., 2008; Hetzel et al., 2009). The result was a proliferation of organic-rich, laminated black shales in the deep basin and less commonly across continental shelves, particularly at sites along the tropical Atlantic shelves—i.e., the southern part of the proto-North Atlantic Basin. A sharp increase in organic matter burial is reflected in a global positive isotope excursion expressed in both organic and inorganic carbon across the basin (Arthur et al., 1988; Schlanger and Jenkyns, 1976). The prominent isotope excursion, particularly its expression in the organic record, is especially useful for correlating basin-wide stratigraphy in the absence of biostratigraphic

controls at paleodepths greater than the carbonate compensation depth (Kuhnt et al., 2005).

A common model for the cause of OAE2 calls upon the expansion of hydrothermal activity (Adams et al., 2010; Frijia and Parente, 2008; Jones and Jenkyns, 2001; Kuroda, 2007; MacLeod et al., 2008; Sinton and Duncan, 1997; Turgeon and Creaser, 2008), resulting in increased concentrations of hydrothermal Fe in the photic zone prior to the onset of the OAE and a concomitant increase in primary production (Leckie et al., 2002; Snow et al., 2005). Studies of the modern ocean tell us that primary production over vast regions can be limited by the availability of Fe, an essential micronutrient (Martin and Fitzwater, 1988). By analogy, hydrothermal Fe is hypothesized as a possible explanation for the increased organic carbon deposition that marks the OAE. The coincidence of the emplacement of the Caribbean large igneous province (LIP) with sedimentary trace metal enrichments (Snow et al., 2005) and marked radiogenic isotope excursions for Nd (Frijia and Parente, 2008; Kuroda, 2007; MacLeod et al., 2008) and non-radiogenic isotope excursions for Sr and Os isotopes (Jones and Jenkyns, 2001; Turgeon and Creaser, 2008) are consistent with a volcanogenic trigger for large-scale ocean anoxia. However, recent work suggests there is also a significant increase in continental weathering or detrital inputs during the event (Blättler et al., 2011; Jones and Jenkyns, 2001) which may complicate these isotopic signals (as reviewed in Jenkyns, 2010).

Importantly, Fe enrichments do not necessarily imply enhanced hydrothermal activity. Therefore, we need to investigate possible Fe sources in great detail. For example, enhanced remobilization of Fe from coastal sediments is an alternative model for the delivery of Fe to the open ocean during ocean-scale anoxia. Benthic Fe fluxes correlate positively with rates of organic matter oxidation until the onset of bacterial

sulfate reduction, and bottom-water oxygen concentrations are inversely proportional (Elrod et al., 2004; Severmann et al., 2010) Consistent with a relationship to high availability of organic matter, modern oxygen minimum zones (OMZ) demonstrate elevated Fe concentrations in the water column (Blain et al., 2008; Bruland et al., 2005; Moffett et al., 2007). The expansion of oceanic anoxia thus provides a positive feedback for enhanced Fe supply from the continental shelf to the open ocean. The mechanistic underpinnings of this model have emerged from careful studies of the Black Sea, the modern world's largest euxinic basin, wherein diverse evidence points to net transport (shuttling) of reactive Fe from shallow oxic and suboxic shelf settings to deep euxinic waters (as reviewed in Lyons and Severmann, 2006). Detailed measurements and models have specifically fingerprinted and quantified net transport of reactive Fe from the shelf to the basin where it is captured through pyrite formation in the water column (Anderson and Raiswell, 2004; Canfield et al., 1996; Wijsman et al., 2001). The shallow, organic carbon-lean, oxic-to-suboxic sites along the basin margin show correlative loss of Fe from the sediment pore waters and thus from the bulk sediments through reductive cycling in the absence of appreciable dissolved H_2S.

Our goal is to evaluate the relative roles of basinal redox controls and increased volcanic activity in the enhanced delivery of Fe during the OAE. To better understand the origin of Fe enrichments we have investigated sections from seven different locations (Fig. 6.1) representing continental shelf, continental rise, and deep abyssal plain settings spanning the Cenomanian-Turonian boundary and associated with clear records of OAE2. Most of the sites have previously been described to have enrichments in redox-sensitive trace metals such as Fe, Cu, Mo, and V (Brumsack, 1980; Hetzel et al., 2009; Jiménez Berrocoso et al., 2008; van Bentum et al., 2009), and several sites show organic biomarker evidence for pervasive photic-zone euxinia prior to and throughout the OAE

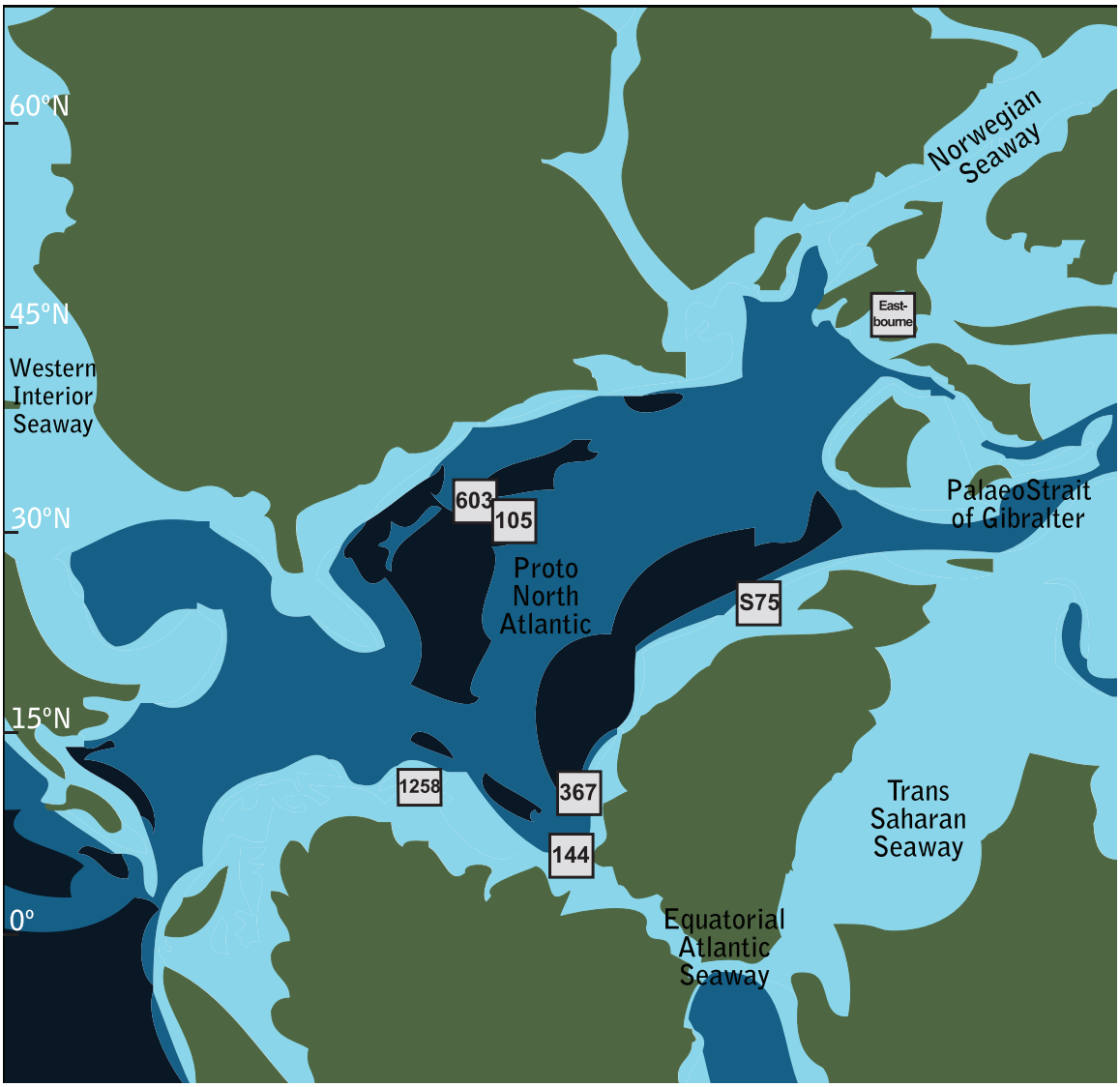

Figure 6.1: Sample location for the seven sections investigated within the proto-North Atlantic; paleogeography adapted from Trabucho Alexandre et al. (2010). The blue gradient indicates estimated water depths with the lighter colors indicating shallower depths and greater depths marked with darker colors; the landmasses are shaded green and gridded.

(Kuypers et al., 2002; Pancost et al., 2004; Sinninghe Damsté and Köster, 1998). Here we couple Mo concentration data to our Fe analyses as an independent constraint on the local depositional redox conditions. We are using Fe concentrations and isotopes to understand the basin-wide Fe geochemistry in the proto-North Atlantic and specifically the pathways

of Fe cycling, from source to sink. Included in this mix is the possible role of an iron "shuttle" analogous to that operating today in the Black Sea but on the scale of a large ocean basin. This is the first exploration of the shuttle model at such a scale and under the likely strong influence of hydrothermal contributions. Hydrothermal inputs may mask the shelf-to-basin shuttling of Fe that is perhaps best seen in marginal marine basins and epicontinental seaways under a favorable source-to-sink mass balance.

Background: Iron isotopes as a source tracer

Elevated bulk iron (Fe_T) to aluminum (Al) ratios are a simple indicator of sedimentary Fe enrichment beyond the continental crustal average of ~0.5 (Taylor and McLennan, 1995; Turekian and Wedepohl, 1961) and are among the most dependable indicators of ancient redox conditions and Fe cycling in those settings (Lyons and Severmann, 2006; Raiswell et al., 2008). The differentiation of multiple Fe sources for the enrichment, however, requires additional proxies that can help refine our understanding of environmental conditions and the associated enrichment mechanism(s). Iron isotopes can be important tracers of Fe inputs in these studies because each potential source, in this case hydrothermal fluids versus diagenetic Fe released from (and remobilization within) sediments, should have distinct Fe isotope properties.

The majority of hydrothermal fluids measured to date show only minimal deviation in their Fe isotope compositions ($\delta^{56}Fe$, see below for further explanation) relative to average igneous rocks (~0.0‰ to -0.5‰) (Beard et al., 2003; Severmann et al., 2004; Sharma et al., 2001). Deviations from this value are typically only observed for low temperature fluids, which have much lower Fe concentrations; therefore it would be difficult for this source to significantly alter the isotope geochemistry. In the

modern oxic ocean the isotopic compositions of freshly precipitated Fe in hydrothermal plumes suggest a more complex picture as different mineral phases, such as pyrite and Fe oxides, form upon mixing of hot fluids with cold seawater. However, despite the potential for isotopic fractionation during hydrothermal fluid entrainment into the bottom water, Fe isotope compositions of distal hydrothermal plume particles have been shown to span a relatively narrow range, with values approaching the fluid source (Bennett et al., 2009; Severmann et al., 2004). The geologic record confirms that sediments containing hydrothermally sourced Fe also span a narrow range in δ^{56}Fe values similar to modern hydrothermal fluids, but show a large range in Fe_T/Al ratio (Czaja et al., 2010; Halverson et al., 2011; Johnson et al., 2008). Consequently, the Fe isotope composition of hydrothermally impacted sediments is relatively invariant, regardless of the degree of Fe enrichment. It is difficult to distinguish detrital inputs from hydrothermal contributions using Fe isotopes alone; however, the use of Fe_T/Al ratios helps us discern relative contributions—with detrital Fe_T/Al values of ~0.5 and hydrothermal values typically much greater than 0.5. An increase in detrital material via weathering patterns could add an additional complication because hydrothermal isotopic and enrichment signatures in a marginal environment can be diluted by enhanced continental delivery.

The iron shuttle initiates with preferential release of isotopically light Fe during reduction of oxide phases coupled to diagenetic carbon remineralization beneath the oxic/suboxic shelfal bottom waters of the source region (Severmann et al., 2006). As a result, the residual bulk sedimentary Fe becomes preferentially depleted in total Fe and isotopically enriched with a positive δ^{56}Fe signature. The remobilized, shuttled light Fe is subsequently captured through water-column pyrite formation in the euxinic basin (Lyons, 1997). Iron capture in the sulfidic water column is near quantitative, and the mass balance implies that the isotopic composition of the precipitated Fe

remains indistinguishable from the dissolved source. As a consequence, the sediments show increasingly light Fe isotope values with progressive Fe enrichments (Lyons and Severmann, 2006; Severmann et al., 2008). This pattern, specifically the inverse relationship between $\delta^{56}Fe_T$ and Fe_T/Al, can provide a robust fingerprint of Fe shuttling in ancient basins (Czaja et al., 2010; Duan et al., 2010). However, the role and fingerprints of the shuttle on the scale of a deep ocean OAE are not well studied—a gap that motivated the approach taken here.

Sampling: Sites and collection protocols

Here we present data from seven sample localities deposited under variable redox conditions. The sample locations were strategically selected with an eye toward wide spatial distribution in the proto-North Atlantic (Fig. 6.1). Most of the samples used for this study were obtained from DSDP and ODP sample archives. Our existing sample collections (DSDP sites 105, 144, 367 and 603B and ODP site 1258 [Berger and von Rad, 1972; Hayes et al., 1972; Hollister et al., 1972; Shipboard Scientific Party, 2004; Thurow, 1988; van Hinte et al., 1987]) were complemented with additional samples obtained from the core repository in Bremen, Germany, in 2008. Samples from Tarfaya core S75 were collected as part of the oil shale campaign undertaken by Shell International Exploration and Production (Kuhnt et al., 1997), and the Eastbourne outcrop section was logged and sampled at the Gun Gardens locality in East Sussex, England. Three sites were located in the northern region of the proto-North Atlantic and four from the southern region (Fig. 6.1).

The Eastbourne locality from the northern proto-North Atlantic represents a shallow oxic shelf (Paul et al., 1999; Tsikos et al., 2004) with very low total organic

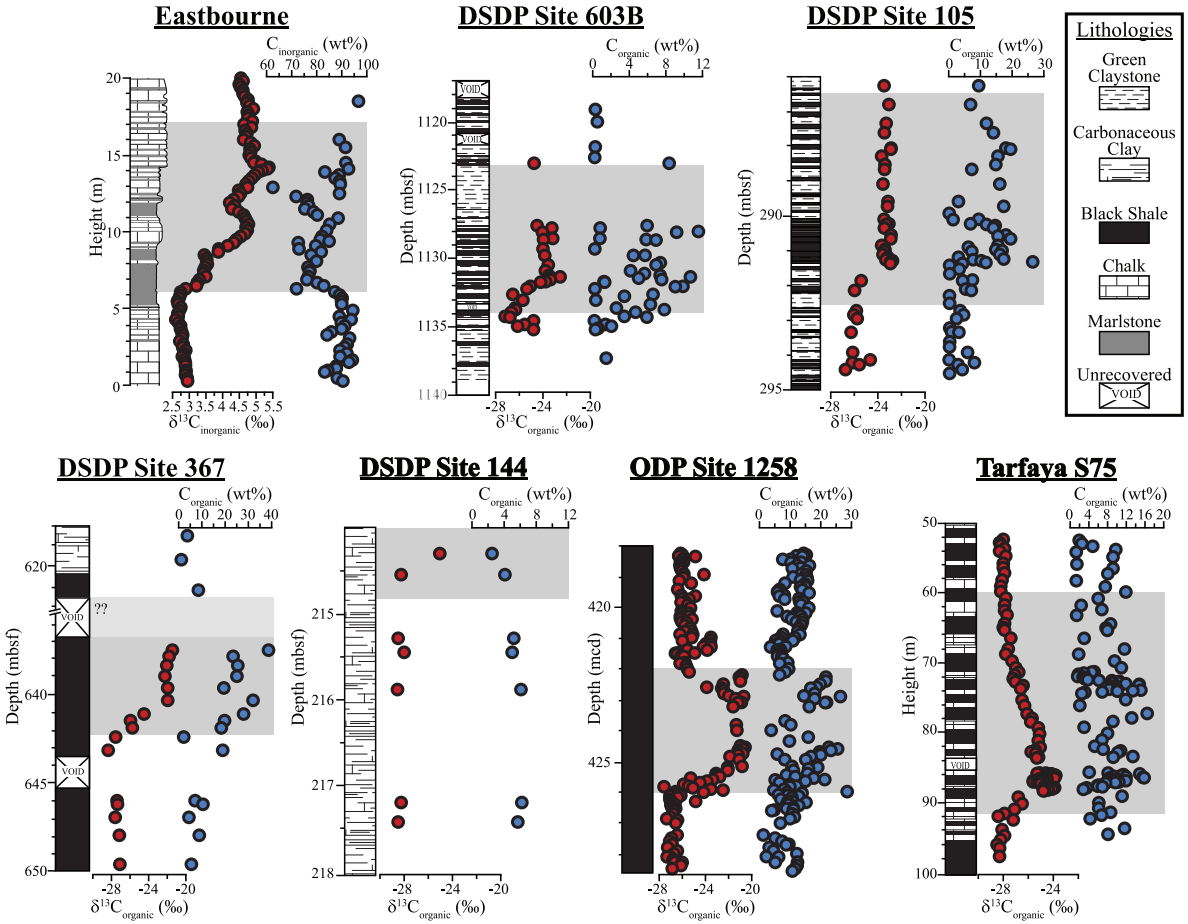

Figure 6.2: Lithostratigraphy and carbon isotope stratigraphy. The rapid positive shift in the $\delta^{13}C$ of organic carbon (●) denotes the excursion of OAE-2 (gray box), although the termination of the event is not always well defined. Total organic carbon is also plotted (●). Note: the positive $\delta^{13}C$ shift at Eastbourne is represented in the data for inorganic carbon, with inorganic carbon concentrations also plotted. Eastbourne lithostratigraphy and carbon isotopes from Tsikos et al. (2004), DSDP 603B and DSDP 105 from Kuypers et al. (2004) with additional lithostratigraphy from van Hinte et al. (1987), DSDP 367 from Kuypers et al. (2002), ODP 1258 carbon isotopes from Erbacher et al. (2005) and lithostratigraphy from Shipboard Scientific Party. (2004), Tarfaya S75 from Kuhnt et al. (2005).

carbon (TOC) content (Fig. 6.2; TOC of 0.1 to 0.2 wt. %) and lithologies (Fig. 6.2) dominated by bioturbated nannofossil (coccolithophore) calcareous ooze and clay (Gale, 1996; Keller et al., 2001). Despite fundamental differences in the depositional environment of this oxic site relative to our other localities, carbonate-C and organic-C isotope records of OAE2 are well correlated with those from the other sites (Fig. 6.2).

Two northern proto-North Atlantic sites, Deep Sea Drilling Project (DSDP) sites 603B and DSDP 105, have mixed lithologies that document fluctuating redox conditions. Deposition during the OAE at both sites is marked by alternating organic-poor green claystone (TOC ~1 wt. %) and organic-rich black shales (TOC up to 25 wt. %) (Fig. 6.2) with consistently low carbonate abundance (<10 wt. %) (Herbin et al., 1987), suggesting periodic anoxia/euxinia and possible orbital forcing of organic carbon deposition and associated depositional redox (Kuypers et al., 2004). The main distinction between these two sites is that 603B was under stronger influence of coastal oceanic processes, and the sediments are therefore distinctly hemipelagic (Herbin et al., 1987). The intermittence of the laminated, metal-enriched black shales, along with biomarker evidence (Kuypers et al., 2004), suggests that this part of the North Atlantic was only periodically euxinic during the OAE. Consistent with this inferred redox-oscillation, the green claystones (Fig. 6.2) are bioturbated and do not show enrichments of redox-sensitive metals, suggesting oxic conditions of deposition (Kuypers et al., 2004); this alternation occurs at very regular intervals (0.11 - 0.13 m), and the lithologies before and after the OAE at both sites are dominantly bioturbated organic-lean green claystones with some fine layers of organic rich shales.

Black shale deposition was particularly prominent in the southern portion of the proto-North Atlantic during the OAE (Trabucho Alexandre et al., 2010). Of the four sites from the southern part of the basin (Fig. 6.1), DSDP site 367 near Cape Verde was

the deepest, with a paleodepth of ~3700 m located on the abyssal plain in the vicinity of the ancestral mid-ocean ridge (Kuypers et al., 2002). Even before the onset of the OAE (as marked by the positive C-isotope excursion, Fig. 6.2), sediments show pronounced lamination (Fig. 6.2; (Herbin et al., 1986)) and high TOC that increases to exceptionally high concentrations of up to 40 wt. % during the event. Previously noted at this site was the appearance of isorenieratene and chlorobactene, sulfurbound molecular fossils, produced by brown and green strains of phototrophic sulfur bacteria, indicating that euxinic conditions extended at least episodically into the photic zone during the OAE (Kuypers et al., 2002).

ODP site 1258 (all samples from 1258A) from the Demerara Rise is marked by finely laminated black shales that extend before, during, and after OAE2, with TOC contents reaching maximum values of 30 wt. % during the event. Previous records of Fe enrichment, the S isotope compositions, and prevalent lamination indicate persistent euxinia during the OAE at this site (Hetzel et al., 2009) while a positive Nd isotope excursion (MacLeod et al., 2008) may hint at hydrothermal contributions to the local bottom waters. The core depths [specifically meter core depth (MCD) below the seafloor] for data presented here for Fe and Mo were adjusted to correlate with the carbon isotope stratigraphy of Erbacher et al. (2005) using the method presented in the supplementary material of MacLeod et al. (2008).

S75 from Tarfaya, Morocco, is a relatively shallow, shelfal site (<200 m paleo-water depth; Kuhnt et al., 1997) with high sedimentation rates exceeding 10 cm/ky, making its accumulation rates for organic matter the world's highest known for the C/T transition. Sediments are comprised of organic rich (TOC up to 15 wt. %) dark laminated chalks and carbonate-diluted shales (Kolonic et al., 2005) intercalated with non-laminated, lighter colored limestones (Fig. 6.2). Isorenieratane abundance increases

dramatically up section in a nearby core (Tarfaya S13) during the OAE, indicating photic zone euxinia, although there is a slight increase just before the OAE, and concentrations remain high slightly after the OAE (Kuypers et al., 2002). Previously, a similar Tarfaya site (section S57) was analyzed by Jenkyns et al., (2007) for Fe, C and N isotopes. Details are discussed below.

Lastly, sediments at another open ocean site from the southern proto-North Atlantic, DSDP 144, were deposited at a relatively shallow paleodepth of ~1300 m on the ancestral mid-ocean ridge (Berger and von Rad, 1972) , supporting the likelihood of high hydrothermal inputs at this site. Sediments consist of laminated carbonaceous limestone and calcareous clay with TOC contents reaching 30 wt.% during the OAE. Isorenieratane is present at this site, although the abundances are lower than those at site 367 (Kuypers et al., 2002).

Analytical methods

Once inspected and cleaned, the samples were powdered using a trace metal-clean ceramic ball mill and ashed for 12 hours at ~850°C to volatilize any organic material and sulfides. The samples were then weighed to determine loss on ignition, and 50-75 mg of ashed sample were digested by a standard three-acid sequential protocol using HNO3/HCl/HF at ~150°C. All acids used were Aristar/trace metal clean. Fully digested samples were analyzed on an Agilent 7500ce ICP-MS (Inductively Coupled Plasma-Mass Spectrometer) using H2 and He in the collision cell. Standard reference materials (SDO-1 and SCO-1 shales) were digested and analyzed with each set of extractions, and in all cases were within the accepted analytical error for all elements: Fe and Al had % errors of less than ±5, and Mo had an error of ±8, which is better than the certified value. We

emphasize total Fe in this study because most of the cores have oxidized since collection, which precludes detailed speciation such as that of Poulton and Canfield (2005). Fortunately, the depositional and diagenetic conditions of interest are well expressed in the Fe properties of the bulk sediment (Lyons and Severmann, 2006).

Splits from the previously dissolved materials were used to measure the Fe isotope composition of the bulk sample ($\delta^{56}Fe_T$). To eliminate matrix effects, samples were purified using anion exchange resin (0.5 ml of Biorad AGMP-1 M) and a standard ion chromatography protocol for Fe separation (Arnold et al., 2004; Skulan et al., 2002). Column yields were monitored before and after chromatographic purification using a modified ferrozine colorimetric method (Stookey, 1970; Viollier et al., 2000) with UV-Vis spectrophotmetry (λ = 562nm). Samples with yields of 95% or better were dried down and diluted with 0.32 M HNO3 for isotopic analysis.

Isotopic compositions were measured on a Neptune Thermo Scientific MC-ICP-MS (Multiple Collector-Inductively Coupled Plasma-Mass Spectrometer) at Arizona State University using the methods described in Arnold et al. (2004). The samples were run in a 0.32 M HNO3 matrix at ~2-3 ppm Fe concentration and spiked with equal proportion of Cu standard for mass bias correction. We measured the certified international reference material IRMM-014 as a bracketing standard between each sample as a further monitor for accurate mass bias correction. Corrected data are reported relative to average igneous rock using the standard delta notation (Coplen, 2011):

$$\delta^{56}Fe(‰)=\left[\frac{(({}^{56}Fe/{}^{54}Fe)_{sample}}{(({}^{56}Fe/{}^{54}Fe)_{IgnRx}}\right]\text{-}1 \qquad \text{(Equation 6.1)}$$

The measured Fe isotope composition of IRMM-014 is $\delta^{56}Fe_T$ -0.09‰ on this scale (Beard et al., 2003) with a long-term internal precision of ±0.08‰ (2-STD).

Results and Discussion

This study is the most comprehensive Fe isotope study to date of an OAE, although not the first Fe isotope data set for OAE2 (Jenkyns et al., 2007) or Cretaceous black shales (Clayton et al., 2007). The uniqueness of this study lies with our inclusion of extensive data for Fe and Mo concentrations and samples from diverse settings and depositional conditions spanning from before, during, and after the event (Fig. 6.3). We begin our discussion by reconstructing paleoenvironmental conditions using Mo concentrations. These data provide an essential framework for interpreting the Fe-isotope and Fe_T/Al relationships and, specifically, for unraveling Fe sourcing during this time period.

Paleoredox environment of the proto-North Atlantic: Mo and biomarker records

The redox conditions at each site are independently constrained by previous studies (Brumsack, 1980; Hetzel et al., 2009; Kuhnt et al., 1997; Kuypers et al., 2004; Kuypers et al., 2002; Tsikos et al., 2004) and through our use of Mo abundances. Molybdenum provides an effective, independent constraint on the paleoredox conditions of the local settings (Scott et al., 2008). Specifically, no enrichment (i.e., crustal values of 1 to 2 ppm) is expected under oxic conditions compared to enrichments of 10 to 30 ppm in 'suboxic' settings (defined by low oxygen bottom waters but with H_2S confined to the pore waters) and the roughly 40 to hundreds of ppm levels that characterize euxinia (Lyons et al., 2009). Molybdenum enrichments are controlled by ambient redox conditions in the water column and sediment, in particular the availability of hydrogen sulfide and organic carbon and the starting concentration of Mo in the basin or ocean [e.g., (Algeo and Lyons, 2006; Helz et al., 1996; Lyons et al., 2009)]. Euxinic

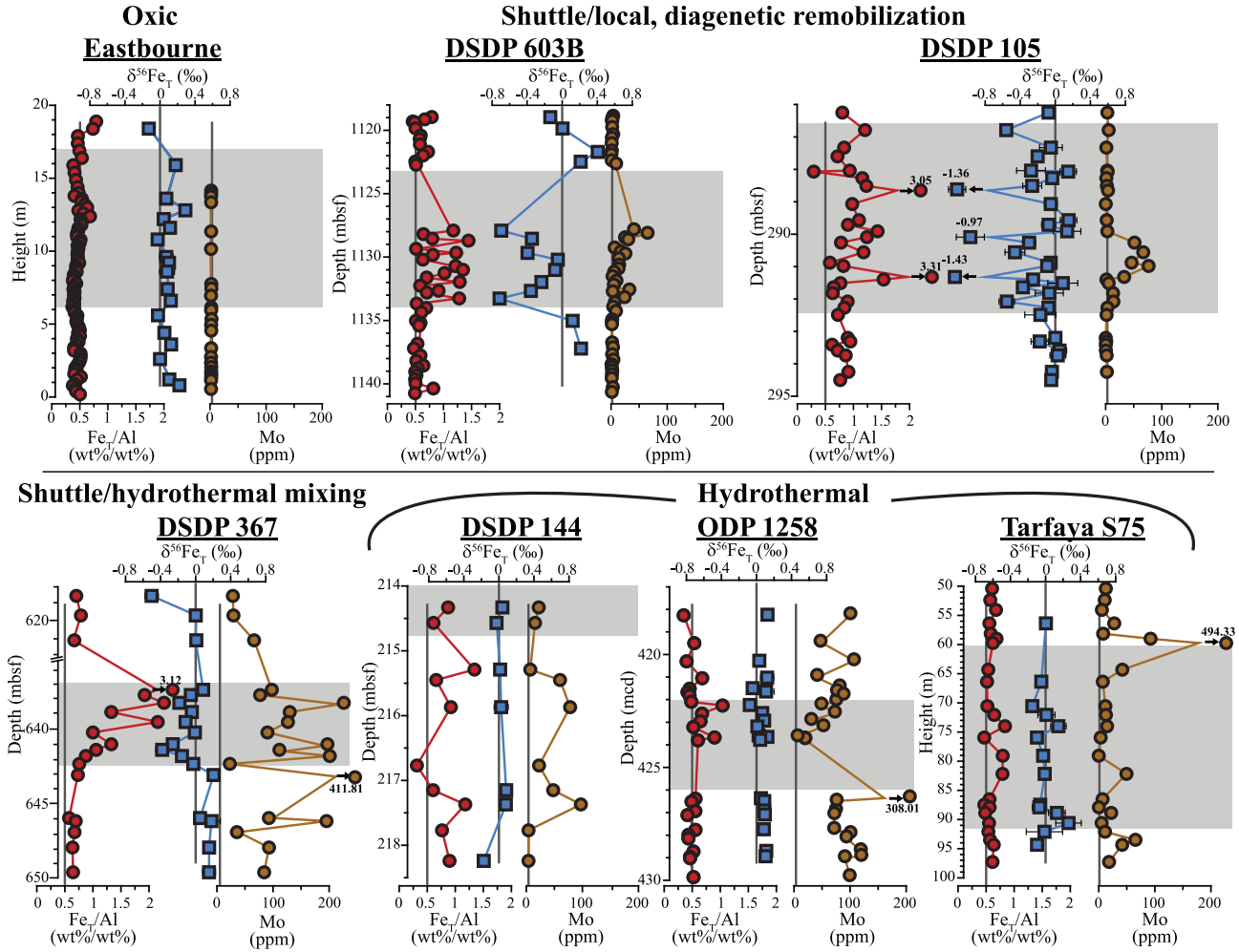

Figure 6.3: Detailed Fe and Mo data for each site plotted stratigraphically. The gray bar indicates the OAE as defined by the carbon isotope stratigraphy. The solid lines indicate the crustal average for each elemental concentration. The $\delta^{56}Fe_T$ data are shown with horizontal error bars (2 SD).

enrichments are diagnostically high and variable, principally tracking TOC availability and the dissolved Mo inventory in the local and/or global setting.

Our Mo data (Fig. 6.3) confirm previous findings that euxinic conditions were more pervasive in the southern part of the proto-North Atlantic than in the north (Trabucho Alexandre et al., 2010). The highest concentrations were observed at site 367 (maximum value of 412 ppm), which is also the site with the highest TOC concentrations and reported occurrences of the molecular fossils isorenieratane and chlorobactane, suggesting that hydrogen sulfide was present in the water column and extended into the photic zone (Kuypers et al., 2002). Although the maximum TOC concentrations and biomarkers indicative of shallow euxinia are associated with the OAE proper, they initiate before the onset of the OAE as delineated by the positive C-isotope excursion (Fig. 2 and Kuypers et al., 2002). Molybdenum enrichments consistent with euxinic conditions are observed at all four southern sites even before the expansion of ocean anoxia that defines the OAE, in contrast to the limited evidence for euxinia in the north. A notable feature of the Demarara Rise (1258) and Tarfaya (S75) sites is a marked decrease in Mo concentrations during the OAE, an observation that was also highlighted by Hetzel et al. (2009) for other sites along the Demerara Rise shelf transect. The lack of a concurrent decrease in TOC across these intervals suggests that—rather than waning euxinia or a drop in TOC content—these muted Mo enrichments reflect a shift in the Mo inventory, perhaps on a broad scale. If we are correct, this Mo pattern marks a transition from dominantly local to regional/oceanic euxinia and back, with a corresponding depletion in the seawater Mo reservoir during the period of expanded euxinia. Such expansion may have extended across a wide part of the ocean. Site 367 shows concentrations as high as 200 ppm during the OAE, which is still a drop compared to the pre-OAE enrichments.

The incomplete core recovery at this site, however, may preclude evidence for the full drop in Mo enrichment we expect during the OAE.

At the northern sites 603B and 105, Mo enrichments are confined to the OAE (Fig. 6.3). Frequent fluctuations in Mo concentrations at these sites during the OAE generally match variations in lithology and TOC contents, suggesting varying redox conditions rather than reservoir effects. At the Eastbourne locale, Mo shows uniformly low values throughout the sampled interval, with concentrations typically below the 1 to 2 ppm crustal average. These data, along with the prevailing Fe relationships (see below), indicate that this site was dominantly if not persistently oxic. In fact, the lowest values for Mo fall below the crustal average and likely reflect average detrital inputs with concentrations reduced by substantial carbonate dilution. However, a suite of redox proxies that are sensitive to the early onset of ocean deoxygenation (specifically, Ca-normalized I, Ce, and Mn concentrations) suggest that even the shallow waters at Eastbourne experienced some degree of oxygen depletion before and during the OAE (Lu et al., 2010), although there is no indication that bottom water ever became anoxic or euxinic at this site. We can now view the Fe distributions and likely sources among these sites within a paleoredox context informed by straightforward patterns of Mo enrichment.

Iron release from the oxic continental shelf

We begin our discussion of Fe with the most oxic site. The coastal Eastbourne locale shows Fe_T/Al ratios typically at or below the continental crustal average of ca. ~0.5. This average is assumed to represent typical siliciclastic (detrital) input. The Eastbourne samples are complicated by their high carbonate contents (mean ~85%); but Fe_T/Al averages for carbonates are, if anything, typically elevated (~0.9) compared

with average continental crust (Turekian and Wedepohl, 1961). In this light, the average Fe_T/Al ratios of 0.46 over the ~20 meters are consistent with net loss of Fe from the sediments. Loss of Fe, which should be isotopically light (Severmann et al., 2010), is further indicated by the observation that the $\delta^{56}Fe_T$ data cluster slightly above 0‰ with an average of +0.08‰ (Fig. 6.3 and 6.4). Sedimentary Fe reduction promoted Fe build up in the pore fluids and, with pervasive bioturbation, transport from the sediment (Lyons and Severmann, 2006; Severmann et al., 2010). These conditions were ultimately facilitated by a lack of appreciable sulfate reduction due to the overall paucity of organic matter at this site (average TOC contents are 0.12 wt%). The results at Eastbourne for Fe_T/Al and $\delta^{56}Fe_T$ are invariant before, during, and after the OAE, defined by the $\delta^{13}C$ excursion (Fig. 6.2). The lowest $\delta^{56}Fe_T$ value is from a sample that also shows slightly higher Fe_T/Al ratios and could reflect transient euxinia. Overall, the Eastbourne data point to dominantly oxic deposition, with robust signals that are not complicated by the very high carbonate contents.

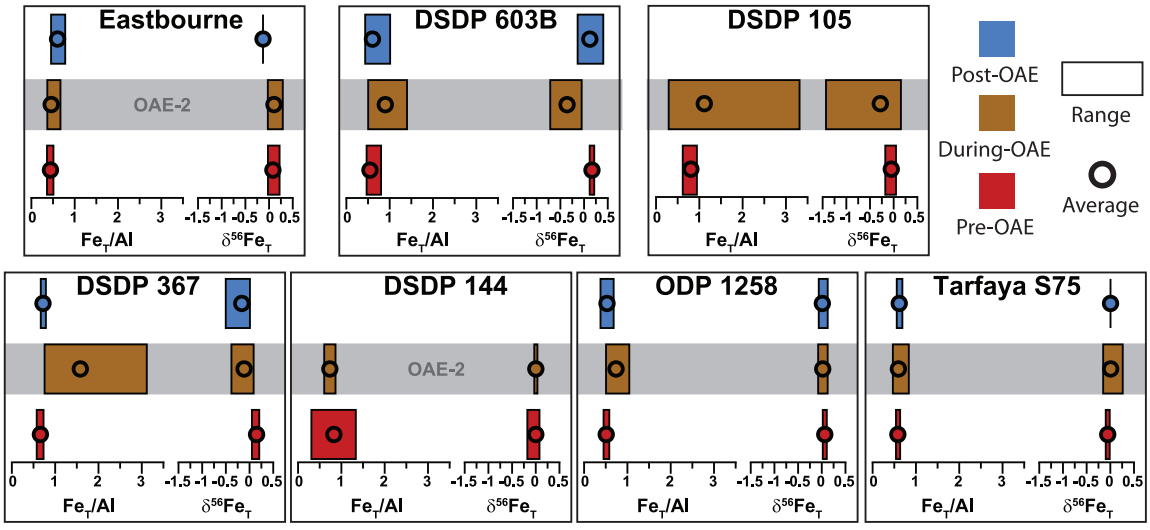

Figure 6.4: Averages and ranges for the iron isotope data and Fe concentrations (relative to Al) at each section before, during, and after OAE-2.

Iron cycling in the southern basin: hydrothermal sources and euxinic sinks

Our highest Fe_T/Al ratios, with several samples exceeding values of 2, were measured during the OAE at the southern site 367 and site 105 in the north (Fig. 6.3 and 6.4). Surface sediments representing the current euxinic stage in the Black Sea, our best modern analog, have markedly elevated Fe_T/Al ratios when compared to average continental crust. The magnitude of the enrichment as driven by the Fe shuttle is constrained by sedimentation rates and the mass balance of the source-to-sink relationship (Lyons and Severmann, 2006; Raiswell and Anderson, 2005). Nevertheless, Fe_T/Al values exceeding 1.2, as we have observed during OAE2, are not recorded in the Black Sea and are only rarely observed throughout the Phanerozoic. As such, more extreme Fe enrichments, exceeding ~1.5, may be a flag signaling hydrothermal augmentation (Cruse and Lyons, 2004) or secondary remobilization within the sediment column. Broader tectonic and paleogeographic parameters must also be considered.

Due to its location on the ancestral mid-ocean ridge, DSDP site 144 is the best candidate among our study sites for a strong hydrothermal signal from ridge-style venting. This locale shows high Fe_T/Al ratios before the OAE (average 0.83), with smaller enrichments during the OAE (0.73) and marked variability in the magnitude of enrichment. All the Fe isotope data are relatively uniform, including the data corresponding with the Fe enrichments, with pre-OAE and syn-OAE $\delta^{56}Fe_T$ averages of 0.00‰. Because hydrothermal Fe and background detrital sources of Fe have similar isotopic properties, variations in Fe enrichment without parallel isotopic variability may be diagnostic of hydrothermal inputs. The pervasive euxinic conditions throughout the southern part of the proto-North Atlantic, in combination with the pattern of oceanic circulation, likely aided in the relatively short dispersal distance of hydrothermal Fe to the nearby southern sites with little associated isotope fractionation during transport.

The shelfal Fe shuttle has likely contributed to Fe inputs to at least one of our southern sites, specifically the deepest site 367, which has some of the most negative $\delta^{56}Fe_T$ values among the four southern sites (minimum $\delta^{56}Fe_T$ = -0.50‰). That said, the lack of a continuous negative shift in $\delta^{56}Fe_T$ that tracks the level of Fe enrichment argues for a shuttle signal that, if present, was typically swamped by hydrothermal Fe with a $\delta^{56}Fe_T$ near 0‰. The data at site 1258 (Fig. 6.4) do not argue for significant source variations based on the Fe isotope records before, during, and after the OAE (with averages of 0.09, 0.04, 0.07‰, respectively) despite Fe_T/Al ratios that increase significantly during the event (average pre-OAE: 0.50, during: 0.70, and post-OAE: 0.47). Clayton et al. (2007) analyzed Fe isotopes at another Demerara Rise site, ODP 1260, with low sample resolution that does not cover the OAE and methods that focused on separate Fe minerals. It is difficult therefore to compare their data to ours. The most reasonable interpretation is that the Fe delivered to this site is dominantly from a hydrothermal source, although a subtle negative shift at the end of the OAE may reflect input via the shuttle. The pronounced Mo enrichments suggest persistently euxinic deposition at this site before, during, and after the OAE. Comparatively low Fe enrichments before and after OAE2 likely mirror the inefficiency by which hydrothermal and/or shuttled Fe is transported to a locally euxinic site via the surrounding oxic ocean. In contrast, suppressed signals during the event reflect the 'competition' for hydrothermal and shuttled Fe under the spatially extensive sulfidic conditions in the southern portion of the proto-North Atlantic.

At the shallow Tarfaya shelf site S75, high sedimentation rates may have favored dilution of the hydrothermal signal by detritally sourced Fe, consistent with relatively smaller Fe enrichments compared to the other southern sites (Fig. 6.3 and 6.4). Despite its location on the continental shelf—and in contrast to our northern shelf site from

Eastbourne—there is no indication that site S75 acted as an iron source at any time around OAE2. These Fe isotope data agree well with those generated for a different Tarfaya shelf section, S57, by Jenkyns et al., (2007). They too show relatively small isotopic variability with values near 0‰. In general, the details of the Fe mass balance, the transport mechanisms, and the local/regional overprints, including spatially varying hydrothermal inputs, remain incompletely defined pending additional analyses at other sites and more general exploration of the mechanisms behind benthic Fe fluxes and basin-ward transport. Nevertheless, the relatively stable $\delta^{56}Fe_T$ throughout the measured section (overall average of 0.00‰) and only slightly elevated but consistent Fe_T/Al (overall average of 0.60), our data are best explained by high terrigenous inputs against a relatively small source of hydrothermal Fe, which mildly enriched the Fe without shifting the isotopic composition appreciably.

Despite our claim above for possible inputs via the Fe shuttle, the narrow range in $\delta^{56}Fe_T$ between -0.5 and 0.0‰ at site 367, despite a large range in Fe_T/Al (0.57 to 3.12), is most consistent with a signal dominated by hydrothermal sources for the excess reactive Fe during OAE2. The same hydrothermal dominance likely applies for the other southern sites (DSDP 144, ODP 1258, and Tarfaya S75). All four sites show moderate (in the case of S75) to intense (site 367) enrichments in reactive Fe (Fig. 6.3 and 6.4), coupled to poor correlation between Fe_T/Al and $\delta^{56}Fe_T$ (Fig. 6.5) and Fe isotope compositions near 0‰. These relationships are even expressed by the samples with highly elevated Fe_T/Al ratios. The source of the Fe might be linked to faster spreading rates and attendant increased hydrothermal venting within the basin (Conrad and Lithgow-Bertelloni, 2007) or emplacement of the Caribbean LIP in the equatorial Eastern Pacific (Sinton and Duncan, 1997), which may have triggered OAE2, although long-distance Fe transport is challenged by the low solubility of Fe in euxinic and, in particular, oxic waters. While

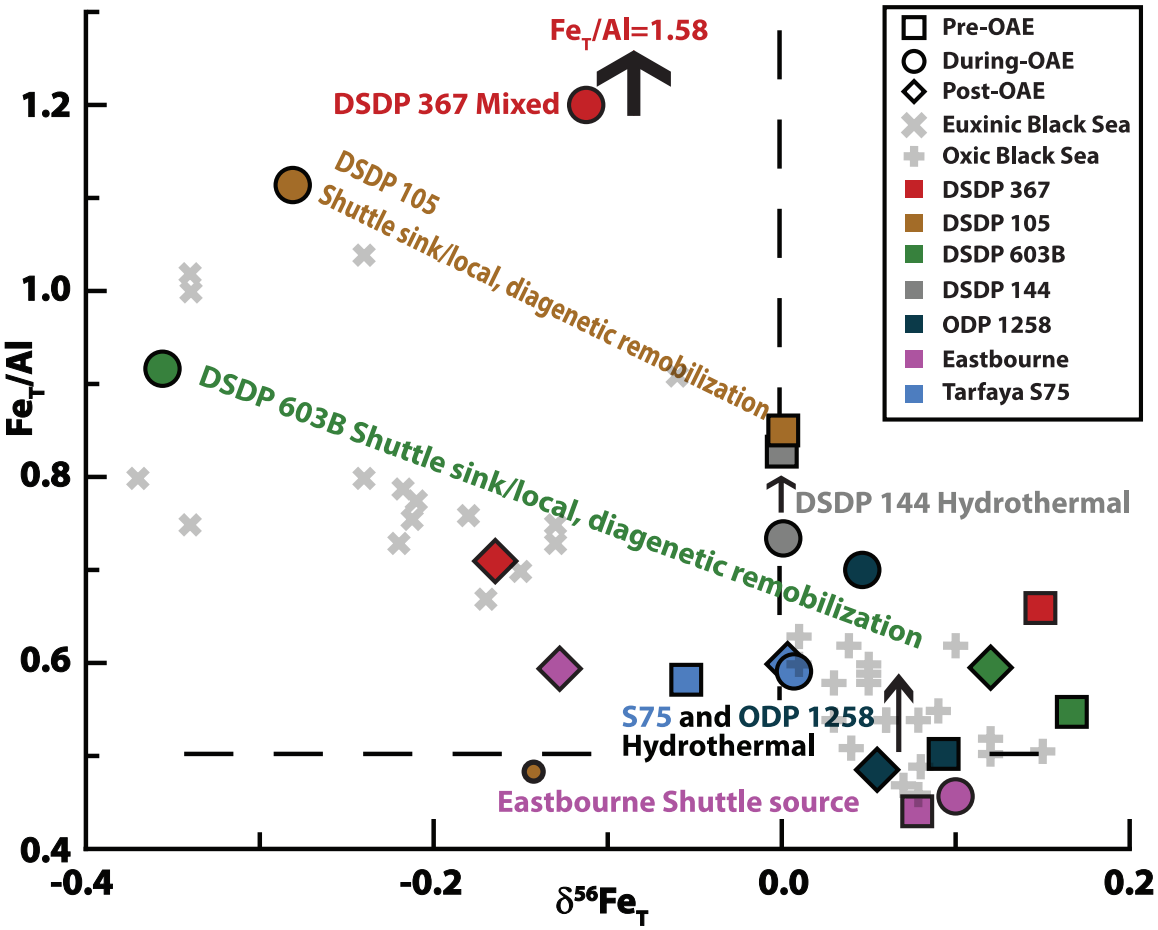

Figure 6.5: $\delta^{56}Fe_T$ averages for each site grouped as pre (□), post (○) and during (◇) OAE-2. In the background are data from euxinic (✖) and oxic (✚) [Severmann et al., 2008]. Post-OAE $\delta^{56}Fe_T$ at Eastbourne is represented by only one data point. Black dashed lines indicate average crustal values. Note that DSDP 144 is proximal to a mid-ocean ridge, and S75 and ODP 1258 are distal. Generally, sites 144, S75 and 1258 show variable Fe_T/Al enrichment without sympathetic isotopic change suggesting hydrothermal sourcing, but with different magnitudes of enrichment as a function of position relative to ridge.

sites 1258 and S75 show relatively small ranges in Fe_T/Al ratios (averaging 0.54 and 0.60, respectively) and isotope compositions (averaging 0.06 and 0.00‰, respectively) throughout the entire sections, site 367 shows marked Fe_T/Al enrichment during the OAE (average 1.58) with a relatively small negative $\delta^{56}Fe_T$ shift (average -0.11‰), perhaps, pointing to locally sourced Fe tied to mid-ocean ridge venting.

Iron cycling in the northern basin: diagenetic overprinting and the shuttle

In contrast to the southern sites, the two northern localities DSDP 603B and DSDP 105, do not show Mo enrichments before the OAE, implying that conditions remained largely oxic. However, despite the lack of Mo enrichments, site 105 shows elevated Fe_T/Al ratios that coincide with intermittent periods of black shale deposition even before the OAE (see lithostratigraphy in Fig. 6.2), which could mark anoxic conditions that were only weakly sulfidic. The OAE yielded samples at both sites with significantly elevated Fe_T/Al ratios, and black shales became more abundant, although oxic conditions likely dominated based on the lithostratigraphy and only slightly elevated Mo contents. Furthermore, both sites show high-low oscillations in Fe_T/Al roughly similar to the variability observed in TOC contents and lithofacies patterns (Figs. 6.2 and 6.3). Although the northern site 105 and southern site 367 have similarly large Fe enrichments, we infer based on the large negative shifts in $\delta^{56}Fe_T$ that site 105 received very little, perhaps, no hydrothermally sourced Fe.

The distinctly negative Fe isotope values (min. $\delta^{56}Fe_T$ = -1.43‰) measured at site 105 are similar to values measured by Jenkyns et al. (2007) in the Scaglia Bianca at Furlo, Italy (min. $\delta^{56}Fe_T$ = -1.7‰), and the sites share similar lithostratigraphic patterns with relatively thin black shale units intercalated within dominantly bioturbated oxic units. In the case of the Scaglia Bianca, shale units alternate with cherty limestones; at site 105 the laminated shales alternate with green claystones. The pattern of seemingly rapid $\delta^{56}Fe_T$ variability suggests redox controls during the OAE that correlate to the varying sedimentary facies, with positive $\delta^{56}Fe_T$ for the bioturbated sediments and negative $\delta^{56}Fe_T$ for the laminated organic-rich black shales. Such a relationship could reflect time-varying operation of the shuttle model over short, perhaps orbital, time scales. More likely, however, is small-scale diagenetic remobilization of Fe within

the sediment column, yielding Fe-poor to Fe-rich layers. Although the depositional conditions may have been dominantly oxic, some elevated molybdenum concentrations (in all lithologies) at sites 105 and 603B are consistent with transiently euxinic episodes during the OAE at these sites as also recorded in the organic richness of the black shales. However, the predominance of comparatively low Mo concentrations (OAE averages at 105 and 603 of 16 and 18, respectively) argues against persistent euxinia and suggests that the observed Fe patterns could be a secondary phenomenon tied mostly to stratigraphic variability in TOC content. Specifically, we suggest that the data reflect Fe mobilization within the sediments, whereby the organic- and sulfide-rich black shales capture Fe that is released from adjacent layers lacking organic matter and thus favoring bacterial iron reduction over sulfate reduction. Similar processes can be observed today in the Black Sea where a sulfidization front is formed by the opposing gradient between an organic-rich marine sapropel and an organic-lean but Fe-rich limnic unit (Neretin et al., 2004). Our Fe paleoredox proxies must thus be used with caution when interpreting juxtapositions (interlayering) of sediments with very different concentrations of TOC and methane in the case of sulfate reduction driven by AOM (anaerobic oxidation of methane). In a sense, though, the post-depositional remobilization and repartitioning of Fe mirrors the processes of the Fe shuttle, which, by contrast, operates on a basin scale rather than within the sediment column. In other words, isotopically light Fe migrates from organic-poor layers dominated by reductive Fe mobilization to organic- and sulfide-rich layers where the remobilized iron is recaptured quantitatively as pyrite. These two facies reflect dominantly oxic deposition and at least transient euxinia, respectively.

Of all the sites investigated, site 603B shows the most convincing fingerprint of enrichment via the Fe shuttle, with nearly all of the samples (11 out of 14) demonstrating a systematic anti-correlation between $\delta^{56}Fe_T$ and Fe_T/Al (Fig. 6.5), as defined by the Black

Sea trend. During the OAE, site 603B shows overall enrichments in Fe_T/Al (average: 0.92) and more negative $\delta^{56}Fe_T$ values (average: -0.36‰)—compared to pre- and post-OAE Fe_T/Al values that fall close to crustal averages (0.56 and 0.61, respectively), with $\delta^{56}Fe_T$ values that are shifted heavy compared to average crust (pre-OAE average: 0.17‰; post-OAE average: 0.12‰). Importantly, the high average Fe concentration and negative average $\delta^{56}Fe_T$ during the OAE were calculated using all the data, regardless of the lithofacies, and the largest Mo concentrations (extending up to 64 ppm) generally correlate with the more negative $\delta^{56}Fe_T$. The data point to euxinic condition with signs of redox variability. Unlike site 105, the Fe and Mo data point to a high frequency and persistence of euxinia during the OAE at site 603B, making it a better candidate for Fe inputs via the iron shuttle, despite lithologic observations from site 603B that indicate marked redox-transitions similar to those of site 105. Of course, diagenetic remobilization could overprint the primary shuttle signals. Most obvious is the challenge we face in untangling the shuttle signal from possible diagenetic overprint in sediments marked by alternating and thinly bedded organic-rich and organic-lean intervals.

Synthesis

Figures 6.4 and 6.5 provide us with a way to simplify a complex data set. For example, although there are similarities in their Fe_T/Al ratios, we note a distinctly smaller range in $\delta^{56}Fe_T$ values at site 367 compared to those at site 105 (Fig. 6.4), which likely points to differences in the Fe sources and enrichment processes. Past work has revealed a straightforward relationship between Fe_T/Al ratios and $\delta^{56}Fe_T$ seen at diverse times and places in the geologic record (e.g., Johnson et al., 2008). In the absence of strong hydrothermal inputs, euxinic enrichments in reactive iron expressed as elevated Fe_T/Al

ratios have consistently resulted in lower $\delta^{56}Fe_T$ values, mirroring corresponding Fe loss at shallow, oxic source regions—i.e., our shuttle model. These benthic processes at oxic sites leave a fingerprint of lowered Fe_T/Al with corresponding heavy $\delta^{56}Fe_T$. A systematic trend is observed between Fe_T/Al ratios and $\delta^{56}Fe_T$ in the modern, marginal marine Black Sea (Severmann et al., 2008) and ancient epicontinental Devonian shales (Duan et al., 2010). We assert that such processes likely operated during OAE2 (Fig. 6.5), although the signals are far more complex because of the much larger scale spatial scale of Fe cycling in the Cretaceous proto-Atlantic Ocean and the likelihood of large and pervasive hydrothermal inputs associated with activity along mid-ocean ridges within that basin.

Conclusions

The Fe cycle in the proto-North Atlantic during the Cretaceous is, not surprisingly, complex with multiple sources and sinks whose relative roles vary with position in the basin. The highly productive and anoxic shelves of the southern equatorial portions served as sinks, while the oxic shelves of the northern proto-North Atlantic seem to have served as Fe sources. Our data show that the southern portion of the proto-North Atlantic was influenced by hydrothermal Fe, but with a large portion of the northern basin lacking evidence for significant hydrothermal inputs. This contrast might reflect the difficulty of transporting Fe a significant distance in an oxic or sulfidic water column, since iron oxides and pyrite quickly precipitate and settle. Although Fe is more soluble in a sulfidic water column, pyrite precipitation poses a challenge to transporting Fe the great distances needed to enrich all of the proto-North Atlantic, whether sourced by hydrothermal or shuttle inputs. Our most enriched sites are restricted to the southern proto-North Atlantic and, based on the combined Fe_T/Al and $\delta^{56}Fe_T$ data, argue for an iron cycle dominated

by hydrothermal inputs, although site 367 likely bears the low-temperature impact of the shuttle as well.

When the data from this study are plotted with those from the Black Sea (Fig. 6.5), the northern sites (Eastbourne, 603B, and 105) are consistent with the predictions for shuttled Fe—i.e., Fe enrichments or depletions that vary systematically and antithetically with the Fe isotope trend. On the other hand, the Fe trends at 105 and 603B could reasonably be tied to secondary remobilization during burial diagenesis. We argue, particularly for site 603B, that both of these mechanisms are recorded. The potential for diagenetic overprints offers a cautionary note, but it is our good fortunate that such overprints can be independently anticipated by the often fine stratigraphic scale of extreme geochemical variability they reflect (e.g., sapropel layers in an package of oxic sediments). We can expect oxically deposited, organic-lean beds marked by Fe loss and a residual, heavy isotopic signature in close proximity to organic-rich shales with correspondingly high Fe concentrations and low isotopic compositions. Also, we can expect fundamentally different sulfur isotope properties for pyrite formed via two scenarios, with primary, water-column-formed euxinic pyrite often showing very light and uniform δ34S values (Lyons, 1997; Lyons et al., 2003) compared to secondary, diagenetic pyrite tied to Fe remobilization, which can be marked by pronounced δ34S enrichments (Jørgensen et al., 2004). The organic biomarkers for photic euxinia also provide independent insight. The hydrothermal signals, by contrast, should enrich Fe_T/Al without appreciable parallel variability in the $\delta^{56}Fe_T$.

Many authors have postulated that a major hydrothermal pulse predated the OAE and may have catalyzed the large positive carbon isotope excursion of the anoxic event through expanded primary production—perhaps linked to increased inputs of Fe and its importance as a micronutrient (Jenkyns, 2010, and references therein). Our data support

the presence of hydrothermal inputs, particularly in the southern proto-North Atlantic, and it is probably not a coincidence that this is the same portion of the basin that shows the strongest evidence for persistent and pervasive euxinia (see also Jenkyns, 2010). Nevertheless, the hydrothermal signal is neither consistently strong nor basin-wide; its global role as an essential OAE precursor awaits additional study.

Although complex, the Fe signals demonstrate that there were multiple Fe sources operating in the proto-North Atlantic before, during, and after the OAE. Unlike most pastapplications of the Fe proxies, our study captures processes operating on the scale of an ocean basin with an active mid-ocean ridge, in contrast to the marginal basins and epicontinental seas that have been emphasized in many past studies of Fe paleoproxies. Not surprisingly, the signals are confounded by the challenges of transporting Fe long distances under both oxic and anoxic-sulfidic conditions, given its insolubility in both cases. Furthermore, the vast spatial extents of Fe sequestration under large-scale euxinia place high demands on the end-member sources and specifically their abilities to dominate the Fe archived in the sediments at any particular site. We should expect that the elemental and isotopic signals are subtle in a system of this size, and they are. Our most important take-home message may be that the proto-Atlantic received elevated Fe inputs from several sources and that the redox state of the basin was not exclusively euxinic during OAE2. Both results point to previously unknown heterogeneity in depositional conditions and the associated biogeochemical cycling of iron.

References

Adams, D.D., Hurtgen, M.T., Sageman, B.B., 2010. Volcanic triggering of a biogeochemical cascade during Oceanic Anoxic Event 2. Nature Geoscience 3, 201–204.

Algeo, T.J., Lyons, T.W., 2006. Mo–total organic carbon covariation in modern anoxic marine environments: Implications for analysis of paleoredox and paleohydrographic conditions. Paleoceanography 21, PA1016.

Anderson, T.F., Raiswell, R., 2004. Sources and mechanisms for the enrichment of highly reactive iron in euxinic Black Sea sediments. American Journal of Science 304, 203–233.

Arnold, G.L., Weyer, S., Anbar, A.D., 2004. Fe Isotope Variations in Natural Materials Measured Using High Mass Resolution Multiple Collector ICPMS. Analytical Chemistry 76, 322–327.

Arthur, M.A., Dean, W.E., Pratt, L.M., 1988. Geochemical and climatic effects of increased marine organic carbon burial at the Cenomanian/Turonian boundary. Nature 335, 714–717.

Barron, E.J., 1983. A warm, equable Cretaceous: The nature of the problem. Earth-Science Reviews 19, 305–338.

Beard, B.L., Johnson, C.M., Skulan, J.L., Nealson, K.H., Cox, L., Sun, H., 2003. Application of Fe isotopes to tracing the geochemical and biological cycling of Fe. Chemical Geology: Isotopic records of microbially mediated processes 195, 87–117.

Bennett, S.A., Rouxel, O., Schmidt, K., Garbe-Schönberg, D., Statham, P.J., German, C.R., 2009. Iron isotope fractionation in a buoyant hydrothermal plume, 5°S Mid-Atlantic Ridge. Geochimica et Cosmochimica Acta 73, 5619–5634.

Berger, W.H., von Rad, U., 1972. Cretaceous and Cenozoic sediments from the Atlantic Ocean, in Hayes, D.E., Pimm, A.C., et al., *Init. Repts. DSDP,* 14: Washington (U.S. Govt. Printing Office), 787–886.

Blain, S., Bonnet, S., Guieu, C., 2008. Dissolved iron distribution in the tropical and sub tropical South Eastern Pacific. Biogeosciences 5, 269–280.

Blättler, C.L., Jenkyns, H.C., Reynard, L.M., Henderson, G.M., 2011. Significant increases in global weathering during Oceanic Anoxic Events 1a and 2 indicated by calcium isotopes. Earth and Planetary Science Letters 309, 77–88.

Bruland, K.W., Rue, E.L., Smith, G.J., DiTullio, G.R., 2005. Iron, macronutrients and diatom blooms in the Peru upwelling regime: brown and blue waters of Peru. Marine

Chemistry 93, 81–103.

Brumsack, H.J., 1980. Geochemistry of Cretaceous black shales from the Atlantic Ocean (DSDP Legs 11, 14, 36 and 41). Chemical Geology 31, 1–25.

Canfield, D.E., Lyons, T.W., Raiswell, R., 1996. A model for iron deposition to euxinic Black Sea sediments. American Journal of Science 296, 818–834.

Clayton, R.E., Nederbragt, A.J., Malinovsky, D., Andersson, P., Thurow, J., 2007. Data report: iron isotope geochemistry of mid-Cretaceous organic-rich sediments at Demerara Rise (ODP Leg 207). In Mosher, D.C., Erbacher, J., and Malone, M.J. (Eds.), Proc. ODP, Sci. Results, 207: College Station, TX (Ocean Drilling Program), 1–14.

Conrad, C.P., Lithgow-Bertelloni, C., 2007. Faster seafloor spreading and lithosphere production during the mid-Cenozoic. Geology 35, 29–32.

Coplen, T.B., 2011. Guidelines and recommended terms for expression of stable-isotope-ratio and gas-ratio measurement results. Rapid Communications in Mass Spectrometry 25, 2538–2560.

Cruse, A.M., Lyons, T.W., 2004. Trace metal records of regional paleoenvironmental variability in Pennsylvanian (Upper Carboniferous) black shales. Chemical Geology 206, 319–345.

Czaja, A.D., Johnson, C.M., Beard, B.L., Eigenbrode, J.L., Freeman, K.H., Yamaguchi, K.E., 2010. Iron and carbon isotope evidence for ecosystem and environmental diversity in the ~2.7 to 2.5 Ga Hamersley Province, Western Australia. Earth and Planetary Science Letters 292, 170–180.

Duan, Y., Severmann, S., Anbar, A.D., Lyons, T.W., Gordon, G.W., Sageman, B.B., 2010. Isotopic evidence for Fe cycling and repartitioning in ancient oxygen-deficient settings: Examples from black shales of the mid-to-late Devonian Appalachian basin. Earth and Planetary Science Letters 290, 244–253.

Elrod, V., Berelson, W., Coale, K., Johnson, K., 2004. The flux of iron from continental shelf sediments: a missing source for global budgets. Geophysical Research Letters 31, L12307.

Erbacher, J., Friedrich, O., Wilson, P.A., Birch, H., Mutterlose, J., 2005. Stable organic carbon isotope stratigraphy across Oceanic Anoxic Event 2 of Demerara Rise, western tropical Atlantic. Geochemistry, Geophysics, Geosystems 6, Q06010.

Frijia, G., Parente, M., 2008. Strontium isotope stratigraphy in the upper Cenomanian shallow-water carbonates of the southern Apennines: Short-term perturbations

of marine $^{87}Sr/^{86}Sr$ during the oceanic anoxic event 2. Palaeogeography, Palaeoclimatology, Palaeoecology 261, 15–29.

Gale, A.S., 1996. Turonian correlation and sequence stratigraphy of the Chalk in southern England. Geological Society, London, Special Publications 103, 177–195.

Halverson, G.P., Poitrasson, F., Hoffman, P.F., Nédélec, A., Montel, J.-M., Kirby, J., 2011. Fe isotope and trace element geochemistry of the Neoproterozoic syn-glacial Rapitan iron formation. Earth and Planetary Science Letters 309, 100–112.

Hayes, D.E., Pimm, A.C., Benson, W.E., Berger, W.H., Rad, U.v., Supko, P.R., Beckmann, J.P., Roth, P.H., 1972. Shipboard site reports, Sites 143 and 144. 14, 283–301.

Helz, G.R., Miller, C.V., Charnock, J.M., Mosselmans, J.F.W., Pattrick, R.A.D., Garner, C.D., Vaughan, D.J., 1996. Mechanism of molybdenum removal from the sea and its concentration in black shales: EXAFS evidence. Geochimica et Cosmochimica Acta 60, 3631–3642.

Herbin, J.P., Masure, E., Roucaché, J., 1987. Cretaceous formations from the lower continental rise off Cape Hatteras: organic geochemistry, dinoflagelate cysts, and the Cenomanian/Turonian boundary event at Sites 603 (Leg 93) and 105 (Leg 11). Init. Rep. Deep Sea Drill. Proj. 93, 1139–1160.

Herbin, J.P., Montadert, L., Muller, C., Gomez, R., Thurow, J., Wiedmann, J., 1986. Organic-rich sedimentation at the Cenomanian-Turonian boundary in oceanic and coastal basins in the North Atlantic and Tethys. Geological Society, London, Special Publications 21, 389–422.

Hetzel, A., Böttcher, M.E., Wortmann, U.G., Brumsack, H.-J., 2009. Paleo-redox conditions during OAE 2 reflected in Demerara Rise sediment geochemistry (ODP Leg 207). Palaeogeography, Palaeoclimatology, Palaeoecology 273, 302–328.

Hollister, C.D., Ewing, J.I., Habib, D., Hathaway, J.C., Lancelot, Y., Luterbacher, H., Paulus, F.J., Poag, F.J., Wilcoxon, J.A., Worstell, P., 1972. Site 105; lower continental rise hills, in *Initial reports of the Deep Sea Drilling Project* covering Leg 11 of the cruises of the drilling vessel “”Glomar Challenger””, Miami, Florida to Hoboken, New Jersey, April-June, 1970.

Huber, B.T., Hodell, D.A., Hamilton, C.P., 1995. Middle-Late Cretaceous climate of the southern high latitudes: Stable isotopic evidence for minimal equator-to-pole thermal gradients. Geological Society of America Bulletin 107, 1164–1191.

Jenkyns, H.C., 2010. Geochemistry of oceanic anoxic events. Geochemistry, Geophysics, Geosystems 11, Q03004.

Jenkyns, H.C., Matthews, A., Tsikos, H., Erel, Y., 2007. Nitrate reduction, sulfate reduction, and sedimentary iron isotope evolution during the Cenomanian-Turonian oceanic anoxic event. Paleoceanography 22, PA3208.

Jiménez Berrocoso, Á., MacLeod, K.G., Calvert, S.E., Elorza, J., 2008. Bottom water anoxia, inoceramid colonization, and benthopelagic coupling during black shale deposition on Demerara Rise (Late Cretaceous western tropical North Atlantic). Paleoceanography 23, PA3212.

Johnson, C.M., Beard, B.L., Roden, E.E., 2008. The Iron Isotope Fingerprints of Redox and Biogeochemical Cycling in Modern and Ancient Earth. Annual Review of Earth and Planetary Sciences 36, 457–493.

Jones, C.E., Jenkyns, H.C., 2001. Seawater Strontium Isotopes, Oceanic Anoxic Events, and Seafloor Hydrothermal Activity in the Jurassic and Cretaceous. American Journal of Science 301, 112–149.

Jørgensen, B.B., Böttcher, M.E., Lüschen, H., Neretin, L.N., Volkov, I.I., 2004. Anaerobic methane oxidation and a deep H_2S sink generate isotopically heavy sulfides in Black Sea sediments. Geochimica et Cosmochimica Acta 68, 2095–2118.

Keller, G., Han, Q., Adatte, T., Burns, S.J., 2001. Palaeoenvironment of the Cenomanian-Turonian transition at Eastbourne, England. Cretaceous Research 22, 391–422.

Kolonic, S., Wagner, T., Forster, A., Sinninghe Damsté, J.S., Walsworth-Bell, B., Erba, E., Turgeon, S., Brumsack, H.-J.r., Chellai, E.H., Tsikos, H., Kuhnt, W., Kuypers, M.M.M., 2005. Black shale deposition on the northwest African Shelf during the Cenomanian/Turonian oceanic anoxic event: Climate coupling and global organic carbon burial. Paleoceanography 20, PA1006.

Kuhnt, W., Luderer, F., Nederbragt, S., Thurow, J., Wagner, T., 2005. Orbital-scale record of the late Cenomanian-Turonian oceanic anoxic event (OAE-2) in the Tarfaya Basin (Morocco). International Journal of Earth Sciences 94, 147–159.

Kuhnt, W., Nederbragt, A., Leine, L., 1997. Cyclicity of Cenomanian-Turonian organic-carbon-rich sediments in the Tarfaya Atlantic Coastal Basin (Morocco). Cretaceous Research 18, 587–601.

Kuroda, J., 2007. Contemporaneous massive subaerial volcanism and late cretaceous Oceanic Anoxic Event 2. Earth and Planetary Science Letters 256, 211–223.

Kuypers, M.M.M., Lourens, L.J., Rijpstra, W.I.C., Pancost, R.D., Nijenhuis, I.A.,

Sinninghe Damsté, J.S., 2004. Orbital forcing of organic carbon burial in the proto-North Atlantic during oceanic anoxic event 2. Earth and Planetary Science Letters 228, 465–482.

Kuypers, M.M.M., Pancost, R.D., Nijenhuis, I.A., Sinninghe Damsté, J.S., 2002. Enhanced productivity led to increased organic carbon burial in the euxinic North Atlantic basin during the late Cenomanian oceanic anoxic event. Paleoceanography 17.

Leckie, R.M., Bralower, T.J., Cashman, R., 2002. Oceanic anoxic events and plankton evolution: Biotic response to tectonic forcing during the mid-Cretaceous. Paleoceanography 17, PA000623.

Lu, Z., Jenkyns, H.C., Rickaby, R.E.M., 2010. Iodine to calcium ratios in marine carbonate as a paleo-redox proxy during oceanic anoxic events. Geology 38, 1107–1110.

Lyons, T.W., 1997. Sulfur isotopic trends and pathways of iron sulfide formation in upper Holocene sediments of the anoxic Black Sea. Geochimica et Cosmochimica Acta 61, 3367–3382.

Lyons, T.W., Anbar, A.D., Severmann, S., Scott, C., Gill, B.C., 2009. Tracking Euxinia in the Ancient Ocean: A Multiproxy Perspective and Proterozoic Case Study. Annual Review of Earth and Planetary Sciences 37.

Lyons, T.W., Severmann, S., 2006. A critical look at iron paleoredox proxies: New insights from modern euxinic marine basins. Geochimica et Cosmochimica Acta 70, 5698–5722.

MacLeod, K.G., Martin, E.E., Blair, S.W., 2008. Nd isotopic excursion across Cretaceous ocean anoxic event 2 (Cenomanian-Turonian) in the tropical North Atlantic. Geology 36, 811–814.

Martin, J.H., Fitzwater, S.E., 1988. Iron deficiency limits phytoplankton growth in the north-east Pacific subarctic. Naute 331, 341–343.

Moffett, J.W., Goepfert, T.J., Naqvi, S.W.A., 2007. Reduced iron associated with secondary nitrite maxima in the Arabian Sea. Deep Sea Research Part I: Oceanographic Research Papers 54, 1341–1349.

Neretin, L.N., Böttcher, M.E., Jørgensen, B.B., Volkov, I.I., Lüschen, H., Hilgenfeldt, K., 2004. Pyritization processes and greigite formation in the advancing sulfidization front in the upper Pleistocene sediments of the Black Sea. Geochimica et Cosmochimica Acta 68, 2081–2093.

Pancost, R.D., Crawford, N., Magness, S., Turner, A., Jenkyns, H.C., Maxwell, J.R., 2004. Further evidence for the development of photic-zone euxinic conditions during Mesozoic oceanic anoxic events. Journal of the Geological Society 161, 353–364.

Paul, C.R.C., Lamolda, M.A., Mitchell, S.F., Vaziri, M.R., Gorostidi, A., Marshall, J.D., 1999. The Cenomanian-Turonian boundary at Eastbourne (Sussex, UK): a proposed European reference section. Palaeogeography, Palaeoclimatology, Palaeoecology 150, 83–121.

Poulton, S.W., Canfield, D.E., 2005. Development of a sequential extraction procedure for iron: implications for iron partitioning in continentally derived particulates. Chemical Geology 214, 209–221.

Raiswell, R., Anderson, T., 2005. Reactive iron enrichment in sediments deposited beneath euxinic bottom waters: constraints on supply by shelf recycling In: McDonald, I., Boyce, A.J., Butler, I., Herrington, R.J., Polya, D. (Eds.). Mineral Deposits and Earth Evolution London. Geol Soc London Spec Publ 218, 179–194.

Raiswell, R., Newton, R., Bottrell, S.H., Coburn, P.M., Briggs, D.E.G., Bond, D.P.G., Poulton, S.W., 2008. Turbidite depositional influences on the diagenesis of Beecher's Trilobite Bed and the Hunsruck Slate; sites of soft tissue pyritization. American Journal of Science 308, 105–129.

Schlanger, S.O., Arthur, M.A., Jenkyns, H.C., Scholle, P.A., 1987. The Cenomanian-Turonian Oceanic Anoxic Event, I. Stratigraphy and distribution of organic carbon-rich beds and the marine $\delta^{13}C$ excursion, in *Marine Petroleum Source Rocks*, edited by J. Brooks and A. J. Fleet. Geological Society, London, Special Publications 26, 371–399.

Schlanger, S.O., Jenkyns, H.C., 1976. Cretaceous anoxic events: causes and consequences. Geologie en Mijnbouw 55, 179–184.

Scholle, P.A., Arthur, M.A., 1980. Carbon isotope fluctuations in Cretaceous pelagic limestones; potential stratigraphic and petroleum exploration tool. AAPG Bulletin 64, 67–87.

Scott, C., Lyons, T.W., Bekker, A., Shen, Y., Poulton, S.W., Chu, X., Anbar, A.D., 2008. Tracing the stepwise oxygenation of the Proterozoic ocean. Nature 452, 456–459.

Severmann, S., Johnson, C.M., Beard, B.L., German, C.R., Edmonds, H.N., Chiba, H., Green, D.R.H., 2004. The effect of plume processes on the Fe isotope composition of hydrothermally derived Fe in the deep ocean as inferred from the Rainbow vent site, Mid-Atlantic Ridge, 36°14'N. Earth and Planetary Science Letters 225, 63–76.

Severmann, S., Johnson, C.M., Beard, B.L., McManus, J., 2006. The effect of early diagenesis on the Fe isotope compositions of porewaters and authigenic minerals in continental margin sediments. Geochimica et Cosmochimica Acta 70, 2006–2022.

Severmann, S., Lyons, T.W., Anbar, A., McManus, J., Gordon, G., 2008. Modern iron isotope perspective on the benthic iron shuttle and the redox evolution of ancient oceans. Geology 36, 487–490.

Severmann, S., McManus, J., Berelson, W.M., Hammond, D.E., 2010. The continental shelf benthic iron flux and its isotope composition. Geochimica et Cosmochimica Acta 74, 3984–4004.

Sharma, M., Polizzotto, M., Anbar, A.D., 2001. Iron isotopes in hot springs along the Juan de Fuca Ridge. Earth and Planetary Science Letters 194, 39–51.

Shipboard Scientific Party, 2004. Leg 207 summary, in Erbacher, J., Mosher, D.C., Malone, M.J., et al., *Proc. ODP, Init. Repts*., 207: College Station, TX (Ocean Drilling Program). 1–89.

Sinninghe Damsté, J.S., Köster, J., 1998. A euxinic southern North Atlantic Ocean during the Cenomanian/Turonian oceanic anoxic event. Earth and Planetary Science Letters 158, 165–173.

Sinton, C.W., Duncan, R.A., 1997. Potential links between ocean plateau volcanism and global ocean anoxia at the Cenomanian-Turonian boundary. Economic Geology 92, 836–842.

Skulan, J.L., Beard, B.L., Johnson, C.M., 2002. Kinetic and equilibrium Fe isotope fractionation between aqueous Fe(III) and hematite. Geochimica et Cosmochimica Acta 66, 2995–3015.

Snow, L.J., Duncan, R.A., Bralower, T.J., 2005. Trace element abundances in the Rock Canyon Anticline, Pueblo, Colorado, marine sedimentary section and their relationship to Caribbean plateau construction and oxygen anoxic event 2. Paleoceanography 20, PA3005.

Stookey, L.L., 1970. Ferrozine---a new spectrophotometric reagent for iron. Analytical Chemistry 42, 779–781.

Taylor, S.R., McLennan, S.M., 1995. The Geochemical Evolution of the Continental Crust. Reviews of Geophysics 33, 241–265.

Thurow, J., 1988. Cretaceous radiolarians of the North Atlantic Ocean: ODP Leg 103 (Sites 638, 640, and 641) and DSDP Legs 93 (Site 603) and 47B (Site 398), in Boillot, G., Winterer, E.L., et al., *Proc. ODP, Sci. Results*, 103: College Station, TX (Ocean Drilling Program), 379–418.

Trabucho Alexandre, J., Tuenter, E., Henstra, G.A., van der Zwan, K.J., van de Wal, R.S.W., Dijkstra, H.A., de Boer, P.L., 2010. The mid-Cretaceous North Atlantic nutrient trap: Black shales and OAEs. Paleoceanography 25, PA4201.

Tsikos, H., Jenkyns, H.C., Walsworth-Bell, B., Petrizzo, M.R., Forster, A., Kolonic, S., Erba, E., Premoli Silva, I., Baas, M., Wagner, T., Sinninghe Damsté, J.S., 2004. Carbon-isotope stratigraphy recorded by the Cenomanian–Turonian Oceanic Anoxic Event: correlation and implications based on three key localities. Journal of the Geological Society 161, 711–719.

Turekian, K.K., Wedepohl, K.H., 1961. Distribution of the Elements in Some Major Units of the Earth's Crust. Geological Society of America Bulletin 72, 175–192.

Turgeon, S.C., Creaser, R.A., 2008. Cretaceous oceanic anoxic event 2 triggered by a massive magmatic episode. Nature 454, 323–326.

van Bentum, E.C., Hetzel, A., Brumsack, H.-J., Forster, A., Reichart, G.-J., Sinninghe Damsté, J.S., 2009. Reconstruction of water column anoxia in the equatorial Atlantic during the Cenomania-Turonian oceanic anoxic event using biomarker and trace metal proxies. Palaeogeography, Palaeoclimatology, Palaeoecology 280, 489–498.

van Hinte, J.E., Wise, S.W., Jr., Biart, B.N.M., Covington, J.M., Dunn, D.A., Haggerty, J.A., Johns, M.W., Meyers, P.A., Moullade, M.R., Muza, J.P., Ogg, J.G., Okamura, M., Sarti, M., von Rad, U., Blakeslee, J.H., Whalen, E., 1987. Initial reports of the Deep Sea Drilling Project covering Leg 93 of the cruises of the drilling vessel Glomar Challenger, Norfolk, Virginia, to Norfolk, Virginia, May-June, 1983. 93, 1423.

Viollier, E., Inglett, P.W., Hunter, K., Roychoudhury, A.N., Van Cappellen, P., 2000. The ferrozine method revisited: Fe(II)/Fe(III) determination in natural waters. Applied Geochemistry 15, 785–790.

Wijsman, J.W.M., Middelburg, J.J., Heip, C.H.R., 2001. Reactive iron in Black Sea Sediments: implications for iron cycling. Marine Geology 172, 167–180.

Table 6.1: Geochemical data for DSDP site 105.

Sample ID	Depth (mbsf)	Al (wt%)	Fe_T (wt%)	Mo (ppm)	$\delta^{56}Fe_T$ (‰)	Error (2 STD)	Replicate $\delta^{56}Fe_T$ (n)
11 105 9-1 24-25	286.25	6.11	4.90	3	-0.08	0.05	2
11 105 9-1 79-80	286.79	5.87	7.08	5	-0.56	0.05	2
11 105 9-1 133-134	287.33	6.73	5.61	1	-0.05	0.13	2
11 105 9-2 10-11	287.60	8.82	6.32	BSC	-0.20	0.06	2
11 105 9-2 54-55	288.04	7.46	6.97	3	-0.28	0.16	2
11 105 9-2 57-58.5	288.07	6.10	1.78	4	0.15	0.09	4
11 105 9-2 77-78	288.27	5.83	6.75	1	-0.04	0.02	2
11 105 9-2 101-102	288.51	6.00	7.38	2	-0.26	0.11	2
11 105 9-2 115-116	288.65	4.23	12.90	4	-1.36	0.10	3
11 105 9-3 7-8	289.07	5.61	5.49	0	-0.05	0.07	3
11 105 9-3 57.5-58.5	289.57	5.34	5.86	2	0.15	0.09	3
11 105 9-3 71-72	289.71	6.37	5.75	BSC	-0.08	0.08	2
11 105 9-3 91-92	289.91	5.01	7.16	3	0.14	0.16	3
11 105 9-3 109-110	290.09	5.79	7.18	BSC	-0.97	0.16	2
11 105 9-3 126-127	290.26	3.11	2.42	51	-0.30	0.08	3
11 105 9-4 6-7	290.56	3.91	4.61	67	-0.46	0.11	3
11 105 9-4 38-39.5	290.88	6.47	3.75	46	-0.05	0.04	2
11 105 9-4 48-49	290.98	3.53	2.90	77	-0.09	0.07	3
11 105 9-4 82-83	291.32	3.50	11.60	33	-1.43	0.05	2
11 105 9-4 90-91	291.40	3.63	5.58	1	-0.25	0.03	2
11 105 9-4 101-103	291.51	4.10	3.15	5	0.09	0.17	2
11 105 9-4 114-115	291.64	4.59	2.97	BSC	-0.37	0.04	3
11 105 9-4 132-133	291.82	5.02	3.16	13	-0.07	0.16	3
11 105 9-5 8-9	292.08	5.00	4.48	14	-0.55	0.09	2
11 105 9-5 27-28	292.27	5.71	4.78	3	-0.08	0.00	2
11 105 9-5 49-50	292.49	6.11	4.43	2	-0.17	0.18	3
11 105 9-5 120-121	293.20	5.28	4.74	0	0.00	0.03	2
11 105 9-5 131-132	293.31	5.83	5.50	1	-0.18	0.10	2
11 105 9-5 141-142	293.41	6.63	4.09	0	-	-	-
11 105 9-6 8.5-9.5	293.59	6.06	4.37	0	0.05	0.08	4
11 105 9-6 24-25	293.74	6.44	5.55	2	0.03	0.09	3
11 105 9-6 75-76	294.25	5.86	5.33	2	-0.04	0.03	2
11 105 9-6 100-101	294.50	6.99	5.34	BSC	-0.05	0.04	3
11 105 10-1 50-51	295.50	5.07	5.61	2	0.42	0.07	2
11 105 10-1 94-95	295.94	5.02	5.34	0	0.38	0.01	2
11 105 10-1 146-147	296.46	4.82	4.54	2	-	-	-

Table 6.1: *continued*

Sample ID	Depth (mbsf)	Al (wt%)	Fe_T (wt%)	Mo (ppm)	$\delta^{56}Fe_T$ (‰)	Error (2 STD)	Replicate $\delta^{56}Fe_T$ (n)
11 105 10-2 12-13	296.62	7.40	7.10	1	0.21	0.02	2
11 105 10-2 65-66	297.15	5.79	4.13	BSC	0.09	0.07	2
11 105 10-2 79-80	297.29	5.70	3.81	1	-	-	-

Table 6.2: Geochemical data for DSDP site 144.

Sample ID	Depth (mbsf)	Al (wt%)	Fe_T (wt%)	Mo (ppm)	$\delta^{56}Fe_T$ (‰)	Error (2 STD)	Replicate $\delta^{56}Fe_T$ (n)
144 4-1 130-135	214.33	0.27	0.23	21	0.03	0.05	2
144 4-2 7-10	214.57	0.40	0.24	15	-0.03	0.00	2
144 4-2 78-80	215.29	0.05	0.07	6	0.01	0.02	2
144 4-2 94-97	215.45	1.06	0.69	59	-	-	-
144 4-2 136-138	215.87	0.72	0.66	77	0.02	0.08	1
144 4-3 77-78	216.77	1.05	0.32	22	-	-	-
144 4-3 115-116	217.15	1.08	0.65	47	0.08	0.03	2
144 4-3 137-138	217.37	0.77	0.90	97	0.07	0.00	2
144 5-1 27-28	217.77	3.13	2.37	3	-	-	-
144 5-1 74-75	218.24	2.37	2.11	3	-0.18	0.04	2

Table 6.3: Geochemical data for DSDP site 367.

Sample ID	Depth (mbsf)	Al (wt%)	Fe_T (wt%)	Mo (ppm)	$\delta^{56}Fe_T$ (‰)	Error (2 STD)	Error (2 STD)
367 17-2 102-107	618.52	7.10	5.00	28	-0.50	0.08	3
367 17-3 68-74	619.70	6.34	4.98	29	0.00	0.02	2
367 17-4 74-80	621.20	6.13	4.09	66	0.01	0.03	2
367 18-1 120-124	637.20	2.89	9.00	98	0.09	0.03	2
367 18-2 6-9	637.56	3.33	6.40	77	-0.05	0.02	2
367 18-2 59-62	638.09	3.42	7.76	226	-0.19	0.03	2
367 18-2 121-125	638.71	3.88	5.14	130	-0.04	0.04	2
367 18-3 39-42	639.39	2.86	6.17	127	-0.12	0.06	4
367 18-3 111-114	640.11	3.87	3.87	90	-0.01	0.06	4
367 18-4 40-43	640.90	2.57	3.42	197	-0.26	0.02	3
367 18-4 79-83	641.29	4.10	4.34	111	-0.38	0.07	3
367 18-4 121-125	641.71	3.60	3.14	201	-0.16	0.06	3
367 18-5 24-30	642.24	5.07	3.83	23	-0.03	0.00	2
367 18-5 100-106	643.00	3.85	2.82	412	0.20	0.05	2
367 19-1 143-147	645.93	4.46	2.56	93	0.05	0.01	2
367 19-2 14-18	646.14	5.46	3.79	195	0.18	0.10	3
367 19-2 89-94	646.89	6.48	4.35	36	-	-	-
367 19-3 43-47	647.93	4.88	3.10	93	0.15	0.05	3
367 19-4 62-66	649.62	4.38	2.83	84	0.15	0.07	2

Table 6.4: Geochemical data for DSDP site 603B.

Sample ID	Depth (mbsf)	Al (wt%)	Fe_T (wt%)	Mo (ppm)	$\delta^{56}Fe_T$ (‰)	Error (2 STD)	Replicate $\delta^{56}Fe_T$ (n)
93 603B 32-1 38-41	1109.88	6.31	2.79	2	-	-	-
93 603B 32-1 98-100	1110.48	5.74	2.77	2	-	-	-
93 603B 32-1 117-119	1110.67	5.09	3.84	2	-	-	-
93 603B 32-1 140-142	1110.90	5.42	3.46	3	-	-	-
93 603B 32-2 40-43	1111.40	4.57	4.59	2	-	-	-
93 603B 32-2 73-75	1111.73	6.16	4.16	2	-	-	-
93 603B 33-1 46-48	1118.96	5.60	4.44	3	-0.14	0.04	3
93 603B 33-1 65-68	1119.15	4.51	3.01	2	-	-	-
93 603B 33-1 82-83	1119.32	3.47	1.58	1	-	-	-
93 603B 33-1 87-89	1119.37	5.14	2.50	2	-	-	-
93 603B 33-1 136-138	1119.86	5.14	2.59	1	0.00	0.01	2
93 603B 33-2 42-44	1120.42	4.44	2.64	3	-	-	-
93 603B 33-2 70-72	1120.70	4.33	2.50	1	-	-	-
93 603B 33-2 112-114	1121.12	4.44	2.59	1	-	-	-
93 603B 33-3 21-23	1121.71	4.62	3.35	1	0.41	0.03	3
93 603B 33-3 50-52	1122.00	0.49	0.31	0	-	-	-
93 603B 33-3 98-100	1122.48	4.43	2.21	1	0.21	0.02	3
93 603B 33-3 122.5-124	1122.73	3.59	1.84	8	-	-	-
93 603B 34-1 42-43	1127.92	2.80	3.29	40	-0.70	0.03	3
93 603B 34-1 70-71	1128.20	4.52	2.91	64	-	-	-
93 603B 34-1 105-106	1128.55	4.42	3.55	24	-0.35	0.02	3
93 603B 34-1 121-122	1128.71	2.91	4.20	30	-	-	-
93 603B 34-2 36-37	1129.36	3.49	1.80	6	-	-	-
93 603B 34-2 67-68.5	1129.67	2.89	3.55	17	-0.40	0.03	2
93 603B 34-2 83-85	1129.83	3.27	2.66	25	-	-	-
93 603B 34-2 121-122	1130.21	3.89	2.47	13	-0.05	0.03	3
93 603B 34-3 21-22	1130.71	2.05	2.48	14	-	-	-
93 603B 34-3 51-52	1131.01	2.54	3.42	13	-0.08	0.01	3
93 603B 34-3 77-78	1131.27	4.57	4.67	5	-	-	-
93 603B 34-3 112-113	1131.62	3.85	2.71	2	-	-	-
93 603B 34-3 147-148	1131.97	4.12	5.31	9	-0.24	0.03	2
93 603B 34-4 27-29	1132.27	2.82	1.65	4	-	-	-
93 603B 34-4 67-68	1132.67	2.65	2.42	32	-0.36	0.02	3
93 603B 34-4 81-83	1132.81	4.20	2.96	2	-	-	-
93 603B 34-4 127-128	1133.27	2.45	3.14	24	-0.71	0.03	2
93 603B 34-5 18-22	1133.68	4.25	2.23	6	-	-	-

Table 6.4: *continued*

Sample ID	Depth (mbsf)	Al (wt%)	Fe_T (wt%)	Mo (ppm)	$\delta^{56}Fe_T$ (‰)	Error (2 STD)	Replicate $\delta^{56}Fe_T$ (n)
93 603B 34-5 52-54	1134.02	5.70	3.96	3	-	-	-
93 603B 34-5 87-89	1134.37	3.63	2.21	8	-	-	-
93 603B 34-6 3-4	1135.03	5.58	2.86	1	0.12	0.04	2
93 603B 34-6 21-22	1135.21	4.76	2.81	1	-	-	-
93 603B 34-6 41-42	1135.41	5.84	3.30	1	-	-	-
93 603B 35-1 34-35	1136.84	5.40	2.90	1	-	-	-
93 603B 35-1 72-73	1137.22	4.29	2.04	3	0.21	0.03	3
93 603B 35-1 127-129	1137.77	4.53	2.69	1	-	-	-
93 603B 35-2 20-21	1138.20	4.41	2.28	4	-	-	-
93 603B 35-2 57-58	1138.57	0.52	0.34	0	-	-	-
93 603B 35-2 78.5-80	1138.79	4.55	2.47	1	-	-	-
93 603B 35-2 106-108	1139.06	5.28	2.63	1	-	-	-
93 603B 35-2 135-137	1139.35	4.22	2.19	1	-	-	-
93 603B 35-3 16-17	1139.66	4.97	2.46	1	-	-	-
93 603B 35-3 48-49	1139.98	4.98	2.51	BSC	-	-	-
93 603B 35-3 87-89	1140.37	4.11	3.37	3	-	-	-
93 603B 35-3 125-127	1140.75	4.96	2.45	1	-	-	-

Table 6.5: Geochemical data for ODP site 1258. Italicized meter core depth (mcd) was adjusted according to MacLeod et al. (2008).

Sample ID	Depth (mcd)	Al (wt%)	Fe_T (wt%)	Mo (ppm)	$\delta^{56}Fe_T$ (‰)	Error (2 STD)	Replicate $\delta^{56}Fe_T$ (n)
1258A 42-2 52-55	416.77	5.11	1.91	105	0.12	0.04	2
1258A 42-3 60-62	418.24	5.51	1.95	102	0.13	0.04	3
1258A 42-4 77-78.5	419.48	1.02	0.55	49	-	-	-
1258A 42-5 12-15	420.29	2.68	1.09	107	0.03	0.03	3
1258A 42-5 87-88	421.04	0.79	0.54	42	0.12	0.08	3
1258A 42-6 2-4	421.51	2.07	0.95	81	-0.04	0.04	3
1258A 42-6 17-18	421.66	2.15	0.91	78	0.11	0.09	2
1258A 42-6 32-34	421.81	2.49	1.14	89	-	-	-
1258A 42-6 60-62	422.09	2.18	1.07	76	-	-	-
1258A 42-6 77-79	422.26	3.11	3.25	49	-0.08	0.03	2
1258A 42-6 113-115	422.62	3.59	2.44	73	0.07	0.03	3
1258A 42-7 7-9	422.96	3.32	2.16	31	0.09	0.02	3
1258A 42-7 33-35	423.22	3.15	1.66	53	0.01	0.02	3
1258A 42-7 79-80	423.68	1.44	1.30	7	0.12	0.05	3
1258A 42-7 92-94	423.81	2.86	1.74	20	0.04	0.04	2
1258A 42-7 132-135	*426.41*	3.17	1.79	308	0.05	0.03	3
1258A 42-CCW 4-5	*426.54*	1.88	0.93	77	0.09	0.04	2
1258A 43-1 41-42	*426.96*	1.06	0.60	75	0.09	0.02	2
1258A 43-1 66-68	*427.14*	2.43	1.02	72	0.09	0.06	3
1258A 43-2 4-5	*427.80*	1.16	0.65	73	0.08	0.04	3
1258A 43-2 26-28	*428.02*	2.80	1.23	100	-	-	-
1258A 43-2 42-44	*428.18*	2.63	1.15	94	-	-	-
1258A 43-2 100-105	*428.76*	2.30	1.21	119	0.11	0.01	2
1258A 43-2 124-126	*429.00*	3.10	1.44	120	0.10	0.05	3
1258A 43-3 4-7	*429.06*	3.19	1.49	92	-	-	-
1258A 43-3 88.5-90	*429.91*	1.39	0.73	100	-		

Table 6.6: Geochemical data for Eastbourne.

Sample ID	Height (m)	Al (wt%)	Fe_T (wt%)	Mo (ppm)	$\delta^{56}Fe_T$ (‰)	Error (2 STD)	Replicate $\delta^{56}Fe_T$ (n)
WC ±650	18.90	0.63	0.50	-	-	-	-
WC ±600	18.40	0.16	0.12	BSC	-0.13	0.00	2
WC ±550	17.90	1.63	0.75	-	-	-	-
WC ±500	17.40	1.55	0.71	-	-	-	-
WC ±450	16.90	0.43	0.21	-	-	-	-
WC ±400	16.40	0.71	0.38	-	-	-	-
WC ±350	15.90	0.93	0.35	BSC	0.18	0.01	2
WC ±300	15.40	0.76	0.30	BSC	-	-	-
WC ±250	14.90	0.54	0.23	-	-	-	-
WC ±200	14.40	0.57	0.26	BSC	-	-	-
WC ±160	14.00	0.58	0.27	0.11	-	-	-
WC ±140	13.80	1.41	0.56	0.14	-	-	-
WC ±120	13.60	0.82	0.43	0.07	0.07	0.02	2
PM ±100	13.40	0.90	0.47	BSC	-	-	-
PM ±80	13.20	0.80	0.47	0.14	-	-	-
PM ±60	13.00	0.72	0.45	BSC	-	-	-
PM ±40	12.80	2.91	1.36	BSC	0.29	0.02	2
PM ±20	12.60	0.76	0.42	BSC	-	-	-
PM+640	12.40	0.65	0.43	BSC	-	-	-
PM+620	12.20	2.05	1.03	BSC	0.04	0.01	2
PM+600	12.00	1.68	0.88	BSC	-	-	-
PM+580	11.80	1.76	0.91	BSC	-	-	-
PM+560	11.60	1.57	0.73	BSC	0.11	0.05	2
PM+540	11.40	1.72	0.79	BSC	-	-	-
PM+520	11.20	1.57	0.69	0.12	-	-	-
PM+500	11.00	1.42	0.63	BSC	-	-	-
PM+480	10.80	0.87	0.44	BSC	-0.03	0.03	2
PM+460	10.60	0.83	0.41	BSC	-	-	-
PM+440	10.40	1.16	0.52	BSC	-	-	-
PM+420	10.20	1.02	0.48	BSC	-	-	-
PM+400	10.00	1.11	0.50	0.00	-	-	-
PM+380	9.80	1.12	0.50	BSC	-	-	-
PM+360	9.60	1.39	0.64	BSC	0.07	0.08	2
PM+340	9.40	1.44	0.65	BSC	-	-	-
PM+320	9.20	2.11	1.01	BSC	0.10	0.05	2
PM+300	9.00	2.16	0.92	BSC	-	-	-

Table 6.6: *continued*

Sample ID	Height (m)	Al (wt%)	Fe_T (wt%)	Mo (ppm)	$\delta^{56}Fe_T$ (‰)	Error (2 STD)	Replicate $\delta^{56}Fe_T$ (n)
PM+280	8.80	2.27	0.96	BSC	-	-	-
PM+260	8.60	1.60	0.70	BSC	0.08	0.08	2
PM+240	8.40	1.87	0.72	BSC	-	-	-
PM+220	8.20	1.61	0.62	BSC	-	-	-
PM+200	8.00	1.69	0.62	BSC	-	-	-
PM+180	7.80	1.81	0.78	BSC	-	-	-
PM+160	7.60	1.89	0.74	0.37	-	-	-
PM+140	7.40	1.92	0.73	BSC	0.09	0.02	2
PM+120	7.20	1.79	0.71	BSC	-	-	-
PM+100	7.00	2.11	0.82	BSC	-	-	-
PM+80	6.80	2.03	0.80	0.07	-	-	-
PM+60	6.60	1.74	0.65	BSC	0.12	0.00	2
PM+40	6.40	1.52	0.59	BSC	-	-	-
PM+20	6.20	2.44	0.88	BSC	-	-	-
GC-0	6.00	1.03	0.41	0.38	-	-	-
GC-20	5.80	0.87	0.35	0.27	-	-	-
GC-40	5.60	0.72	0.32	BSC	-0.02	0.04	2
GC-60	5.40	0.63	0.28	BSC	-	-	-
GC-80	5.20	0.71	0.31	0.85	-	-	-
GC-100	5.00	0.64	0.29	BSC	-	-	-
GC-120	4.80	0.45	0.22	0.16	-	-	-
GC-140	4.60	0.41	0.20	BSC	-	-	-
GC-160	4.40	0.50	0.23	0.49	0.05	0.07	3
GC-180	4.20	0.44	0.22	BSC	-	-	-
GC-200	4.00	0.56	0.24	BSC	-	-	-
GC-220	3.80	0.46	0.22	BSC	-	-	-
GC-240	3.60	0.67	0.29	BSC	0.13	0.03	2
GC-260	3.40	1.06	0.41	BSC	-	-	-
GC-280	3.20	1.11	0.43	0.20	-	-	-
GC-300	3.00	0.44	0.22	BSC	-	-	-
GC-320	2.80	0.45	0.23	BSC	-	-	-
GC-340	2.60	0.43	0.22	0.07	-0.00	0.01	2
GC-360	2.40	0.52	0.25	BSC	-	-	-
GC-380	2.20	0.80	0.36	0.08	-	-	-
GC-400	2.00	0.83	0.34	BSC	-	-	-
GC-410	1.90	0.66	0.29	0.41	-	-	-

Table 6.6: *continued*

Sample ID	Height (m)	Al (wt%)	Fe_T (wt%)	Mo (ppm)	$\delta^{56}Fe_T$ (‰)	Error (2 STD)	Replicate $\delta^{56}Fe_T$ (n)
GC 420	1.80	0.75	0.31	BSC	-	-	-
GC-440	1.60	0.76	0.30	0.16	-	-	-
GC-480	1.40	0.51	0.26	0.40	-	-	-
GC-500	1.20	0.77	0.34	0.26	0.11	0.04	3
GC-520	0.90	1.23	0.50	BSC	-	-	-
GC-540	0.80	1.25	0.46	BSC	0.22	0.06	2
GC-560	0.60	0.85	0.35	BSC	-	-	-
GC-580	0.40	0.85	0.36	0.06	-	-	-
GC-600	0.20	0.52	0.26	BSC	-	-	-

Table 6.6: Geochemical data for Tarfaya S75.

Sample ID	Height (m)	Al (wt%)	Fe_T (wt%)	Mo (ppm)	$\delta^{56}Fe_T$ (‰)	Error (2 STD)	Replicate $\delta^{56}Fe_T$ (n)
S 75 34	50.41	0.58	0.35	13	-	-	-
S 75 36	52.37	0.97	0.55	11	-	-	-
S 75 40	54.05	1.10	0.74	6	-	-	-
S 75 43	56.37	1.87	1.04	28	0.00	0.04	2
S 75 45	58.14	0.35	0.21	8	-	-	-
S 75 46	59.00	2.24	1.54	92	-	-	-
S 75 48	59.74	6.86	4.26	494	-	-	-
S 75 54	64.31	3.43	1.84	42	-	-	-
S 75 59	66.36	0.80	0.41	7	-0.05	0.06	3
S 75 64	70.55	1.09	0.57	12	-0.15	0.05	4
S 75 65 AI	72.06	2.07	1.33	13	0.01	0.10	3
S 75 65 BE	74.00	2.02	1.69	15	0.15	0.09	4
S 75 67	75.94	0.55	0.26	3	-0.10	0.04	3
S 75 72	79.06	0.01	0.00	0	-0.03	0.05	3
S 75 76B	82.18	1.17	0.93	49	-0.01	0.03	2
S 75 76E	86.51	2.24	1.25	7	-	-	-
S 75 77U	87.46	0.46	0.22	BSC	-0.06	0.06	2
S75 77X	87.90	0.38	0.21	0	-0.07	0.08	2
S 75 79	88.87	2.29	1.11	22	0.13	0.09	4
S 75 81	90.60	0.36	0.20	5	0.26	0.15	4
S 75 84	92.09	0.54	0.29	11	-0.01	0.21	3
S75 85	93.48	2.31	1.31	65	-	-	-
S75 86	94.33	1.11	0.71	42	-0.10	0.04	2
S 75 90	97.28	0.91	0.56	18	-	-	-

Chapter 7

Final Synthesis

Conclusions

It was widely thought that once oxygen rose to near modern values at the Precambrian-Cambrian boundary that the Phanerozoic climate was relatively stable (with the exception of the "big 5" extinctions) but the last several decades of research have documented numerous natural and cyclic climate perturbations that have transformed the Earth's chemical and biological evolution. The most well documented of these events during the Cretaceous had been hypothesized to have global anoxia and pervasive euxinia that had global implications extinction record preserved in the geologic record. The data presented in preceding chapters suggest that the extent of euxinia might be limited to much smaller portion of the ocean than previously estimated based on two geochemical proxies using several lithologies, it is nonetheless clear that the global redox state of the ocean had profound effects on the climate and biological realms. However, our understanding of the extent and timing of low oxygen and/or anoxia remains unclear and will require additional redox proxy development for this frontier.

Even less is understood about the underpinning mechanisms behind the initiation and termination of these events but it seems OAE2, and other OAEs, is likely tied to numerous initiation mechanisms. For example, Fe isotopes suggest that only euxinic portions of the ocean were influenced by hydrothermal activity delivering an important biolimiting element to the ocean and increasing low oxygen/anoxia preceding the OAE could enhance phosphorus regeneration from sediments thus increase primary production. It is difficult to untangle the relative importance of these mechanisms but both likely played a role in the magnitude of this event. Continuing to comprehend trace metal availability during periods of low marine dissolved oxygen and understanding the duration of the climatic and biological feedbacks during periods of high atmospheric oxygen concentrations is important for past and future climate perturbations. A

vast amount of information remains to be deciphered in the chemical archive of the sedimentary record delving further into the integrated record with the intersection of modeling, geochemistry, geobiology and computer simulations.